UNIVERSITY OF LEEDS

COMPUTATIONAL MODELLING OF CLOSE-COUPLED GAS ATOMIZATION

Aadhithya Priyadharshini Ashokkumar

School of Chemical and Process Engineering

University of Leeds

Submitted in accordance with the requirement for the degree of

Doctor of philosophy

University of Leeds

School of Chemical And Process Engineering

October 2020

The candidate confirms that the work submitted is his/her own and that appropriate credit has been given where reference has been made to the work of others.

This copy has been supplied on the understanding that it is copyright material and that no quotation from the thesis may be published without proper acknowledgement.

Assertion of moral rights:

The right of Aadhithya Priyadharshini Ashokkumar to be identified as Author of this work has been asserted by her in accordance with the Copyright, Designs and Patents Act 1988.

© <October 2020> The University of Leeds and of Aadhithya Priyadharshini Ashokkumar

Acknowledgement

I would like to thank the following people for helping me complete this research, and without whom I would not have made it through my doctoral degree.

Foremost, I would like to express my sincere gratitude to Professor Andrew Mullis for providing this opportunity and for his insight and knowledge into the subject matter steered me through this research. I would like to thank him for the patience and the continued support through these four years.

I would like to express my gratitude to Dr Duncan Borman for his insights and support.

I would like to thank my mother and my father for funding my doctoral degree. I am ever so grateful to my parents and my brother for all support they provided through this research. I would like to thank my soon-to-be husband, Swapnil for the continued support and patience to put up with my stresses and moans.

I would like to apologise to all my fur-babies for being busy (and away) through this period.

Finally, I would like to thank everyone for believing in me.

Abstract

The demand for metal powders have increased with the recent advancements in additive manufacturing technology and this increase in demand has led to a tight powder size distribution constraint. The production of powders through CCGA is a complicated process and the relationship between various process and geometrical parameters is not completely understood. Few features of CCGA process cannot be analysed in depth experimentally. The high temperature of melt prevents the interaction between the melt and the gas from being analysed. The pressure developed in front of the melt nozzle i.e., the aspiration pressure with the presence of melt in the chamber cannot be studied due to the high temperature of the melt. The flow features such as recirculation zone also cannot be analysed in detail. A three-dimensional model of the whole CCGA process is computationally intensive and requires appropriate approximations. The thesis can be divided into two parts. In the first part, the axisymmetric nature of the annular slit nozzle has been taken advantage and a two-dimensional model has been developed. This model has been validated against the Schlieren images of gas flow pattern produced by a conventional discrete-jet atomizer nozzle. This model is used to analyse the flow features in Eulerian approach and the melt-gas interaction in Lagrangian approach. The relationship between flow features (shocks, stagnation point, Mach disk) and melt droplet movement have been analysed in depth for the annular slit atomizer. The pulsation phenomenon observed in CCGA has also been analysed. Finally, the aspiration pressure has been analysed comprehensively in flow fields with and without melt. In the second part, flow features around two discrete-jet atomizer nozzles has been analysed in Eulerian approach. Periodic models have been implemented to overcome high computational requirements. The wake condition and aspiration pressure has been found for all the pressures considered for these both nozzles. Few of the main results obtained in this study are as follows.

- Presence of melt affects the aspiration pressure and hence gas-only flow field aspiration pressures are not good guide for commercial atomizers.
- Movement of particles depends on the relative position of shocks and the expansion waves. This in turn affects the residence times and the velocity possessed by the particles which influences the final particle size.
- A three-dimensional model is required to model the flow features in discrete-jet atomizers due to the presence of intermittent spacing between the discrete jets.

CONTENTS

1 INTRODUCTION 1

1.1 Challenges 2

1.2 Objectives 3

1.3 Outline of the thesis 3

2 BACKGROUND SCIENCE 5

2.1 Gas Atomization 6

2.2 Flow Physics 7

2.2.1 Compressibility: 8

2.2.2 Ideal gas: 10

2.2.3 Different kinds of flows: 11

2.2.4 Reflection and intersection of shocks and expansion waves: 13

2.2.5 Multiphase flow: 15

2.3 Computational Fluid Dynamics: 16

2.3.1 Single phase flows: 16

2.3.2 Boussinesq Approximation: 23

2.3.3 Different turbulence models 23

2.3.4 Multiphase phase flows: 26

2.3.5 Discrete phase method 29

2.3.6 Solution methods 31

3 LITERATURE REVIEW 33

3.1 Fundamental Science 33

3.1.1 Breakup mechanism: 33

3.1.2 Primary breakup: 35

3.1.3 Secondary breakup: 39

3.2 Wake Closure Phenomenon 40

3.3 Design parameters affecting the performance. 44

3.3.1 Gas jet delivery design 44

3.3.2 Melt delivery nozzle 48
3.4 Effect of the atomizing gases 51
3.5 Gas Metal Ratio 52
3.6 Powder size distribution 53
3.7 Review of numerical works 55
4 TWO-DIMENSIONAL SINGLE PHASE (GAS) ANALYSIS 59
4.1 METHODOLOGY 59
4.1.1 Establishing a numerical domain 59
4.1.2 Mesh generation 62
4.1.3 Material used 63
4.1.4 Boundary condition 63
4.2 RESULTS AND DISCUSSION 64
4.2.1 Mesh Independence study 64
4.2.2 Boundary Independence study: 68
4.2.3 Turbulence model sensitivity study: 71
4.2.4 Atomizer profile. 73
4.3 FLOW DYNAMICS OF VARIOUS ATOMIZING PRESSURES. 75
4.3.1 1 MPa atomizing pressure: 75
4.3.2 3MPa atomizing pressure: 77
4.3.3 4.5 MPa atomizing pressure: 79
4.3.4 5 MPa atomizing pressure: 81
5 TWO-DIMENSIONAL TWO-PHASE ANALYSIS 85
5.1 METHODOLOGY 86
5.1.1 Eulerian settings and assumptions: 87
5.1.2 Lagrangian settings and assumptions: 87
5.1.3 Use of Stochastic modelling 92
5.1.4 Particle Mass concentration 93
5.1.5 Aspiration pressure 94
5.2 RESULTS AND DISCUSSION 95

5.2.1 Particle Mass concentration 95
5.2.2 Volumetric flow rate at recirculation zone's eye 98
5.2.3 Particle Trajectories 99
5.2.4 Changes in flow field 121
5.2.5 Residence time of particles 126
5.2.6 Velocity of the particles 130
5.2.7 Aspiration pressure 135
6 THREE-DIMENSIONAL SINGLE PHASE (GAS) ANALYSIS 139
6.1 METHODOLOGY 141
6.1.1 Establishing the numerical domain 141
6.1.2 Mesh Generation 143
6.1.3 Material used: 145
6.1.4 Boundary conditions: 145
6.1.5 General Setup 145
6.2 RESULTS AND DISCUSSION 145
6.2.1 Mesh Independence study. 145
6.2.2 Flow dynamics for the conventional discrete jet atomizer 147
6.2.3 Flow dynamics for the novel discrete jet atomizer 153
7 NEED FOR THREE-DIMENSIONAL MODEL 161
7.1 METHODOLOGY 161
7.2 RESULTS AND DISCUSSION 163
8 DISCUSSION 169
8.1 Flow features 169
8.2 Influence of geometrical parameters 179
8.2.1 Intermittent spacing 179
8.2.2 Offset distance 180
8.3 The particle movement and GMR dependence 182
8.4 Velocity of the particles 183
8.5 Residence time of the particles 185

8.6 Aspiration pressure 187
8.7 Pulsatile model 192
8.8 Critical assessment of the models. 193
9 CONCLUSION 197
REFERENCES i
A. APPENDIX vi

LIST OF FIGURES

Figure 1.1 Different types of powder production techniques [6]. *1*
Figure 2.1 Schematic representation of free-fall and confined atomizer. [22] *6*
Figure 2.2 Flow separation over the plate (a) Initial flow over the plate (b) Flow just before separation (c) separated flow. [27] *8*
Figure 2.3 Flow changes in nozzle and diffuser. [22] *11*
Figure 2.4 Behaviour of shock at concave point (recompression shocks) and convex points (expansion waves). [26] *12*
Figure 2.5 Shock waves formed in an over-expanded flow field. [26] *14*
Figure 2.6 Shock-waves formed in an under-expanded flow field with the Mach disk [26] *14*
Figure 2.7 Schematic representation of fluid element with mass flowing in and out of it. [29] *16*
Figure 2.8 Schematic representation of stress components on the fluid element [29] *18*
Figure 2.9 Fluid element with x-component of pressure forces and viscous forces *18*
Figure 3.1 Schematic representation of melt and the nozzle *34*
Figure 3.2 Schematic representation of the melt breakup.[54] *35*
Figure 3.3 Various types of liquid column breakup mechanism. [74] *37*
Figure 3.4 various types of liquid film breakup. [55] *37*
Figure 3.5 different types of secondary breakup. (a) Twins: 10.7≤We (b) bag breakup 12≤We≤100 (c) Film stripping 100≤We≤350 (d) Catastrophic 350≤We. [81] *39*
Figure 3.6 Gas flow field in the nearfield region. [22] *40*
Figure 3.7 Schematic representation of open and closed wake conditions. [22] *41*
Figure 3.8 Schematic representation of the pulsation seen during atomization. [23] *43*
Figure 3.9 schematic representation of bottom view of annular slit confined feed (left) and discrete jet confined feed (right). [92] *44*
Figure 3.10 cross-sectional view of the USGA atomization nozzle(a) and HPGA nozzle(b). [93] *45*
Figure 3.11 schematic representation of CD nozzle. [96] *46*
Figure 3.12 schematic representation of HPGA 111 atomizer. [93] *47*
Figure 3.13 cross-sectional view of an atomizer *48*
Figure 3.14 schematic representation of different protuberance lengths. [91]] *49*
Figure 3.15 Cross-sectional view of the atomizer with concave melt tip. [91] *50*
Figure 3.16 Bottom view of the conventional gas die and gas die with increased diameter. [100] *51*
Figure 3.17 Designs considered by Motaman that produced low WCPs. [101] *51*
Figure 3.18 powders with different morphologies. [106] *54*
Figure 3.19 a distribution curve highlighting d50, d10 *and* d90. *[107]* *55*
Figure 4.1 Schematic representation of the nozzle with dimensions *60*
Figure 4.2 Schematic representation of the domain *60*
Figure 4.3 schematic representation of the domain with melt delivery tube *61*
Figure 4.4 Velocity vector plots for the melt delivery tube modelled as outlet (top) and inlet(bottom) for 1MPa atomizing pressure *61*

Figure 4.5 Schematic representation of boundary conditions 63
Figure 4.6 Schematic representation of compartmentalized domains 65
Figure 4.7 Schematic representation of the mesh considered in this study (18000 elements) 65
Figure 4.8 Location of rakes in the flow domain 66
Figure 4.9 Velocity magnitudes across the rake 1 near the gas jet expansion 66
Figure 4.10 Velocity magnitudes across rake 2 near the melt delivery tube 67
Figure 4.11 velocity contour plots for 1MPa atomizing pressure for all three meshes considered. 68
Figure 4.12 velocity contour plots for domains with lengths 50mm and 70mm along z direction 69
Figure 4.13 Variation of velocity magnitude in the Z-direction 69
Figure 4.14 velocity contours for various domain lengths in r-direction 70
Figure 4.15 Comparisons of various turbulence models for 1MPa atomizing pressure 71
Figure 4.16 Velocity magnitude along the axis using the three turbulence models considered 72
Figure 4.17 Velocity contour plots for 4.5 MPa operating pressure in all the turbulence models considered in this study 72
Figure 4.18 Comparison of 4.5 MPa velocity contour plots with Schlieren photograph produced by Motaman 73
Figure 4.19 velocity contour plots showing the flow separation for a longer protuberance length (3.16 mm) 74
Figure 4.20 Velocity contour plots for 1MPa atomizing pressure for the whole domain and the recirculation zone 75
Figure 4.21 Velocity vector plots for 1MPa atomizing pressure for the whole domain and the recirculation zone 76
Figure 4.22 pressure plots of the recirculation zone for 1MPa atomizing pressure 76
Figure 4.23 Velocity contour plots for 3MPa atomizing pressure for the whole domain and the recirculation zone 77
Figure 4.24 Velocity vector plots for 3MPa atomizing pressure for the whole domain and the recirculation zone 78
Figure 4.25 pressure plots of the recirculation zone for 3MPa atomizing pressure 78
Figure 4.26 Velocity contour plots for 4.5MPa atomizing pressure for the whole domain and the recirculation zone 79
Figure 4.27 Velocity vector plots for 4.5MPa atomizing pressure for the whole domain and the recirculation zone 80
Figure 4.28 pressure plots of the recirculation zone for 4.5 MPa atomizing pressure 80
Figure 4.29 Velocity contour plots for 5MPa atomizing pressure for the whole domain and the recirculation zone 81
Figure 4.30 Velocity vector plots for 5MPa atomizing pressure for the whole domain and the recirculation zone 82
Figure 4.31 pressure plots of the recirculation zone at 5MPa atomizing pressure 82
Figure 5.1 schematic representation of the melt nozzle and the melt. 88
Figure 5.2 different types of injection systems considered 90

Figure 5.3 The injections with their corresponding numbers as used in study.. 92
Figure 5.4 comparison of particle trajectories between models with and without stochasticity..... 93
Figure 5.5 Location of the plane in the recirculation zone..... 93
Figure 5.6 Location of rake (with 20 points) where aspiration pressure is calculated. 94
Figure 5.7 Graph showing particle mass concentration ($mgmm^{-3}$) vs time steps (ms) 96
Figure 5.8 the vector plots of recirculation zone for 3MPa atomizing pressure showing the eye of recirculation zone.....97
Figure 5.9 Velocity vector plots for the 5 MPa case with the line along which the volumetric flow rate is measured..... 98
Figure 5.10 Velocity vector plots and particle trajectories for flow time t= 0 ms 99
Figure 5.11 Velocity vector plots and particle trajectories for flow time t= 0.1 ms 99
Figure 5.12 Velocity vector plots and particle trajectories for flow time t= 0.5 ms..... 100
Figure 5.13 Velocity vector plots and particle trajectories for flow time t= 1 ms 100
Figure 5.14 Velocity vector plots and particle trajectories for flow time t= 1.5 ms 101
Figure 5.15 Velocity vector plots and particle trajectories for flow time t= 2 ms..... 101
Figure 5.16 Velocity vector plots and particle trajectories at various flow times t= 5ms, 8ms 10ms 102
Figure 5.17 Velocity vector plots and particle trajectories at various flow times t= 12 ms and 15 ms 104
Figure 5.18 Velocity vector plots and particle trajectories at various flow times t= 18 ms and 20 ms 105
Figure 5.19 Velocity vector plots and particle trajectories for various flow times t =22 ms and t =25 ms 106
Figure 5.20 Velocity vector plots and particle trajectories for various flow times t=28 ms and t= 30 ms 107
Figure 5.21 Velocity vector plots and particle trajectories for various flow times t=32 ms and t= 35 ms 108
Figure 5.22 Velocity vector plots and particle trajectories for various flow times t=38 ms and t= 40 ms 109
Figure 5.23 Particle trajectories and velocity vectors plots for flow time t= 42 ms and t= 45 ms..... 110
Figure 5.24 particle trajectories and velocity vector plots for flow time t= 48ms and t= 50ms 111
Figure 5.25 Velocity vector plots for flow time t= 0 ms 112
Figure 5.26 Particle trajectories and velocity vector plots for flow..... 112
Figure 5.27 Particle trajectories and velocity vector plots for flow time t= 0.5 ms..... 112
Figure 5.28 Particle trajectories and velocity vector plots for flow time t= 1 ms 113
Figure 5.29 Particle trajectories and velocity vector plots for flow time t = 1.5 ms 113
Figure 5.30 Particle trajectories and velocity vector plots for flow time t = 2 ms 114
Figure 5.31 Particle trajectories and velocity vector plots for flow time t = 5ms, t = 8 ms and t =10 ms 115
Figure 5.32 Particle trajectories and velocity vector plots for flow time t= 12 ms 116
Figure 5.33 Particle trajectories and velocity vector plots for t= 15 ms, t = 18 ms and 20 ms 117

Figure 5.34 particle trajectories and velocity vector plots for t= 22 ms, t=25 ms and t= 28 ms 118
Figure 5.35 Particle trajectories and velocity vector plots for flow time t= 30 ms 119
Figure 5.36 Particle trajectories and velocity vector plots for flow time t=35 ms and t=40 ms 119
Figure 5.37 Particle trajectories and velocity vector plots for flow time t= 45 ms and t= 50 ms..... 120
Figure 5.38 Velocity contour plots of the recirculation zone for flow times from t= 0 ms to t= 50 ms for 1.5 MPa operating pressure 121
Figure 5.39 Velocity contour plots of the recirculation zone for flow times from t= 0 ms to t= 50 ms for 3MPa operating pressure 123
Figure 5.40 Velocity contour plots of the recirculation zone for flow times from t= 0 ms to t= 50 ms for 4.5 MPa operating pressure 124
Figure 5.41 Velocity contour plots of the recirculation zone for flow times from t= 0 ms to t= 50 ms for 5 MPa operating pressure 125
Figure 5.42 Graph showing the Maximum Particle Residence Time (ms) vs Timesteps (ms) 126
Figure 5.43 Particles coloured according to their residence time in a velocity vector plots at 1.5 MPa pressure.....127
Figure 5.44 Particles coloured according to their residence time in a velocity vector plots at 3 MPa pressure.....128
Figure 5.45 Particles coloured according to their residence time in a velocity vector plots at 4.5 MPa pressure.....129
Figure 5.46 Particles coloured according to their residence time in a velocity vector plots at 5 MPa pressure.....130
Figure 5.47 Particles coloured according to their velocities in a velocity vector plots at 1.5 MPa operating pressure..... 131
Figure 5.48 Particles coloured according to their velocities in a velocity vector plots at 3 MPa operating pressure.....132
Figure 5.49 Particles coloured according to their velocities in a velocity vector plots at 4.5 MPa operating pressure.....132
Figure 5.50 Particles coloured according to their velocities in a velocity vector plots at 5 MPa operating pressure.....133
Figure 5.51 Graph showing the maximum velocity of the particles (ms^{-1}) vs Timesteps (ms).....134
Figure 5.52 Graph showing the Aspiration pressure (kPa) vs Timesteps (μs) 136
Figure 5.53 Graph showing the Aspiration pressure (kPa) vs Timesteps (ms) 136
Figure 6.1 three-dimensional rendering of the conventional discrete jet atomizer in bottom view and isometric view 139
Figure 6.2 three-dimensional rendering of the novel discrete jet atomizer in bottom view and isometric view 140
Figure 6.3 Schematic representation of conventional discrete jet atomizer with all dimensions 140
Figure 6.4 Schematic representation of novel discrete jet atomizer with all dimensions..... 141
Figure 6.5 Schematic representation of the flow domain for both the designs in isometric view.....142
Figure 6.6 Schematic representation of the flow domain overlapped with a period of the nozzles...142

Figure 6.7 cross-section of mesh through the gas-chamber, gas delivery tube and area surrounding the melt nozzle 143
Figure 6.8 Schematic representation of the side-view of the flow domain and the location of the rake 143
Figure 6.9 Schematic representation of the side-view of the flow domain and the location of the rake 144
Figure 6.10 Schematic representation showing different boundaries used in this study 144
Figure 6.11 Graph showing the variation of velocity along the rake in all the four meshes. 146
Figure 6.12 Velocity contour plots for 1MPa atomizing pressure in side-view and isometric view ..148
Figure 6.13 Velocity vector plots for 1MPa atomizing pressure in side- view 149
Figure 6.14 Velocity contour plots for 3MPa atomizing pressure in side- view and isometric view .149
Figure 6.15 Velocity vector plots for 3 MPa atomizing pressure in side- view 150
Figure 6.16 Velocity contour plots for 4.5 MPa atomizing pressure in side-view and isometric view 151
Figure 6.17 velocity vector plots for 4.5 MPa atomizing pressure in side-view.....152
Figure 6.18 Velocity contour plots for 5 MPa atomizing pressure in side- view and isometric view 152
Figure 6.19 velocity vector plots for 5 MPa atomizing pressure in side- view 153
Figure 6.20 Velocity contour plots for 1 MPa atomizing pressure in cross-sectional and isometric view 154
Figure 6.21 Velocity vector plots for 1 MPa atomizing pressure in side-view 155
Figure 6.22 Velocity contour plots for 3 MPa atomizing pressure in cross-sectional and isometric view 155
Figure 6.23 Velocity vector plots for 1 MPa atomizing pressure in side-view.....156
Figure 6.24 Velocity vector plots for 4.5 MPa operating pressure in side-view.....156
Figure 6.25 Velocity contour plots for 4.5 MPa atomizing pressure in cross-sectional and isometric view 157
Figure 6.26 Velocity contour plots for 5 MPa atomizing pressure in cross-sectional and isometric view 158
Figure 6.27 Velocity vector plots for 5 MPa operating pressure in side-view 158
Figure 7.1 Bottom view of annular-slit design and discrete-jet design 161
Figure 7.2 Schematic representation of the numerical domain used in this study......162
Figure 7.3 Velocity contour plots for the (a) periodic model and (b) axisymmetric model with gas tube width = 0.5 mm at 3 MPa operating pressure 164
Figure 7.4 Velocity contour plots for the (a) periodic model and (b) axisymmetric model with gas tube width = 0.1 mm at 3 MPa operating pressure.....165
Figure 7.5 Velocity contour plots for the (a) periodic model and (b) axisymmetric model with gas tube width = 0.21 mm at 3 MPa operating pressure.....166
Figure 8.1 Velocity contour plots for all the three nozzle at 1 MPa operating pressure.....169
Figure 8.2 Cross-sectional velocity contour plots for 1 MPa atomizing pressure in the conventional discrete-jet atomizer 171

Figure 8.3 Cross-sectional velocity contour plots for 1 MPa atomizing pressure in the novel discrete-jet atomizer *171*
Figure 8.4 Velocity contour plots for all the three nozzles at 3 MPa operating pressure *172*
Figure 8.5 Cross-sectional velocity contour plots for 3 MPa atomizing pressure in the conventional discrete-jet atomizer *173*
Figure 8.6 Cross-sectional velocity contour plots for 3 MPa atomizing pressure in the novel discrete-jet atomizer *173*
Figure 8.7 Velocity contour plots for all the three nozzles at 4.5 MPa operating pressure *174*
Figure 8.8 Cross-sectional velocity contour plots for 4.5 MPa atomizing pressure in the conventional discrete-jet atomizer *176*
Figure 8.9 Cross-sectional velocity contour plots for 4.5 MPa atomizing pressure in the novel discrete-jet atomizer *176*
Figure 8.10 Velocity contour plots for all the three nozzle at 5 MPa operating pressure *177*
Figure 8.11 Cross-sectional velocity contour plots for 5 MPa atomizing pressure in the conventional discrete-jet atomizer *178*
Figure 8.12 Cross-sectional velocity contour plots for 5 MPa atomizing pressure in the novel discrete-jet atomizer *178*
Figure 8.13 Velocity contour plots of expansion around the nozzle for both the discrete jet designs *181*
Figure 8.14 Particles coloured by velocity and velocity vector plots. *184*
Figure 8.15 Variation of aspiration pressure (kPa) wrt operating pressures (MPa) *188*
Figure 8.16 Variation in aspiration pressure(kPa) wrt operating pressure (MPa) with and without particles *191*
Figure A.1 Velocity vector plots for flow time t = 0 ms ..... *vi*
Figure A.2 particle trajectories and velocity vector plots for flow time t = 0.1 ms ..... *vi*
Figure A.3 particle trajectories and velocity vector plots for flow time t= 0.5 ms ..... *vii*
Figure A.4 particle trajectories and velocity vector plots for flow time t= 1ms ..... *vii*
Figure A.5 particle trajectories and velocity vector plots for flow time t= 1.5 ms ..... *viii*
Figure A.6 Particle trajectories and velocity vector plots for flow time t = 2ms ..... *viii*
Figure A.7 Particle trajectories and velocity vector plots for flow times t= 5 ms, t = 8 ms and t =10 ms ..... *ix*
Figure A.8 Particle trajectories and velocity vector plots for flow time t= 12 ms ..... *x*
Figure A.9 Particle trajectories and velocity vector plots for flow times t= 15 ms, t= 18 ms and t= 20 ms ..... *xi*
Figure A.10 Particle trajectories and velocity vector plots for flow time t= 22 ms and t=25 ms ..... *xii*
Figure A.11 Particle trajectories and velocity vector plots for flow times t = 28 ms and t= 30 ms ..... *xiii*
Figure A.12 Particle trajectories and velocity vector plots for t= 32 ms ..... *xiii*
Figure A.13 Particle trajectories and velocity vector plots for t= 35 ms, t= 38 ms and t= 40 ms ..... *xiv*
Figure A.14 Particle trajectories and velocity vector plots for t= 42 ms and, t= 45 ms ..... *xv*
Figure A.15 Particle trajectories and velocity vector plots for t= 50 ms ..... *xvi*
Figure A.16 Velocity vector plots for flow time t= 0 ms ..... *xvi*

Figure A.17 Particle trajectories and velocity vector plots for flow time t= 0.1 ms xvii
Figure A.18 Particle trajectories and velocity vector plots for flow time t =0.5 ms xvii
Figure A.19 Particle trajectories and velocity vector plots for flow time t= 1 ms xvii
Figure A.20 Particle trajectories and velocity vector plots for flow time t= 1.5 ms xviii
Figure A.21 Particle trajectories and velocity vector plots for flow time t = 2 ms..... xviii
Figure A.22 Particle trajectories and velocity vector plots for t= 5 ms, t= 8 ms and t= 10 ms xix
Figure A.23 Particle trajectories and velocity vector plots for flow time t= 12 ms xxi
Figure A.24 Particle trajectories and velocity vector plots for flow tile t= 15 ms.....xxi
Figure A.25 Particle trajectories and velocity vector plots for flowtimes t= 18 ms and t= 20 ms xxii
Figure A.26 Particle trajectories and velocity vector plots for flow times t= 22 ms and t= 25 ms .. xxiii
Figure A.27 Particle trajectories and velocity vector plots for the flowtimes t= 28 ms and t= 30 ms xxiv
Figure A.28 Particle trajectories and velocity vector plots for flowtimes t= 32 ms and, t= 35 ms xxv
Figure A.29 Particle trajectories and velocity vector plots for flow time t= 38 ms and t= 40 ms ...xxvi
Figure A.30 Particle trajectories and velocity vector plots for flow time t=45 ms and t = 50 ms... xxvii

LIST OF TABLES

Table 4.1 Various elements used in the mesh in this study 68

Table 4.2 Table listing all the settings used in Ansys Fluent to generate results 74

Table 5.1 Settings used to define injections 91

Table 5.2 Settings used in Ansys Fluent in this study 94

Table 5.3 Various pressures considered in this study and the corresponding GMRs 95

Table 5.4 Volumetric flow rate inside the recirculation zone for all pressures 98

Table 6.1 Element size and the corresponding number of elements and the degree of fineness of all the meshes considered in this study 146

Table 6.2 Settings used to generate results in this study 147

Table 7.1 Settings used to generate results in this study 162

Table 8.1 Table containing aspiration pressures for all operating pressures 188

Abbreviations used in this thesis.

AS-CF	Annular Slit Confined Feed
CCGA	Close-Coupled Gas Atomization
CFD	Computational Fluid Dynamics
CD nozzle	Convergent-Divergent Nozzle
DJ-CF	Discrete-Jet Confined Feed
DNS	Direct Numerical Simulation
GMR	Gas Melt Ratio
HPGA	High Pressure Gas Atomization
LES	Large Eddy Simulation
PM	Powder Metallurgy
RANS	Reynolds Averaged Navier Stokes
VOF	Volume of Fluid
WCP	Wake Closure Pressure
We	Weber Number

Units used in this thesis

kPa	Kilopascal
MPa	Megapascal
ms	millisecond
μs	microsecond

1 INTRODUCTION

Powder Metallurgy (PM) is the study of the production techniques, characteristics of metal powders and their utilization in the manufacturing of engineering components. These processes are economical and environmentally clean as the end products have a satisfactory surface finish and dimensional tolerance.[1] PM generally include powder manufacturing, sintering, isostatic compaction, and finishing operations. Few applications which use metal powders are Thermal Spray Forming, Metal Injection Moulding, Additive manufacturing. [2, 3]

A major challenge faced by the PM industries is that the recent developments in surface technologies has led to an industrial demand for metal powders with specific characteristics. Two constraints on the demand are as follows:

- a narrow size distribution with average particle size of 10µm resulting in high energy utilization and product wastage leading to high costs.
- Powders with high degree of purity since impurities in melt can affect the solidification and hence the quality of the final product.[4]

Metal powders can be produced by various techniques. The production technique of fine powders can be broadly categorized as mechanical (e.g. milling), chemical (e.g. decomposition of compounds), electrolytic and atomization techniques. [5]

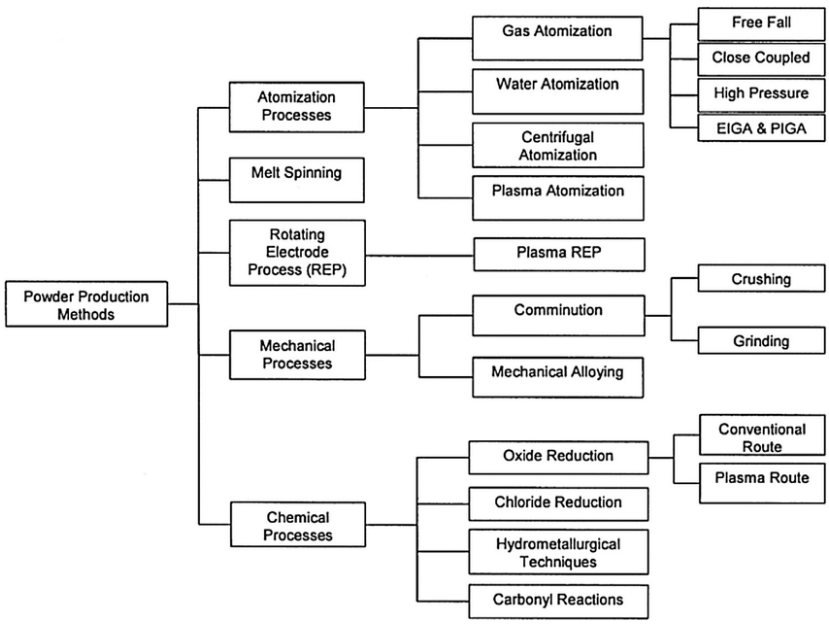

Figure 1.1 Different types of powder production techniques [6].

Figure 1.1 shows the different powder metallurgy processes involved in powder production. [6]

Atomization techniques produce metal powders with better properties than those produced by conventional methods due to the rapid solidification of the droplets. The powders produced by the rapid solidification have better uniformity leading to decreased segregation, better microstructure and increased grain size homogeneity, workability and reproducibility. Also, rapid solidification offers production of new alloys by allowing new phases to be formed by extending the equilibrium phase fields. Rapid solidification is brought about by high cooling rates of about 10^5 Ks^{-1}. These effects of rapid solidification on powders is achieved only when the droplet size is as small as possible, and the heat transfer is high. [7, 8]

Atomization is the technique in which molten metal is disintegrated by gas or water. The high cooling rates in gas atomization are brought about by convective cooling through atomizing gases. Gas atomization is widely used to manufacture powders of aluminum, super alloys, copper, iron, tin and low-alloy powders.[9] The efficiency of atomization process can be improved by understanding the gas flow, melt break up, movement of melt and the influence of process parameters on particle size.

1.1 Challenges

Atomization is a complicated process and is considered an art as it is not completely understood. A lot of research about Close-Coupled Gas Atomization is focused on gas-only analysis as the presence of melt results in unfavorable environment for experimental analysis. It is difficult to observe the gas atomization and measure the continuous changes in melt and gas properties due to high temperature and high velocities within the complex flow field structures. The presence of melt influences the flow features inside the atomizer. Therefore, it is necessary to understand the interaction between the melt and gas jets in order to improve the efficiency of the process.

The development in the computational fluid dynamics in the recent times have led to an increased research interest in multiphase flow analysis of CCGA. The process of CCGA involves melt break-up, melt movement and solidification of droplets. It is computationally intensive to create a numerical model to simulate all these processes. Also, due to rapid changes in temperature and velocity, it is difficult to develop a model to simulate the process effectively. Therefore, several models have been developed to simulate each process separately as it reduces the computational requirement.

1.2 Objectives

This thesis investigates the CCGA process through numerical modelling. The aims of the project are given below:

- To establish a two-dimensional flow domain and validate it with experimental data available.
- To analyse the flow features and particle trajectories for a range of atomizing pressures.
- To analyse particle trajectories along with the changes in the flow for a range of pressures
- To study the influence of the particles on various process parameters such as aspiration pressure and particle residence time for the considered pressures.
- To establish a three-dimensional periodic flow domain for a conventional discrete jet atomizer and a novel discrete jet atomizer in order to analyse the flow features for a range of atomizing pressures.

1.3 Outline of the thesis

Chapter 1 presents the general introduction to the close-coupled gas atomization and the motivation for the project. Chapter 2 discusses the general literature related to powers and computational fluid dynamics. Chapter 3 discusses the literature related to CCGA. Chapter 4 presents and discusses the results of the two-dimensional gas-only flow analysis for a range of pressures in an annular-slit nozzle. Chapter 5 investigates the melt interaction with atomizing gases in Lagrangian approach for a range of pressure in an annular-slit nozzle. Chapter 6 deals with two discrete-jet nozzle designs and presents the results for a three-dimensional analysis for a range of pressures. Chapter 7 presents the need for three-dimensional analysis by studying three different cases. Chapter 8 gives an overall discussion of the project. Chapter 9 presents conclusion and possible future investigation.

2 BACKGROUND SCIENCE

Powder Metallurgy is the art and science of metal powder production and manufacturing semi-finished and finished objects from powders with or without addition of non-metallic constituents. Powder Metallurgy [PM] methods were initially used to manufacture materials with high melting temperatures which were difficult to produce by traditional methods such as ingot metallurgy methods and fusion metallurgy methods. PM methods have high material utilization and hence can be less expensive compared to ingot metallurgy methods. The parts manufactured by this method have up to 90% of materials theoretical density and reasonable strengths. [10, 11]

The raw material for parts manufactured by PM methods is powders. These powders are bespoke engineered materials as they are manufactured to precise specification to aid subsequent processing and can be made of pure elements, elemental blends or pre-alloyed ingots. The metal powders are characterized by their morphology and powder size. It can also be characterised by physical properties such as hardness and ductility, chemical properties such as reactivity and impurities and bulk properties such as flow properties, density and compressibility. [12]

A wide range of structural and functional materials require high quality fine powders with no refractory and oxide contaminants and narrow particle distribution. Several PM methods ensure very fine microstructure of materials which influences the physical properties of materials. The materials obtained by other metallurgical processes such as fusion metallurgy have coarse microstructures due to slow cooling and segregation of impurities during solidification. [13]

Overall, PM processes have more advantages than other fabrication processes such as casting or machining. PM is the preferred method for high strength and wear resistance or high temperature requirements. It also offers greater precision thereby eliminating defects and the need for finishing operations. However as the tooling cost is high, PM methods are economical only when the production rates are higher. [14]

Powders used in PM can be obtained by atomization, chemical reduction, mechanical crushing and electrolysis. [15] The atomization and reduction processes are widely used for producing powders in large quantities while mechanical crushing and electrolysis is used for producing bespoke materials in small quantities. Most common method is atomization which produces nearly 80% of the total volume of powders.

2.1 Gas Atomization

The process of atomization involves disintegration of liquid metal by high-speed jet into droplets and rapid solidification of droplets into metal powders. The disintegration of melt droplets is achieved through water or gas jets. Water is the most economical method of atomization but it is not suitable for the production of clean spherical particles.[16] Gas atomization is the most commonly utilized technique to produce ultrafine metal and alloy powder. Gas atomization can be used to produce alloy powders that cannot be produced by other conventional manufacturing methods. This technique produces highly spherical and fine powders which are conventionally used in application with dense packing and good flow characteristics requirement. [17] Rapid solidification of powders results in high cooling rates which in turn produces many favourable properties. Some of the notable properties include but not limited to decrease in segregation, higher solid solubility, and a finer microstructure which in turn gives better chemical homogeneity, a more corrosion-resistant end product and more favourable hot- and cold-working properties. [18-20] Rapid solidification also can be used to produce amorphous powders with unique properties. [17] The powders obtained by gas atomization have a particle size range between 1μm to 1 mm in diameter. [21]

Gas atomization is achieved through two methods: free-fall gas atomization and close-coupled gas atomization. Figure 2.1 shows a schematic representation of free-fall atomizer and confined atomizer. [22]

In free-fall atomization, the melt flows *freely* for a short distance due to gravity and is

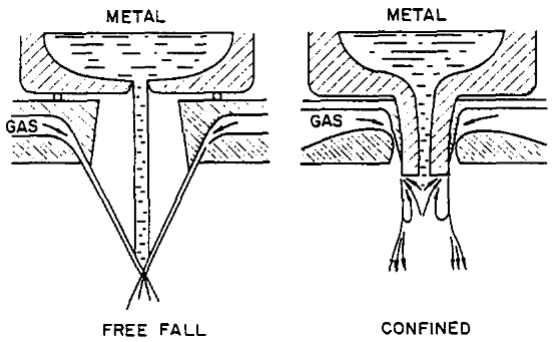

Figure 2.1 Schematic representation of free-fall and confined atomizer. [22]

atomized by impinging gas jets. Though gas-metal interaction is much easier to control as it is a simple process, there is not much control over powder size distribution. The process efficiency is also much lower compared to Close-coupled gas atomizers.[23] In close coupled gas atomization, the free-fall distance is eliminated thereby enabling the gas jets to disintegrate the melt more efficiently due to close proximity. Also, there is a reduction in

energy dissipation in gas jets resulting in finer particle size distribution and reduction in energy consumption compared to free fall atomization. [24]

CCGA is the preferred method of powder production in most of the commercial atomizer companies due to the above-mentioned reasons.

2.2 Flow Physics

Fluid movement in a physical domain is due to various properties of it and forces acting on it. Fluid flow can be broadly classified based on a non-dimensional number called Reynolds number.[25] Reynolds number is the ratio of inertial forces to the viscous force of the fluid and given by

$$Re = \frac{\rho u L}{\mu} \qquad \textit{eq 2.1}$$

ρ is the density of the fluid.

u is the velocity of the fluid.

L is a characteristic linear dimension.

μ is the dynamic viscosity of the fluid.

Fluid flow can be classified as laminar and turbulent flow depending on the Reynolds number. Laminar flows are characterised by no eddies, swirls or currents and have low Reynold number. On the other hand, turbulent flows have flow instabilities, eddies and swirls. Reynolds number depends on the properties of the fluid such as density, viscosity and whether the flow is external or internal. There exists a critical Reynolds number where the flow undergoes transition between laminar and turbulent regimes. The flow belongs to laminar regime when the Reynolds number is less than 2300 (Re < 2300). The flow belongs to the transition regime when the Reynolds number is between 2300 and 4000 (2300 < Re<4000). The flow is in turbulent regime when the Reynolds number is greater than 4000 (Re>4000). [26]

Flow separation is another important aspect of flows. Flow separation occurs when the fluid comes in contact with a wall or free boundary. The fluid nearest to the boundary experiences momentum lose resulting in loss in velocity due to viscosity. This layer of fluid affects the surrounding layers of fluid which in turn affects its surroundings. Therefore, the flow will be characterised by layers of fluid with a decreasing order of momentum lose starting from the

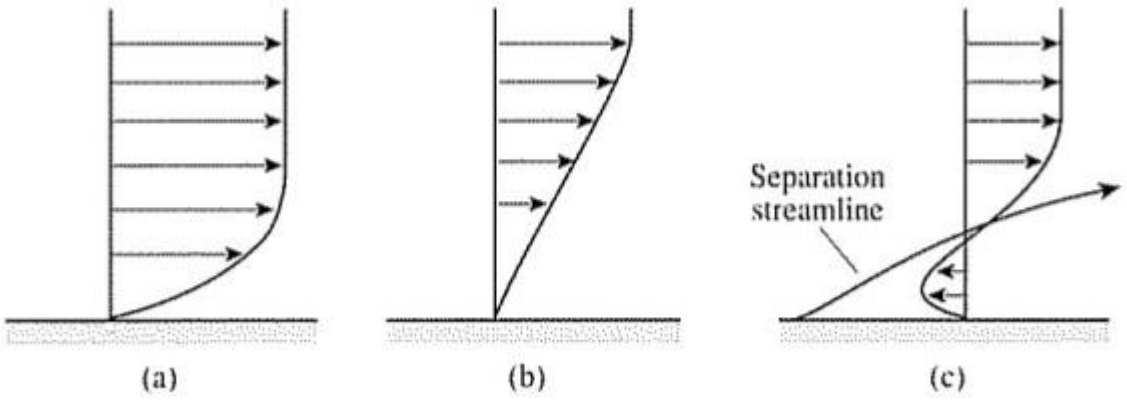

Figure 2.2 Flow separation over the plate (a) Initial flow over the plate (b) Flow just before separation (c) separated flow. [27]

boundary towards the centre of the flow. This region of fluid with decreased velocity and momentum is termed as boundary layer. [27]. Figure 2.2 shows the flow separation over a plate. [27]

Generally, fluids flow through a pressure gradient i.e., from a region of high pressure to low pressure. Adverse pressure gradient causes separation in flow. When the fluid in the boundary layer region experiences an adverse pressure gradient, the fluid moving with reduced velocity will lose more momentum and velocity. If the gradient is sufficiently high, it can cause the fluid in the boundary layer to flow in the opposite direction. This is termed as recirculation.

Recirculating flow deteriorates while flowing in the opposite direction to the flow and reattaches to the flow when it experiences a favourable pressure gradient.

The point in the fluid flow where the flow undergoes a change in direction is characterised by zero-velocity and is called stagnation point. Pressure at the stagnation point is the highest in the flow. Both laminar and turbulent flows can experience boundary layer separation. [27]

2.2.1 Compressibility:

Compressibility of the fluid is defined as the change in density of the fluid due to forces acting on it. Based on compressibility constraint, fluids are classified as incompressible and compressible. When the fluid is moving, volume flow rate is constant in incompressible flow and mass flow rate is constant in compressible flow.

The speed at which the sound waves travel in a medium is known as the speed of the sound in that medium. A dimensionless quantity called Mach number is used to classify the moving fluid based on the relative speed to the speed of the sound waves in the medium.[26] Mach number is defined as

$$M = \frac{v}{a} \qquad \textit{eq 2.2}$$

Where M is the Mach number of the flow.

v is the velocity of the moving fluid in the medium

a is the speed of the sound waves in the medium

The classification is as follows:

- Subsonic flows are flows with 0<M<0.8.
- Transonic flows are flows with 0.8<M<1.2.
- Supersonic flows are flows with 1.2<M<5.
- Hypersonic flows are flows with M>5.

Subsonic flows are generally considered as incompressible flows as density changes are negligible even for high forces applied to the fluid. Also, the thermodynamic constraints are not needed as the kinetic energy possessed by the flow is very small and negligible to the heat content of the fluid.[26]

In transonic and supersonic flows, the kinetic energy of the flow is substantial in comparison to the heat content of the flow. Therefore, thermodynamic constraints are of great importance for these flows. [26]

Few thermodynamics concepts related to this study has been discussed here.

A thermodynamics system is a fixed quantity of matter with defined boundaries. A process is defined as the change in the system from an initial state to a final state.

A process which is accompanied with no heat transfer is called as adiabatic process. A process can be adiabatic if the boundary of the system is well insulated that heat transfer from the system to the surroundings is negligible or the system and the surroundings are at the same temperature. A reversible process is a process in which the system can be reversed from the final state to the initial state without leaving any trace on the surroundings. A process which is adiabatic and reversible is called isentropic process. Generally isentropic processes are considered as idealised process as in real life situations, the system and the surroundings never return to the initial states at the end of the process. Isentropic processes can be used to model actual processes involving adiabatic devices like nozzles, diffusers and turbines when the factors affecting their reversibility such as friction are minimised. [28]

2.2.2 Ideal gas:

Gas that satisfies thermal equation of state and caloric equation of state is termed as ideal gas.

Thermal equation of state is given by $PV = nRT$ where P is the pressure of the gas, V is the volume of the gas, R is the gas constant, T is the temperature of the gas and n is the number of moles per unit volume.

Caloric equation of state is given by $c_p = \frac{\partial h}{\partial T}$, $c_v = \frac{\partial u}{\partial T}$ where c_v is the specific heat constant at constant volume is given by change in enthalpy, h per unit temperature T and c_p is the specific heat constant at constant pressure given by change in internal energy u per unit temperature T.

Gases like air, nitrogen, oxygen and noble gases such as helium, argon, neon and krypton can be treated as ideal with negligible errors for a wide range of applications. [16]

For isentropic flow processes, density and pressure are related by a constant as $\frac{p}{\rho^{\gamma}} = constant.$

where p is the pressure, ρ is the density of the gas and γ is the specific heat ratio given by c_p/c_v.

The compressible Bernoulli equation for an ideal gas

Compressible Bernoulli equation is given by

$$\frac{V^2}{2} + \int \frac{1}{\rho}\frac{\partial p}{\partial s} ds = constant \qquad \text{eq 2.3}$$

Pressure, density and temperature are fluid properties that can be defined as static properties and stagnation properties of the fluid. Static properties are flow properties i.e. they are measured at a point in the flow. Stagnation properties are defined by constraints at a point I the flow. Stagnation properties are the static properties of the fluid measured when the fluid is brought to stop isentropically at that point.[26]

Stagnation and static properties at a point is related by the following equations:

$$\frac{P_0}{P} = \left[1 + \frac{\gamma - 1}{2} M^2\right]^{\frac{\gamma}{\gamma - 1}} \qquad \text{eq 2.4}$$

$$\frac{T_0}{T} = \left[1 + \frac{\gamma - 1}{2} M^2\right] \qquad \textit{eq 2.5}$$

$$\frac{\rho_0}{\rho} = \left[1 + \frac{\gamma - 1}{2} M^2\right]^{\frac{1}{\gamma - 1}} \qquad \textit{eq 2.6}$$

Where P, T and ρ are the static properties and the P_0, T_0 and ρ_0 are the stagnation properties. Generally, stagnation properties are denoted by a subscript 0. [26]

2.2.3 Different kinds of flows:

Gas flow through pipe, nozzle and diffusers can be brought about by pressure gradient between the initial point and the exit point. As mentioned before, mass flow rate is constant in the compressible flow at every point in the flow. Mass flow rate is given by

$$\dot{m} = \rho A v \qquad eq\ 2.7$$

ρ is the density of the fluid.

A is the area of the pipe.

v is the velocity of the fluid.

$\dot{m}$ is the mass flow rate of the fluid.

As the pressure difference between initial point and exit point increases, mass flow rate increases in a pipe. Every pipe with a constant area A has a maximum pressure difference above which the mass flow rate does not increase which is specific to the design and this is called choked flow.

	Subsonic M<1	Supersonic M>1
Converging Duct 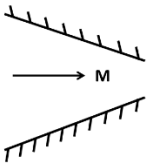	As P decreases, then *v* increases Subsonic nozzle	As P increases, then *v* decreases Supersonic diffuser
Diverging Duct 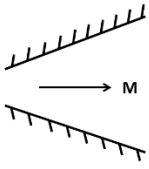	As P increases, then *v* decreases Subsonic diffuser	As P decreases, then *v* increases Supersonic nozzle

Figure 2.3 Flow changes in nozzle and diffuser. [22]

In nozzle and diffuser, the pressure of the flowing fluid changes according to the flow area. For subsonic flows, the pressure at the inlet is less than the pressure at the exit in a nozzle whereas the inlet pressure is higher than the exit pressure in the diffuser. For the supersonic flows, it is vice versa. The change in flow parameters are shown in Figure 2.3 [22]

In supersonic flows, when the fluid exits at a pressure higher than the surrounding pressure (also called backpressure), it is called under expanded jets and when the fluid exits at a pressure lower than the surrounding pressure, it is called over expanded jet. These mismatched pressures result in shock development in supersonic flows. [28]

Generally, shocks are considered as a compressed region in the supersonic flow where flow properties such as pressure, temperature and density undergo abrupt change. Shocks have high temperature gradient and velocity gradient that provide heat conduction and viscous dissipation which makes shocks irreversible. Therefore, flow through shock waves is adiabatic and irreversible. In most of the physical situations, shock waves are always inclined at an angle to the flow. Such shock waves are called oblique shock waves. [26]

When the flow encounters a change in flow direction, it experiences shocks or expansion depending on the directional change. Figure 2.4 shows the schematic representation of the inclined flow in two situations. [26]

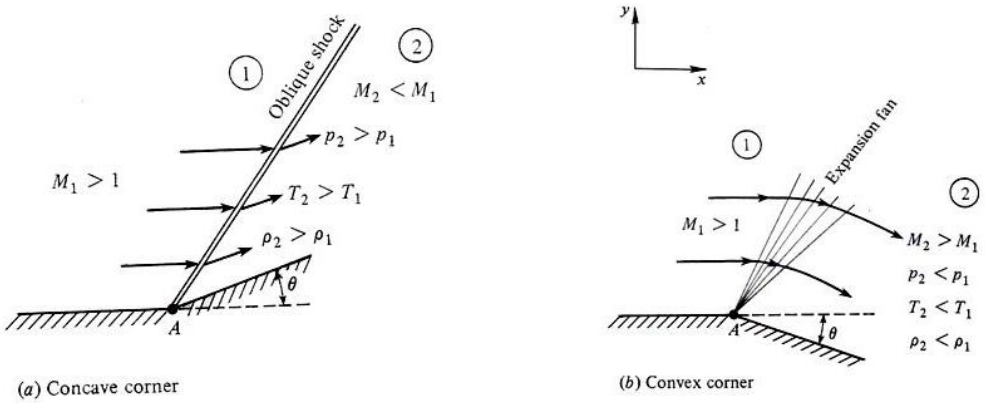

Figure 2.4 Behaviour of shock at concave point (recompression shocks) and convex points (expansion waves). [26]

In the case of the concave corner, the supersonic flow turns into itself resulting in an oblique shock as a compression region is formed near the inclined wall. The flow decelerates in this case and the static properties such as density and temperature increase while the pressure decreases. Oblique shocks are classified as weak shocks and strong shocks. When the Mach number of the flow after the shock is greater than unity, the shock wave is termed weak oblique wave. Most of the physical situations encounter weak oblique waves. On the other hand, when the Mach number of the flow after the shock wave is less than unity, the oblique shocks are termed as strong oblique wave. Normally special arrangements are necessary to produce strong oblique shock waves.

On the other hand, if the flow encounters a convex corner, supersonic flow turns away i.e. expands. This flow experiences expansion waves where the flow accelerates. The static properties such as density and temperature decrease, and the pressure increases. Expansion

waves are isentropic everywhere except at the vertex denoted by A in the Figure 2.4. Supersonic flow undergoes small yet finite changes in flow properties across each expansion wave and hence the overall change in flow properties will be smooth and gradual across an expansion fan. Prandtl Meyer expansion in a supersonic flow consist of an infinite number of expansion waves sharing a vertex Through which the flow changes gradually and smoothly with reduced losses. [26]

2.2.4 Reflection and intersection of shocks and expansion waves:

When an oblique shock comes across a solid wall, it gets reflected. If the shock is adequately weak, the incident shock and the reflected shock are of same strength. If the oblique shock is strong, it changes the flow direction towards the wall. An additional shock of opposite but equal strength is required to change the flow direction back to initial state.

When two oblique shocks interact, they either “pass through” or “coalesce” depending on the interacting oblique shock. Oblique shocks originating from the same vertex are termed as shocks of same family. When the two oblique shocks are from different families of shocks, the shocks pass through each other but gets deflected in the process. When the oblique shocks are from the same family, they all coalesce into one strong oblique wave. The oblique wave shown in the Figure 2.4 consists of infinite number of weak oblique waves also called as Mach lines that coalesced into a strong oblique wave.[26]

In some problems in fluid mechanics, boundaries are defined by the viscous and pressure forces possessed by the fluid flow. Such boundaries are called free-boundaries and the shape of free-boundaries must be solved in order to solve the flow. When an oblique shock wave interacts with a free boundary condition, it is reflected as an expansion wave. When an expansion fan interacts with a free boundary condition, they are reflected as compression waves which coalesce as an oblique wave. [26]

There are two kinds of expansion observed when the exiting gases interacts with the surrounding gases. When the pressure of the exiting gases is lesser than the ambient pressure, it is called over-expanded. The gases turn inward due to this higher ambient pressure and undergo compression to form weak oblique shocks. The oblique shocks form expansion waves on interaction with the free boundary. These expansion waves move towards the free boundary where they are reflected back as oblique shocks. These weak oblique shocks continue to move towards the free boundary and form expansion waves on interaction and the process repeats

itself till the gas jets deteriorate. Figure 2.5 shows the shockwaves formed in an over-expanded flow field. [26]

When the pressure of the exiting gases is greater than the ambient pressure, it is called under-expanded. When a gas jet exits an orifice, it expands through expansion waves while losing

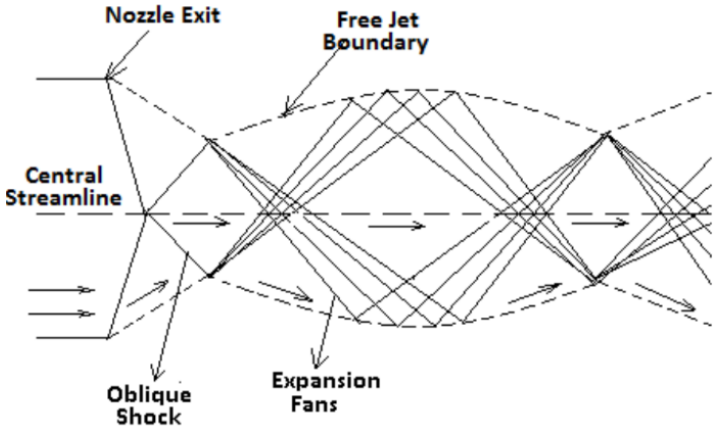

Figure 2.5 Shock waves formed in an over-expanded flow field. [26]

pressure till it reaches the jet boundary where the pressure is equal to the ambient pressure. The expansion waves get slightly deflected and pass through the expansion waves from the other sides of the flow.

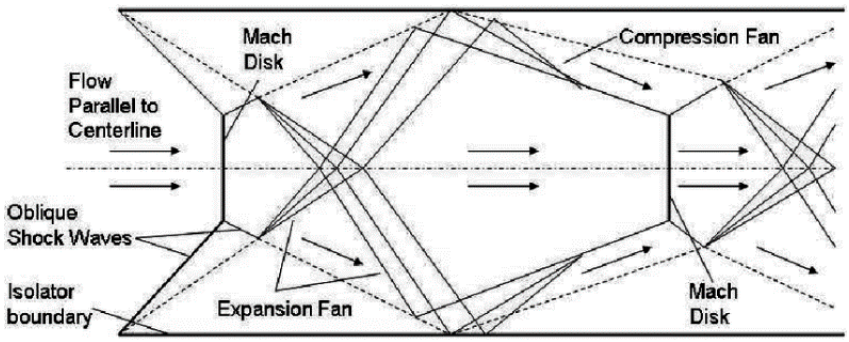

Figure 2.6 Shock-waves formed in an under-expanded flow field with the Mach disk [26]

Since it is a free boundary condition, the expansion waves are reflected as compression waves and these form the barrel shocks. When the ratio of the gas jet pressure and the ambient pressure is high, the compression waves are strong enough to merge and form a normal shock wave called the Mach disk. The oblique shock waves get reflected and continue moving towards the free boundary where they are reflected as expansion waves. The process repeats itself till the expanding gas jets have deteriorated. This pattern of expansion and compression

waves along with Mach disk is called diamond shock. [26] Figure 2.6 shows the shockwaves formed in an under-expanded flow field. The Mach disk is highlighted in it. [26]

In CCGA, a diamond shock forms downstream the melt nozzle at high atomizing pressures. This is called a closed wake and is an area of interest for a lot of researchers.

2.2.5 Multiphase flow:

Multiphase flows in CCGA are a complicated process. Two dimensionless numbers that play an important role in multiphase flow analysis are discussed below.

Weber number

Weber number is a dimensionless number used for analysing the deformation. Weber number is the ratio of inertial forces to the cohesive forces acting on a fluid. Weber number is given by

$$We = \frac{\rho v^2 L}{\sigma} \qquad \textit{eq 2.8}$$

Where *We* is the weber number

ρ is the density of the fluid.

v is the velocity at which the fluid is flowing.

σ is the surface tension of the fluid.

L is the characteristic length of the flow.

When the inertial forces are high, (We>>1) the fluid can be easily deformed and dispersed. A low weber number denotes that the cohesive forces are high. Cohesive forces prevent the fluid deformation. Therefore, fluids cannot be deformed easily. This number plays a major role in determining the final droplet size of a fluid. [25]

Ohnesorge number

Ohnesorge number is the ratio of internal viscosity dissipation to the surface tension energy. This is the dimensionless quantity used to quantify the droplet formation. Ohnesorge number can also be expressed as the square-root of Weber number divided by Reynolds number.[25]

$$Z = \frac{\sqrt{We}}{Re} \qquad \textit{eq 2.9}$$

Where Z is the Ohnesorge number

We is the weber number

Re is the Reynolds number

2.3 Computational Fluid Dynamics:

This project involves single phase flows and multiphase phase flows. The numerical models used for both have been reviewed here.

2.3.1 Single phase flows:

The governing equations of fluid flow must obey the mass, momentum and energy conservation laws i.e.

- The mass of a fluid is conserved.
- The rate of change of momentum equals the sum of the forces on a fluid particle (Newton's second law).
- The rate of change of energy is equal to the sum of the rate of heat addition to and the rate of work done on a fluid particle (first law of thermodynamics). [29]

Mass conservation

The continuity equation is based on the mass conservation law. As the fluid is considered a continuum, the mass of the fluid flowing through a reference control volume (RCV) must be conserved.

$$Rate\ of\ increase\ of\ mass\ in\ the\ RCV\ =\ Mass\ influx - mass\ outflux$$
$$=\ Net\ mass\ flow\ rate\ through\ the\ RCV$$

Let us consider an infinitesimal fluid element with sides $\delta x, \delta y$, δz and density ρ as the RCV. Mass flowing through the RCV is shown in Figure 2.7. [29]

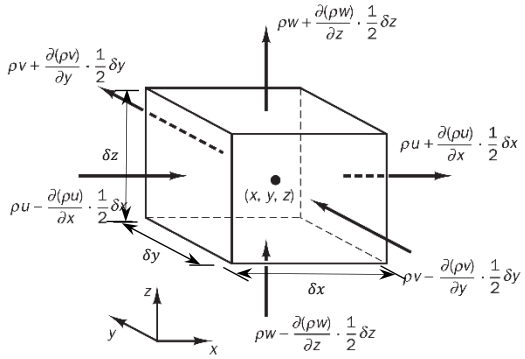

Figure 2.7 Schematic representation of fluid element with mass flowing in and out of it. [29]

The rate of increase of mass in RCV is given by

$$\frac{\partial \rho}{\partial t}\delta x\delta y\delta z \qquad \textit{eq 2.10}$$

The net mass flow rate through RCV is given by

$$\left(\rho u - \frac{\partial(\rho u)}{\partial x}\frac{1}{2}\delta x\right)\delta y\delta z - \left(\rho u + \frac{\partial(\rho u)}{\partial x}\frac{1}{2}\delta x\right)\delta y\delta z + \left(\rho v - \frac{\partial(\rho v)}{\partial y}\frac{1}{2}\delta y\right)\delta x\delta z \qquad \textit{eq 2.11}$$
$$- \left(\rho v + \frac{\partial(\rho v)}{\partial y}\frac{1}{2}\delta y\right)\delta x\delta z + \left(\rho w - \frac{\partial(\rho w)}{\partial z}\frac{1}{2}\delta z\right)\delta x\delta y$$
$$- \left(\rho w + \frac{\partial(\rho w)}{\partial z}\frac{1}{2}\delta z\right)\delta x\delta y$$

$$\frac{\partial \rho}{\partial t} + \frac{\partial(\rho u)}{\partial x} + \frac{\partial(\rho v)}{\partial y} + \frac{\partial(\rho z)}{\partial z} = 0 \qquad \textit{eq 2.12}$$

$$\frac{\partial \rho}{\partial t} + \ div(\rho \boldsymbol{u}) = 0 \qquad \textit{eq 2.13}$$

This is the compressible, three-dimensional continuity equation. [29]

Momentum conservation

Navier Stokes equation is based on momentum conservation i.e. rate of change of momentum of a fluid particle is equal to the forces acting on the particle.

$$Rate\ of\ momentum\ increase\ =\ Sum\ of\ forces\ acting\ on\ the\ fluid.$$

The rates of momentum increase in x, y, z direction is given by

$$\rho\frac{Du}{Dt}, \qquad \rho\frac{Dv}{Dt}, \qquad \rho\frac{Dw}{Dt}$$

Where $\rho\frac{D(velocity\ component)}{Dt} = \frac{\partial(\rho velocity\ component)}{\partial t} + div(\rho \boldsymbol{u}(velocity\ component))$

The forces acting on the body can be classified into surface forces (pressure force, viscous force, gravity) and body forces (centrifugal force, EM force).

The surface forces acting on the fluid can be defined in terms of pressure p and nine viscous stress components (τ). Let us consider an infinitesimal fluid element with sides $\delta x, \delta y, \delta z$ and density ρ as the RCV.

Figure 2.8 shows the stress component acting on the fluid element. [29]

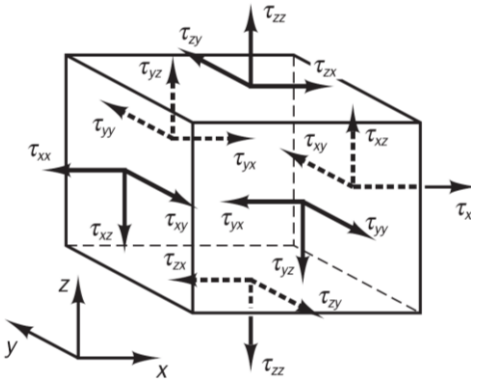

Figure 2.8 Schematic representation of stress components on the fluid element [29]

Figure 2.9 shows the x-components of the pressure forces and viscous forces. [29] The magnitude of force due to viscous stress is the product of stress and area.

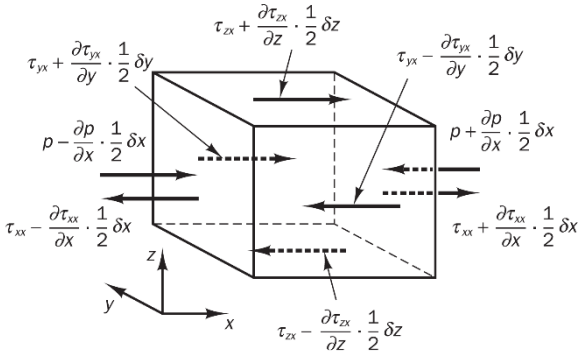

Figure 2.9 Fluid element with x-component of pressure forces and viscous forces

In the x-direction,

$$\left[\left(p-\frac{\partial p}{\partial x}\frac{1}{2}\delta x\right)-\left(\tau_{xx}-\frac{\partial\tau_{xx}}{\partial x}\frac{1}{2}\delta x\right)\right]\delta y\delta z \qquad \textit{eq 2.14}$$
$$+\left[-\left(p+\frac{\partial p}{\partial x}\frac{1}{2}\delta x\right)+\left(\tau_{xx}+\frac{\partial\tau_{xx}}{\partial x}\frac{1}{2}\delta x\right)\right]\delta y\delta z=\left[-\frac{\partial p}{\partial x}+\frac{\partial\tau_{xx}}{\partial x}\right]\delta x\delta y\delta z$$

In the y-direction,

$$-\left(\tau_{yx}-\frac{\partial\tau_{yx}}{\partial y}\frac{1}{2}\delta y\right)\delta x\delta z+\left(\tau_{yx}+\frac{\partial\tau_{yx}}{\partial y}\frac{1}{2}\delta y\right)\delta x\delta z=\frac{\partial\tau_{yx}}{\partial y}\delta x\delta y\delta z \qquad \textit{eq 2.15}$$

In the z-direction,

$$-\left(\tau_{zx}-\frac{\partial\tau_{zx}}{\partial z}\frac{1}{2}\delta z\right)\delta x\delta y+\left(\tau_{zx}+\frac{\partial\tau_{zx}}{\partial z}\frac{1}{2}\delta z\right)\delta x\delta y=\frac{\partial\tau_{zx}}{\partial z}\delta x\delta y\delta z \qquad \textit{eq 2.16}$$

The total x-component forces per unit volume is

$$\frac{\partial(-p+\tau_{xx})}{\partial x}+\frac{\partial \tau_{yx}}{\partial y}+\frac{\partial \tau_{zx}}{\partial z} \qquad \textit{eq 2.17}$$

The body forces acting on the fluid element is given by S_{M_x}, S_{M_y} and S_{M_z}.

Now, the x-component of momentum equation is given as

$$\rho\frac{Du}{Dt}=\frac{\partial(-p+\tau_{xx})}{\partial x}+\frac{\partial \tau_{yx}}{\partial y}+\frac{\partial \tau_{zx}}{\partial z}+S_{M_x} \qquad \textit{eq 2.18}$$

Similarly,

y-component of momentum equation is given as

$$\rho\frac{Dv}{Dt}=\frac{\partial \tau_{xy}}{\partial x}+\frac{\partial(-p+\tau_{yy})}{\partial y}+\frac{\partial \tau_{zy}}{\partial z}+S_{M_y} \qquad \textit{eq 2.19}$$

z-component of momentum equation is given as

$$\rho\frac{Dw}{Dt}=\frac{\partial \tau_{xz}}{\partial x}+\frac{\partial \tau_{yz}}{\partial y}+\frac{\partial(-p+\tau_{zz})}{\partial z}+S_{M_z} \qquad \textit{eq 2.20}$$

In Newtonian fluids, the viscous stresses are proportional to the rates of deformation (strain *S*).

$$\tau=\mu(S_L)+\lambda(S_V) \qquad \textit{eq 2.21}$$

Where μ is the dynamic viscosity, S_L is the linear strain, S_V is the volumetric strain and λ is the second viscosity. This λ is not well researched as its influence is small.

The stress component acting normal to the fluid element surface produces elongating deformation:

$$S_{xx}=\frac{\partial u}{\partial x}, S_{yy}=\frac{\partial v}{\partial y}, S_{zz}=\frac{\partial w}{\partial z} \qquad \textit{eq 2.22}$$

The stress component acting along the fluid element surface produces shearing deformation as follows

$$S_{xy} = S_{yx} = \frac{1}{2}\left(\frac{\partial u}{\partial y} + \frac{\partial v}{\partial x}\right), \qquad S_{xz} = S_{zx} = \frac{1}{2}\left(\frac{\partial u}{\partial z} + \frac{\partial w}{\partial x}\right), \qquad S_{yz} = S_{zy} = \frac{1}{2}\left(\frac{\partial v}{\partial z} + \frac{\partial w}{\partial y}\right)$$

eq 2.23

Also, volumetric deformation is given by

$$\frac{\partial u}{\partial x} + \frac{\partial v}{\partial y} + \frac{\partial w}{\partial z} = div\, \boldsymbol{u} \qquad \textit{eq 2.24}$$

Viscous stresses in terms of deformation rates are given as follow

$$\tau_{xx} = 2\mu\frac{\partial u}{\partial x} + \lambda div\, \boldsymbol{u} \qquad \tau_{yy} = 2\mu\frac{\partial v}{\partial y} + \lambda div\, \boldsymbol{u} \qquad \tau_{zz} = 2\mu\frac{\partial w}{\partial z} + \lambda div\, \boldsymbol{u} \qquad \textit{eq 2.25}$$

$$\tau_{xy} = \tau_{yx} = \mu\left(\frac{\partial u}{\partial y} + \frac{\partial v}{\partial x}\right) \quad \tau_{xz} = \tau_{zx} = \mu\left(\frac{\partial u}{\partial z} + \frac{\partial w}{\partial x}\right) \quad \tau_{yz} = \tau_{zy}\ \mu\left(\frac{\partial v}{\partial z} + \frac{\partial w}{\partial y}\right) \qquad \textit{eq 2.26}$$

Substituting the stress components in the momentum equation yields the Navier-Stokes equations.

$$\rho\frac{Du}{Dt} = -\frac{\partial p}{\partial x} + \frac{\partial\left(2\mu\frac{\partial u}{\partial x} + \lambda div\, \boldsymbol{u}\right)}{\partial x} + \frac{\partial\left(\mu\left(\frac{\partial u}{\partial y} + \frac{\partial v}{\partial x}\right)\right)}{\partial y} + \frac{\partial\left(\mu\left(\frac{\partial u}{\partial z} + \frac{\partial w}{\partial x}\right)\right)}{\partial z} + S_{M_x} \qquad \textit{eq 2.27}$$

$$\rho\frac{Dv}{Dt} = -\frac{\partial p}{\partial y} + \frac{\partial\left(\mu\left(\frac{\partial u}{\partial y} + \frac{\partial v}{\partial x}\right)\right)}{\partial x} + \frac{\partial\left(2\mu\frac{\partial v}{\partial y} + \lambda div\, \boldsymbol{u}\right)}{\partial y} + \frac{\partial\left(\mu\left(\frac{\partial v}{\partial z} + \frac{\partial w}{\partial y}\right)\right)}{\partial z} + S_{M_Y} \qquad \textit{eq 2.28}$$

$$\rho\frac{Dw}{Dt} = -\frac{\partial p}{\partial z} + \frac{\partial\left(\mu\left(\frac{\partial u}{\partial z} + \frac{\partial w}{\partial x}\right)\right)}{\partial x} + \frac{\partial\left(\mu\left(\frac{\partial v}{\partial z} + \frac{\partial w}{\partial y}\right)\right)}{\partial y} + \frac{\partial\left(2\mu\frac{\partial w}{\partial z} + \lambda div\, \boldsymbol{u}\right)}{\partial z} + S_{M_z} \qquad \textit{eq 2.29}$$

Rearranging the above equations, the Navier Stokes equations can be expressed as follows:

$$\rho\frac{Du}{Dt} = -\frac{\partial p}{\partial x} + div(\mu\, grad\, u) + S_{M_X} \qquad \textit{eq 2.30}$$

$$\rho\frac{Dv}{Dt} = -\frac{\partial p}{\partial y} + div(\mu\, grad\, v) + S_{M_Y} \qquad \textit{eq 2.31}$$

$$\rho \frac{Dw}{Dt} = -\frac{\partial p}{\partial z} + div(\mu\ grad\ w) + S_{M_z} \qquad \textit{eq 2.32}$$

These are the three-dimensional Navier Stokes. [29] In most of the scenarios, the flow field can be solved by considering only the continuity (mass conservation) and Navier Stokes equation (momentum conservation).

As mentioned in section 2.2, turbulent flows are characterised by randomness and chaos caused by instabilities, eddies and swirls and this makes it impossible to describe the motion of all the fluid particles in the flow. The velocity component of the turbulence can be defined by Reynolds decomposition in which a steady mean value is superimposed with a fluctuating time-dependant component. This Reynold's decomposition is exhibited by flow properties such as density, pressure and temperature. The flow property at a point in the flow can be defined as

$$\varphi = \Phi + \varphi' \qquad \textit{eq 2.33}$$

Where φ is the flow property at a point in the flow

Φ is the steady mean value component.

φ' is the fluctuating time-dependent component.

The Reynolds-averaged Navier-Stokes equations for compressible flows is given as follow

Continuity:

$$\frac{\partial \bar{\rho}}{\partial t} + \mathrm{div}\left(\bar{\rho}\widetilde{U}\right) = 0 \qquad \textit{eq 2.34}$$

Reynolds equations

$$\frac{\partial\left(\bar{\rho}\widetilde{U}\right)}{\partial t} + \mathrm{div}\left(\bar{\rho}\widetilde{U}\widetilde{\boldsymbol{U}}\right) = -\frac{\partial \bar{P}}{\partial x} + div\left(\mu\ grad\ \widetilde{U}\right) \qquad \textit{eq 2.35}$$

$$= \left[-\frac{\partial\left(\overline{\bar{\rho}\underline{u}'^2}\right)}{\partial x} - \frac{\partial\overline{\left(\bar{\rho}\underline{u}'\underline{v}'\right)}}{\partial y} - \frac{\partial\overline{\left(\bar{\rho}\underline{u}'\underline{w}'\right)}}{\partial z}\right] + S_{Mx}$$

$$\frac{\partial\left(\bar{\rho}\widetilde{V}\right)}{\partial t} + \mathrm{div}\left(\bar{\rho}\widetilde{V}\widetilde{\boldsymbol{U}}\right) = -\frac{\partial \bar{P}}{\partial y} + div\left(\mu\ grad\ \widetilde{V}\right) \qquad \textit{eq 2.36}$$

$$= \left[-\frac{\partial\overline{\left(\bar{\rho}\underline{u}'\underline{v}'\right)}}{\partial x} - \frac{\partial\left(\overline{\bar{\rho}\underline{v}'^2}\right)}{\partial y} - \frac{\partial\overline{\left(\bar{\rho}\underline{v}'\underline{w}'\right)}}{\partial z}\right] + S_{My}$$

$$\frac{\partial(\bar{\rho}\widetilde{W})}{\partial t} + \mathrm{div}(\bar{\rho}\widetilde{W}\widetilde{\boldsymbol{U}}) = -\frac{\partial \bar{P}}{\partial z} + div(\mu\, grad\, \widetilde{W}) = \left[-\frac{\partial(\overline{\bar{\rho}\underline{u}'\underline{w}'})}{\partial x} - \frac{\partial(\overline{\bar{\rho}\underline{v}'\underline{w}'})}{\partial y} - \frac{\partial(\overline{\bar{\rho}\underline{w}'^2})}{\partial z}\right] + S_{Mz} \qquad \textit{eq 2.37}$$

Scalar transport equations

$$\frac{\partial(\bar{\rho}\widetilde{\boldsymbol{\phi}})}{\partial t} + \mathrm{div}(\bar{\rho}\widetilde{\boldsymbol{\phi}}\widetilde{\boldsymbol{U}}) = \mathrm{div}(\Gamma_{\phi}\,\mathrm{grad}\,\widetilde{\boldsymbol{\phi}}) + \left[-\frac{\partial(\overline{\bar{\rho}\underline{u}'\varphi'})}{\partial x} - \frac{\partial(\overline{\bar{\rho}\underline{v}'\varphi'})}{\partial y} - \frac{\partial(\overline{\bar{\rho}\underline{\omega}'\varphi'})}{\partial z}\right] + S_{\phi} \qquad \textit{eq 2.38}$$

Where the overbar indicates a time-averaged variable and the tilde indicates a density-weighted variable. [29]

These Reynolds equations mentioned above have three normal stresses (τ_{xx}, τ_{yy}, τ_{zz}) and three shear stresses (τ_{xy}, τ_{xz} τ_{yz}) called the Reynolds stresses. These Reynolds stresses are the properties of the flow and don't have any available relations [27]

$$\tau_{xx} = -\overline{\rho\underline{u}'^2}\ \tau_{yy} = -\overline{\rho\underline{v}'^2}\ \tau_{zz} = -\overline{\rho\underline{w}'^2} \qquad \textit{eq 2.39}$$

$$\tau_{xy} = \tau_{yx} = -\overline{\rho\underline{u}'\underline{v}'}\ \tau_{xz} = \tau_{zx} = -\overline{\rho\underline{u}'\underline{w}'}\ \tau_{zy} = \tau_{yz} = -\overline{\rho\underline{w}'\underline{v}'} \qquad \textit{eq 2.40}$$

Turbulence models are necessary to solve the turbulent flows with RANS equations. Turbulence models predict the Reynolds stresses and the unknown terms in the scalar transport equations. Most of the turbulence models require additional transport equations to solve the flow. Industry-standard models such as k-e model and k-w models require two additional transport equations to solve the turbulent flows. [29]

These two-equation models are based on Boussinesq approximation to predict the Reynolds stresses and the scalar transport terms.

2.3.2 Boussinesq Approximation:

Boussinesq proposed that the Reynolds stresses are proportional to the mean velocity gradients (strain rates) through the turbulent viscosity μ_T. Using suffix notation, the Reynolds stress can be expressed as

$$\tau_{ij} = -\rho\overline{\underline{u}'_i\underline{u}'_j} = \mu_T\left[\frac{\partial U_i}{\partial x_j} + \frac{\partial U_j}{\partial x_i}\right] - \frac{2}{3}\rho k\delta_{ij} \qquad \textit{eq 2.41}$$

Where δ is the Kronecker delta used to predict the normal Reynolds stresses accurately. In the last term, k is the kinetic energy per unit mass.

The transport equations utilize this approximation to relate the scalar terms to the gradient of the mean value of the flow property proportionally. The scalar can be expressed in suffix notation as

$$-\overline{\rho u_i'\varphi'} = \Gamma_t\frac{\partial\phi}{\partial x_i} \qquad \textit{eq 2.42}$$

Where Γ_t is the turbulent diffusivity. [29]

2.3.3 Different turbulence models

Three different models are considered in the single-phase study to determine the best model for predicting results similar to the real atomizer.[30] The three models are explained below.

K-ε RNG

The k-ε turbulent is a two-equation model and is commonly used in the industry. This model utilized kinetic energy k and turbulent dissipation ε as the scalars for the two transport equations. There are three different types of k-ε models namely standard k-ε model, realisable k-ε model and RNG k-ε model. An RNG k-ε model has been considered in chapter 4 for the turbulence model sensitivity study. The RNG k-ε model is based on the renormalization group theory and utilizes a different form of epsilon equation to model the eddy viscosity for various scales of motions.[31] The two transport equations are given as

$$\frac{\partial}{\partial t}(\rho k) + \frac{\partial}{\partial x_i}(\rho k u_i) = \frac{\partial}{\partial x_j}\left(\alpha_k\mu_{eff}\frac{\partial k}{\partial x_j}\right) + G_k + G_b - \rho\epsilon - Y_M + S_k \qquad \textit{eq 2.43}$$

$$\frac{\partial}{\partial t}(\rho\epsilon) + \frac{\partial}{\partial x_i}(\rho\epsilon u_i) = \frac{\partial}{\partial x_j}\left(\alpha_\epsilon\mu_{eff}\frac{\partial\epsilon}{\partial x_j}\right) + C_{1\epsilon}\frac{\epsilon}{k}(G_k + C_{3\epsilon}G_b) - C_{2\epsilon}\rho\frac{\epsilon^2}{k} - R_\epsilon + S_\epsilon \qquad \textit{eq 2.44}$$

In eq 2.43 and eq 2.44,

G_k and G_b are the generation of turbulence kinetic energy due to mean velocity gradients and buoyancy.

Y_M is the contribution of the fluctuating dilatation in compressible turbulence to the overall dissipation rate.

μ_{eff} is the effective turbulent vicosity.

S_k and S_ϵ are user-defined source terms.

$C_{1\epsilon} = 1.42$ and $C_{2\epsilon} = 1.68$ are model constants.

α_k and α_ϵ are inverse effective Prandtl numbers.

$R_\epsilon = \frac{C_\mu \rho \eta^3 (1-\frac{\eta}{\eta_0}) \epsilon^3}{k(1+\beta\eta^3)}$ where $\eta = S\frac{k}{\epsilon}$, η_0 = 4.38 and β= 0.012. [31]

This method is suitable for rapidly strained flows and swirling flows. This model provides a differential viscosity model for low Reynolds number flows and also has an analytically derived model for turbulent Prandtl numbers. Also, this model was derived through a rigorous statistical technique. Generally k-ε models are used in external flows and do not perform well with no-slip walls, adverse pressure gradients, strong curvature into flow and jet flows. [29],[31]

standard k-ω model

This is also a commonly used turbulence model and requires two equations to solve the flow. The first transported variable is turbulent kinetic energy k and specific dissipation ω specific dissipation rate is the dissipation rate per unit kinetic energy

$$\omega = \frac{\varepsilon}{k} \qquad \textit{eq 2.45}$$

The two transport equations are given as

$$\frac{\partial}{\partial t}(\rho k) + \frac{\partial}{\partial x_i}(\rho k u_i) = \frac{\partial}{\partial x_j}\left(\Gamma_k \frac{\partial k}{\partial x_j}\right) + G_k - Y_k + S_k \qquad \textit{eq 2.46}$$

$$\frac{\partial}{\partial t}(\rho \omega) + \frac{\partial}{\partial x_i}(\rho \omega u_i) = \frac{\partial}{\partial x_j}\left(\Gamma_\omega \frac{\partial k}{\partial x_j}\right) + G_\omega - Y_\omega + S_\omega \qquad \textit{eq 2.47}$$

In eq 2.46 and eq 2.47,

G_k is the generation of turbulence kinetic energy due to mean velocity gradients

G_ω represents the generation of ω

Γ_k and Γ_ω are the effective diffusivity of k and ω.

Y_k and Y_ω are the dissipation of k and ω.

S_k and S_ϵ are user-defined source terms

A Different modification has been applied to this model over time by different researchers such as Saiy (1974), [32] Spalding (1979), [33] Wilcox (1988), [34] Speziale et al. (1990) [35] and Menter (1993). [36] This model predicts the flow separation due to adverse pressure gradient accurately. This model is sensitive to the inlet free stream turbulence properties which can be solved by using the k-ω SST model. [30], [31].

k-ω SST

k-ω shear stress transport model utilises a modified version of turbulent viscosity formulation to deal with the principal turbulent shear stress. The two transport equations are given by

$$\frac{\partial}{\partial t}(\rho k) + \frac{\partial}{\partial x_i}(\rho k u_i) = \frac{\partial}{\partial x_j}\left(\Gamma_k \frac{\partial k}{\partial x_j}\right) + \overline{G}_k - Y_k + S_k \qquad \textit{eq 2.48}$$

$$\frac{\partial}{\partial t}(\rho \omega) + \frac{\partial}{\partial x_i}(\rho \omega u_i) = \frac{\partial}{\partial x_j}\left(\Gamma_\omega \frac{\partial k}{\partial x_j}\right) + G_\omega - Y_\omega + D_\omega + S_\omega \qquad \textit{eq 2.49}$$

In eq 2.48 and eq 2.49,

$\overline{G}_k$ is the generation of turbulence kinetic energy due to mean velocity gradients.

G_ω represents the generation of ω.

Γ_k and Γ_ω are the effective diffusivity of k and ω.

Y_k and Y_ω are the dissipation of k and ω.

D_ω represents the cross-diffusion term.

S_k and S_ϵ are user-defined source terms.

It is useful for flow separation and stagnation region prediction. This model predicts the separation form a smooth surface and transonic shock waves accurately compared to all other

models. As this model uses the k-ω formulation in the inner parts of the boundary layer, it could be used to predict the flow without any additional damping functions. In high Reynolds number flows, the model switches to the k-ε function in the free stream to avoid the sensitivity to the inlet turbulence properties. This model is utilized in problems with separated flows and jets but is difficult to converge. [30], [31]

2.3.4 Multiphase phase flows:

Two types of models are used to solve a large variety of multiphase flows. They are Euler-Euler and Euler-Lagrangian model. In Euler-Euler model, the motion of the group of suspended particles and the gas that carries it are modelled as a continuum and the solution is obtained. In Euler-Lagrangian model, the gas phase is solved as a continuum and the motion of the suspended particles are solved by Lagrangian equations which are integrated along their trajectories. [37]

Euler-Euler approach

The same set turbulent equations can be utilized to solve both the motion of the gas phase and the motion of the group of suspended particles in Euler-Euler model. Closure problem in CFD modelling is the presence of terms in the flow equations that do not have any relations. This problem is solved by introduction of assumptions in the flow equations. Different types of closure assumptions are made for gas-phase and suspended phase. The properties of the dispersed phase such as velocity, mass transfer, momentum transfer and energy transfer are obtained by averaging over a control volume. The mass of particles per unit volume is also a continuous property in this approach. A major drawback in this approach is that the information about the motion of the individual particle cannot be obtained. Also, this model give rise to problems in constructing the boundary conditions of the dispersed phase on the surfaces enclosing the flow. In order to model the group of particles as a continuum, the geometric scale of the particles must be minor compared to the scale of variation of the flow parameters and also there should be a significant number of particles in order to obtain an accurate determination of the averaged parameters. [37] Generally, flows with high concentration of particles are solved using this approach. Gosman et al.[38], Ishii [39-42], Delhaye [43], Drew [44, 45], Hirt [46], Enwald et al [47] carried out important works in Eulerian-Eulerian models.

Lagrangian approach

Detailed information about the motion of the individual particles is obtained in Euler-Lagrangian approach as the equation of motion of the particles is integrated in a solved gas field. The gas field is solved with RANS equation with appropriate turbulent models. The

equation of motion of particles along with the forces acting on it as well as the mass, momentum and energy transfer are solved for the dispersed phase. The flow around the individual particle is not solved and the finite dimensions of the particle are not considered. Therefore, a constraint of this approach is that the particle dimensions must be smaller than the grid size. This approach can be utilised for flows ranging from dilute phase to dense phase. Concentration of particles play as major role in obtained the solution through this approach. An increase in concentration influences the gas flow parameters thereby requiring additional iterations to solve the flow. Also, the possibility of particle-particle collision increases with increase in concentration leading to entangled trajectories. When the particle size is very small, there will be many particles for the same concentration. In this circumstance, entanglement complicates the computations as it is essential to obtain the interaction between the particles and all the turbulent eddies in the flow to calculate the average of the dispersed phase parameters.

There are different kinds of Lagrangian approach. A classical Lagrangian approach utilises a parcels method for the dispersed phase modelling. Both DPM (Discrete Phase model) and DEM (Discrete Element Model) tracks individual particles in the flow. In parcel method, the parcels represent a definite number of real particles of same properties. The particle mass flux is realised in this approach.

The DPM and DEM method tracks all the individual particles in the system and therefore has system size constraints. In DEM, particle-particle interaction and particle-wall interactions are tracked. These interactions are considered as a continuous process that occurs over a finite time and the contact force is calculated as a continuous function of the distance between colliding particle or distance between particle and the wall. This model gives accurate results for flows with high volume of dispersed phase but requires a lot of computational resources. DPM can be utilised for flows with dispersed phase accounting for less than 10% of the total volume of the flow. An advantage of this model is that it accepts high mass loading i.e. $\dot{m}_{particles} \geq \dot{m}_{fluid}$. DPM allows us to solve the flow for various degrees of coupling. In an uncoupled approach, the pressure and viscous stresses due to the particles are neglected when constructing the gas phase equations. The gas flow field is not influenced by the presence of the particle. In one-way coupling, the influence of the particles on the gas field is considered. The interaction between the particles is not considered in this approach. In two-way coupling, the particle-particle interaction is also considered. Though the two-way coupled approach provides a much accurate results, it is computationally intensive. [37]

In a dilute flow, particles are influenced by gas transport effects i.e. drag forces, lift forces and turbulence. The interaction between the particles is not very high. On the other hand, flows

with dense dispersed phases are characterised by high interparticle collisions and the gas transport effects are negligible compared to the effect of the inter-particle collision. The flows with dilute dispersed phase and dense dispersed phase can be classified based on the ratio of the particle response time τ_P to the average time between collisions τ_c as follows:

Dilute two-phased flow:

$$\tau_P < \tau_c \Rightarrow \frac{\tau_P}{\tau_c} < 1 \qquad \textit{eq 2.50}$$

Dense two-phased flow:

$$\tau_P > \tau_c \Rightarrow \frac{\tau_P}{\tau_c} > 1 \qquad \textit{eq 2.51}$$

In a dense dispersed phase flows, the collision time lesser than the particle response time and therefore the particle cannot respond to the fluid flow between collisions. This type of flow will contain dispersed phase with large number of particles with low density or small number of particles with high density. Hence gas transport effects are negligible compared to the force due to inter-particle collision. In dilute dispersed phase flows, the inter-particle collision occurs but the particles will have time to respond to the gas transport effects. In this flow, gas transport effects will be the dominant effect. [37]

In the DPM model, the particle trajectory is predicted by integrating the force balance on the particle. The force balance is computed by summing the forces acting on the particle and is given by

$$\frac{du_p}{dt} = F_D(u - u_p) + \frac{g_x(\rho_p - \rho)}{\rho_p} + F_x \qquad \textit{eq 2.52}$$

F_x is an additional acceleration.

$F_D(u - u_p)$ is the drag force per unit particle mass given by

$$F_D = \frac{18\mu}{\rho_p d_p^2}\frac{C_D Re}{24} \qquad \textit{eq 2.53}$$

u is the fluid phase velocity.

u_p is the particle velocity.

μ is the molecular viscosity.

ρ is the fluid density.

ρ_p is the density of the particle.

d_p is the particle diameter.

Re is the relative velocity given by $Re = \frac{\rho d_p |u_p - u|}{\mu}$

2.3.5 Discrete phase method

A discrete phase method has been used in this study. Different aspects related to this method are discussed below.

Forces on the particle:

The main forces acting on the dispersed phase are as follows

Aerodynamic drag force: This force arises due to the shearing forces experienced by the particles due to the gas. Numerous drag laws are available. Spherical drag law has been utilised in this study.

Gravity force: This is an important force acting on the particles. This plays a major role in flows with free falling particles.

Saffman force: This is a lift force arising due to the variations in the average velocity of the carrier gas. This force will have a significant effect on particles in flows where the gradients of the average velocity is high.

Magnus force: This is a lifting force arising due to the particle rotation. A rotating particle entrains the gas. The side where the force due to the flow past the particle and the rotational force coincide, a lifting force develops acting on the particle.

Turbophoresis force: This force arises due to the variation in the fluctuating velocity component of the gas phase i.e. the variation in the turbulence of the flow. This force is significant during the near wall interaction of the particles.

Thermophoresis: This force arises due to the variation in the temperature profile of the gas field.

Only aerodynamic drag force has been considered in this study and spherical drag law has been applied. [31]

Turbulent dispersion of particles:

Turbulent flow parameters can be expressed as a sum of mean steady component and fluctuating component. Stochastic models utilise probability density function to estimate the instantaneous components. The distribution of concentration of the particles about the mean trajectory path can be obtained through a gaussian probability density function whose variance is based on the extent of the particle dispersion due to the turbulent fluctuations. In order to predict the particle dispersion, integral time scale T is required. Integral time scale T is the total time spent by the particle in the turbulent motion and is given by

$$T = \int_0^\infty \frac{\underline{u}'_p(t)\underline{u}'_p(t+s)}{\overline{\underline{u}'^2_p}} ds \qquad \textit{eq 2.54}$$

Where T is the integral time scale.

$\underline{u}'_p(t)$ is the fluctuating component of velocity of the particle at the time t.

$\underline{u}'_p(t+s)$ is the fluctuating component of velocity of the particle at the time t+s.

$\overline{\underline{u}'^2_p}$ is the root mean square of the fluctuating component of velocity at time t.

Considering a small particle moving along the fluid, the integral time T_L is approximated in k-ε models as

$$T_L = C_L \frac{k}{\varepsilon} \qquad \textit{eq 2.55}$$

Where C_L is unknown and needs to be determined.

In k-ω models, ω can be substituted as $\varepsilon/_k$ and integral time T_L is approximated as

$$T_L = \frac{C_L}{\omega} \qquad \textit{eq 2.56}$$

In Discrete Random walk model (also known as stochastic model), the particles interaction is simulated as an interaction with turbulent eddies in the gas flow. The eddies are defined by fluctuating component of the velocities governed by Gaussian probability density function and timescale. The only input required in stochastic modelling is the timescale constant C_L. [31, 37]

2.3.6 Solution methods

Flows are described by partial differential equations and obtaining solutions by solving them is impossible for most complex problems. Discretization methods are used to solve complex problems by approximation. There are three different types of discretization methods namely Finite Difference method, Finite element method and Finite Volume method.

Finite difference method [FDM] is a straightforward method in discretizing partial differential equations. In FDM, the flow at the point is replaced by a set of discrete equations and these equations are solved for obtaining a solution. This is a very efficient solution method for structured grids. Therefore, this method cannot be used for irregular geometries to obtain high fidelity results.

Finite element method [FEM] is suitable for a wide variety of multi-physics problems. FEM divides the geometry into smaller domains called elements. The partial differential equations (PDEs) are set up for each element by introducing approximations in the form of simple linear or quadratic polynomial equations. When the PDEs over all elements are combined, they give rise to a matrix of equation systems which can be solved by well-known solvers.

Finite Volume Method [FVM] also involves dividing geometry into smaller domains. FVM method utilizes the conservation laws to solve the flow, and this gives rise to flux conservation equations averaged over the cells. ANSYS and other commercial software utilize this method to solve the equations. Second order discretization schemes of FVM methods are utilized in this project to generate results.[31]

3 LITERATURE REVIEW

The literature review presented in this chapter has been divided into three parts. The fundamental science behind the close-coupled gas atomization has been reviewed in first chapter. The second part deals with the design aspects of the atomizer. The third part reviews the numerical works related to close-coupled gas atomization. In the beginning, the research about CCGA was only through experiments as the computational resources were limited. As the computational power advanced, research through modelling activity increased as the extreme conditions of CCGA such as high temperature and high pressure is unfavourable for thorough experimental analysis.

3.1 Fundamental Science

Close-Coupled Gas Atomization (CCGA) is a complex, chaotic and turbulent interaction between gas jets of high velocity and melt. The earliest work on CCGA was done by Thompson in 1948 in which the influence of process parameters and different nozzle designs were studied.[48] Most of the early works concentrated on the influence of process parameter such as gas-melt ratio, gas pressure, flow rate on particle sizes.[49, 50] However, it was only during 1980s, the research activity increased due to increased interest in powder microstructure and powder properties. This section consists of breakup mechanism, design parameters affecting the atomization and wake closure phenomenon.

3.1.1 Breakup mechanism:

In CCGA, the atomization of melt is obtained by the transfer of kinetic energy from high velocity gas jet to the stream of molten metal resulting in ligands and then melt droplets. [51] The size of the melt droplets is affected by density, surface tension and viscosity. Generally, a large average particle size distribution is the result of higher surface tension and higher viscosity. [5, 24, 52] The melt exiting the nozzle is destabilized by the aerodynamic forces exerted by the gas jets. During the primary breakup, the internal resistance provided by surface tension and the viscosity acts against this destabilization and damps the unstable perturbation. The force distribution on the melt droplet surface changes with deformation. As the aerodynamic forces exceed the internal resistance result in disruption of melt into smaller droplets. The breakup of melt continues till these forces balance each other. [53]

In the CCGA process, the atomizing gases form a recirculation zone in front if the nozzle and the melt exiting the nozzle enters the recirculation zone. Figure 3.1 shows the schematic representation of melt with the nozzle.

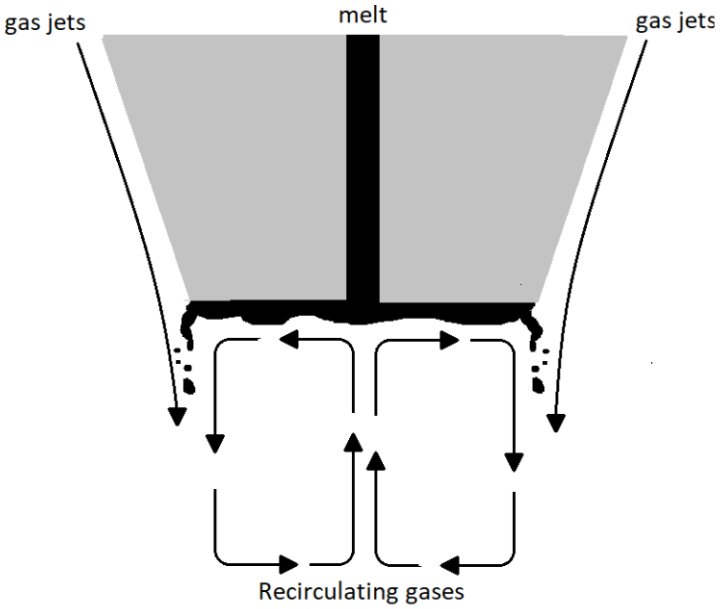

Figure 3.1 Schematic representation of melt and the nozzle

The recirculating gases push the melt against the nozzle surface as a film and this is termed as pre-filming. [54] The melt break-up can be broadly categorised as primary breakup, secondary breakup and solidification of melt droplets.

The melt break-up can be broadly categorised as primary breakup, secondary breakup and solidification of melt droplets. The melt film is broken into ligands in primary atomization and the ligands are broken into melt droplets in secondary atomization which solidify. Figure 3.2 shows the melt breakup to droplets.[54]

a) During the pre-filming step, the melt exiting the delivery tube is acted upon by the forces exerted by the recirculating gas resulting in stagnation pressure upstream and an ambient pressure downstream. This forces the melt to spread across the nozzle exit area in the form of thin film. [55]
b) In primary breakup step, the film is broken into ligaments due to the perturbations and instability induced by the aerodynamic forces.
c) In secondary breakup step, the ligaments are further atomized by the high-speed gas flow into droplets which solidify to form powders eventually.

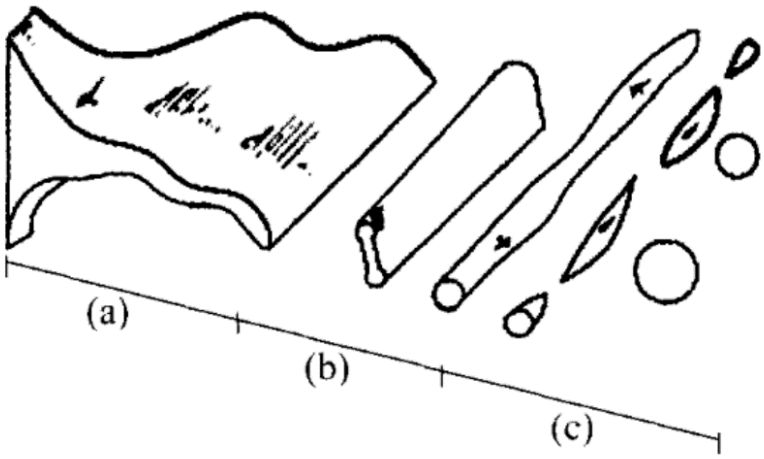

Figure 3.2 Schematic representation of the melt breakup.[54]

3.1.2 Primary breakup:

Savart conducted the earliest analysis on droplet formation in 1833. Plateau investigated the influence of surface tension on liquid disintegration and introduced the "plateau tank" to get rid of gravity effect in his study. [56, 57] This was followed by Lord Rayleigh who proposed that the liquid breakup is due to the hydrodynamic instability in 1879.[58] Rayleigh's investigations were developed by other people such as Eotvos (1886), [59] Quincke (1877), [60] Lenard (1887),[61] and Bohr (1909). [62]

Dombrowski and John developed the earliest model of liquid jet disintegration.[63] A more refined model was developed by Bradley in which compressible gas with uniform velocity was flowing over horizontal liquid sheet of zero velocity. [50, 64]. Bradley's model did not consider the influence of process parameters such as nozzle geometry, Gas to metal ratio and melt properties. Data obtained from this model was found to match with experimental data obtained by See within a factor of 2. [65] Most of the models developed initially did not consider the normal component of gas velocity on melt and assumed that gas and melt flowed in parallel.

Primary breakup of melt occurs through one of the four mechanisms listed below:

- Liquid dripping
- Liquid column breakup
- Liquid film breakup
- Ligament breakup

Liquid dripping

At this stage in atomization (primary breakup), force of gravity is less effective on the melt breakup therefore this mechanism is highly unlikely to occur.

Liquid column breakup

Rayleigh noticed this mechanism for the first time which is commonly observed in low pressure conditions in free fall gas atomization.

Then this mechanism was expanded through different methods by Kuehn (1925), [66] Weber (1931), [67] and DeJuhasz et al. (1931). [68] Laufer (1950) [69] and Ranz (1956) [70] investigated the behaviour of turbulent jet on liquid column break-up. Tennekes & Lumley (1972), [71] Hinze (1975) [72] and Schlichting (1979) [73] also investigated the same. Moreover, Fargo & Chigier (1992) [74] used high speed imaging technique to reveal various breakup mechanism based on weber number.

Based on the Weber number, three types of column breakup is observed as shown in Figure 3.3 [74]

(a) Rayleigh type breakup also normal pulsing is observed between $0 < W_{eA} < 25$
(b) Membrane type breakup observed between $25 < W_{eA} < 70$
(c) Fibre type breakup also known as super pulsing observed between $70 < W_{eA} < 500$

Liquid film breakup

Film breakup happens through a pre-filming mechanism and is observed throughout the CCGA process. The aerodynamic forces exerted by the gases on the melt exiting the delivery tube causes the melt to spread into a thin film across the nozzle exit surface. This leads to the atomization of melt film across the nozzle edges. Pre-filming mechanism is affected by gas, melt properties, internal resistance and aerodynamic forces. Frazer et al. [55] reported a model of three steps for film break-up during gas atomization process at the air blast atomizer which was also observed by Mansour and Chigier. [75] These are (a) rim disintegration, (b) wave disintegration, and (c) perforated film break-up. Figure 3.4 shows the types of breakup mechanism. [55]

Rim disintegration is observed in fluids with high viscosity and high surface tension. In this type, the fluid becomes thicker around the free edges and break into larger droplets which further break into smaller droplets. In wave disintegration, fluid breakup is brought about by fluctuations in the film that are in distinct wavelengths. The waves break-up the film into whole or half wavelength sections and these sections disintegrate into smaller droplets. In

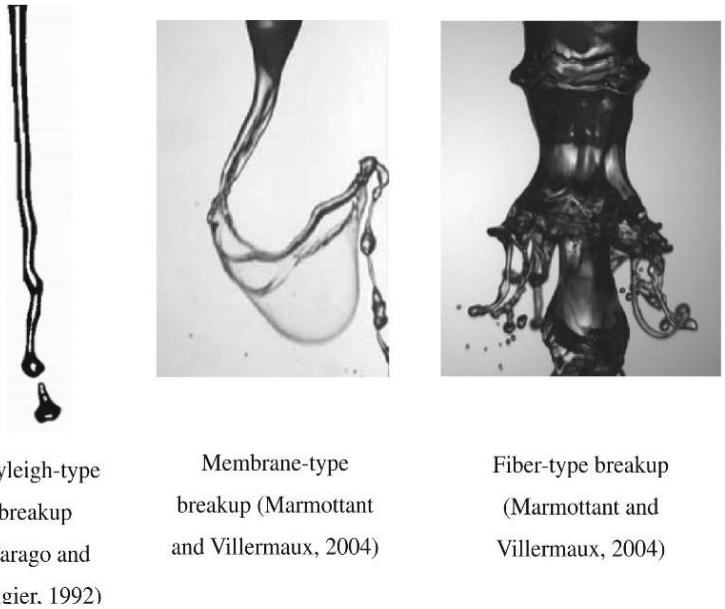

Figure 3.3 Various types of liquid column breakup mechanism. [74]

perforated film breakup, droplets of various sizes are formed due to holes developed in the liquid sheet. As the size of the holes increases, the rims get thicker. The holes continue to increase in their sizes until they encounter other rims to coalesce. [55]

Carvalho and Heitor (1998) [76] established a relationship between the liquid breakup and the aerodynamic forces causing it. They studied the liquid film breakup of water with an air blasted chamber using shadowgraph technique and found that the air velocity affects the breakup.

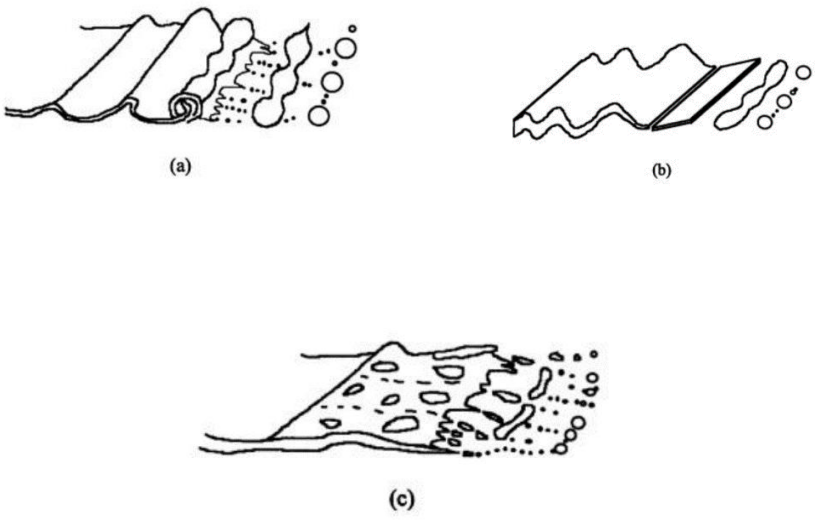

Figure 3.4 various types of liquid film breakup. [55]

Liquid ligament breakup

The liquid ligament breakup follows the film breakup method. Frazer et all [55] established the Rayleigh mode of ligament breakup which is the main mechanism of melt breakup. Based on the experimental results, they reported the relationship between mean particle diameter and the melt film thickness in CCGA. As a wide range of droplet sizes were observed, they concluded that more control must be exerted in this method.

During the filming process, the thickness of film depends on the contact angle θ of the liquid to delivery tube orifice. The minimum thickness of the film ($H_{min}\ mm$) is related to the contact angle θ by [77]

$$H_{min} = (1 - cos\theta)^{0.22} \qquad eq\ 3.1$$

The diameter of ligament d_L obtained from the melt film is determined by the film thickness H and the maximum instable wave number K [78]

$$d_L = \sqrt{\frac{16H}{K}} \qquad eq\ 3.2$$

$$K = \frac{\rho_g V^2}{2\sigma} \qquad eq\ 3.3$$

where ρ_g is the gas density, V is the gas to melt flow velocity.

σ is the melt surface tension and is a function of temperature T[79]:

$$\sigma = \sigma_m - k(T - T_m) \qquad eq\ 3.4$$

where σ_m is the melt's surface tension at melting point T_m, k is a constant related to material property.

Obeying the Rayleigh instability, liquid ligament is broken into fine droplets. And the diameter of these droplets d_P can be calculated with the following equation:

$$d_P = 1.88 d_L (1 + 3Oh)^{1/6} \qquad eq\ 3.5$$

where $d_P$is diameter of droplet,

Oh is Ohnesorge number.

However, this breakup process is random in nature due to Rayleigh instability leading to random distribution of droplet diameter.

3.1.3 Secondary breakup:

The melt is further atomized to finer droplets through secondary breakup and heavily influences the final particle size distribution in CCGA. Hsiang and Faeth (1992)[80] revealed some similarities between this mechanism and liquid column break-up. Therefore, weber number plays an important role in this breakup mechanism.

Different modes of breakup observed are: (a) twin breakup (b) bag breakup (c) film stripping (d) catastrophic breakup. Figure 3.5 shows the different breakup modes. [81]

Each breakup mode is characterised by different deformation process and the microstructure of the powder is determined by the initial cooling rate.[81]

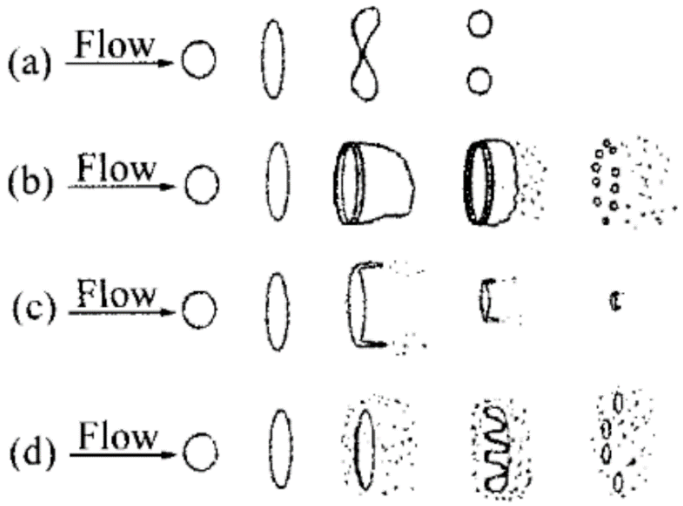

Figure 3.5 different types of secondary breakup. (a) Twins: 10.7≤We (b) bag breakup 12≤We≤100 (c) Film stripping 100≤We≤350 (d) Catastrophic 350≤We. [81]

The first type of breakup is the twin breakup denoted by (a) in the Figure 3.5. The type of breakup is seen for the flow with 10.7≤We<12.0. The next type of breakup is the bag breakup and is denoted by (b) in the Figure 3.5. Bag breakup is seen for the flows with 12≤We≤100 where the ring edge breaks into larger droplets. The film stripping breakup is seen for flows with 100≤We≤350 where the edges are disintegrated into finer droplets. Catastrophic breakup is a complicated process that is not well understood yet, but it yields ultrafine and uniform sized powders. It occurs for the flow with 350 ≤ We.[54]

3.2 Wake Closure Phenomenon

The characteristic feature of CCGA is the complex gas-flow field surrounding the melt delivery nozzle. The efficiency and powder size distribution can be increased by understanding this complex gas flow field.[22, 81-83] The gas flow field can be divided into near field and far field. The area downstream the melt nozzle about 3-4D lengths is termed as near field area. Here, D is the diameter of the melt nozzle. The gas jets in the near field area are characterised by high kinetic energy and a great degree of atomization happens in this region. The area further downstream is termed as far field region. [82]

The gas flow field has been studied comprehensively through Schlieren method. It has been concluded from these studies that the melt disintegration occurs not only through shearing of melt by the gas jets but also occurs in recirculation zone. Figure 3.6 shows the near field of the CCGA for a convergent divergent nozzle. [22]

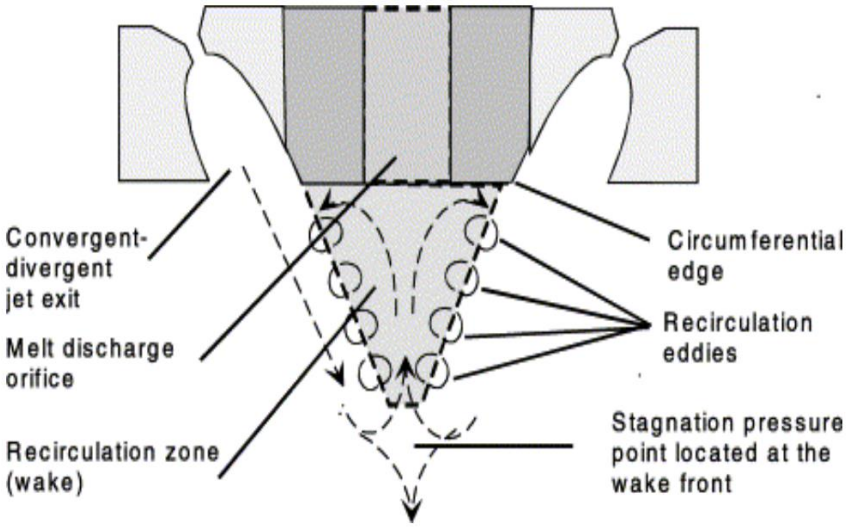

Figure 3.6 Gas flow field in the nearfield region. [22]

The melt stream entering the recirculation zone in front of the melt nozzle is acted upon by the recirculating gases which pushes the melt into a thin film around the melt nozzle tip. [22] This phenomenon of melt breakup in the recirculation zone is chaotic and not well-understood. Different hypotheses have been published by various researchers. [22, 83, 84]

One of the popular hypotheses about the recirculation mechanism proposes aspiration pressure as the reason for its formation. Also, aspiration pressure influences the volume of melt entering inside the recirculation zone. Aspiration pressure is the pressure measured at the melt orifice and is the time/average mass balance of the gas entering and exiting the control volume. Aspiration pressure depends on the operating gas pressure. [22, 85]

In choked nozzles, the gas jets undergo expansion on exiting the gas die and lose energy. They continue to expand till the free boundary while producing shocks. The expanding gas jets meet the other expanding gas jets at the focal point. The part of the flow turns towards the melt nozzle tip forming the recirculation zone. This recirculation zone is entrained by the wake boundary of expanding gas jets which is formed by the recompression shock waves formed by the flow at subsonic speeds. [23] Figure 3.6 shows the wake boundary region with the recirculation zone. [22]

The operating gas pressure of the atomizer decides the type of the wake formed. The wake can be either open or closed. A closed wake occurs at higher pressures (>4.5 MPa) and is caused by the oblique shock waves crossing each other in front of the melt nozzle forming a Mach disk. An open wake is formed at lower pressures where the oblique shockwaves don't cross each other and hence no Mach disk is formed. [22, 23] The recirculation zone in both the cases has a stagnation point which moves downstream as the operating pressure increases. This in turn leads to increased gas flow into the recirculation zone. The primary breakup in the recirculation zone was studied by Settles and Mates through schlieren images of pre-filming of molten tin in front of the melt delivery nozzle tip. [85] The melt stream entering the recirculation zone is forced across the melt nozzle surface to form a thin film by the radial forces due to the recirculating flow through pre-filming. It was found that the thickness of the film formed in this stage influences the particle size. [84]

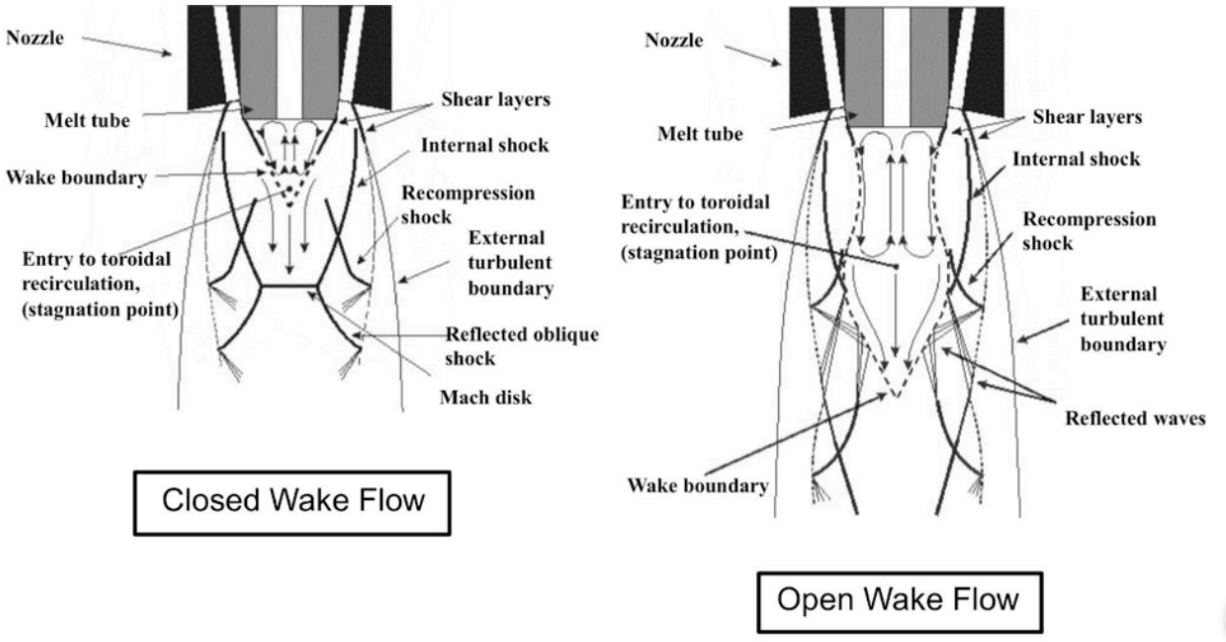

Figure 3.7 Schematic representation of open and closed wake conditions. [22]

Figure 3.7 shows the gas flow field for open and closed wake conditions in an atomizer with square tipped melt delivery tube. [22]

The size and the shape of the recirculation zone is influenced by the gas die design, atomizing pressure and melt delivery system design. The Mach disk has been discussed in section 2.2.4. In the single-phase analysis (gas-only), a stable Mach disk is observed in all the atomizing pressures that produce a closed wake. Also, the flow exhibits steady behaviour in the absence of melt. In physical process, the Mach disk deteriorates and the flow exhibits unsteady behaviour for all pressures that produce a closed wake.[86] Ting et al analysed the open and close wake conditions and proposed a pulsation model.[87] They analysed a range of pressures in a atomizer with a tapered tipped melt delivery tube.

In this model, the melt spreads in the recirculation zone due to shallow aspiration pressure when the atomizing pressure is less than 4.95 MPa in the considered atomizer design. As the wake region increases for the open wake condition, gas flow into the recirculation zone increases leading to a significant increase in aspiration pressure. This significant increase in aspiration pressure causes disruption in melt flow as the gas forces the melt into the melt orifice. The wake returns to the original shape when the melt flow into the recirculation zone decreases. In closed wake condition, the melt flows in the recirculation zone causing the closed wake to change to open wake. The Mach disk disappears and the gas flows into the recirculation zone resulting in an increase in aspiration pressure and decrease in melt flow. The wake returns to the original shape. This phenomenon is observed at a frequency of 10-50 Hz and can be seen as flickering in the CCGA process. This pulsation of the recirculation zone controls the primary breakup. [22, 23]

Ting et. al. carried out their analysis through high-speed imaging. The captured images were digitised and the number of pixels representing the melt area was used as the input data for discrete Fourier transform. The solution spectrum contained many high-amplitude peaks in the low frequency range which corresponds to the fluctuations in melt flow in the recirculation zone. [21]

Mullis et al also carried out high speed imaging of the melt plume movement in recirculation zone. They also carried out Fourier transform of the pixel data obtained from the images containing the melt movement in the recirculation zone. They found that the plume oscillates at a frequency less than 25Hz and precesses at a higher frequency at about 360 Hz. They also analysed an analogue atomizer where the melt was replaced with water to analyse the precession. They concluded that the precession exhibited by the melt plume is not influenced by the operating gas pressure and depends on the gas die design and melt delivery system design. [88].

Another notable extensive study about CCGA was carried out by Mates and Settles. They studied gas flow field around various converging and converging-diverging nozzles for both annular slit atomizer and discrete jet atomizer. They disputed the pulsation model and suggested that wake closure does not affect the melt movement into the recirculation zone. [[84, 85]

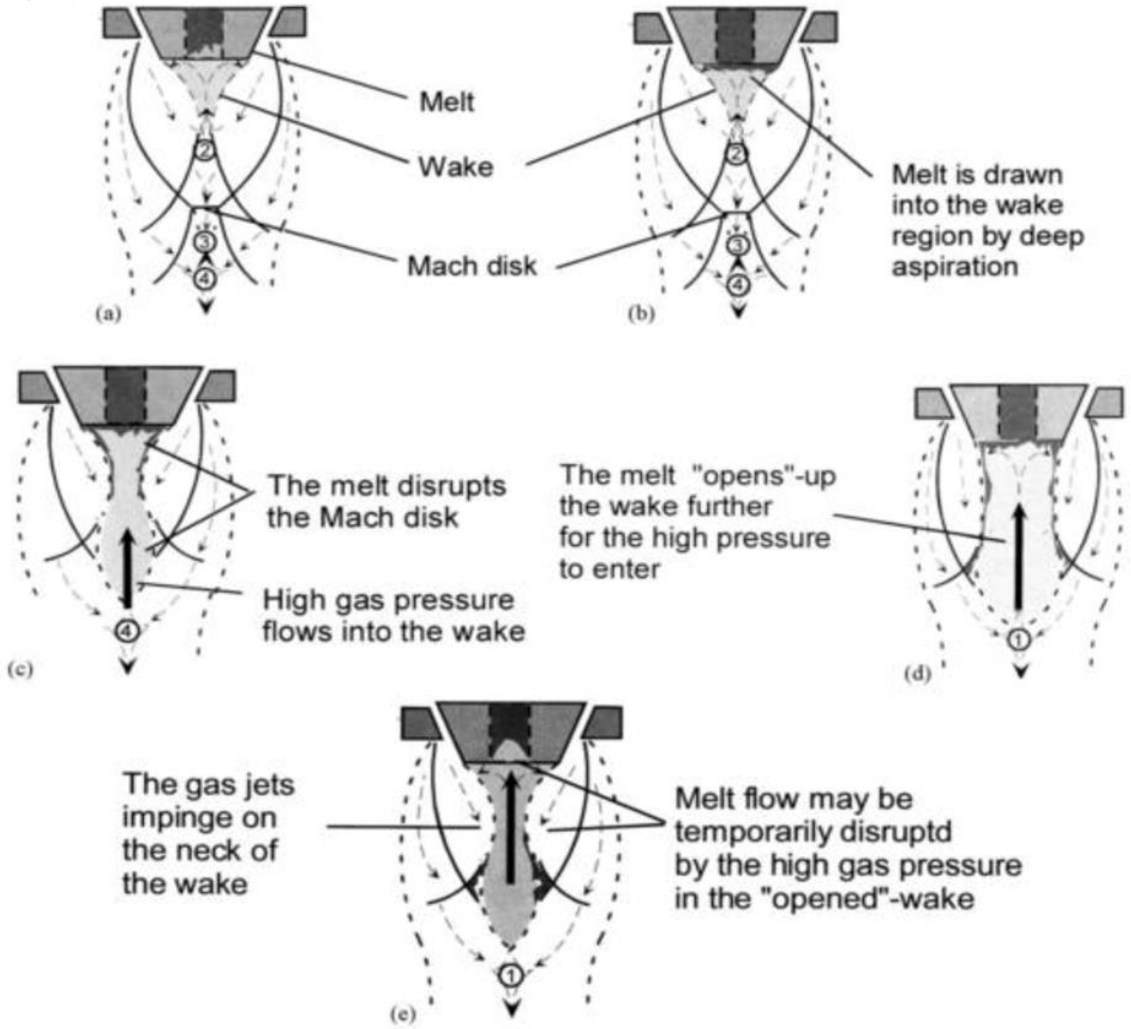

Figure 3.8 Schematic representation of the pulsation seen during atomization. [23]

Figure 3.8 shows the schematic representation of a pulsation model for a closed wake conditions. [23]

The pressure at which the wake transitions between open-wake condition and closed-wake condition is called the Wake Closure Pressure. Gas die design melt delivery design and the operating pressure influence the wake closure pressure (WCP). Ting et al analysed the influence of WCP on powder size of Nickel based alloy.[21] They concluded that the powders obtained by operating the atomizer at a pressure slightly higher than the WCP were 42% finer than the powders obtained through open-wake. [21, 89, 90] These results were disputed by

Mates and Settles who suggested that the WCP does not affect the powder size. They also concluded that closed wake conditions are not preserved in CCGA. [84]

3.3 Design parameters affecting the performance.

Various parameters of atomizer design such as gas jet delivery design, melt delivery tube design and gas die design influences the powder size distribution and efficiency. A lot of research has been focussed on increasing efficiency. [89-91] Optimising these process parameters will result in increased efficiency and higher yield of fine powders. Various factors affecting these process parameters are discussed in this section.

3.3.1 Gas jet delivery design

In CCGA, the melt droplets are formed by kinetic transfer energy between melt and the gas jets. An optimised gas jet die will lead to better kinetic energy transfer which in turn affects the powder size distribution. Gas die system design and gas jet tube design are two aspects influencing the efficiency of the gas jet die that are discussed here.

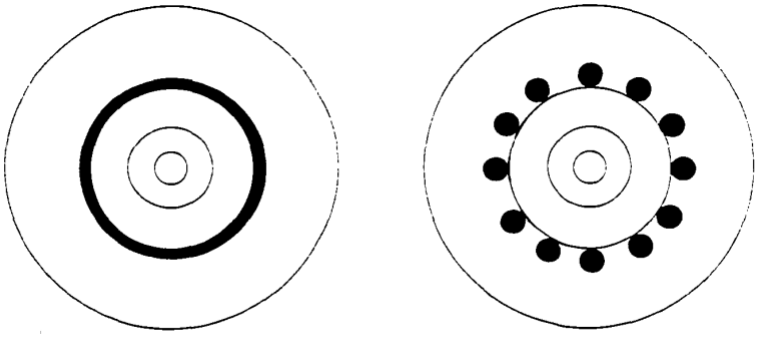

Figure 3.9 schematic representation of bottom view of annular slit confined feed (left) and discrete jet confined feed (right). [92]

Gas die design system:

The design profile of the gas die such as apex angle and gas delivery arrangement affect the gas-melt interaction. There are two types of gas delivery arrangement- Annular Slit Confined Feed (ASCF) and Discrete Jet Confined Feed (DJCF). ASCF have parallel-walled gas passage for the gas delivery surrounding the melt delivery tube in the form of circular slit. The outer wall of the melt nozzle forms the inner gas die surface. DJCF has a system of discrete jets placed strategically around the melt delivery tube. Figure 3.9 shows the front view of the ASCF and DJCF. [92]

ASCF is the most commonly used atomizer design in industries but has high gas consumption. This affects the efficiency of the atomizer negatively. Therefore, these atomizers operate at 2-

4 MPa pressure. Also, asymmetric flow field and alignment of the focal point of gas flow with the melt nozzle axis are other two key issues in this design that affects the efficiency [91, 93]

DJCF is a new atomizer design developed recently to offset the drawbacks in ASCF. This design is known for producing fine and spherical powders. The ring of discrete jets is placed at a distance from the melt nozzle. The gas consumption in this method is less compared to ASCF for the same operating pressure as the gas exit surface area is lesser than ASCF. A high-pressure difference between the entry and exit of the choked gas delivery tube influences the velocity of the gas which in turn affects the gas mass flow rate into the atomization chamber. Therefore, the DJ nozzle with choked delivery tube needs to be operated at a pressure higher than the operating pressure of AS nozzle to achieve the same gas mass flow rate, to compensate for the reduced exit surface area. This is due to the conservation of mass (continuity equation). Therefore, it is possible to increase the operating pressure to obtain finer particles. [49][91] DJCF nozzle is intricate in design and difficult to manufacture and therefore isn't commonly used in industries.

Two famous discrete jet gas die designs are the Ultrasonic Gas atomizer (USGA) and High-Pressure Gas Atomizer (HPGA). USGA is the earliest model and utilised ultrasonic sound waves which is not yet completely understood. This gas die had a special cavity in which high frequency ultrasonic sound waves with sufficient kinetic energy is produced when atomizing gases passed through it. Ultrasonic waves are produced due to boundary layer expansion.[93, 94] Ting et al discovered that increasing operating pressure decreases the particle size

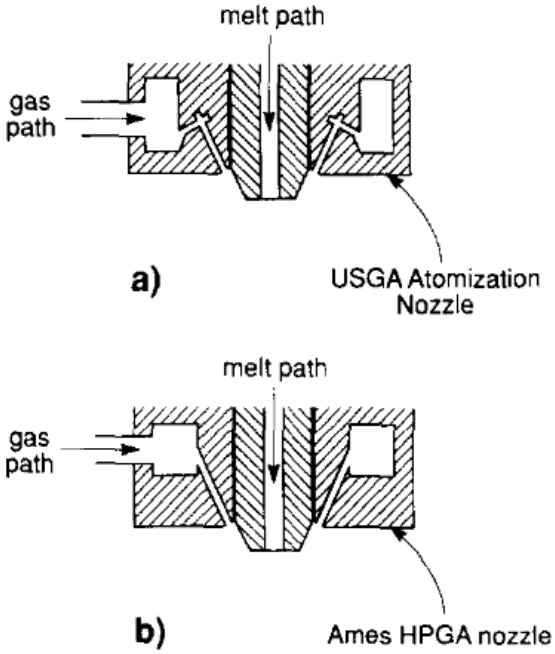

Figure 3.10 cross-sectional view of the USGA atomization nozzle(a) and HPGA nozzle(b). [93]

distribution. The model analysed by Ting has 18 cylindrical gas jets and an apex angle of 45 degree.[93] HPGA was developed by Ting and Anderson in Ames laboratory. This design has 20 cylindrical gas jets and an apex angle of 45 degree. The characteristic feature of HPGA is the ability to operate at high pressure without increasing the gas consumption. Figure 3.10 shows HPGA system.[93]

Mates et al [95] found that the dynamic pressure of the gas jets influence the melt breakup by analysing annular slit atomizers and discrete jet atomizers. The supersonic gas jets exiting the gas die at high velocity will have a large dynamic pressure and on interaction with melt result in fine droplets. When the gas exit surface area of discrete jet atomizer and annular slit atomizer was matched, the annular slit atomizer produced gas jets with higher dynamic pressure compared to discrete jet atomizer for the same pressure as the former required smaller perimeter than discrete holes.

Gas jet tube design

The design of the gas jet tube influences the velocity of the gas jets. A gas jet exiting with higher velocity will have higher energy and momentum to expend which affects the particle size. Ames laboratory studied the design of gas jet profile in HPGA to optimise it. A traditional atomizer uses a cylindrical choked die and the gas jets accelerating through it reaches only subsonic speeds. An innovative design introduced into HGPA was convergent-divergent nozzle. Gas jets can be accelerated to supersonic speeds through CD nozzle. Figure 3.11 shows a schematic representation of CD nozzle. [96]

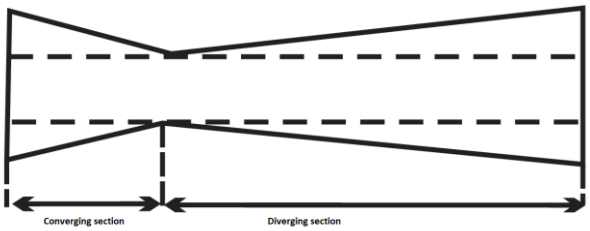

Figure 3.11 schematic representation of CD nozzle. [96]

The ratio of throat to the exit area determines the ideal operating pressure of the gas die for an isentropic flow condition. Therefore, each operating pressure requires a unique gas die design with the specific throat to exit area. When the gas jets exit at ambient pressure, shock waves are not produced. When the operating pressure is lesser than the ideal operating pressure, it leads to over-expansion resulting in subsonic shockwaves. When the operating pressure is higher than the design pressure, it leads to under-expansion resulting in supersonic shockwaves. Shockwaves cause energy lose across them which affects the powder size distribution of the yield.[93, 97] In real situations, the calculated design operating pressure

will not be same as the measured design operating pressure due to machining tolerance. [88, 98]

It has been found that the CD nozzle produces yield with better mean particle size and standard deviation of the powder obtained. [88, 97] Ames laboratory produced a series of HPGA atomizers called HPGA 1 which was designed to produce gas jets at subsonic speed. The next series of HPGA atomizers called HPGA 11 was designed to produce gas jets at supersonic speed. Both these atomizers had an apex angle of 45 degree. Another series of HPGA gas atomizers called HPGA 111 was produced on further optimization of HPGA 11. HPGA 111 atomizers had an apex angle of 22.5 degree instead of 45 degree as in the case of previous series. Also, the number of discrete jets were decreased from 22 holes to 18 holes. Gas dies in this series was able to produce supersonic gas jets at Mach 3 and operate at pressures higher than 7 MPa. The powder size distribution improved considerably from 41 μm in HPGA 11 to

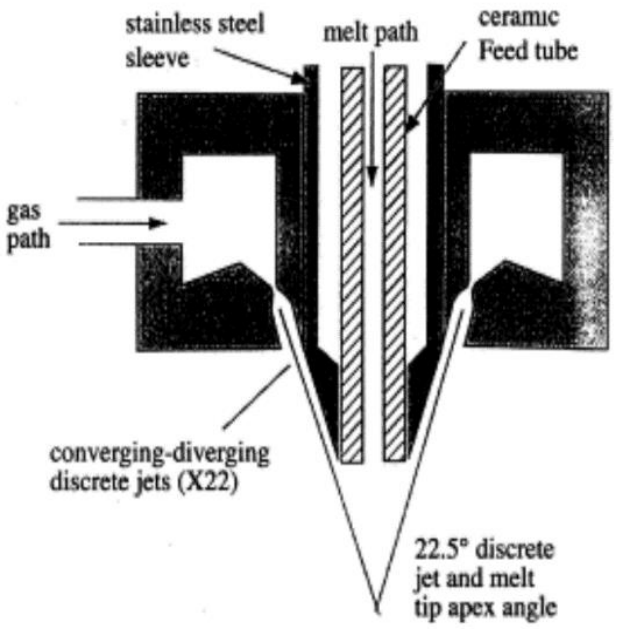

Figure 3.12 schematic representation of HPGA 111 atomizer. [93]

35 μm in HPGA 111. HPGA 111 also has a lower gas consumption compared to HPGA 11 which increases the efficiency of this atomizer. Figure 3.12 schematic representation of HPGA 111 atomizer. [93] shows the schematic representation of a HPGA 111 atomizer. The reduced apex angle also resulted in an increase in the efficiency of this atomizer. [93]

Cui et al [99] analysed a converging and converging-diverging nozzle geometries for different operating pressures and found that the converging nozzle was more sensitive to operating pressures and changes in geometry. They also found that converging nozzle was able to

produce a sub-ambient aspiration pressure avoiding the dynamic energy lose due to jet impact and deflection.

3.3.2 Melt delivery nozzle

In free-fall atomizers, the melt is allowed to fall for a certain distance where it meets the atomizing gas jets but in close-coupled gas atomizers, this distance is eliminated. An inefficient design of the melt delivery system could result in the failure of the atomizer. Therefore, the design of melt nozzle plays a major role in influencing the efficiency of the atomizer.

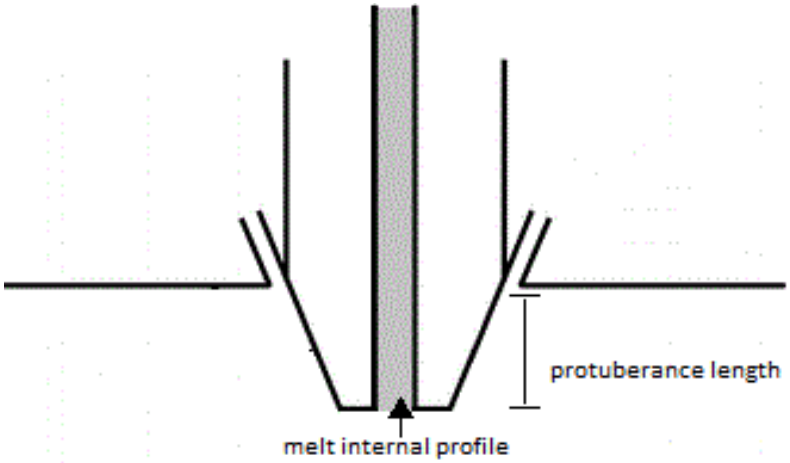

Figure 3.13 cross-sectional view of an atomizer

The profile of the melt nozzle can be changed by altering the protuberance length or the internal design of the tube. Figure 3.13 shows the cross-sectional view of an atomizer.

Aydin et al studied the nozzle deformation problem due to sub-ambient pressure occurring in the recirculation zone during closed-wake conditions. A sub-ambient pressure in front of the melt nozzle is required for the melt to be drawn into the recirculation zone. This sub-ambient pressure also causes issues to the nozzle geometry. The extreme temperature difference between the melt and the gas jets leads to solidification and accumulation of metal resulting in nozzle deformation. This deformation is detrimental to the atomization process and affects the efficiency adversely. [17]

Protuberance length:

The protuberance length plays a major role in operating the atomizer stably. An important problem caused by incorrect nozzle design is the melt freeze-off caused by rapid cooling of melt by high pressure gas inside the nozzle. When the melt delivery design results in a melt flow rate lesser than the optimal melt flow rate for the given gas flow rate, melt freeze-off

happens resulting in a blocked nozzle orifice. This problem could be alleviated by using a gas die system designed for sub-ambient pressure. [88, 91, 93]

Anderson et al studied the influence of the nozzle tip length on the efficiency of the gas atomization. [91] They studied a set of nozzles of different geometries. Figure 3.14 shows the nozzles considered. [91]

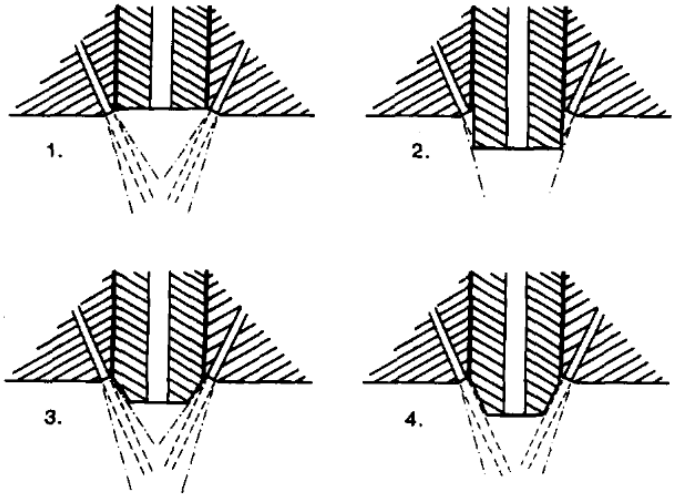

Figure 3.14 schematic representation of different protuberance lengths. [91]]

In nozzle 1, as seen in figure 3.14, the gas die and the melt nozzle tip does not come in contact with each other. It was found that this design provided the most control over the atomization process compared to the other geometries. The nozzle design 2 has a square edged melt delivery tube extending further than the gas die. This design had the strongest interaction between the melt and the gas jets as the melt stream is closer to the focal point of the gas jets. In design 3 and 4, the tapered ends allow a better expansion of gas jets. It was concluded that the melt tip design played a major role in influencing the gas flow pattern in front of the nozzle tip and that in order to improve efficiency, the gas die must be carefully aligned with the melt nozzle. [91]

Unal studied the gas flow field produced by supersonic jets using Schlieren photography in a discrete jet atomizer with converging-diverging nozzle.[51, 90] It was found that the protuberance length affects the particle size. A longer protuberance length resulted in expansion waves that decelerated the flow to subsonic speed at a distance of few diameters downstream the melt nozzle. Unal concluded that process efficiency depends on the dynamic pressure possessed by the supersonic jets and a supersonic jet with large dynamic pressure produced finer particles.

Internal design

Internal design of the melt delivery tube affects the disintegration of the melt entering the atomization chamber. A wide variety of internal designs are used in CCGA process for different application. A flat tip is the most commonly used design in the commercial atomizers. Another commonly used design is the concave tip. The concave tip directs the gas jets in front of the recirculation zone thereby increasing the melt-gas interaction. This model was first developed by Miller and further improved by Anderson et all. [91, 97] Figure 3.15 shows the concave melt tip of the atomizer. [91]

Anderson et al carried out an extensive study on the melt nozzle designs and their influence on particle size distribution. The melt is broken into tiny droplets due to kinetic energy transfer from the gas jets to the melt. The gas jets exiting the gas die will undergo expansion while losing energy. They found that in order to obtain a higher yield of fine particles, the melt must be disintegrated in the primary recirculation zone where the kinetic energy is high. As the melt stream moves downstream where the gas energy decreases, coarser particles are produced.

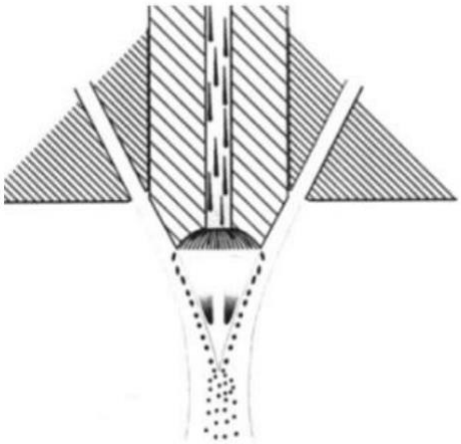

Figure 3.15 Cross-sectional view of the atomizer with concave melt tip. [91]

[91] They decided to increase the melt orifice diameter in a discrete jet system as shown in the Figure 3.15. This lead to an increased spread of the melt film which maximised the melt-gas interaction. [100] Figure 3.16 shows the bottom view of the conventional gas die and gas die with increased diameter. [100] They also attempted to stabilise the chaotic melt flow by introducing slots or channels inside the melt delivery tube which directed the melt from the centre to the nozzle edge where the gas jets atomized it. Another type of melt nozzle called “Bessel horn” or “Trumpet bell” where the interior shape of the melt nozzle is similar to a trumpet bell. This design can be optimized further by introducing slots. Anderson et al designed a trumpet bell shaped melt nozzle with extended slots to facilitate better

disintegration of melt by high-speed jets. One of the major problem with this model was the correct alignment of discrete jets with the slots. [91]

McCarthy et al also studied various designs and concluded that internal and external designs of the melt delivery tube plays a crucial role in pulsation phenomenon.[88, 98]

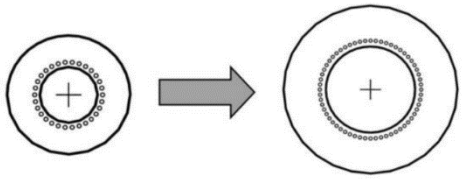

Figure 3.16 Bottom view of the conventional gas die and gas die with increased diameter. [100]

Also, Motaman found that designs with increased melt nozzle surface produced closed wake at significantly lower pressures such as 3 MPa and 3.5 MPa. Two designs were considered with a slanted nozzle surface (3.5 MPa) and a curved nozzle surface (3 MPa). Figure 3.17 shows the two designs considered by Motaman.[101]

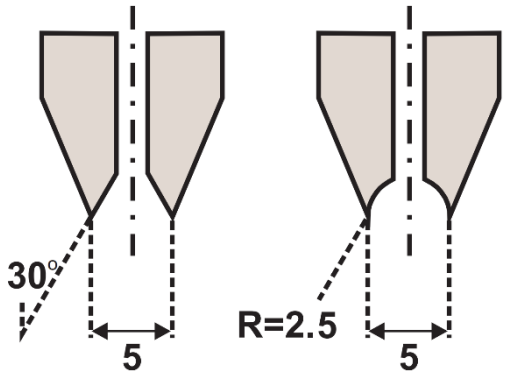

Figure 3.17 Designs considered by Motaman that produced low WCPs. [101]

3.4 Effect of the atomizing gases

Strauss et al investigated the influence of preheated gas in gas atomization. They concluded that the gas temperature affects bigger droplets. They established a new parameter called normalised gas energy rate which is the kinetic energy of the gas normalised by mass flow rate of melt. This parameter involved three other process parameters namely gas velocity, mass flow rate of melt and gas kinetic energy and provided a better correlation with experimental data.[70].

Unal also investigated the various influence of the atomizing gases on the particle size distribution. The influence of the atomizing gas on particle size distribution was analysed by considering three different gases- Helium, Argon and nitrogen. Helium produced the finest particles and argon yielded the coarsest particles. Nitrogen produced intermediate particles.[68]

3.5 Gas Metal Ratio

Gas Metal Ratio also known as GMR is an important parameter in determining the powder size distribution. GMR is the ratio of the mass flow rate of the melt atomized to the ratio of the mass flow rate of the atomizing gas. [48, 89]The first empirical relationship between the particle size and the process parameters was given by Wigg. [102] Wigg's relationship is given by

$$d_{50} = 0.04 v_L \cdot 0.5 M^{0.1} \sigma^{0.2} \rho_A U^{-1} \sqrt{\left(1 + \frac{M}{A}\right)} \qquad \textit{eq 3.6}$$

Where v_L is the liquid kinematic viscosity (m^2s^{-1}),

M is the melt flow rate (kgs^{-1})

A is the gas mass flow rate (kgs^{-1})

d_{50} is the mass median diameter (m)

The term M/A is the gas metal ratio. This equation was modified was Lubanska who also studied the influence of process parameters in particle size distribution.[103] Her empirical relationship is given by

$$\frac{d_{50}}{d} = b \sqrt{\left[\left(\frac{v_L}{v_g we}\right)\left(1 + \frac{M}{A}\right)\right]} \qquad \textit{eq 3.7}$$

Where d is diameter of the nozzle (m)

d_{50} is the mass median diameter (m)

v_L is kinematic viscosity of melt (m^2s^{-1})

v_g is kinematic viscosity of gas (m^2s^{-1})

b is constant which depends on atomization situation.

We is Weber number.

Both these relationships were established by focussing on free-fall atomization. Lubanska's relationship has exhibited good results for certain gas atomization process. From Lubanska's relationship, it is clear that GMR influences the particle size for a given nozzle design and melt composition. A high GMR will help in obtaining a yield with higher percentage of fine powders.

Therefore, GMR is directly related to the production costs and its optimization is an important factor in atomization. For a given GMR, CCGA produces higher yield and has a better efficiency compared to free-fall atomizer. [104]

A general form of the relationship between GMR and mass median particle size reported by some researchers can be given as

$$D = b \,/\, \sqrt{\frac{A}{M}} \qquad \textit{eq 3.8}$$

Where D is the mean particle diameter.

Another empirical relationship related to GMR was given by Strauss and Miller [105] by relating the GMR to the ratio of input and output power. This equation is

$$\frac{P_s}{P_m} = \frac{0.5 M u_g^2}{N_m s_m \sigma} = \frac{1}{6}\left(\frac{M}{A}\right)\left(\frac{u_g^2 r \rho_A}{\sigma}\right) \qquad \textit{eq 3.9}$$

Where $\frac{P_s}{P_m}$ is the ratio of the input power to the output power of the system

u_g is the gas velocity (m^2s^{-1})

r is the average powder radius (m)

3.6 Powder size distribution

The size and the shape of powder plays a major role in influencing the powder properties such as flowability and compaction. Powders produced by gas atomization are not always spherical. Figure 3.18 shows powders with different shapes. [106]

A spherical powder can be characterised by just the diameter of the powder. On the other hand, the powders with non-spherical shapes can be defined by multiple characteristic dimensions such as length and width. Though, these provide a high degree of accuracy, it complicates the characterization process. Therefore, many techniques often utilize the concept of equivalent spheres. In these cases, the particles size is defined by the diameter of an equivalent sphere whose properties such as volume or mass is same as the particle's property. Different measurement techniques use different equivalent spheres and therefore give different results.

In industrial practice, a single diameter is not sufficient to define the quality of the batch of powder produced. A better approach is to report the size distribution with the central point of the distribution along with few more values in the distribution. Generally, the particle size

distribution can be defined by d_{50}, d_{10} and d_{90}. [107] Figure 3.19 shows an example distribution curve. [107]

The median diameter d_{50} is the 50% size of a cumulative distribution curve of the powder sizes. This is the value at which half of the particles are finer than the expressed diameter and the rest are coarser. In a symmetric distribution, this is the mid-point of the curve.

The diameter d_{90} is the value in the distribution below which diameters of 90% of powder in the batch occur. Similarly, d_{10} is the value in the distribution below which diameter of 10% of powder in the batch occur. The spread of the powder size distribution can be defined by the span of the distribution.

Span of the powder size distribution is defined as

$$Span = \frac{d_{90} - d_{10}}{d_{50}} \qquad \textit{eq 3.10}$$

The increase in the demand for fine and ultra-fine powders has led to an increased demand for narrow powder size distribution i.e. a distribution with shorter span. A powder size distribution with wider span will lead to an increased quantity of powders that are not within the required range. In close-coupled gas atomization, one of the main problems in the industry is the wide span of the powder size distribution. It is found that about 65% of powder produced

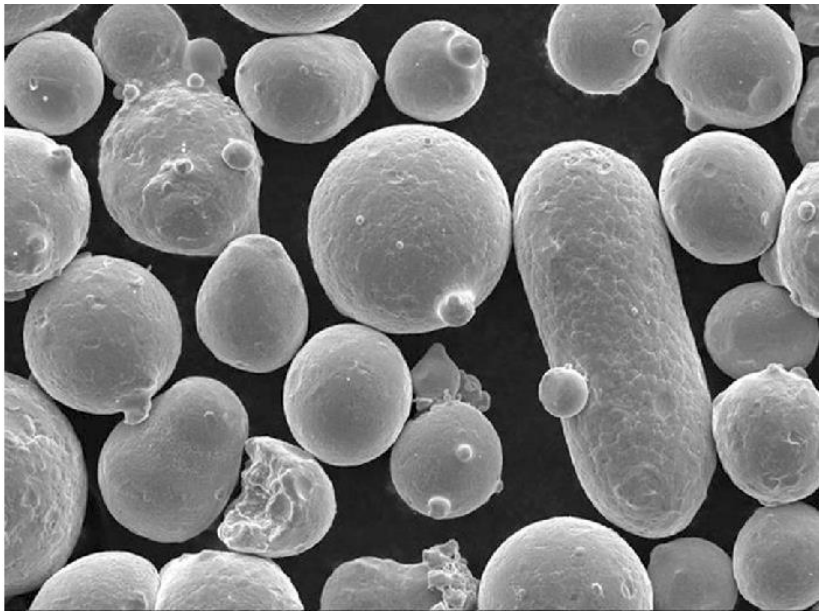

Figure 3.18 powders with different morphologies. [106]

in CCGA are outside the requirement range and has to be melted again to be utilized as the raw material for the further batch. [86]

The consequences of a wide span of the powder size distribution are high re-melt rate and low quantity of final products which increases the cost of production.

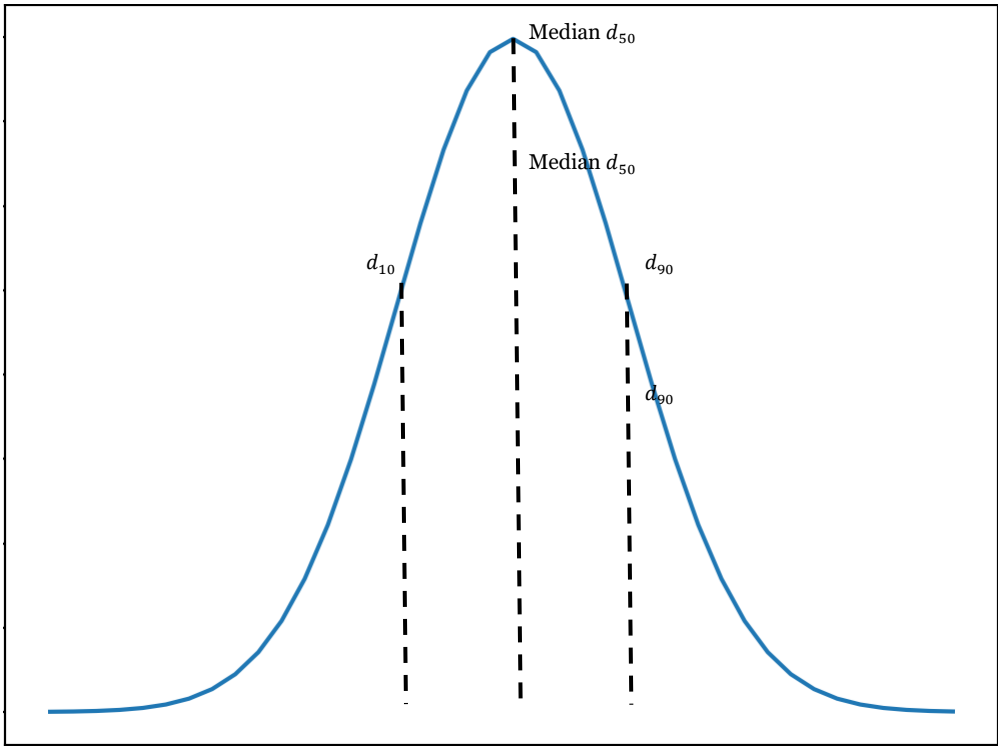

Figure 3.19 a distribution curve highlighting d_{50}, d_{10} and d_{90}. [107]

3.7 Review of numerical works

Numerical works related to close-coupled gas atomization can be analysed broadly in three categories – design parameters such as protuberance length and gas die designs, process parameter such as GMR and aspiration pressure, flow features and interaction between melt and gases.

The efficiency of the CCGA process can be improved by understanding the flow features inside the atomizer. Mi et al carried out numerical analysis of gas flow field around melt nozzle and compared the results with the experimental data. They found that the numerical results were in good agreement with the experimental data by investigating the recirculation zone, shock waves and Mach disk formation.[108] Ting and Anderson studied the wake conditions for a range of pressure in depth in an annular slit atomizer. They proposed the pulsatile model where the wake region oscillated between open wake and closed wake at a frequency of 35-50μm. They analysed the wake closure pressure and the existence of Mach disk.[21] Espina et

al also found the same results as Ting and Anderson by studying the wake conditions and Mach disk formation. [109]

The process parameters such as GMR and aspiration pressure are influenced by the atomizing pressure. XinMing et al studied the relationship between aspiration pressure and the operating pressure. As the operating pressure is increased, they found that the aspiration pressure decreases and then increases. They also observed that the Mach disk moved further away from the melt tip as the operating pressure was increased.[110] Similarly, Xu et al analysed the aspiration pressure of a converging nozzle in an annular slit atomizer with an apex angle of 45 degrees. They concluded that the aspiration pressure is influenced by the recirculating gas and the protuberance length.[111]

The design of the gas die, melt nozzle and apex angle has an impact on the flow features in the near field region. Mi et al also studied the influence of atomizer geometry on the gas flow field by comparing a range of apex angles and protuberance lengths. They concluded that aspiration pressure is greatly influenced by the protuberance length. A fully retracted nozzle resulted in over-ambient pressure at the melt nozzle which affects stability of the atomization. A fully extended nozzle provided a sub-ambient pressure and sucked the melt into the recirculation zone. The apex angle affects the melt movement into the recirculation zone. They predicted that a large apex angle results in the melt being drawn into the melt tube. [112] Zeoli et al studied the flow field produced by two different nozzle types with different protuberance length. One nozzle was the isentropic plug nozzle and the other has a shorter protuberance length. They carried out this analysis to attempt reduction of shock waves and to increase the gas kinetic energy.[113] Ridder et al analysed the influence of the melt pour tube shape on the flow field. They considered two designs for this analysis. The first geometry was a straight surface with no taper angle. The second geometry had a tapering feeding tube that aligns with the tapering angle of the discrete jets. The former geometry resulted in a strong shock wave leading to energy loses. [114]

The chaotic interaction between the melt and the gas jets is very challenging to simulate and the computational resources required for it is quite high. As mentioned in chapter 2, different modelling approaches such as DNS, LES and RANS are available to generate numerical results. Different two-phase analysis carried out are mentioned below.

Tong et al modelled the melt-gas interaction in the recirculation zone using direct numerical simulation method (DNS). Strong hydrodynamic interactions were predicted between the melt and gas jets. They concluded that the process is unsteady and steady-state simulations are not effective in modelling it. Also, the computational requirement for DNS modelling is intensive and it is not easy to develop a robust model. [115]

Neumann et al analysed the primary breakup process in order to understand the subsequent secondary breakup by using a choked nozzle and converging-diverging nozzle. They utilized LES model with VOF method to generate the results. They studied the influence of process parameters and the nozzle designs on the primary breakup in the near-field area. [116]

The gas and the melt interaction in CCGA is a complex interaction between two immiscible phases. The Volume of Fluid method can be utilised to solve this interaction, but the computation requirement is again quite high to sufficiently model a droplet. Most of the two-phase flow analysis of CCGA use discrete phase method. This is a Euler-Lagrangian method where the gas flow field is solved, and the melt is modelled as discrete particles

The first numerical model to predict the powder size distribution in a CCGA was developed by Kuntz and Payne. [117] Gas flow field and melt phase was decoupled in this model. They solved the gas flow field without the melt initially and then modelled the movement of melt stream based on the gas flow path. The predicted results were in agreement with experimental data with a slight discrepancy. This discrepancy was attributed to the one-way coupling approach of this model. Similarly, Figliola et al [118] modelled gas flow field with discrete particles in two-dimensional axisymmetric domain. The numerical results did not agree with the experimental data due to the axisymmetric assumption.

A two-dimensional axisymmetric model was developed by Underhill et al in which the particles were introduced into the flow field. They analysed the droplet trajectory and the temperature and found that the cooling rate was higher for smaller droplets. The results were in agreement with experimental data. [119] The momentum and thermal behaviour of droplets were analysed by Li et al. They modelled a velocity flow field with equations using the previous experimental data. The atomization process was not modelled, and droplets of different sizes were introduced into the flow. They predicted the in-flight conditions, temperature, solidification behaviour and cooling rates of the droplets. [18] Grant et al also modelled the thermodynamic behaviour of droplets. They found that the particle movement and thermal history is greatly influenced by droplet diameters and melt distribution. [120-122]

A model called Surface Wave Formation was proposed by Antipas et al. in which the melt breakup was modelled through a series of sinusoidal waves on the melt surface. The only forces acting on the melt are the aerodynamic force due to gas jets and surface tension of the melt. The results obtained through this model was in good agreement with the experiment. [123] Also, they analysed the size of the ligands formed downstream for various atomizing gases. They found the ligands size to be about 550 microns for nitrogen and 600 microns for argon in the primary atomization zone. [124]

4 TWO-DIMENSIONAL SINGLE PHASE (GAS) ANALYSIS

Methodology, research and discussion.

Close-coupled gas atomization is a complicated powder production process involving high temperature and high velocities. In order to analyse the interaction between melt and the gases in the atomizing chamber during CCGA, the first step is to study the gas dynamic behaviour for a range of operating pressures. Understanding the gas flow field in the nearfield area will assist in improving the efficiency of the process as a substantial quantity of melt breakup occurs in this region.

An annular slit gas atomizer has been chosen for this study. Figure 3.1 shows the gas atomizer along with melt and recirculating gases. Annular slit gas atomizers are axisymmetric. There are variations in radial direction(r) and vertical direction(z) but not in the angular direction (θ) in the axial symmetry. Therefore, a two-dimensional flow domain is sufficient thereby reducing the computational power requirement.

The methodology involved in developing a single-phase two-dimensional model and results obtained from it are discussed it.

4.1 METHODOLOGY

Developing a numerical model of CCGA typically includes establishing a numerical domain, meshing the numerical domain, applying the boundary conditions, solving the governing equations over the numerical domain and postprocessing the results obtained. The steps involved in developing a two-dimensional domain is discussed here.

4.1.1 Establishing a numerical domain

The first step in developing a robust model is defining the geometry of problem. A close coupled gas atomizer with annular slit jet type is chosen for the two-dimensional study. Figure 4.1 shows the schematic representation of the nozzle with an apex angle of 45 degrees.
Figure 4.2 shows the axial section of the atomizer and the numerical domain considered. The domain was created in cylindrical coordinate system due to the axial symmetry. The flow field extended about 10D lengths in radial direction (r-direction) and about 20D lengths in vertical direction (z-direction) where D is the melt nozzle diameter. The dimensions of flow field are

chosen such that there is a sufficient far field area, and the flow is not affected by the boundary conditions. Domain sensitivity has been investigated in section 4.2.

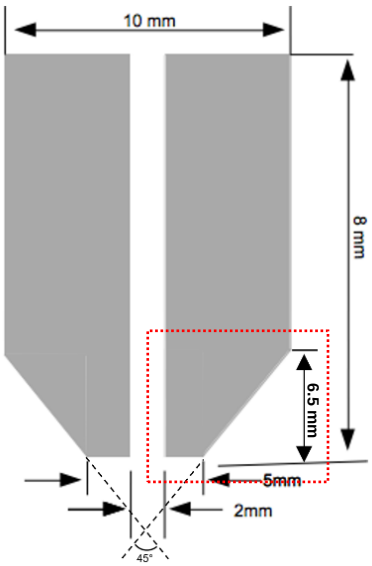

Figure 4.1 Schematic representation of the nozzle with dimensions

The part of the atomizer considered in this study has been highlighted in Figure 4.2. A choked gas die has been chosen for this numerical study as it is commonly used in industrial atomizer. A gas chamber has been included in this study as it was found out in the analysis carried out by Motaman that flow field obtained through a domain with gas chamber produced results similar to the experimental results.[101] The model is based on the experimental setup adapted from the CERAM PSI atomizer design which is a discrete jet atomizer with 18 jets. As the model considered in this study is annular slit atomizer, the gas flow rates will not be the same and hence the width of the annular slit is reduced in order to match the gas flow rate of the discrete jet atomizer. The gas flow rate of the CERAM PSI discrete jet atomizer was found to be 2502 $gmin^{-1}$ at 3MPa atomizing pressure. A range of annular slit width lengths were considered at 3MPa atomizing pressure, and it was found that a width of 0.21 mm was found to match the discrete jet atomizer's gas flow rate. Chapter 6 explores the various approximations that can be implemented in a two-dimensional model to simulate the discrete-

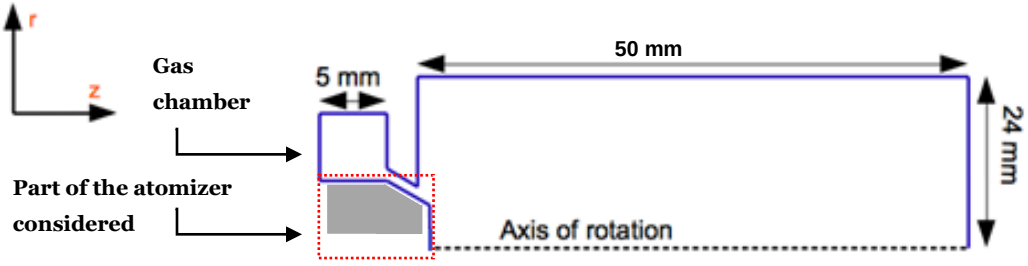

Figure 4.2 Schematic representation of the domain

jet atomizer and whether a two-dimensional model is sufficient to analyse discrete-jet atomizers.

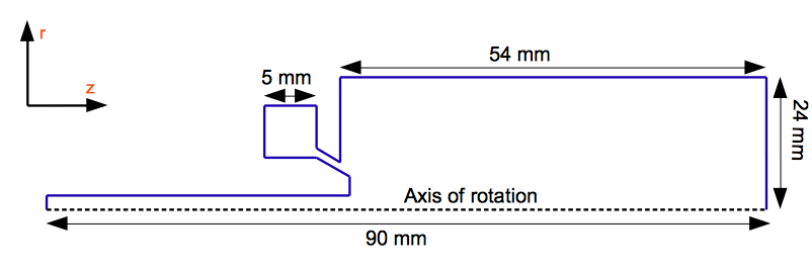

Figure 4.3 schematic representation of the domain with melt delivery tube

Gas die designs used in industrial atomizers have a melt delivery tube through which the melt enters the recirculation zone. Initially, a case with metal delivery tube was considered as shown in Figure 4.3.

As this is a single-phase analysis, there was no melt flowing through the tube resulting in an empty tube. When the melt entry point was modelled either as outlet or far-field condition, the gas in the atomizing chamber exited through the melt delivery tube which is not similar to the real atomizer. Figure 4.4 shows the velocity vector plots when the melt delivery tube is

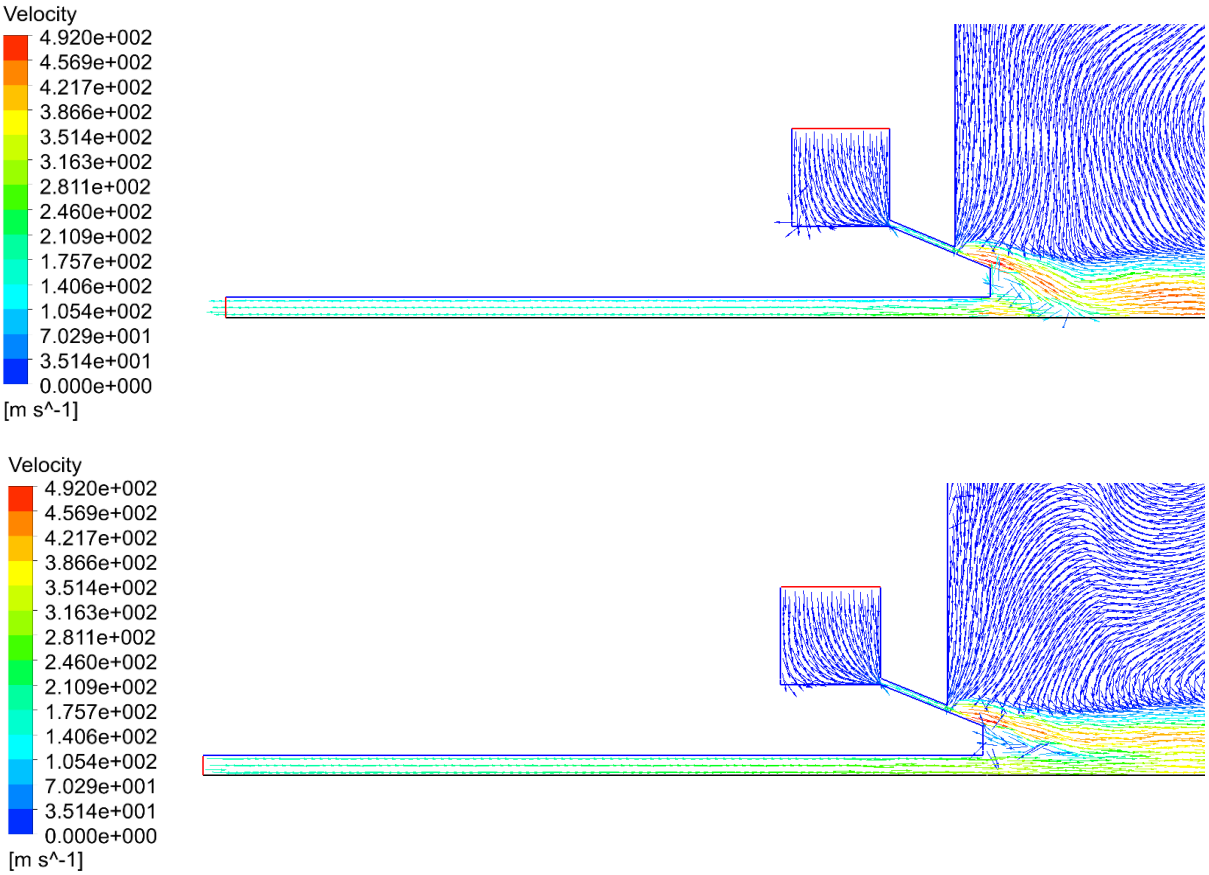

Figure 4.4 Velocity vector plots for the melt delivery tube modelled as outlet (top) and inlet(bottom) for 1MPa atomizing pressure

modelled as outlet (top image). The gases exit which is not observed in the physical process due to the presence of melt.
Another important feature of this nozzle design is that the pressure around the melt nozzle tip is over-ambient and requires the melt to enter the recirculation zone at a pressure of 40 kPa, When the melt delivery tube was modelled as a gas inlet at a pressure of 40kPa, the gas flowed through the tube and joined the gases in the atomizing chamber resulting in increased gas volume compared to the real scenario. Figure 4.4 shows the velocity vector plots when the melt delivery tube is modelled as inlet (bottom image). The gases join the recirculation zone and influence the shape of the recirculation zone.

In physical CCGA process, there is no gases exiting or entering the atomizing chamber through melt delivery tube. Therefore, the melt delivery tube was completely eliminated and replaced with a wall as shown in Figure 4.5

Further optimization of gas die design has been achieved after grid independence and is discussed in section 4.2.

4.1.2 Mesh generation

After creating the geometry, the next step is meshing the numerical domain. In mesh generation step, the flow domain is split into smaller subdomains called elements. The governing equations are then solved for every element in the mesh. These elements can be triangular or quadrilateral shaped in case of two-dimensional domains and can be tetrahedron, quadrilateral pyramid, triangular prism or hexahedron.

Mesh can be classified based on connectivity as structured, unstructured and hybrid meshes. A structured mesh is identified by regular connectivity between the elements and can be expressed as arrays. On the other hand, the unstructured mesh has irregular connectivity and requires larger memory compared to structured mesh. The hybrid mesh is a combination of structured and unstructured mesh. Regular connectivity and repetitiveness of structured mesh results in better alignment between elements leading to a comparatively better-quality mesh with better control in simple geometries

The geometry considered for this study is a simple geometry with no movable parts. Therefore, a structured mesh is utilized in this project. Also, Zeoli modelled multiphase flow of CCGA in a structured mesh. [63] Similarly, Motaman [84] also carried out a single-phase modelling in a structured mesh.

It is important to generate a mesh fine enough to capture all the flow characteristics but also not be very computationally intensive. In other words, the mesh elements should be at the size

where the flow characteristics captured does not change with decreasing element size. A mesh independence study is carried out to generate such a mesh and is discussed in section [4.2]

4.1.3 Material used

As seen in the literature, there are wide variety of gases utilized for atomization. An inert gas is preferred for producing powders with less to no contaminations. Argon is the most widely used gas in the commercial atomizer. Argon is chosen as the atomizing gas in this study. [70] In HPGA, spherical powders are easily produced in an inert environment. [83]

The flow features in the domain are influenced by the density and the specific heat ratio of the gas used in the study. The specific heat ratio of the gas affects the Mach number and the stagnation conditions in a flow. The compressibility effects become more important with increasing Mach numbers and in turn affects the shock and expansion wave formation.

4.1.4 Boundary condition

Mesh generation is followed by establishing boundary condition. Specifying appropriate boundary conditions and initial values are important step in developing a high-fidelity model. There are different kinds of boundary conditions available for the analysis. A wall in the domain can be modelled as stationary or moving with appropriate slip conditions and roughness. The inlets and outlets in the compressible flow domain can be defined by appropriate mass flow rates and pressures. In an incompressible flow domain, the inlets and outlets are velocity based in most cases.

The gas jets entering the atomizer are at high pressure and the domain considered is a compressible flow domain. Therefore, a pressure inlet boundary condition is appropriate for the inlet conditions. The gas jets lose their momentum and reach atmospheric pressure when nearing the outlet. The pressure outlet boundary condition is appropriate in this situation. Since our geometry has axial symmetry, an axis has been defined. The walls in the domain are modelled as stationary no-slip walls.

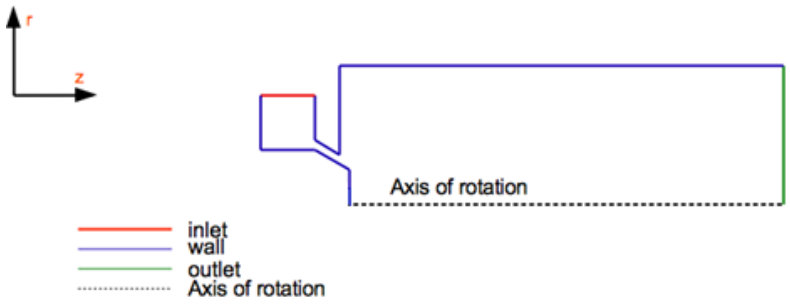

Figure 4.5 Schematic representation of boundary conditions

Compressible flows undergo shocks and expansion waves which are characterised by density gradients. Generally, a density-based solver is utilized in analyses with density gradients. Therefore, a density-based solver is chosen for this analysis.

Figure 4.5 shows the boundary conditions applied to the domain.

The analysis is based on the following assumptions in order to simplify the calculations:

- Flow is considered to be steady state.
- Flow is considered 2D axis symmetric.
- The fluid is considered as argon and modelled as a compressible ideal gas with specific heat ratio $\gamma = 1.66$.
- The impact of the molten metal is not considered.
- For presentation purpose, the model is rotated 90 degree anticlockwise so that the atomization direction is changed from vertically downwards to horizontal as seen in Figure 4.5.

All the simulations were carried out using Ansys 17.1 in a workstation with 32 GB RAM and 64-bit Operating system. Initially the axis of rotation of the model coincided with the z-axis (r=0) but the model diverged. Therefore, the axis of rotation was moved to r=25µm and the problem was overcome.

4.2 RESULTS AND DISCUSSION

The first step in analysing this two-dimensional gas only flow model is the mesh independence study. This is followed by domain independence and turbulence model sensitivity studies for a gas pressure of 1 MPa and the results are presented.

4.2.1 Mesh Independence study

Three different meshes were created with varying degree of fineness with total elements of 12000 in the coarsest mesh, 18000 in the medium mesh and 24000 in the finest mesh. The aim of this study is to establish a mesh with minimum number of elements to capture the flow changes in the domain in order to utilize the computational resources efficiently and solve the model in reasonable time. Therefore, the domain was compartmentalized and meshed. This compartmentalization is derived from the previous works carried out by Motaman. [92] Figure 4.6 shows the compartments in the domain.

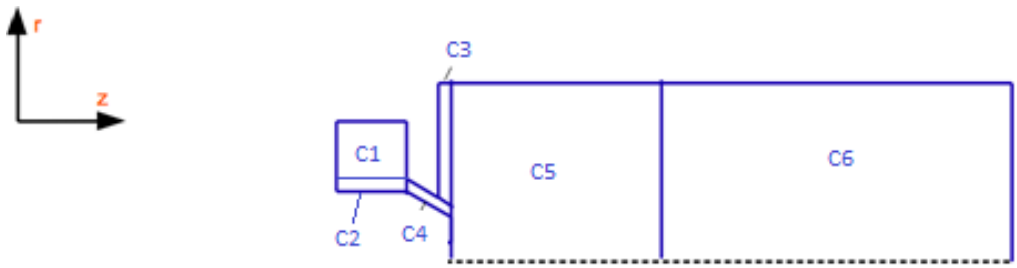

Figure 4.6 Schematic representation of compartmentalized domains

The compartments near the nozzle region were meshed with fine elements and the compartments near the outlet is meshed with coarser elements. In all the meshes considered, the ratios of element sizes were maintained constant. The element size was reduced by 25% in each case from the coarser mesh to finer mesh. Figure 4.11 shows the velocity contour plots for 1MPa atomizing pressure for all three meshes considered. The changes in the recirculation

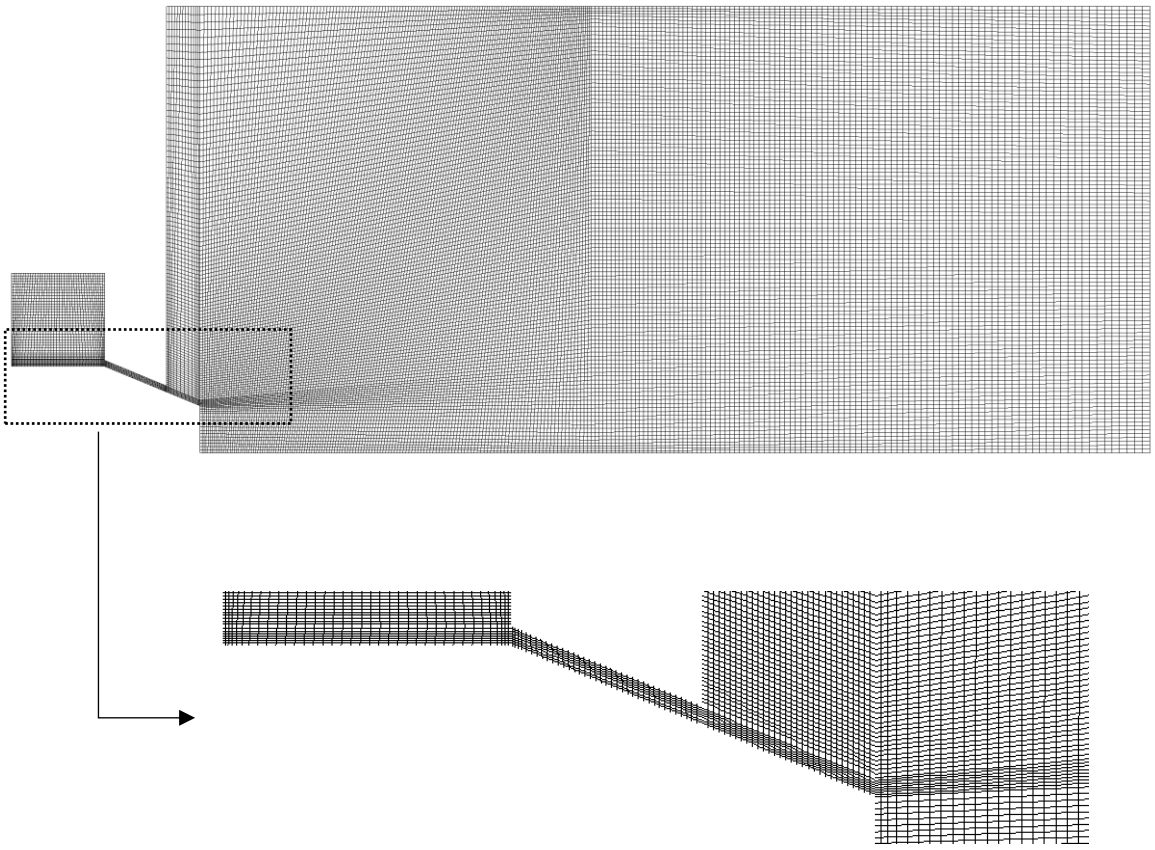

Figure 4.7 Schematic representation of the mesh considered in this study (18000 elements)

zone and in the expansion waves towards the outlet can be seen highlighted in it.

Figure 4.7 shows the mesh in the whole domain and the nozzle region with fine elements. The flow undergoes rapid changes in flow properties when it expands after exiting the gas delivery

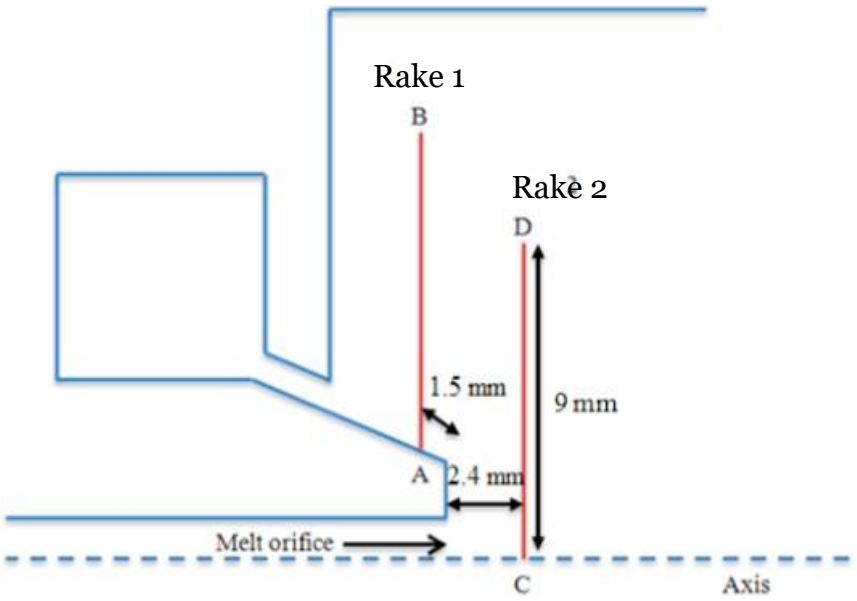

Figure 4.8 Location of rakes in the flow domain

slit. Also, the recirculation zone in front of the melt nozzle is an important flow feature and experiences large gradients in flow properties. Generally, in order to analyse a mesh for grid convergence, a rake is set up and a scalar parameter is measured at all points in the rake. The values obtained at all meshes are compared and the grid convergence is established when the value of the parameter does not change with reduction in element size. Therefore, two rakes

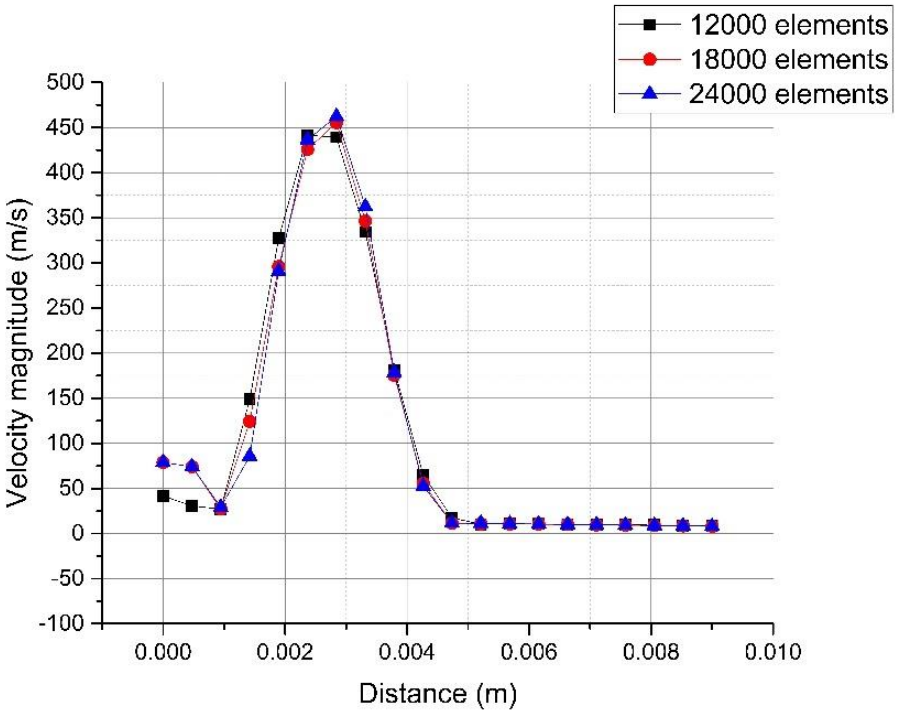

Figure 4.9 Velocity magnitudes across the rake 1 near the gas jet expansion

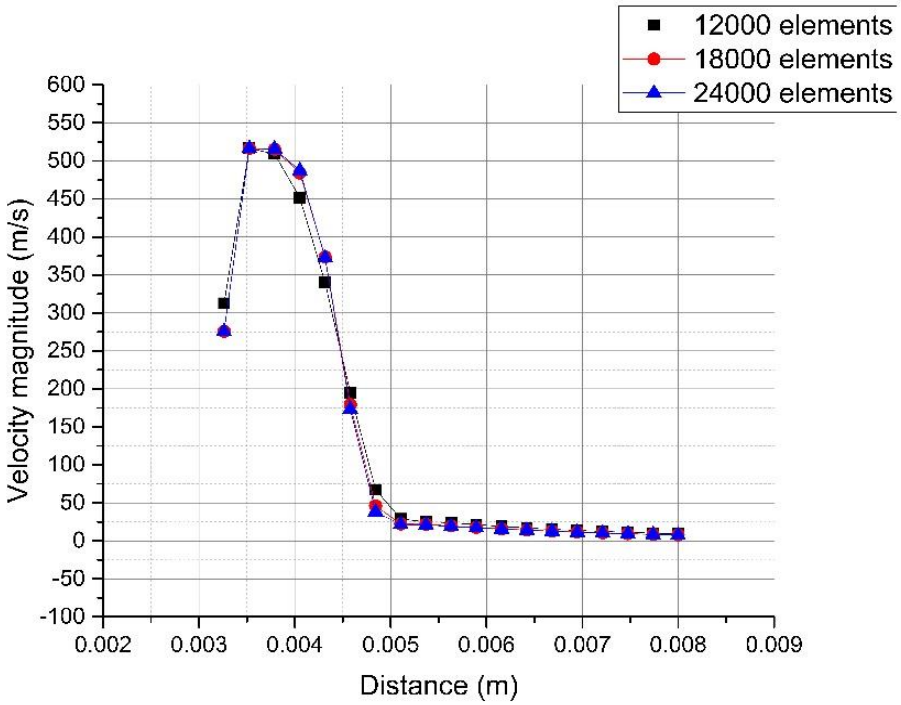

Figure 4.10 Velocity magnitudes across rake 2 near the melt delivery tube

were set up in these two locations to analyse the grid convergence. Figure 4.8 shows the location of both the rakes.

RAKE 1:

Figure 4.9 shows the velocities across the rake for all the meshes. It could be seen that the values of velocities are identical for both the meshes with 18000 and 24000 elements.

RAKE 2:

Figure 4.10 shows the velocities across the rake for all the meshes. It could be seen that the values of velocities are identical for both the meshes with 18000 and 24000 elements. From the above results, it can be concluded that the medium mesh with 18000 elements can be used to generate near accurate results with minimum computation time and resource

Table 4.1 lists the mesh element size utilised in the various compartments of the mesh with 18000 elements.

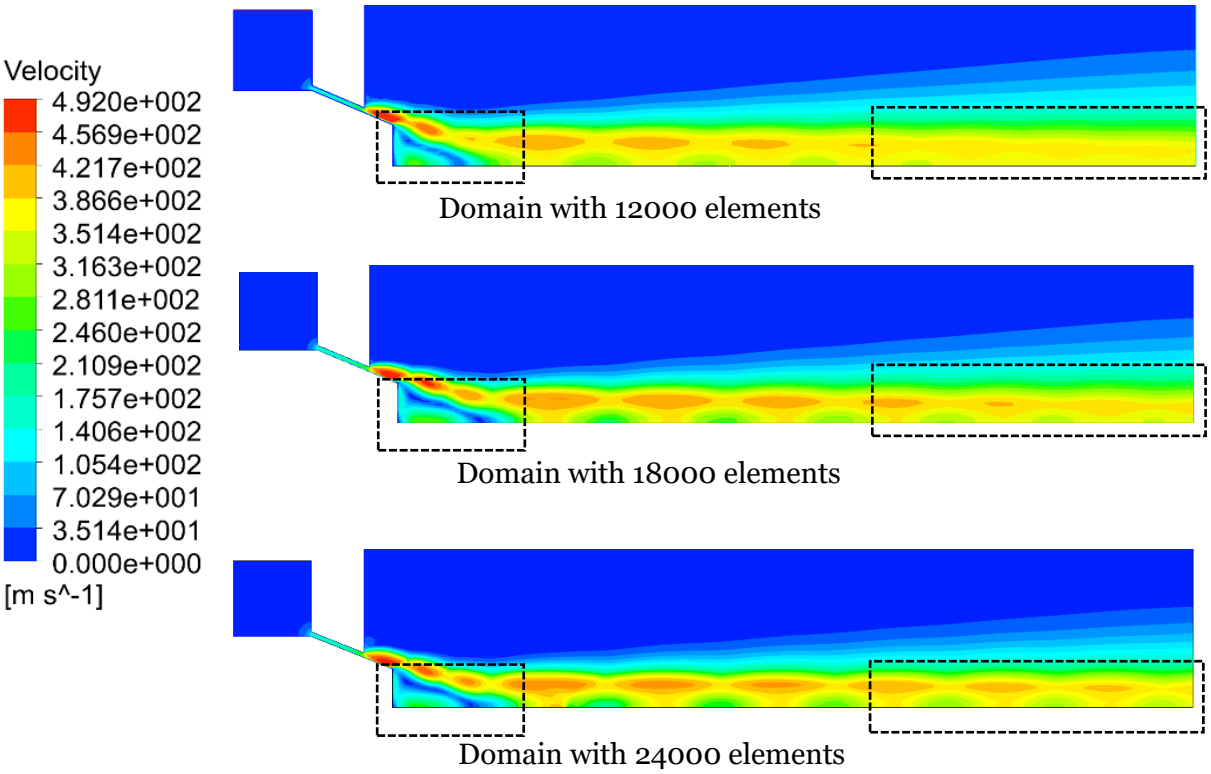

Figure 4.11 velocity contour plots for 1MPa atomizing pressure for all three meshes considered.

Table 4.1 Various elements used in the mesh in this study

Compartment	Mesh element size (horizontal*vertical)
C1	0.15 mm x 0.15mm
C2	0.1 mm x 0.04 mm
C3	0.15 mm x 0.15 mm
C4	0.1mm x 0.04 mm
C5	0.3 mm x 0.1mm
C6	0.3 mm x 0.15mm

4.2.2 Boundary Independence study:

The gases exiting the gas die undergo expansion around the melt nozzle tip. The strength of the shock waves formed reduces as the gases move further away from the nozzle region and understanding the flow in near-field region is important. Therefore, the domain with 90*15 mm^2 as dimensions is considered initially. This initial domain size was adopted from the previous project. [80] The boundary length independence study is carried out in r-direction and z-direction. The flow domain had a length of 90 mm in z direction along with melt delivery tube and 15 mm in r direction.

A standard k-ω model was used in this study with second order discretization scheme. The convergence tolerance of the residuals was set at 1e-06 and the simulation was run for 25000 iteration.

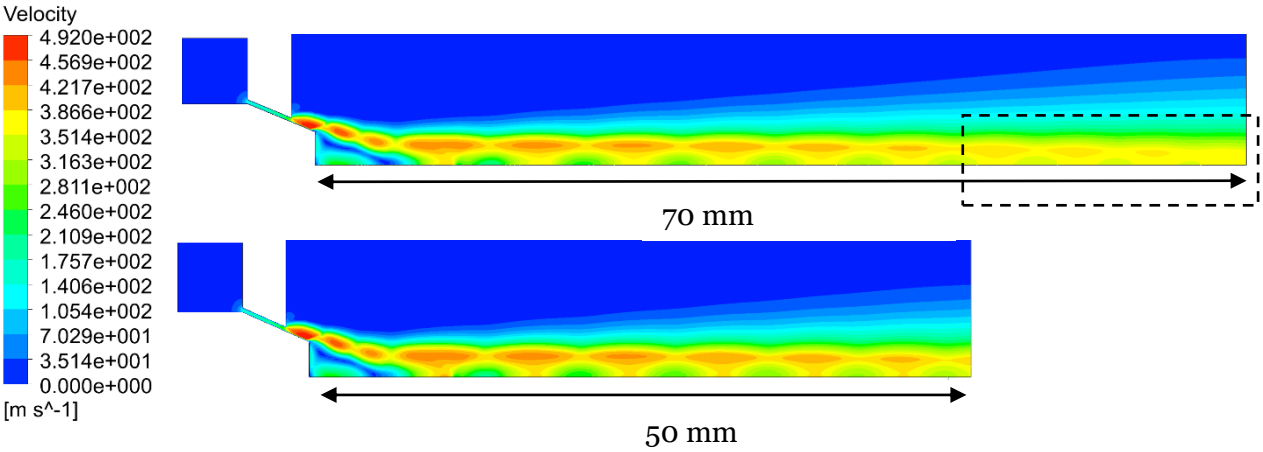

Figure 4.12 velocity contour plots for domains with lengths 50mm and 70mm along z direction

Z DIRECTION:

The flow field in z direction was initially considered at 90 mm along with melt delivery tube. The domain extended to a distance of 50 mm without the melt delivery tube. As mentioned above, the strength of the shock waves reduces as the gases move downstream and the changes in the flow also reduces with it. The flow field was extended to 70 mm to verify whether the flow pattern changed. But the flow field was found to remain unchanged. The flow in the extended domain area did not exhibit any notable changes and the expansion waves begin

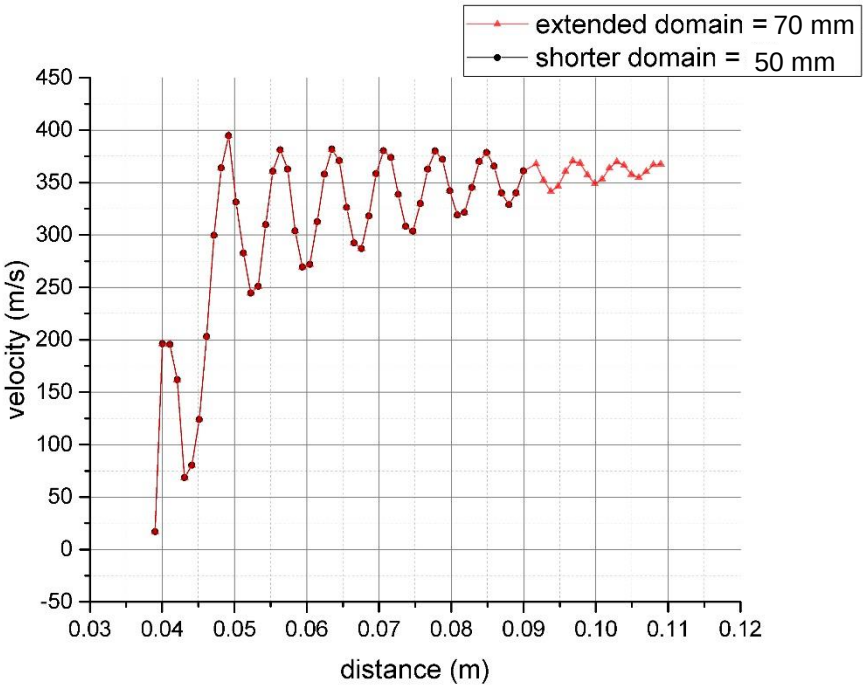

Figure 4.13 Variation of velocity magnitude in the Z-direction

deteriorating. The extended domain has been highlighted in the Figure 4.12 and it can be seen that the flow is approaching mid-range velocities near the outlet area. Figure 4.12 shows the flow field for 50 mm and 70 mm (90 mm and 110 mm along with melt delivery tube in the previous project [92]).

A rake was set up along the horizontal direction and velocity was measure at specific points. It was set up from the wall replacing the melt delivery tube to the outlet at distance of 0.5 mm from the axis with 50 data points. Figure 4.13 shows the velocity variation along the rake. It is found to be identical and the additional 20 mm did not show any major flow pattern and the velocity begins to reach steady values. Therefore, it can be concluded that 50 mm is the boundary length independence in z-direction.

R DIRECTION:

The boundary length in r-direction is considered as 15mm as considered by Motaman [101]. But there exists a non-zero velocity in the far-field region near the upper wall. Therefore, the length of the domain must be increased in r-direction in order to get rid of the non-zero velocity.

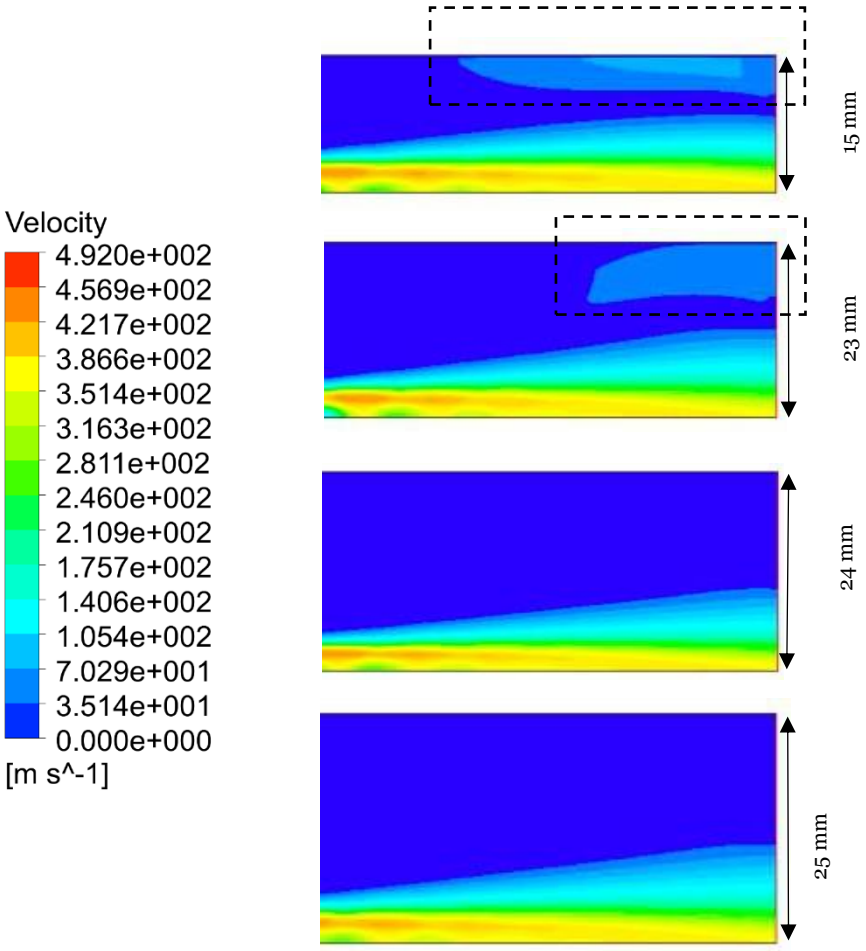

Figure 4.14 velocity contours for various domain lengths in r-direction

The domain length considered were 15 mm, 20 mm, 24 mm and 25 mm. In all the four cases, the element size is maintained constant and as the length is increased, the number of elements increase through the four cases. Figure 4.14 shows the non-zero velocity variation with increasing the boundary length. It can be seen that at the length of 24 mm, the non-zero velocity disappears. Therefore, the dimensions of the flow field are changed from 15 mm to 24 mm.

The final domain dimensions for this study are 60 x 24 mm^2 and is shown in the Figure 4.2 This is measured from the wall of the gas chamber to the outlet in z direction and from axis to the upper boundary wall in the r direction.

4.2.3 Turbulence model sensitivity study:

All the independence studies were carried out in Standard k-ω turbulence model.

Three turbulence models were considered to establish model independence. k-ω-SST, Standard k-ω and k–ε RNG used to determine the best turbulence model for this simulation. The convergence tolerance of the residuals was set at 1e-06 and the simulation was run for 25000 iteration in second order discretization scheme.

Figure 4.15 shows the simulation for 1 MPa using all the considered turbulence model. It can be seen from the Figure 4.15 that the expansion waves deteriorated sooner in k-ε RNG and k-

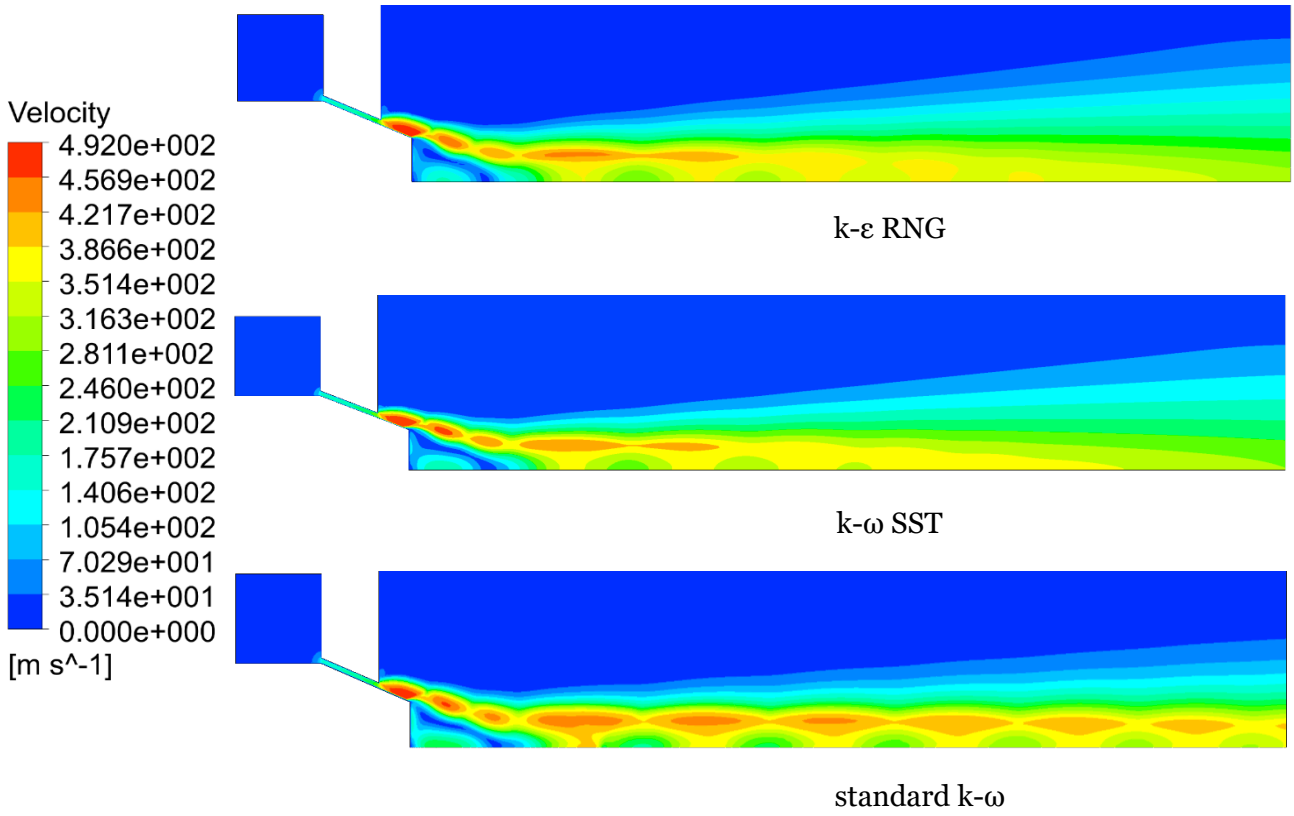

Figure 4.15 Comparisons of various turbulence models for 1MPa atomizing pressure

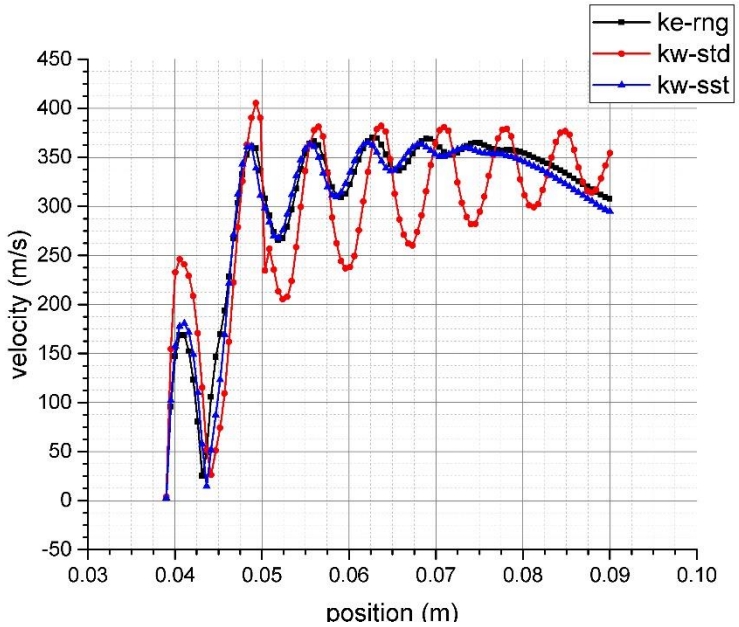

Figure 4.16 Velocity magnitude along the axis using the three turbulence models considered

ω SST models. In both these models, the strength of the shock waves is predicted much higher than the strength of the shock waves in kw standard model leading to gases losing energy rapidly.

A horizontal rake was set up along the axis at a distance of 0.5 mm from the axis and velocity along the rake was plotted. Figure 4.16 shows the velocity variation along the rake. It can be

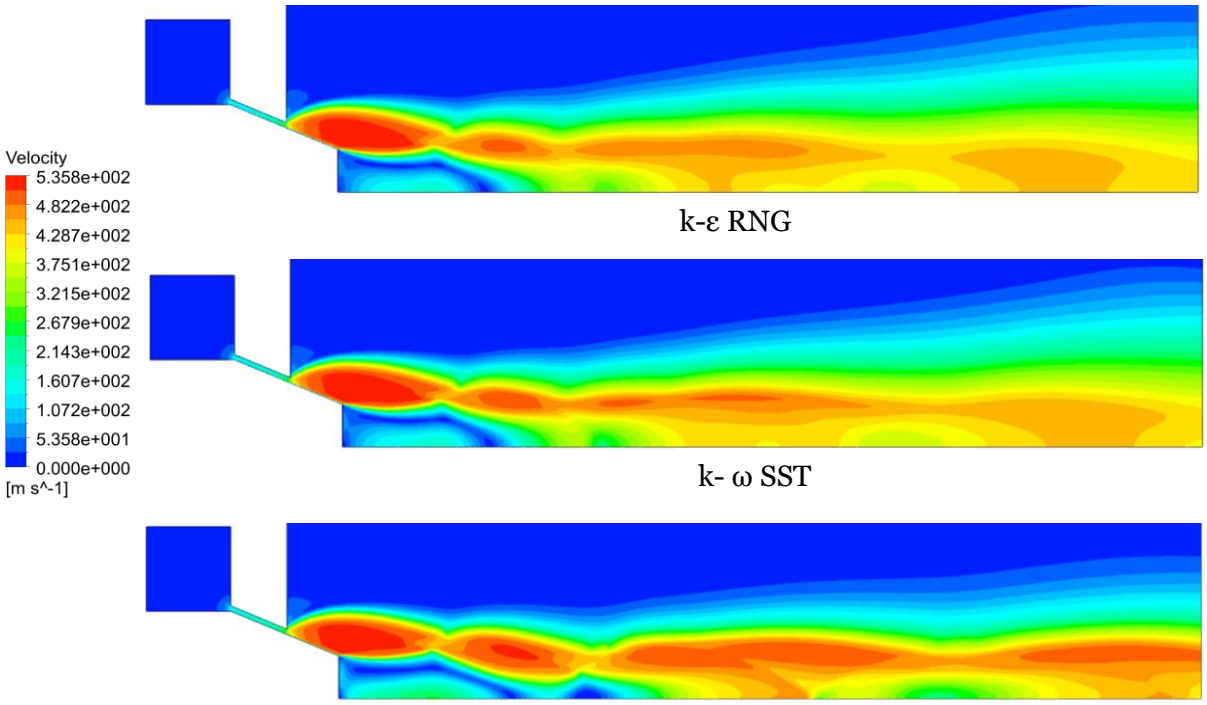

Figure 4.17 Velocity contour plots for 4.5 MPa operating pressure in all the turbulence models considered in this study

seen from the Figure 4.16 that the velocity of the gases increases and decreases in pattern and reach a steady state near the outlet.

In k-ω SST and k-ε RNG models, the velocity of the gases is predicted less than the k-ω std model due to the strength of the shock waves. This in turn affects the flow features developed downstream the melt nozzle. Figure 4.17 shows the velocity contour plots for 4.5 MPa operating pressure. A Mach disk was observed only in standard k-ω model. In the experimental work of Motaman, the Mach disk was observed at 4.5 MPa. [101] Figure 4.18 shows the comparison of velocity contour plots at 4.5 MPa generated in this study with the schlieren photograph obtained by Motaman. [101]

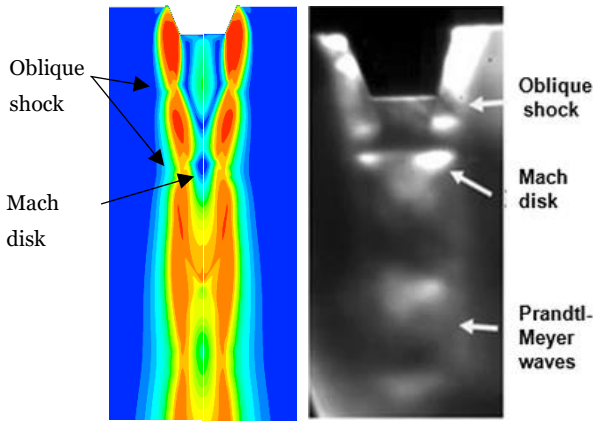

Figure 4.18 Comparison of 4.5 MPa velocity contour plots with Schlieren photograph produced by Motaman

Also, as discussed in chapter 2, k-ω SST model is difficult to converge and k-ε RNG model is generally used in internal flows, therefore standard k-ω model is chosen for this study. From the preliminary analysis, it can be concluded that a mesh with 18000 elements, a domain with dimensions of 60 x 24 mm^2 and standard k-ω turbulence model can be used for generating results in this study.

4.2.4 Atomizer profile.

The length of the melt tip influences the melt-gas jet interaction and thereby influences the efficiency as discussed in the literature review. The protuberance length in this model is set to be 3.06 mm. Any protuberance lengths greater than this results in an adverse flow separation on the melt nozzle surface. Figure 4.19 shows the flow separation due to longer protuberance length. Also, the gas exit slit width was set at 0.21 mm as the gas flow rate for 0.21 mm width was calculated to be 2500 $gmin^{-1}$ which is the gas flow rate measured in a CERAM atomizer for 3MPa atomizing pressure.

The adverse flow separation around the melt nozzle due to longer protuberance length results in melt being drawn into it. The melt solidifies around the nozzle tip leading to deformation of the nozzle. In most of the cases with longer protuberance lengths, the separated flow leads to

nozzle deformation and ending of the process. This separated flow along the melt nozzle edges is called lick-back.

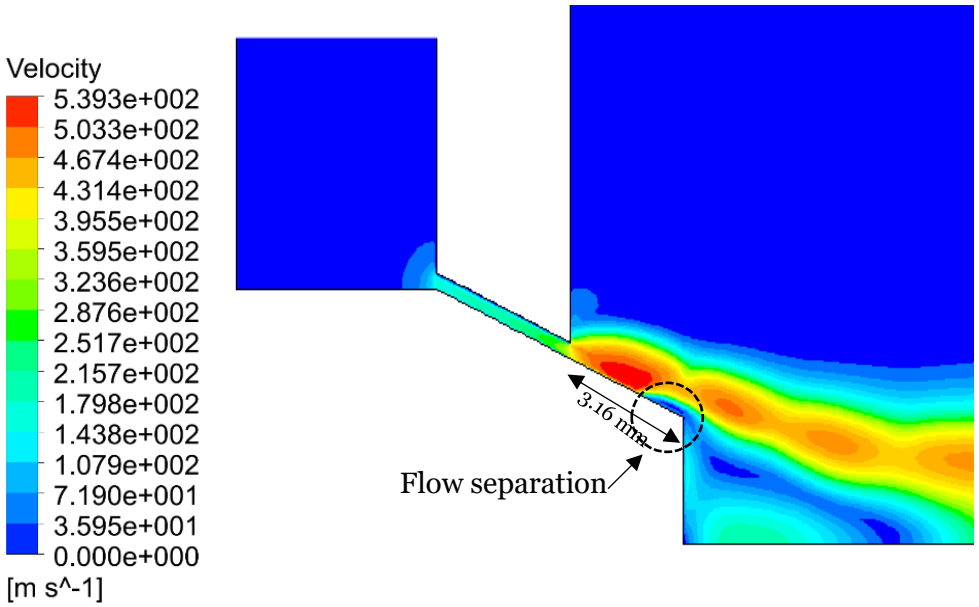

Figure 4.19 velocity contour plots showing the flow separation for a longer protuberance length (3.16 mm)

The settings used in this study to generate results through Ansys Fluent 17.1 are listed in Table 4.1.

Table 4.2 Table listing all the settings used in Ansys Fluent to generate results

Setting	**Option**
Solver type	Density-based
Velocity formulation	Absolute
Time	Steady
2D space	Axisymmetric
Energy	On
Turbulence models	Standard k-w
Formulation	Implicit
Flux type	Roe-FDS
Spatial Discretization	Second Order Upwind
URF Turbulent kinetic energy	0.8
Specific dissipation rate	0.8
Turbulent viscosity	1
Solid	1
Initialization	Hybrid

4.3 FLOW DYNAMICS OF VARIOUS ATOMIZING PRESSURES.

The meshed flow domain was simulated in Fluent using a density-based solver. The domain dimensions are 60 mm and 24 mm. The wake closure pressure observed experimentally for the flat head nozzle is 4.5±0.5 MPa. [101] Motaman computationally modelled the nozzle and the flow field and observed the wake closure pressure at 4.75 MPa. [101] The solution was solved using first order discretization to obtain an approximate solution and then again solved with second order discretization to obtain much accurate solution. The velocity and pressure contour plots for different pressures are discussed below.

4.3.1 1 MPa atomizing pressure:

The first pressure considered in this analysis is 1 MPa. Figure 4.20 shows the velocity contour plots for 1 MPa atomizing pressure. The recirculation zone along with expansion waves and shock waves is highlighted. The gases exiting the gas die begin expanding due to the difference in pressure between the gas jets and the surrounding gases. The gases travel towards the outlet through series of expansion waves and shock waves. The gases undergo compression across the shock waves and begin expanding downstream the shock wave.

At 1MPa atomizing pressure, there exists an open wake. The gas jets impinge at a point (stagnation point) and flow in the opposite direction towards the melt deliver tip. This leads to the formation of recirculation zone. The gas jets expand around the recirculation zone and

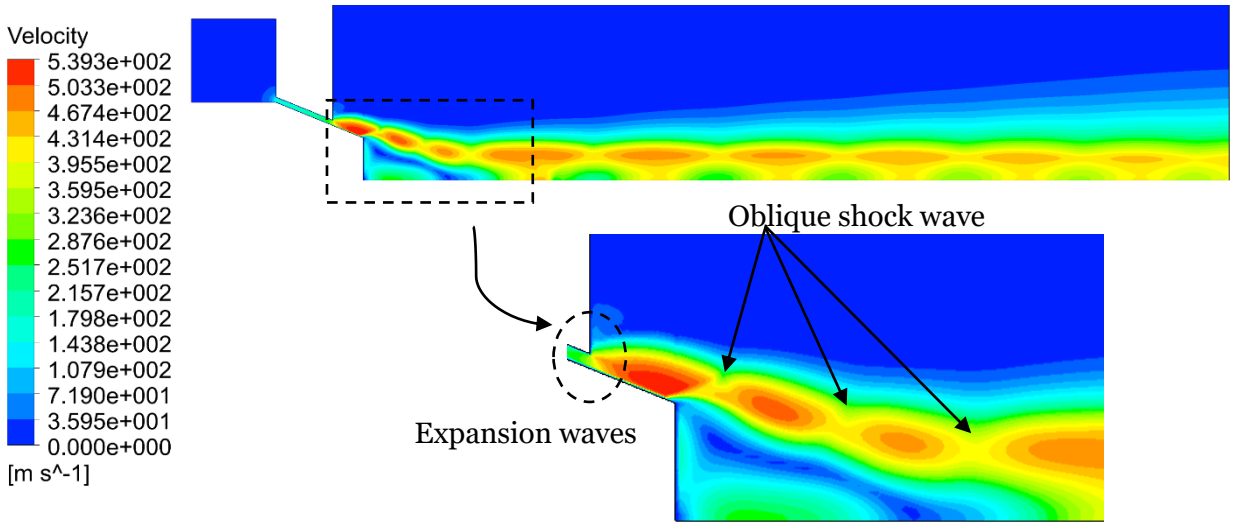

Figure 4.20 Velocity contour plots for 1MPa atomizing pressure for the whole domain and the recirculation zone

continue to flow towards the outlet. Figure 4.21 shows the velocity vector plots near the nozzle region. The recirculating gases can be seen in the Figure 4.21.

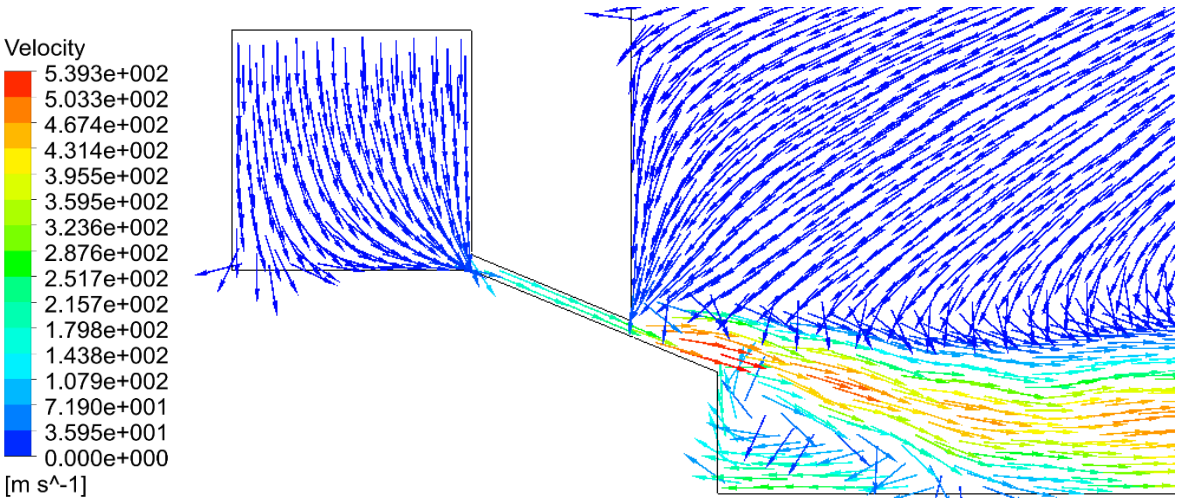

Figure 4.21 Velocity vector plots for 1MPa atomizing pressure for the whole domain and the recirculation zone

The aspiration pressure is measured in front of the melt delivery entrance which has been modelled as wall in this study due to reasons mentioned in section 4.1.1 A rake with 10 points has been defined in front of this wall and the area-weighted average static pressure across the rake was found. Also, this pressure is not the absolute pressure at the location and is over-ambient to the surrounding gases (relative pressure).

Figure 4.22 show the pressure contour plots in front of the melt nozzle. The pressures greater than 0.1 MPa has not been visualised in order to visualise the lower pressures in detail.

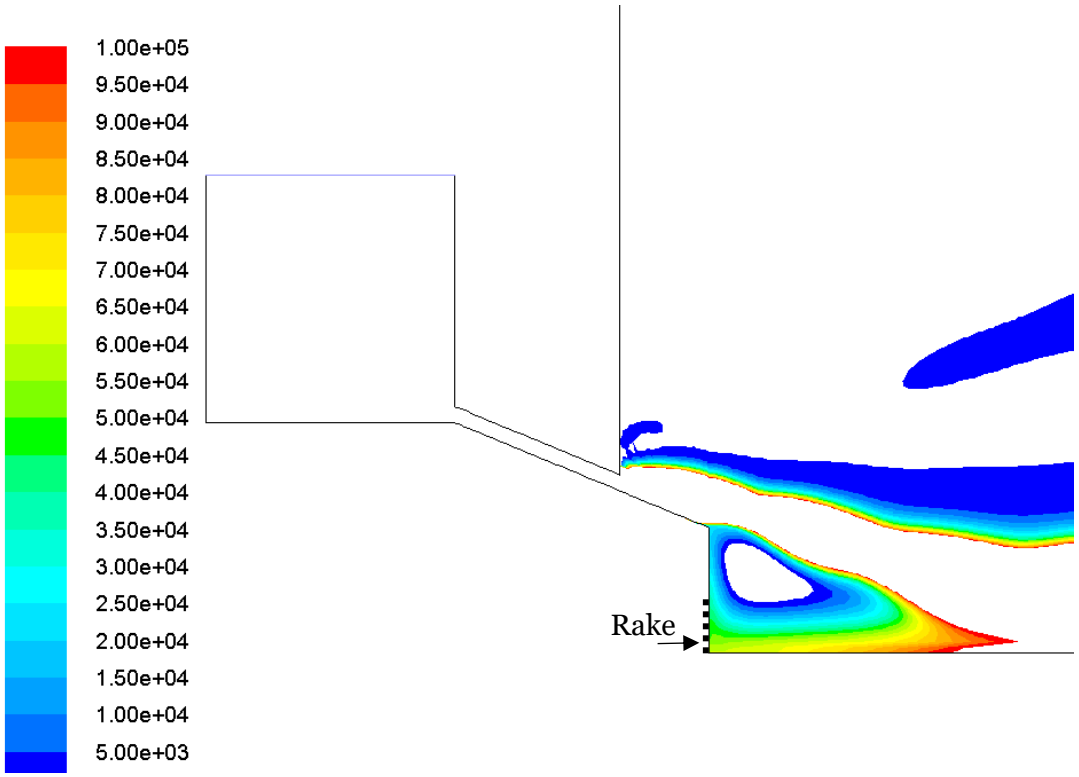

Figure 4.22 pressure plots of the recirculation zone for 1MPa atomizing pressure

As seen in the Figure 4.22, the pressure increases from the melt nozzle towards the inner part of the recirculation zone and is not a sub-ambient pressure. The aspiration pressure is found to be 27.13 kPa. The recirculating gases push the melt inside the melt nozzle, and it can be overcome by introducing the melt at a pressure sufficient to overcome this aspiration pressure. As mentioned in section 4.1.1, this atomizer designs requires the melt to enter the atomizing chamber at a 40 kPa pressure in order to overcome the aspiration pressure.

4.3.2 3MPa atomizing pressure:

The next simulation was carried out for an atomizing pressure of 3MPa. Most of the commercial atomizers use 3MPa as the standard atomizing pressure. Figure 4.23 shows the velocity contour plots at 3 MPa.

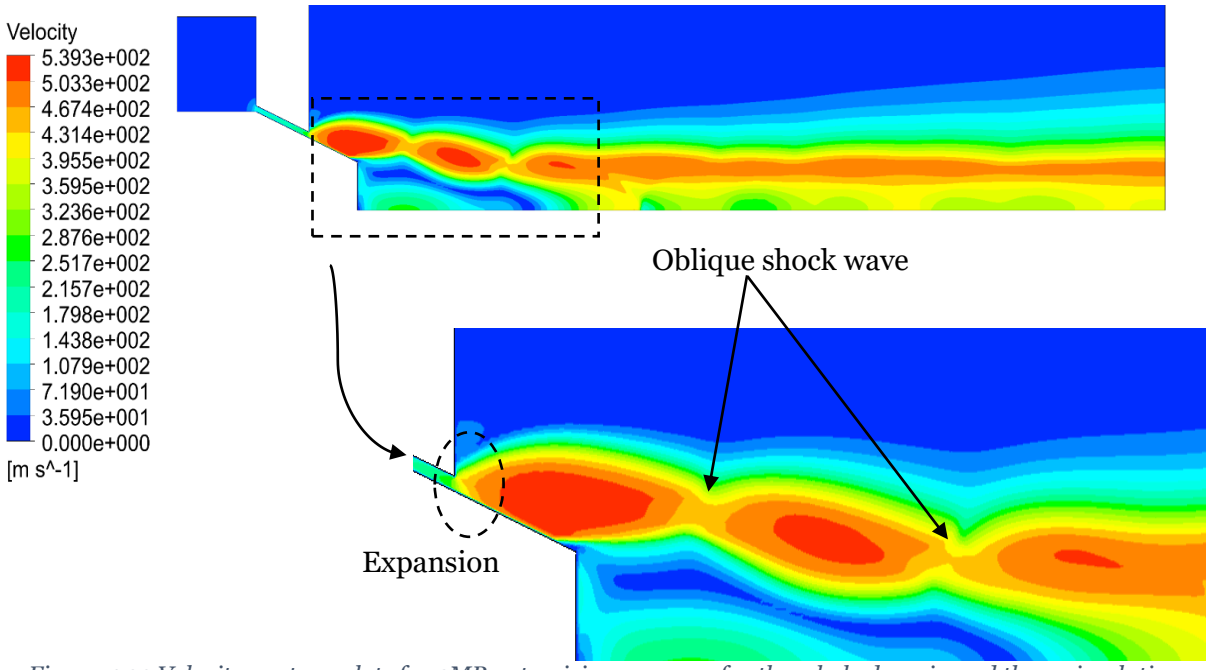

Figure 4.23 Velocity contour plots for 3MPa atomizing pressure for the whole domain and the recirculation zone

The velocity contour plots shown in Figure 4.23 is steady state flow field velocities at 3MPa near the nozzle region. At 3MPa atomizing pressure, the gas flow rate is higher than the previous case. The pressure difference between the exiting gas jets and the ambient is higher and this leads to gases acquiring higher velocities while expanding. Due to the above-mentioned reasons, the gas jets expand more than 1MPa gas jets. The oblique shocks develop similar to 1MPa flow field, but the strength of the shock waves and the expansion waves are higher than those formed in 1MPa pressure due to pressure difference and the increased momentum. The decelerated gas jets accelerate and expand into Prandtl Meyer shock waves through shocks and travel towards to outlet.

The expanding gas jets impinge at a point (stagnation point) and the flow turns towards the

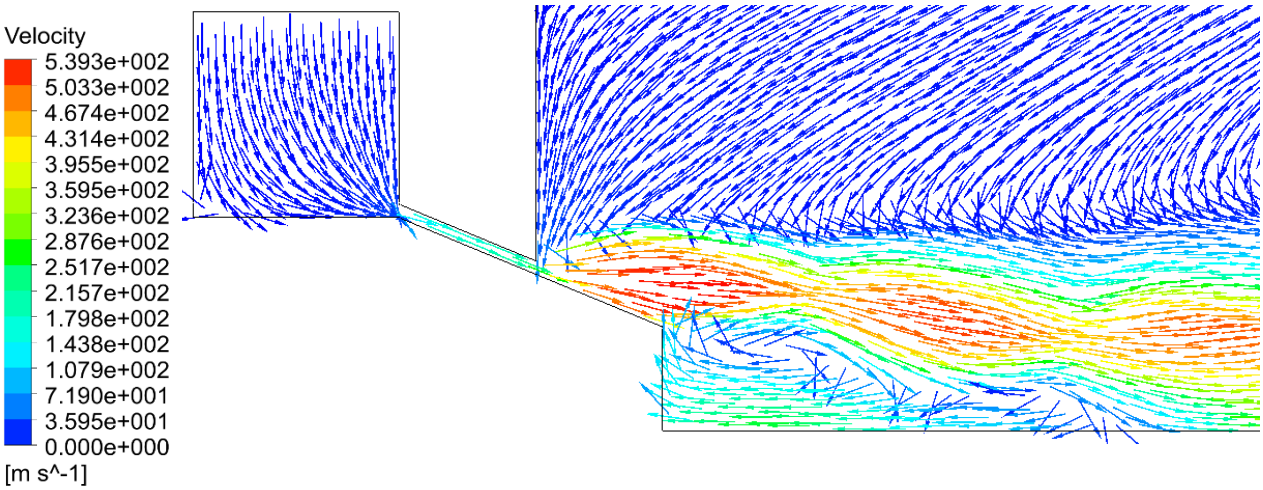

Figure 4.24 Velocity vector plots for 3MPa atomizing pressure for the whole domain and the recirculation zone

melt delivery tip forming a recirculation zone as observed at 1MPa. The recirculation zone formed at 3MPa atomizing pressure is elongated as compared to the 1MPa. As the gas jets expand more as they move towards the outlet (due to pressure difference), they influence the shape of the recirculation zone leading to slight pinching of the recirculation zone.

Therefore, the expanding gases entrain the recirculating gases in an elongated manner.

Figure 4.24 shows the velocity vector plots of the recirculation zone. The recirculating gases can be seen along with the stagnation point.

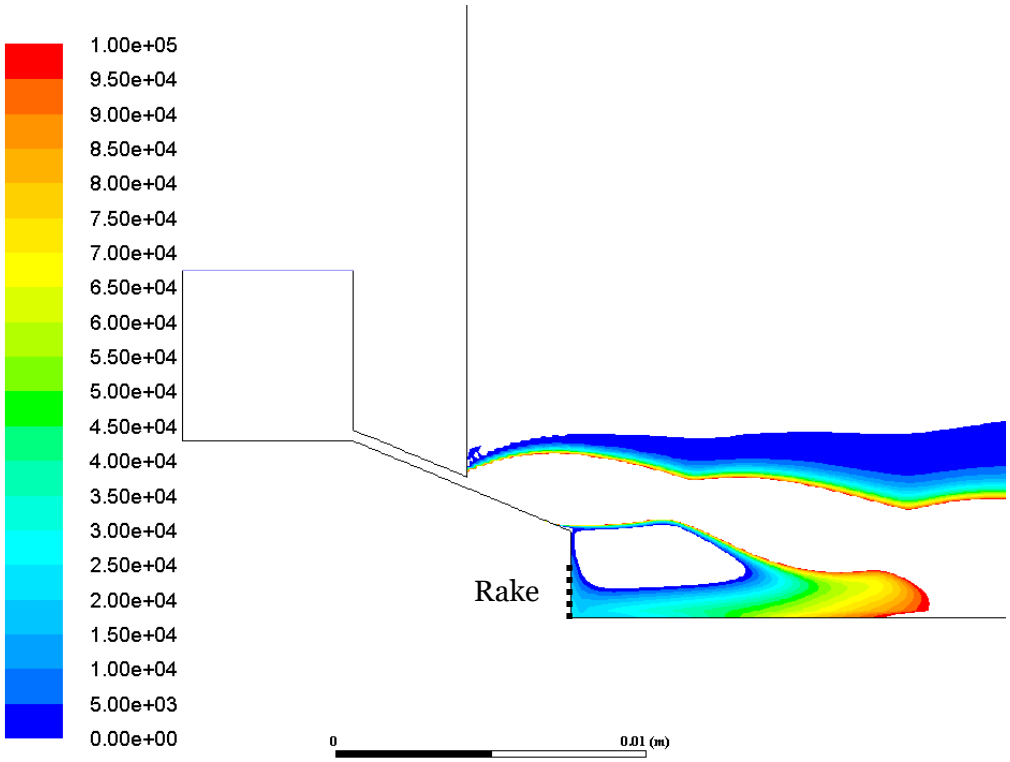

Figure 4.25 pressure plots of the recirculation zone for 3MPa atomizing pressure

As the previous case, a rake with 10 points was set up in-front of the wall replacing the melt delivery tube and the pressure across the rake was found. The aspiration pressure measured at the melt nozzle is 10.682 kPa. Again, a favourable sub-ambient pressure does not occur. The melt will not be drawn into the recirculation zone as the recirculating gases act against the melt flow. The melt must enter the recirculation zone at a pressure higher than this aspiration pressure in order to be atomized.

Figure 4.25 shows the pressure plot at the recirculation zone. Again, only pressures lesser than 0.1 MPa is shown in order to visualise the low pressures better. Once the melt enters the recirculation zone by overcoming the pressure at the melt nozzle, atomization happens. The highlighted zone has swirling gas jets that results in atomized melt being recirculated till they are picked up by the expanding gas jets.

As the atomizing pressure is increased, the incoming gas jets will have more energy to expend and expand more resulting in reduction in recirculation zone size. At much sufficient high atomizing pressure, the open wake becomes close wake, and the flow field changes appropriately due to the formation of Mach disk in front of the melt nozzle.

4.3.3 4.5 MPa atomizing pressure:

The pressure considered for the analysis is 4.5 MPa. A closed wake was observed experimentally by Motaman. [101] Figure 4.26 shows the velocity contour plots at 4.5 MPa.

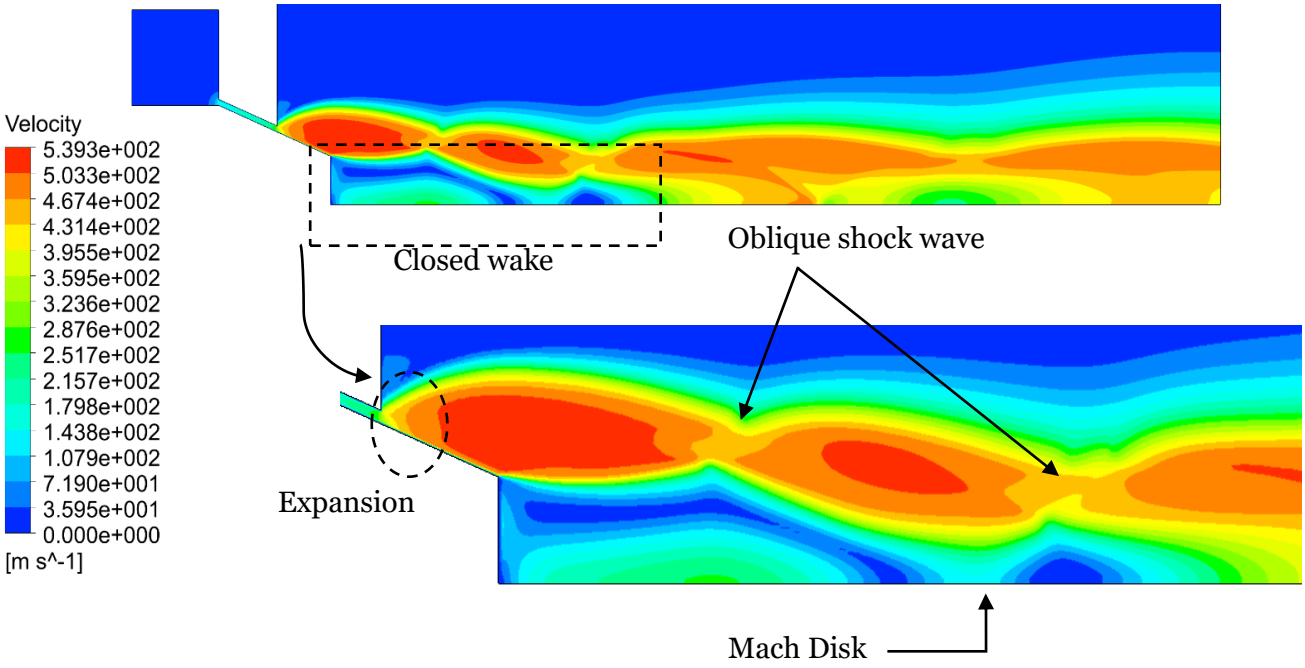

Figure 4.26 Velocity contour plots for 4.5MPa atomizing pressure for the whole domain and the recirculation zone

At atomizing pressure of 4.5 MPa, the gas jets possess higher momentum than the two

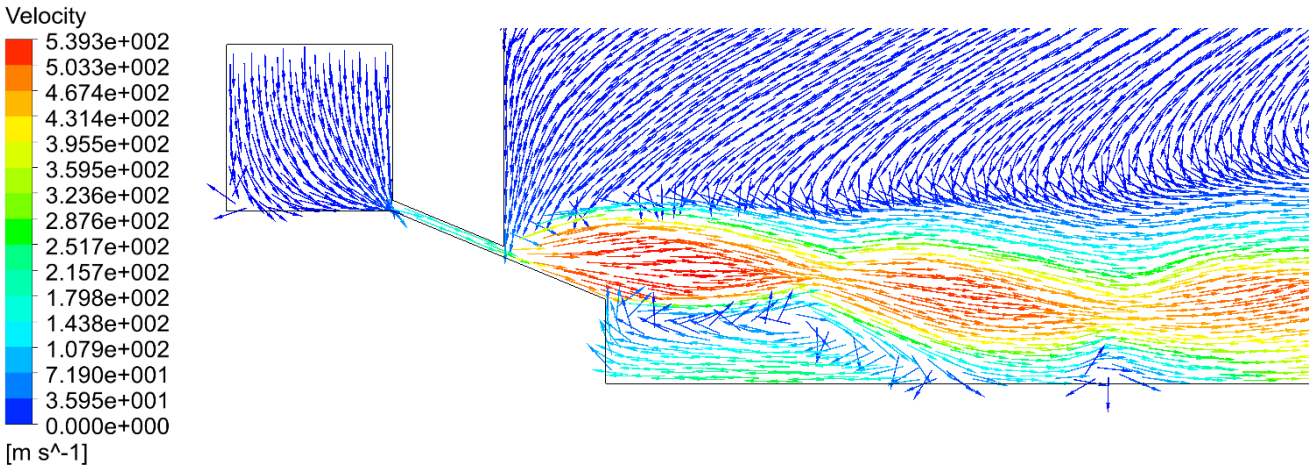

Figure 4.27 Velocity vector plots for 4.5MPa atomizing pressure for the whole domain and the recirculation zone

previous atomizing pressure considered. The oblique shocks are formed similar to the previous pressures. The gas jets impinge at a point (stagnation point) and form recirculation zone. The gas jets expand and impact on the recirculation zone. The impact of the gas jets on

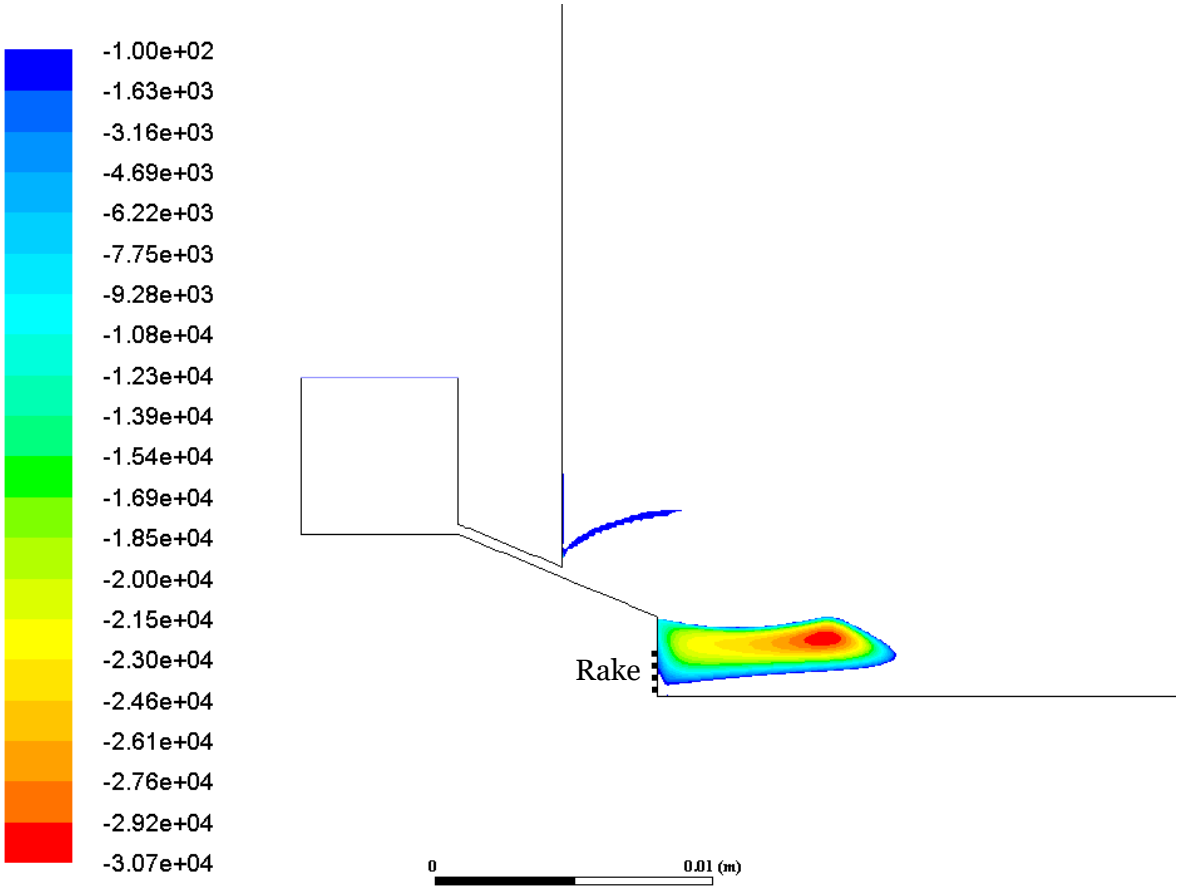

Figure 4.28 pressure plots of the recirculation zone for 4.5 MPa atomizing pressure

recirculation zone causes it to form a narrow and lengthier recirculation zone initially. The expanding gas jets interact in front of the melt nozzle and form a Mach disk. This results in a closed wake. (discussed in chapter 2)

Figure 4.27 shows the velocity vector plots of the recirculation zone. The Mach disk can be seen clearly here.

An interesting point to notice is that as the atomizing pressure is increased, recirculation zone gets elongated. The entrainment causes narrow recirculation zone due to the expansion of the gas jets. This entrainment causes a concave shaping of recirculation zone. This concavity increases with increase in the momentum and the kinetic energy possessed by gas jets and finally results in a closed wake due to the formation of a strong shock in front of the melt nozzle.

Figure 4.28 shows the pressure contour plots of the flow near the nozzle region in which the closed wake can be seen clearly.

A favourable sub-ambient pressure was noted for this pressure. The melt is drawn into the recirculation zone due to this sub-ambient pressure where it is atomized. As the pressure in-front of the melt nozzle is sub-ambient, this atomizer design will not require the melt to enter the recirculation zone at a pressure. The aspiration pressure was measured as -5.178 kPa.

4.3.4 5 MPa atomizing pressure:

The last pressure considered in this study is 5MPa. A closed wake is formed in this case too. Figure 4.29 shows velocity contours at 5 MPa.

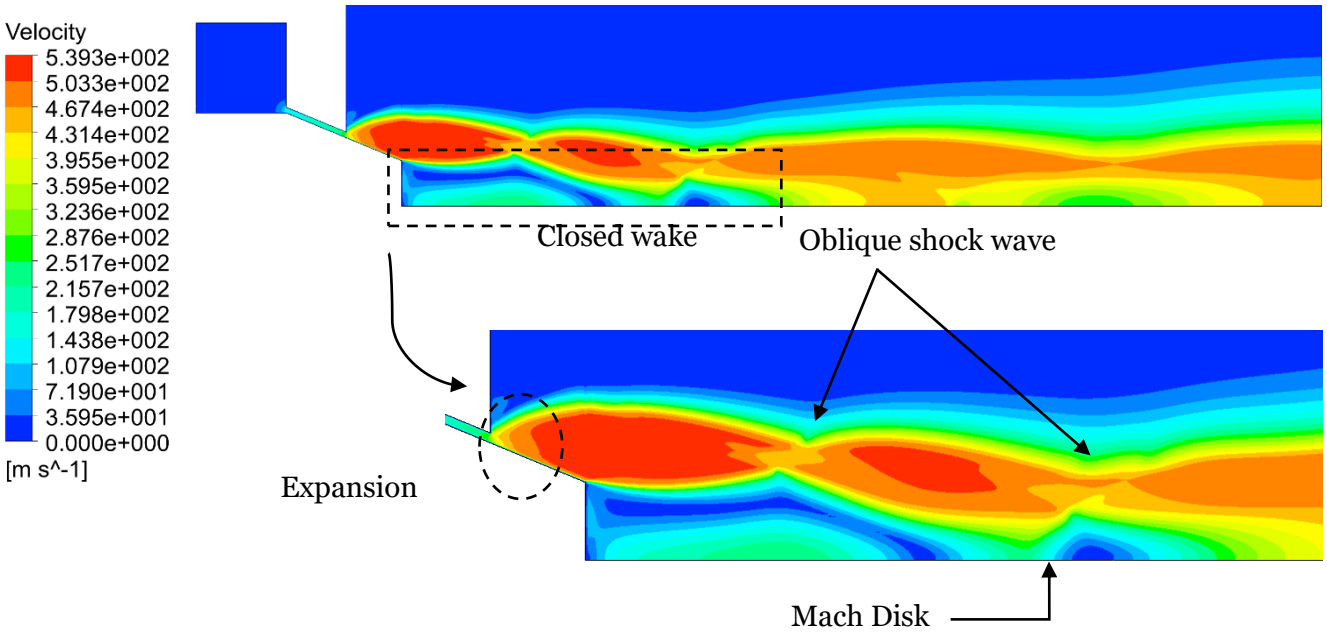

Figure 4.29 Velocity contour plots for 5MPa atomizing pressure for the whole domain and the recirculation zone

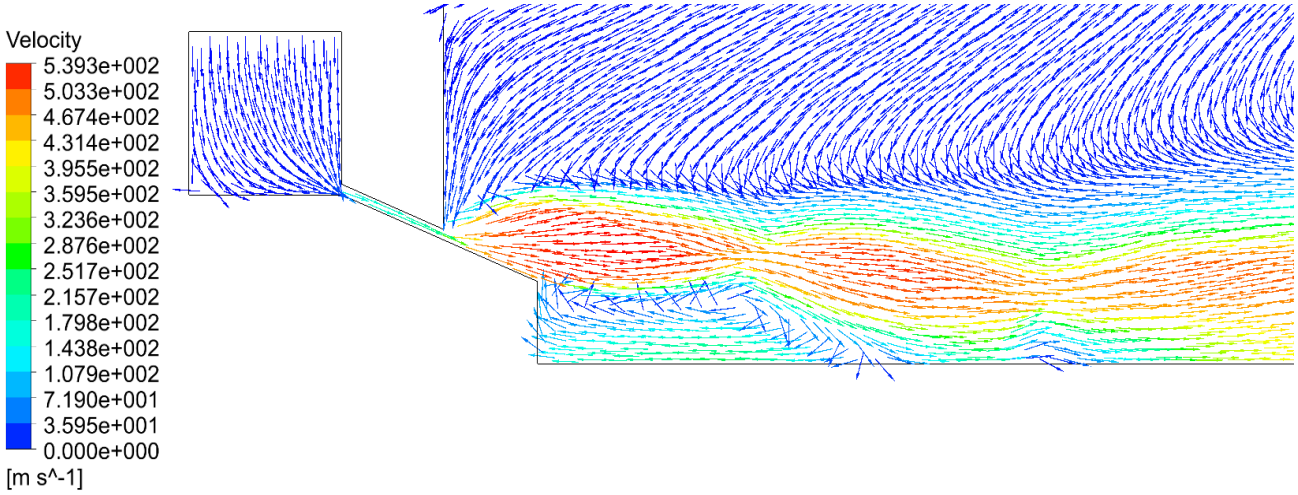

Figure 4.30 Velocity vector plots for 5MPa atomizing pressure for the whole domain and the recirculation zone

A strong shock wave is formed in front of the melt nozzle due to the interaction between the expansion waves. The Mach disk and the expansion waves can be seen observed clearly.
The gas jets exiting the gas die begin expanding as seen in the previous cases. The expanding gas jets interact and form a recirculation zone. Also, the gases possess higher momentum and hence the strength of the expansion waves and oblique shocks are high and hence the closed wake is formed.

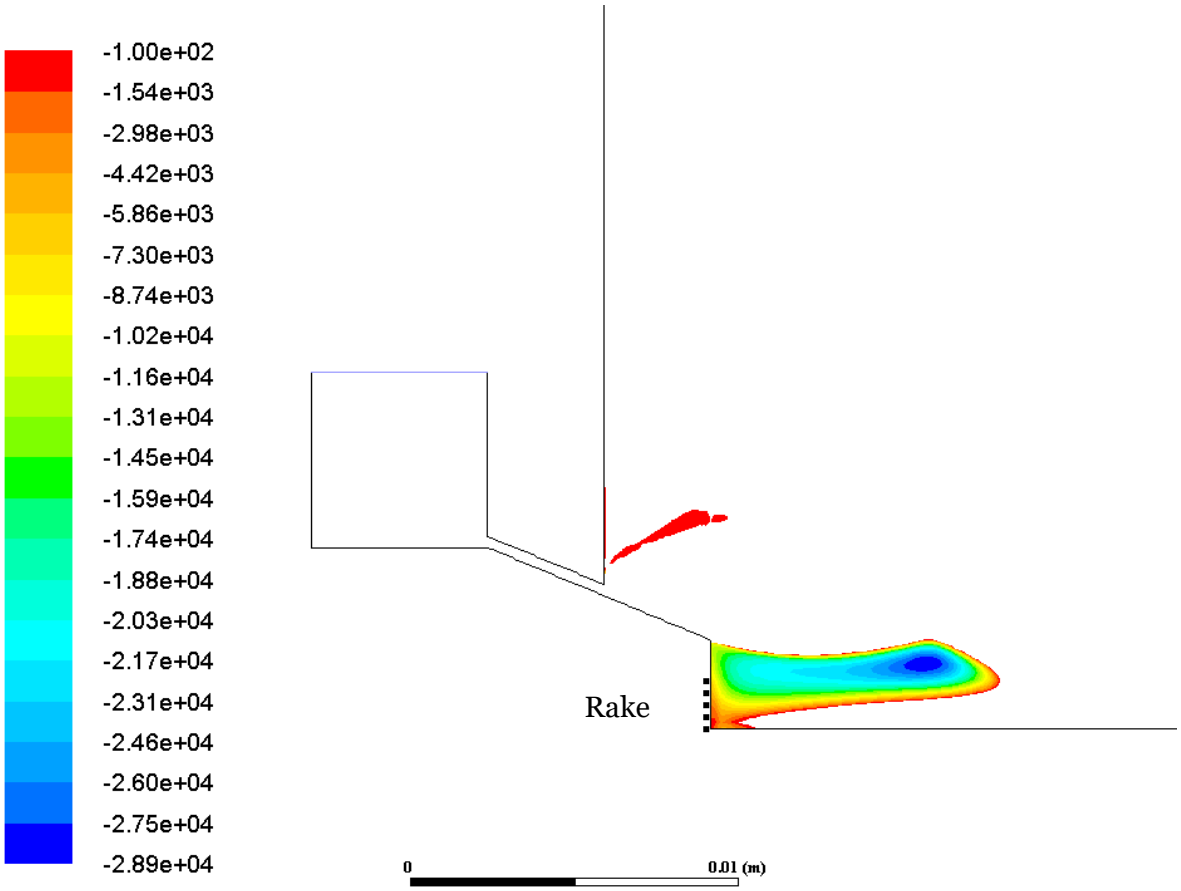

Figure 4.31 pressure plots of the recirculation zone at 5MPa atomizing pressure

The recirculation zone can be seen in this Figure 4.30. The Mach disk can also be noted.

Figure 4.31 shows the pressure plots of the recirculation zone. An aspiration pressure is measured in front of the melt nozzle and found to be -6.982 kPa. This sub-ambient pressure will draw the melt into the recirculation zone. The pressure is calculated in the same approach as in previous cases.

Summary

The primary analysis of the gas only flow in the two dimensions was carried out. The mesh independence, domain length independence and the sensitivity to turbulence model was analysed. A mesh with 18000 cells is found to produce near accurate results with less computational requirement. The domain length has been found to be 60 x 24 mm for this analysis. The gas jet diameter is set at 0.21 mm in order to match the gas flow rate of a CERAM atomizer. The trade-off is the protuberance length which has been reduced from 5.25 mm to 3.06 mm. The flow field was simulated in a density based steady state solver. The steady state was found when the residuals oscillated around a specific value as they did not converge. Various atomizing pressures of 1 MPa, 3MPa, 4.5 MPa and 5 MPa were simulated in a flow domain designed according to the primary results. The wake closure pressure was found to be at 4.5 MPa.

5 TWO-DIMENSIONAL TWO-PHASE ANALYSIS

Methodology, research and discussion.

In Close-coupled gas atomization, the melt is broken into fine droplets by the chaotic interaction between the gas jets and the melt. The mechanism of melt breakup into finer droplets is not completely understood as it is difficult to use experimental tools in the adverse conditions such as high temperature and high velocities. The interaction between melt and gas jets has become a major research interest due to advances in CFD tools.

Figure 3.1 shows the schematic of melt and gas flow in a close coupled gas atomizer. Generally, melt flows into the atomizing chamber by means of a melt delivery tube. The melt is pushed against the melt nozzle surface by pre-filming and is disintegrated into ligands by the high-speed gases. These ligands undergo secondary atomization to form melt droplet which solidifies to form metal powder. An ideal numerical model representing a close-coupled gas atomization process should include the melt flow into the atomizing chamber, melt disintegration, movement of melt droplets in the gas flow field and the solidification of droplets into powders. The computational resource requirement for developing such a model is quite high even in RANS approach. Also, the influence of small-scale interaction between the melt and the gas on melt break-up is not considered in RANS approach and this approximation affects the size of the droplet (ligand) formed and hence the accuracy of the model to a certain extent. Due to this, many researchers have developed models to simulate different steps involved in the CCGA instead of the entire process.

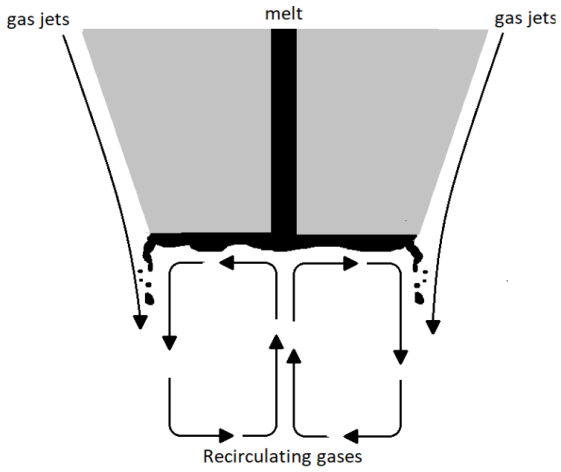

Figure 3.1 Schematic representation of melt and the nozzle Schematic representation of melt and the nozzle

Generally, two-phase flow problems such as close coupled gas atomization can be modelled in two ways; the Eulerian approach where the second phase is modelled as fluid and the Lagrangian approach where the dispersed phase is modelled as particles. The Eulerian approach also known as Euler-Euler approach considers both the gas jets and the melt as fluids and the problem is solved by volume of fluid method (VOF). The breakup of melt and the movement of droplets are solved using VOF method. There are few drawbacks in this approach. The computational resource requirement is high in VOF method as it requires mesh size of order of microns to capture the interaction. Also, due to the mesh size constraint, the domain size will be limited. The Lagrangian approach also known as Euler-Lagrangian approach considers the gas as fluid and the melt as a group of particles. The gas flow field is solved as a continuum and the melt is introduced into the solved gas flow field as set of particles. Depending on the type of coupling between the two phases, the gas flow field and the trajectories of particles are calculated using the set of equations. The mesh size constraint in this approach is that the element size must be larger than the particle size. Therefore, the computational resources requirement is not high compared to VOF. The melt is modelled as set of particles using the discrete phase method in this approach.

This study deals with the movement of melt droplets in the gas flow field and the influence of the gas and melt on each other. A two-way coupled Euler-Lagrangian model (as discussed in chapter 2) can be utilized to study this interaction between the melt droplets and gases for a range of GMRs by modelling melt as Lagrangian particles and gases as Eulerian flow field. Therefore, a Lagrangian approach was adopted in this study. The methodology involved in developing this model and the results obtained from it are discussed here.

5.1 METHODOLOGY

The movement of melt particles in an annular slit confined feed gas atomizer is analysed in this study. As a Euler-Lagrangian approach was used in this study, the flow field must be solved before the Lagrangian particles are introduced. The results obtained from the single-phase analysis were used to establish the solved flow field in which the particles were released. Once the particles are released, the flow field and the particle trajectories are solved to obtain the results as the model is two-way coupled.

Depending on the inlet pressure, two different types of flow fields are observed. The open wake condition is observed below the wake closure pressure where the expanding gas jets do not form a Mach disk in front of the melt entrance. The closed wake condition is observed above the wake closure pressure where the expanding jets form a Mach disk in front of the melt entrance. In the single-phase analysis (gas only), a total of four cases – two open wake

pressures and two closed wake pressures were considered. Similarly, five operating pressures are considered in this study.

5.1.1 Eulerian settings and assumptions:

The Eulerian flow field used in this study is based on the following assumptions:

- Flow is considered to be transient.
- Flow is considered 2D axis-symmetric.
- The fluid is considered as argon and modelled as a compressible ideal gas with specific heat ratio $\gamma = 1.66$.
- The impact of the molten metal is not considered when solving the gas-only flow field.
- For presentation purpose, the model is rotated 90 degree anticlockwise so that the atomization direction is changed from vertically downwards to horizontal.
- As mention in chapter 4, the axis of the model was moved away from the r=0 to r=25µm as the model diverged.

Also, the flow field was solved in a density-based solver with a standard k-ω turbulence model.

5.1.2 Lagrangian settings and assumptions:

In the CCGA, the melt is allowed to flow through the melt delivery tube into the atomizing chamber. Certain atomizer designs require the melt to enter the atomizing chamber at a pressure to overcome the adverse pressure posed by the recirculation zone. The discrete jet atomizer based on which the two-dimensional single-phase model was developed requires the melt to enter at 40 kPa pressure.

In the single-phase study, the melt delivery tube was replaced with a wall as this assumption gave rise to results qualitatively comparable to physical reality. Due to this, the melt particles could not be introduced by means of the melt delivery tube as in the physical process. Therefore, melt is modelled as particles in front of the wall replacing the melt delivery tube. This is a good assumption in Lagrangian approach as the melt enters the chamber at a creeping velocity and acquires velocity only after breakup due to the interaction with the gas jets. The limitations of this assumption are discussed in the later section **8.7.**

The atomizer design adopted in this single-phase study and subsequently in this study was designed to match the gas flow rate of the discrete jet CERAM atomizer. The gas flow rate of the CERAM atomizer is found to be 2502 $gmin^{-1}$ for an inlet pressure of 3 MPa. Also, for the same inlet pressure, two trials with different melt flow of 1041 $gmin^{-1}$ and 1136 $gmin^{-1}$ were carried out with no issues. The metal used in these trials is Ni-50wt%Al with density of 3460 kgm^{-3}. Using this density, the mass flow rate is converted into volumetric flow rate. The

velocity of the melt in the delivery tube was calculated using the cross-sectional area of the tube and the volumetric flow rate. The velocity was found to be approximately 1.5 ms^{-1}. Therefore, the velocity of the particles in this numerical model was set at 1.5 ms^{-1}.

The size of the melt droplets plays a major role in influencing the changes in the gas flow field brought about by the melt movement. In the physical process, the melt is pushed against the melt nozzle surface by the prefilming process on entering the atomization chamber. The melt is then disintegrated along the circumference of the nozzle by the high-speed gas jets into droplets of varying sizes. The force due to the surface tension impedes the deformation brought about by the aerodynamic forces of the atomizing jets. The melt droplets continue to deform and breakup till these two forces balance each other. As mentioned in literature review, the melt is broken into ligands in primary atomization and ligands are broken into melt droplets in the secondary atomization. The size of the powders obtained through CCGA vary between 15 μm to 500 μm depending on various process parameters and flow conditions. As the melt breakup is not modelled and particles are introduced as such in the flow field, sizes of droplets in the model does not change throughout the process.

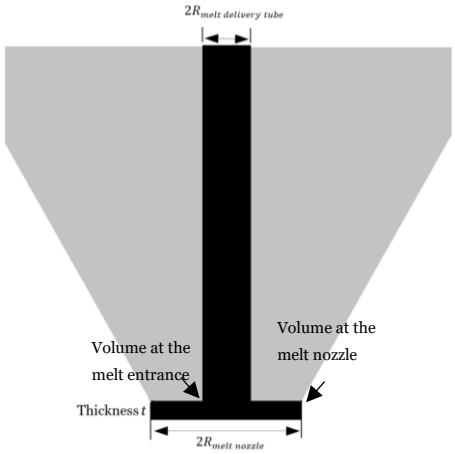

Figure 5.1 schematic representation of the melt nozzle and the melt.

Figure 5.1 shows the nozzle with melt delivery tube diameter $2R_{melt\ delivery\ tube}$ and melt nozzle diameter $2R_{melt\ nozzle}$.

The melt flows through the delivery tube and spreads across the nozzle surface to form a prefilm of thickness t. In order to establish a prefilm of constant thickness, the volume at the melt entrance must be equal to volume exiting the circumference.

Volume at the melt entrance: $V_i = \pi R^2_{melt\ delivery\ tube} v$

Volume exiting at the melt nozzle circumference: $V_o = 2\pi R_{melt\ delivery\ tube} t v_t$

where v and v_t are velocity of the melt at the entrance and at the exit as shown in Figure 5.1.

$$\pi R^2_{melt\ delivery\ tube} v = 2\pi R_{melt\ nozzle} t v_t$$

$$t = \frac{1}{2} * \frac{v}{v_t} * \frac{R^2_{melt\ delivery\ tube}}{R_{melt\ nozzle}}$$

$R_{melt\ delivery\ tube} = 1\ mm$ $R_{melt\ nozzle} = 2.5\ mm$

The velocity of the melt is 1.5 ms^{-1}

$$t = 0.5 * 4 * 10^{-4} * \frac{v}{v_t}$$

$\frac{v}{v_t}$ is unknown but as a limiting case, $v_t \leq v$ and $v_t \geq \frac{R_{melt\ delivery\ tube}}{R_{melt\ nozzle}} v$ and therefore

$$1 \leq \frac{v}{v_t} \leq 2.5$$

Therefore, the thickness *t* was found to be 200-500 μm.

Also, Antipas et al found suggested that the ligand size in the primary atomization zone is between 200-600 μm. [123, 124] Typical run time for this model with particle size of 500 μm and 50 ms flow time was approximately 10 days. One of the model constraints is to be run with practical fixed melt mass flow rates and reducing the particle diameter will increase the number of particles in the system and the run time. For example, if the particle size is reduced by a factor of 2, the number of particles increase by eight-fold. Though the CCGA process produces powders in varying size, this model assumes constant particle size of 500 μm.

In discrete phase method, there are various ways to release particles in the flow. A simple single injection method was chosen for this study. In single injection method, particles are released from a fixed point. In physical CCGA process, the melt is forced against the melt nozzle surface into a film by prefilming and the film is broken into a large number of ligands by the high-speed gas jets. As melt break-up and solidification are not modelled in this study, in order to track the solid Lagrangian particles, they have to be introduced directly. Generally, a system of injections is used to simulate such conditions. Three different system of injections were considered in this study as shown in the Figure 5.2. Also, the number of particles entering the atomization chamber has an important influence on the particle trajectories in terms of presentation. In single injection system, one particle is released into the atomization chamber at a time which means the melt is broken into one droplet at a time. Similarly, in the three-injection system and five injection system, three particles and five particles are released into the atomization chamber at a time which means the melt is broken into three droplets and five

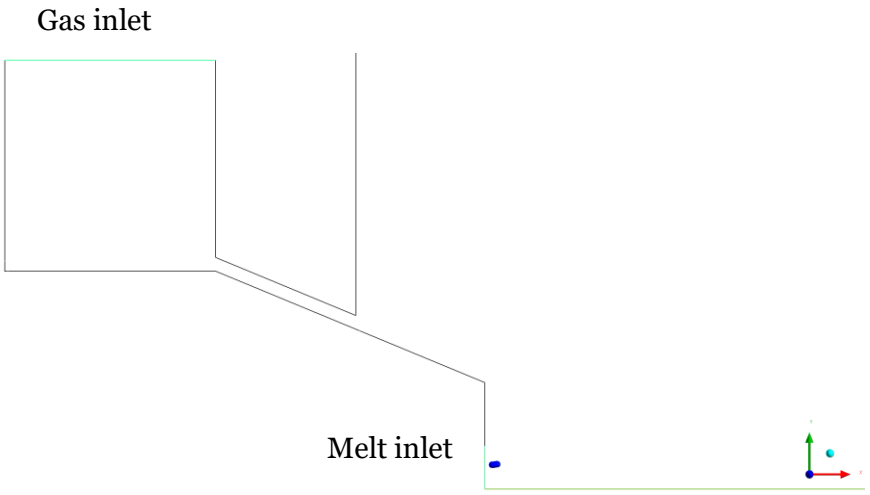

1 injection system

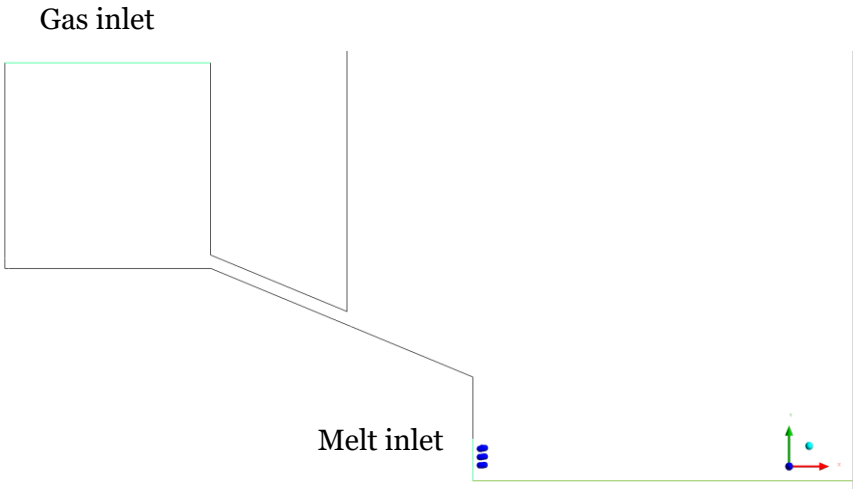

3 injection system

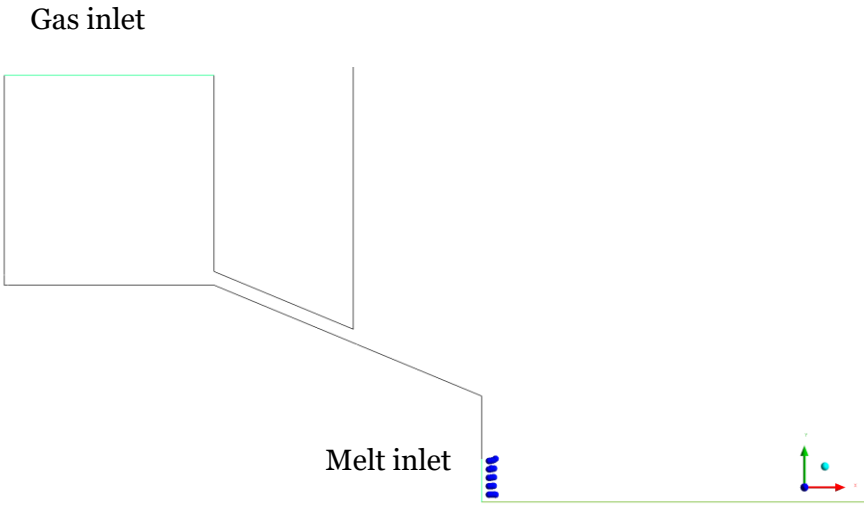

5 injection system

Figure 5.2 different types of injection systems considered

droplets at a time, respectively. The melt is broken into a large number of droplets along the nozzle edges in the physical process.

Therefore, a five-injection system has been selected to analyse the presentation of particle tracks which is not optimum for visualization.
The particles are spherical in shape and 500 microns in size. The material for these particles is chosen to be aluminium with a density of 2700 kgm^{-3}. Therefore, volume and hence mass of a single particle are found to be 0.0065 mm^3 and 0.000176769 grams, respectively. The mass flow rate of the dispersed phase is set at 2 $kgmin^{-1}$ so that a range of GMRs can be established for pressures ranging between 1 MPa to 5 MPa. (The range considered in chapter 4)

The flow was solved for every microsecond with 20 iteration per time-step in a second order discretization scheme. The flow was analysed for 50 milliseconds as the flow did not exhibit any drastic changes at the end of 50 milliseconds. A range of GMRs have been considered in this study.

As discussed in chapter 2, stochastic model is utilized is particle laden flows to simulate the random or probabilistic nature. This is achieved by giving random velocity component to the particles in the set of equations defining the flow. Stochastic modelling or Discrete Random Walk model has been used in this study. The setting used in each injection are tabulated in the table. The injections are numbered as shown Figure 5.3 and the numbers are used in the study throughout to denote the injections. Table 5.1 shows the settings used in this study.

Table 5.1 Settings used to define injections

Setting for each injection	**Value**
Velocity of the particle (x-direction)	1.5 ms^{-1}
Diameter of each particle	500 microns
Discrete Random Walk model	Yes
Flow rate	0.0066 kgs^{-1}
Particle Type	Inert particle
Density	2700 kgm^{-3}
Specific heat	921.096 Jkg^{-1}-K^{-1}
Turbulence dispersion	Discrete Random Walk model, Random Eddy Lifetime
Time scale constant	0.15
Drag law	spherical

The Lagrangian particles used in this study is based on the following assumptions:

- The melt breakup is not considered.
- The flow with particles is considered as transient.
- The melt particles are assumed to be inert and made of aluminium with density of 2700 kgm^{-3} and specific heat of 921.096 Jkg^{-1}-K^{-1}
- Particles were modelled with constant diameter of 500 microns.
- Stochastic modelling is used.
- For the presentation purpose, 5 injections were chosen, and the particle tracks were scaled down.

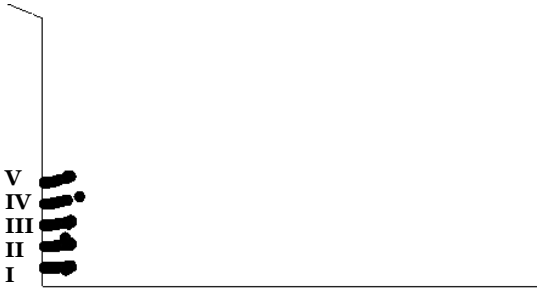

Figure 5.3 The injections with their corresponding numbers as used in study..

5.1.3 Use of Stochastic modelling

Stochastic modelling (also known as discrete random walk model) is used to induce randomness in the model to simulate the physical process. Generally, the numerical models are deterministic i.e. the output of the model is determined by the initial conditions and values of the parameters. The physical processes are characterised by inherent randomness. The same set of initial conditions and values will result in an ensemble of different outputs. Therefore, stochastic modelling has been utilized in this study to induce randomness. Figure 5.4 shows the particle trajectories at flow time t= 5 milliseconds with and without stochastic modelling at 3MPa operating pressure.

In the deterministic model, it can be seen that the particles from the same injection have the same trajectory inside the recirculation zone giving rise to uniform movement of particles. The interaction between the melt and the recirculating gas is complicated and the movement of ligands will not be identical as observed in the numerical model. Therefore, stochastic model has been utilized to produce results comparable to the physical CCGA.

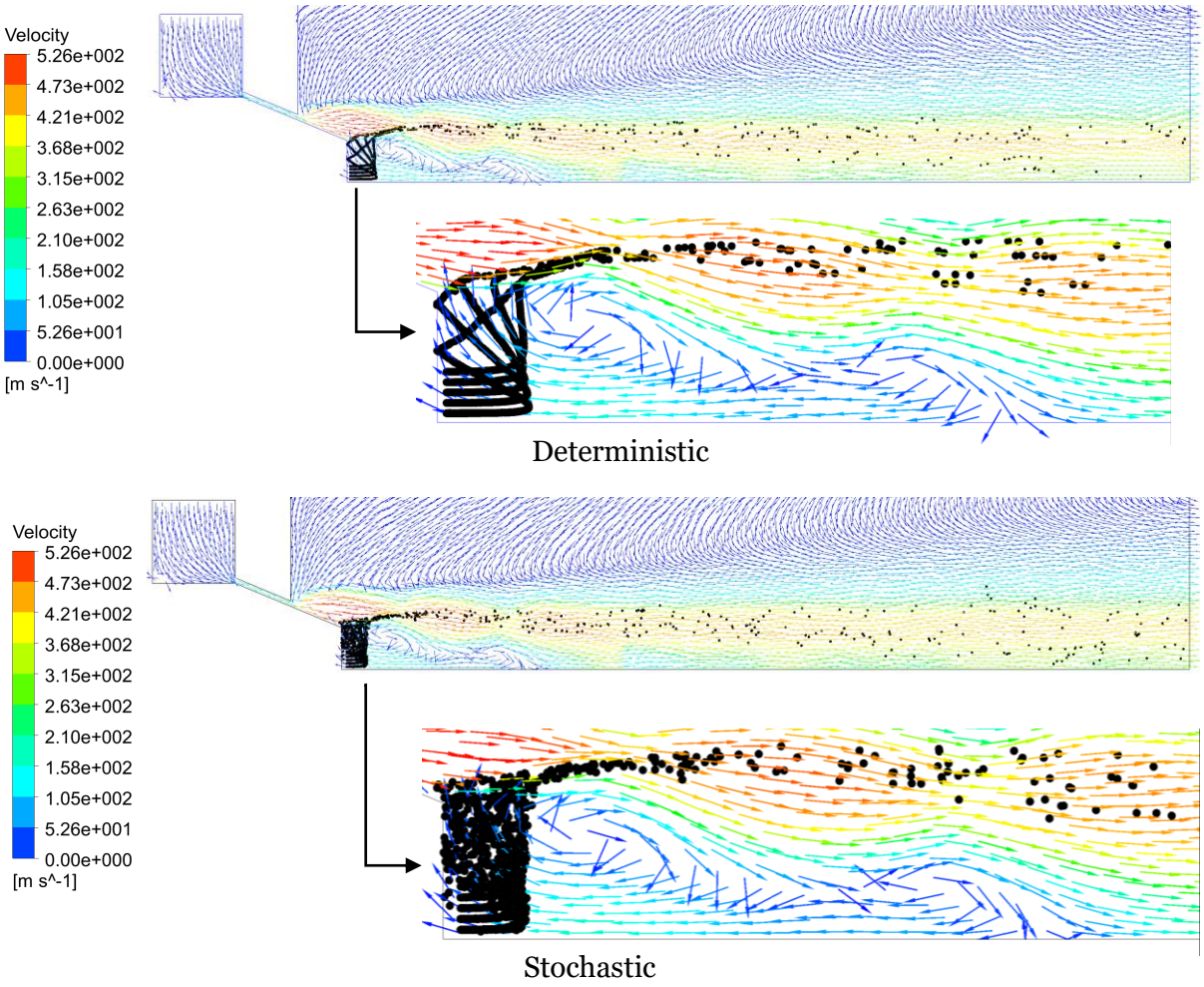

Figure 5.4 comparison of particle trajectories between models with and without stochasticity

5.1.4 Particle Mass concentration

The particle mass concentration in recirculation zone is measured for every millisecond through 50 milliseconds. A plane is set up in the recirculation zone and the average particle mass concentration is calculated. The location of the plane is shown in the Figure 5.5 highlighted by the shaded region. The results are discussed in section 5.2.1.

Figure 5.5 Location of the plane in the recirculation zone

5.1.5 Aspiration pressure

Aspiration pressure is an important process parameter. It was measured for every microsecond through 50 milliseconds along a rake located in the recirculation zone. Figure 5.6 shows the location of the rake (with 20 points). The results are discussed section 5.2.7.

Figure 5.6 Location of rake (with 20 points) where aspiration pressure is calculated.

All the simulations were carried out using Ansys 17.1 in a workstation with 32 GB RAM and 64-bit Operating system. Typical run time for each case was about 200 hours. All settings used to generate results are shown in Table 5.2

Table 5.2 Settings used in Ansys Fluent in this study

Setting	**Option**
Solver type	Density-based
Velocity formulation	Absolute
Time	Steady
Energy	On
Turbulence models	Standard k-w
Turbulence model- DPM	Interaction with continuous phase Unsteady Particle Tracking Track with fluid flow time-step Update DPM sources every flow iteration
Number of continuous phase iterations per DPM iteration	10
Formulation	Implicit

Flux type	Roe-FDS
Spatial Discretization	Second Order Upwind
URF Turbulent kinetic energy	0.8
Specific dissipation rate	0.8
Turbulent viscosity	1
Discrete Phase Source	0.9
Initialization	Hybrid

5.2 RESULTS AND DISCUSSION

The interaction between the dispersed phase and the gas flow field is complicated. The dispersed phase influences the process parameters such as aspiration pressure and important aspects of the flow field such as wake condition and prefilming tendency. Five cases are considered in this study. The particle mass concentration in the recirculation zone, the particle trajectories, changes in the flow field due to particles (two-way coupled), aspiration pressure, prefilming tendency, particle residence time and the velocity of the particles are discussed here.

5.2.1 Particle Mass concentration

The average particle mass concentration is the mass flux of the dispersed phase in the recirculation zone i.e. difference between the mass entering and exiting the recirculation zone. As the mass of the dispersed phase entering the recirculation zone is constant, this average particle mass concentration directly indicates the number of particles exiting the recirculation zone. In this study, the flow rate of the dispersed phase is maintained at 2Kgmin^{-1}. A range of operating pressures were considered in this study.

Table 5.3 shows the various pressures considered along with the corresponding GMR and wake condition.

Table 5.3 Various pressures considered in this study and the corresponding GMRs

Operating Pressure	Wake condition	Gas flow rate	Melt flow rate	GMR
1 MPa	Open wake	0.01376 kgs^{-1}	0.033 kgs^{-1}	2.398
1.5 MPa	Open wake	0.0206 kgs^{-1}	0.033 kgs^{-1}	1.602
3 MPa	Open wake	0.04167 kgs^{-1}	0.033 kgs^{-1}	0.791

4.5 MPa	Closed wake	0.062192 kgs^{-1}	0.033 kgs^{-1}	0.533
5 MPa	Closed wake	0.069016 kgs^{-1}	0.033 kgs^{-1}	0.478

The first pressure considered in this study is 1MPa and with a melt flow rate of 0.033kgs^{-1}, this pressure has a GMR of 2.398. Generally, atomization process with GMRs greater than 1 are unstable and hence this is not a feasible GMR, and the model diverged. Therefore, this pressure was not considered for further analysis.

As discussed above, the particles are released inside the recirculation zone. The gases in the recirculation zone are characterised by a range of low velocities compared to the velocities of expanding gas jets. The particles enter the recirculation zone and begin moving against the flow direction of the recirculating gases. The recirculating gases expend the kinetic energy of the particles and the particles reach a state of zero-velocity. The particles change their flow direction and start moving along with the low velocity gases towards the high-speed gas jets. Average particle mass concentration was calculated over the plane as described in section

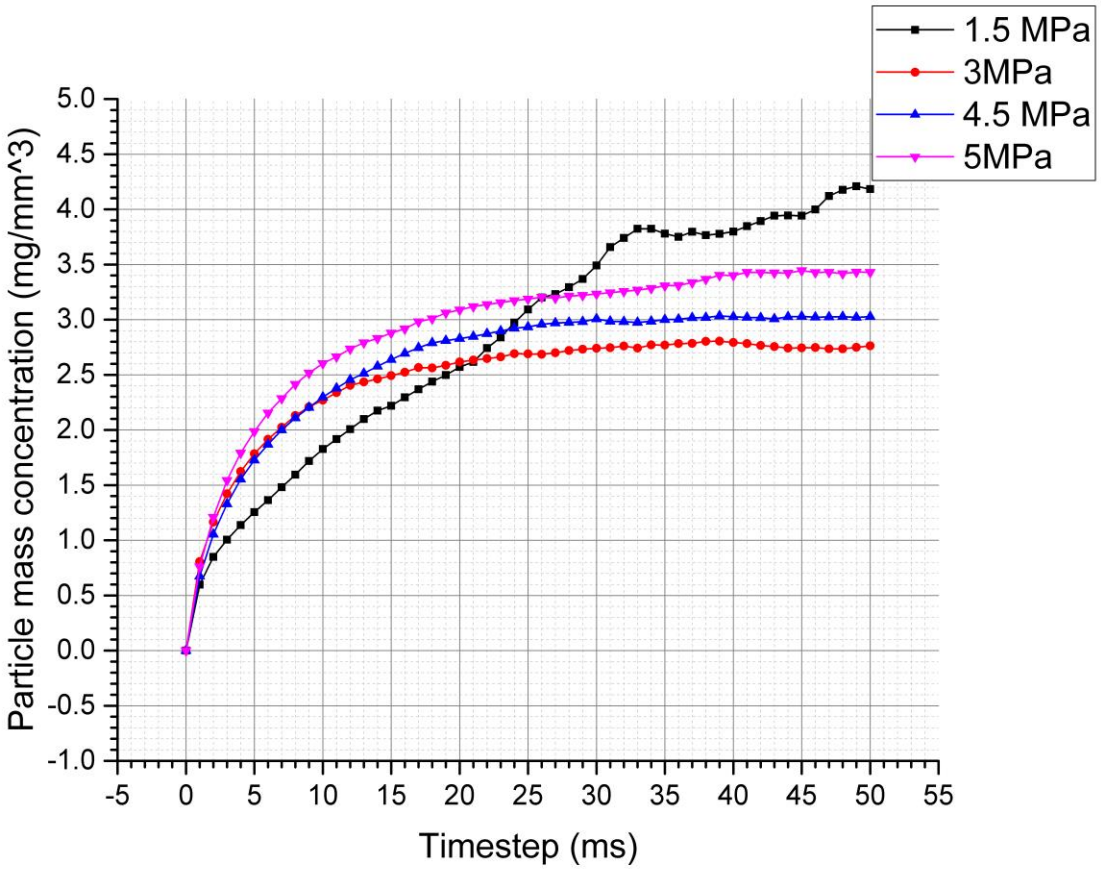

Figure 5.7 Graph showing particle mass concentration ($mgmm^{-3}$) vs time steps (ms)

5.1.4. Figure 5.5 shows the plane location. Figure 5.7 shows the graph of particle mass concentration plotted against the timesteps for the four pressures considered in this study.

The operating pressure 1.5 MPa had a GMR of 1.602 as seen from the Table 5.3. It can be seen that the particle mass concentration increases steadily as the flow time increases through 50 milliseconds. This steady increase in the mass concentration is due to the high GMR i.e. there is not sufficient mass of gases entering the recirculation zone to carry the particles into the high-speed gas jets. This gives rise to stagnation of particles in the recirculation zone which along with constant influx of particles leads to increase in the mass concentration. Also, this high GMR (>1) will eventually lead to failure of the case at some point beyond 50 milliseconds.

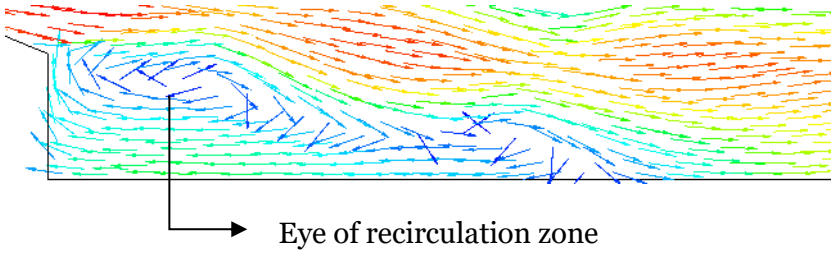

Figure 5.8 the vector plots of recirculation zone for 3MPa atomizing pressure showing the eye of recirculation zone

The shape of the recirculation zone, location of the eye of the recirculation zone and the GMR influence the movement of particles inside the recirculation zone. Figure 5.8 shows the eye of the recirculation zone in a 3MPa flow field. The operating pressure 3 MPa has a GMR of 0.791. The particle mass concentration increases rapidly till 10 milliseconds and continues to increase gradually till 20 milliseconds and becomes constant till 50 milliseconds.

The other two pressure considered in this study (4.5 MPa and 5 MPa) also exhibited the same trend as seen in 3MPa pressure. The operating pressure 4.5 MPa had a GMR 0.533. The particle mass concentration increases rapidly till 10 milliseconds and then increases gradually till 30 milliseconds. The particle mass concentration becomes constant in the last 20 seconds of the analysis. The operating pressure 5 MPa had a GMR 0.478. The particle mass concentration increases rapidly till 10 milliseconds and continues to increase gradually till 40 milliseconds. The particle mass concentration becomes constant in the last 10 milliseconds.

The increase in the particle mass concentration indicates that the number of particles exiting the recirculation zone is lesser than the number of particles entering it leading to stagnation of particles. The constant particle mass concentration indicates that the number of particles exiting the recirculation zone is constant and equal to the number of the particles entering the recirculation zone. The shape of the recirculation zone and the location of it eye along with GMR play an important role in determining the movement of the particles inside the

recirculation zone and hence the particle mass concentration. The trajectories of particles are discussed in next section.

5.2.2 Volumetric flow rate at recirculation zone's eye

The atomizing gas expands around the melt nozzle and form a recirculation zone in front of the melt nozzle. The shape and the size of the recirculation zone are greatly influenced by the operating pressure. The melt particles that enter the recirculation zone are carried to the high-speed jets by the recirculating gas. Figure 3.1 shows the general direction of gas movement inside the recirculation zone. The movement of melt particles is affected by the volume and the velocity of the gas flowing towards the melt nozzle. The volumetric flow rate of the atomizing gas was measured just below the eye of the recirculation zone for all the pressures considered in this study. Figure 5.9 shows the line along which the volumetric flow rate was calculated.

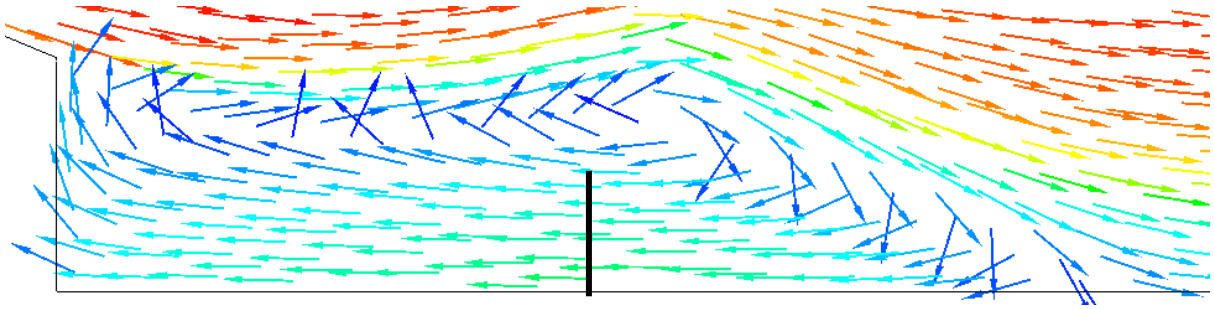

Figure 5.9 Velocity vector plots for the 5 MPa case with the line along which the volumetric flow rate is measured

Table 5.4 Volumetric flow rate inside the recirculation zone for all pressures

Operating Pressure (MPa)	Volumetric flow rate (m^3s^{-1})
1.5	0.0008763573
3	0.001117239
4.5	0.00125039
5	0.001286085

Table 5.4 shows the volume of argon flowing towards the melt nozzle for all pressures. It can be seen from the table that the volume of gas flowing towards the melt nozzle i.e. entering the recirculation zone increases with increasing operating pressure. It should also be noted that the increase in the volume of the argon entering the recirculation zone is not linear. The ratio of the operating pressures is 1:2:3:3.33 but the ratio of the gas volumes in the recirculation zone is 1:1.27:1.43:1.47. The volume gradient of the recirculating gas decreases as the operating pressure increases.

5.2.3 Particle Trajectories

As discussed in section 5.2.1, two open wake cases and two closed wake cases are considered in this study. The trajectories of the particles for 50 milliseconds of flow time are discussed here.

CASE 1: 1.5 MPa

The first case considered in this study is 1.5 MPa operating pressure. This case had a GMR of 1.602 and is an open wake. Figure 5.10 shows the flow field at 0 millisecond. The gas jets exiting the gas die travel towards the outlet through a series of Prandtl Meyer expansion waves.

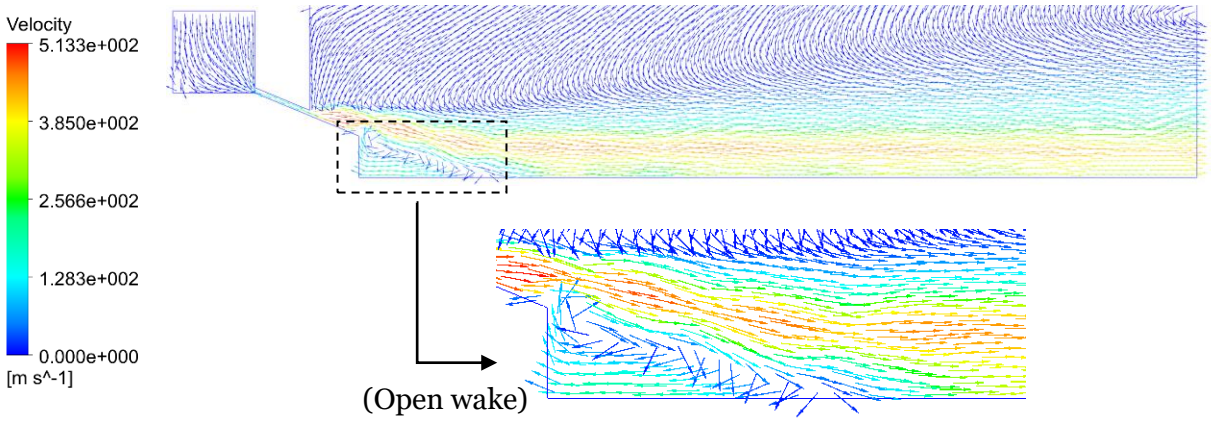

Figure 5.10 Velocity vector plots and particle trajectories for flow time t= 0 ms

Flow time 0.1-10 milliseconds

The particles are released into the recirculation zone due to the absence of melt delivery tube. Figure 5.11 shows the particle trajectories at flow time t=0.1 ms. It can be observed that the particles move against the flow direction of recirculating gases.

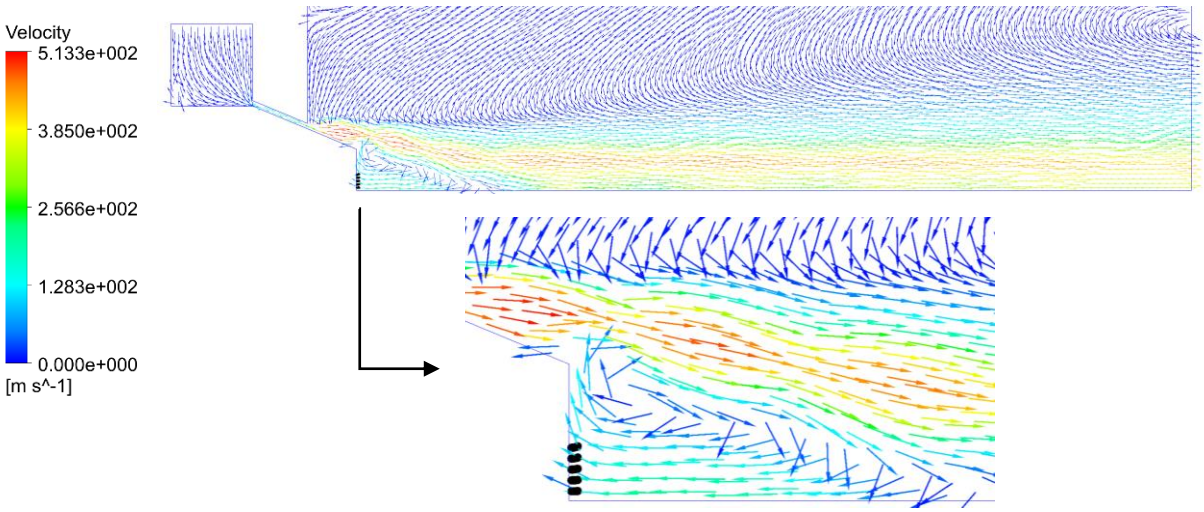

Figure 5.11 Velocity vector plots and particle trajectories for flow time t= 0.1 ms

Figure 5.12 shows the particle trajectories for the flow time t= 0.5 ms. The particles move against the recirculating gases by expending their energy by virtue of velocity. The particles reach a state of zero-velocity as they expend their energy completely and the recirculating gases force the particles to change their flow direction. It can be seen in the Figure 5.12 that the particles are beginning to change their flow direction.

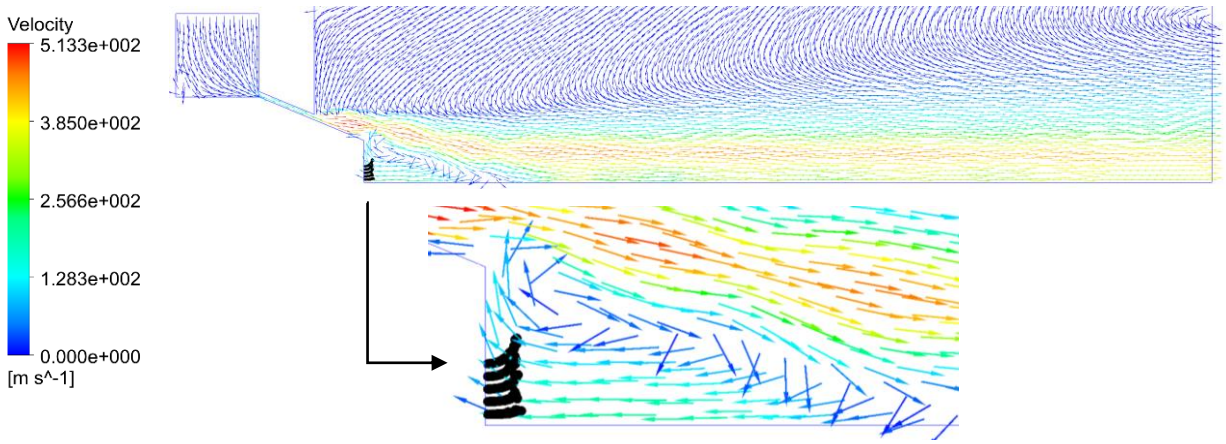

Figure 5.12 Velocity vector plots and particle trajectories for flow time t= 0.5 ms

Figure 5.13 shows the particle trajectories for the flow time t=1ms. It can be observed that the particles move towards the melt nozzle edges along with the recirculating gases.

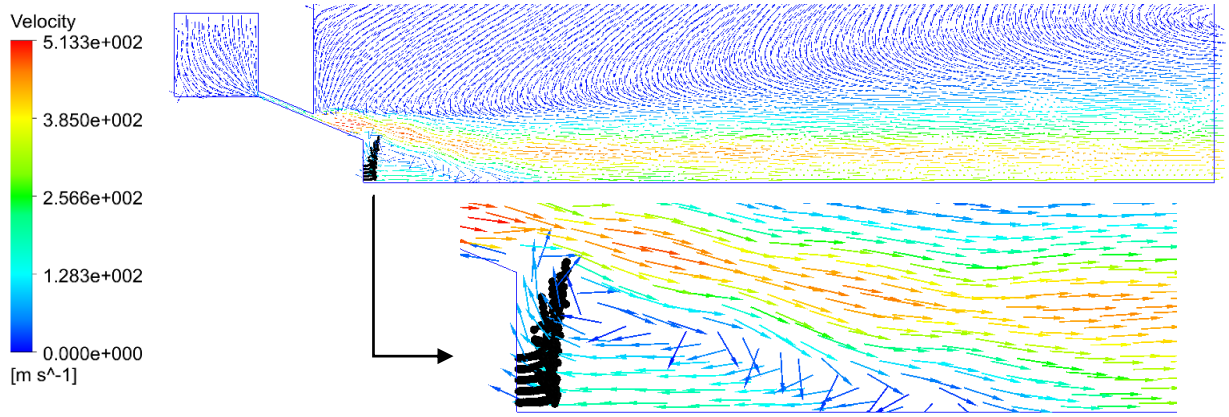

Figure 5.13 Velocity vector plots and particle trajectories for flow time t= 1 ms

Figure 5.14 shows the particle trajectories for flow time t=1.5 ms. The particles flowing towards the melt delivery nozzle and flow across the nozzle surface to reach the high-speed gas jets. As a system of five injection is utilized in this model, particles from each injection enter the high-speed gas jets in different ways. The numbering of the injections has been shown in Figure 5.3. The particles released by the injection closest to the axis (injection I) reach the melt nozzle

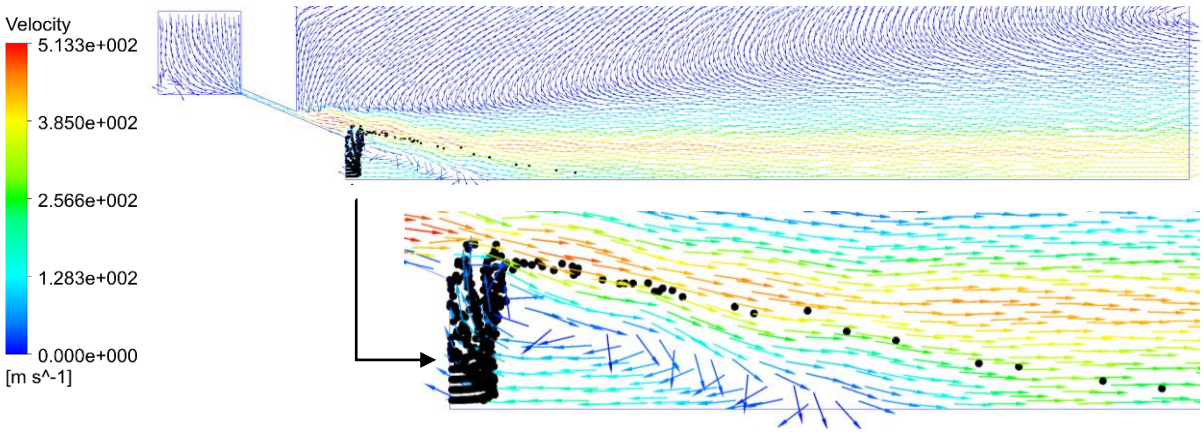

Figure 5.14 Velocity vector plots and particle trajectories for flow time t= 1.5 ms

surface and bounce off to join the high-speed gas jets just after the oblique shock wave. The particles released by the injection-II also reach the melt nozzle surface and travel across it to enter the high-speed expanding jets.

On the other hand, the particles from the other three injection enter the high-speed gas jets without reaching the melt delivery nozzle. The particles released by injection-III travel directly towards the first oblique shock and join the expanding gas jets just before the oblique shock. The particles released by the injection-IV join the expanding gas jets at the oblique shock and the particles released by injection-V join the flow just after the oblique shock. The particles continue to flow along the boundary of the recirculation zone.

Figure 5.15 shows the particle trajectories for the flow time t=2ms. The gas jets undergo compression across the oblique shock and expand after the shock. The particles joining the gas jets before the shock wave also undergo an accumulation across the oblique shock and the trajectories begin diverging after the shock along with the expanding gas jets. The particles

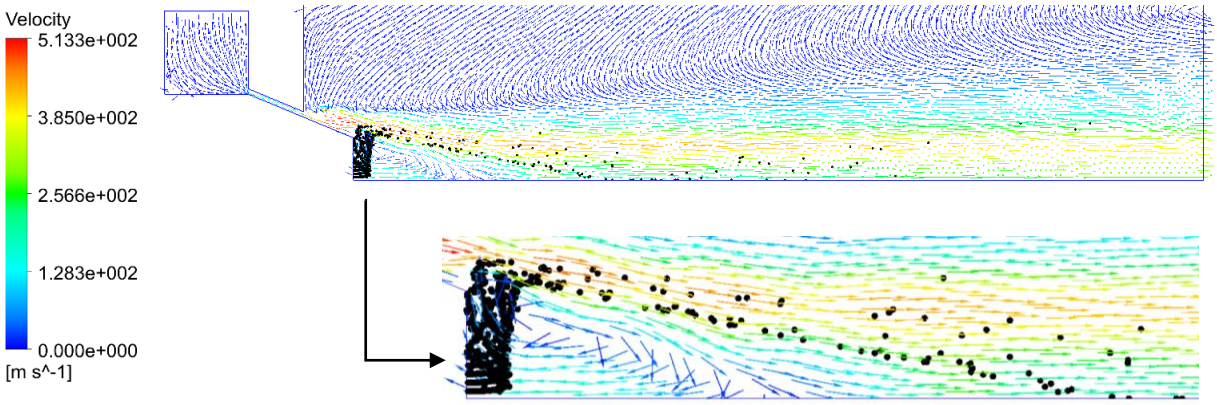

Figure 5.15 Velocity vector plots and particle trajectories for flow time t= 2 ms

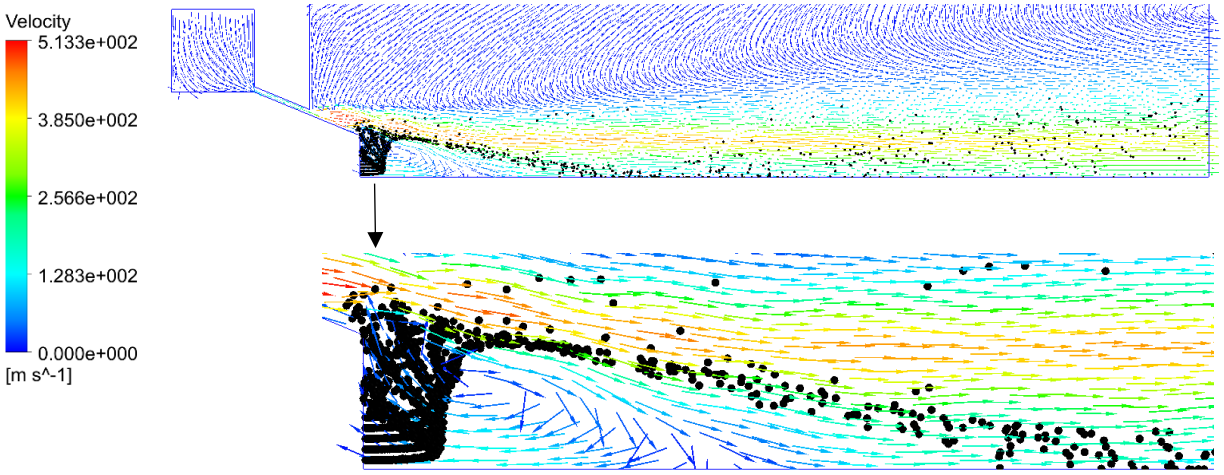

Flow time t = 5 ms

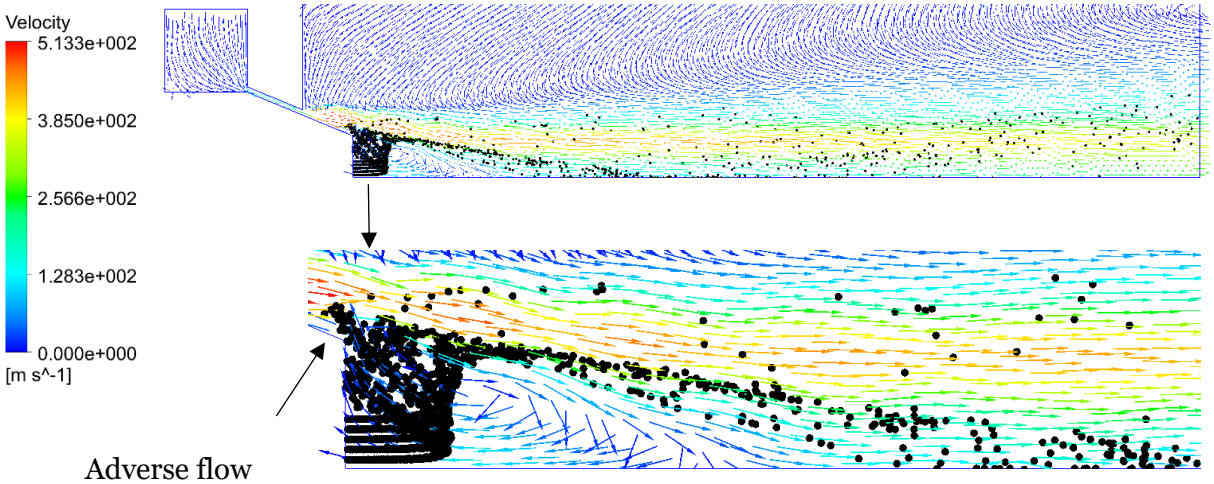

Adverse flow pocket (lick-back)

Flow time t = 8 ms

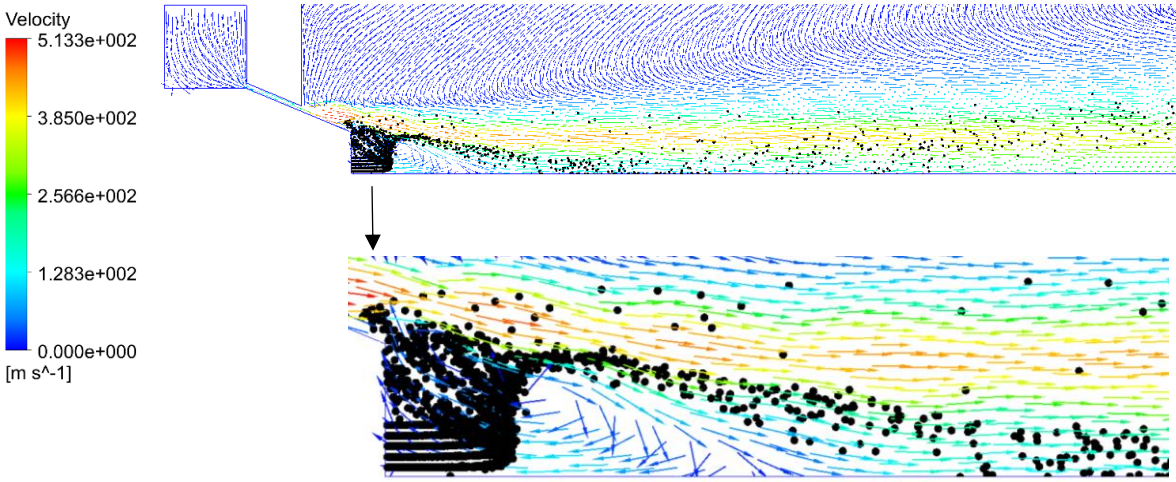

Flow time t = 10 ms

Figure 5.16 Velocity vector plots and particle trajectories at various flow times t= 5ms, 8ms 10ms

entering the gas jets after the first oblique shock begin moving along the boundary of the recirculation zone with the expanding gas jets reach the axis. On reaching the axis, the particle trajectories begin diverging as they bounce on reaching the axis.

Figure 5.16 shows the particle trajectories for flow times t=5, t=8 and t=10 ms. The nozzle design considered for this study produces a pocket of separated flow along the melt nozzle surface for pressures lesser than 3MPa. It can be observed from the Figure 5.16 that the particles are sucked into this pocket of separated flow and those particles join the high-speed gas jets before the oblique shock wave. The trajectories of these particles begin spreading along with the gases.

The particles that join the gas jets after the oblique shock begin moving along the boundary of the recirculation zone. As the gases begin expanding, the particle trajectories also begin scattering along the layers of gases nearer to the axis. It can be seen from the Figure 5.16 that this diverging causes a thickening of the spread of the particle trajectories.

As seen in Figure 5.7, the particle mass concentration increases steadily through 10 milliseconds indicating that the mass of dispersed phase entering the recirculation zone is higher than the mass of the dispersed phase exiting the recirculation zones to enter the high-speed gas jets. As the flow time increases, the particles travel further downstream before reaching the zero-velocity state increasing the mass of dispersed phase in the recirculation zone.

The particles on reaching the axis boundary bounce off and travel towards the outlet. It can be observed from the Figure 5.16 that the spread of the particle trajectories begins moving away from the axis as they approach the outlet with increasing flow time. As this is an axisymmetric model, the particles bounce off from axis but in physical reality, the melt droplets continue to flow across the axis and begin travelling in a different plane. Therefore, the particles that moves towards the axis in this model bounces off as the particle from a different plane.

Flow time 11-20 milliseconds

Figure 5.17 shows the particle trajectories for flow time t=12 ms and t=15 ms and Figure 5.18 shows the particle trajectories for flow time t= 18 ms and t =20ms

The particle mass concentration increases steadily through 20 milliseconds as seen in the Figure 5.7. It can be seen from the Figure 5.17 and Figure 5.18 that the particles move further downstream before changing the direction. The eye of the recirculation plays an important role in particle movement after changing the direction. The particles from the three injections closer to the axis continue to move further downstream to reach the zero-velocity state and

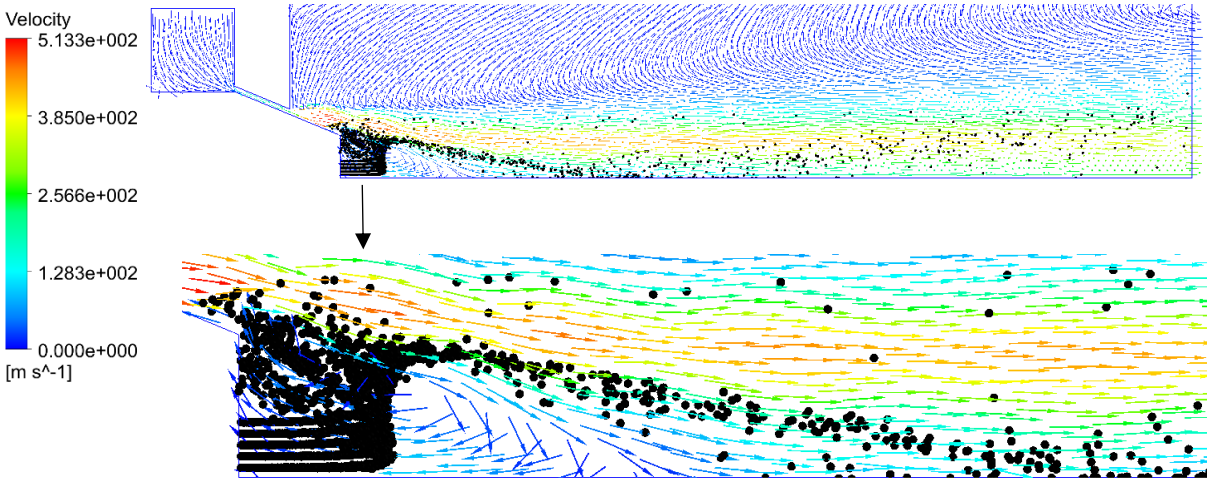

Flow time t = 12 ms

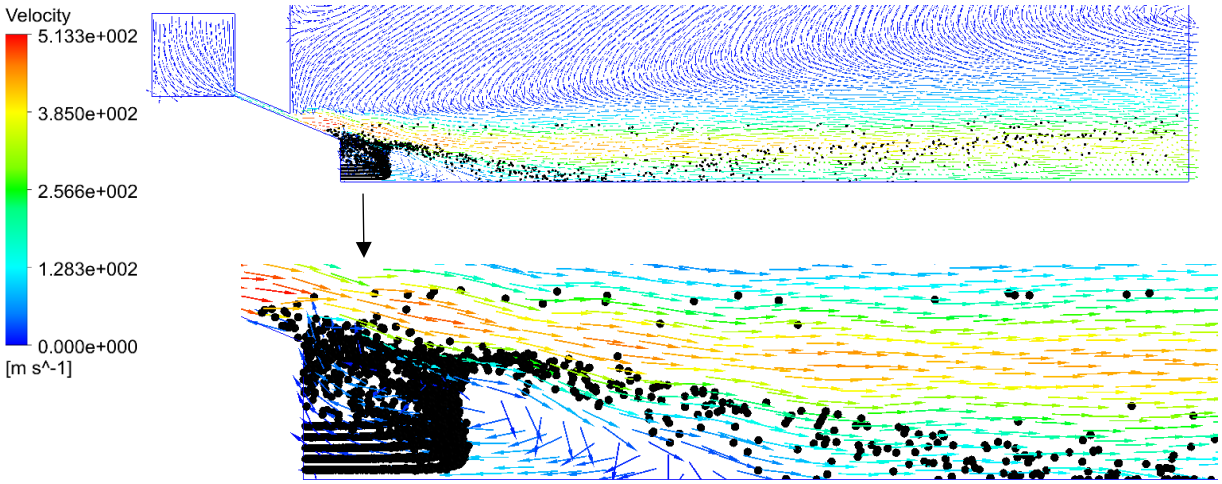

Flow time t = 15 ms

Figure 5.17 Velocity vector plots and particle trajectories at various flow times t= 12 ms and 15 ms

change their jets. Also, few of these particles are drawn into the adverse flow pocket along the melt nozzle surface and start moving along with the gas jets. The gas jets along with the particles begin expanding downstream the first oblique shock and few particle trajectories move along the outer layers of the expanding jets on the near side of wall boundary. These particles flow towards the melt nozzle edge to enter the expanding gas other two injections (farthest from the axis) move downstream to come in contact with the eye of recirculation zone which enables the particles to enter the high-speed gas jets without flowing towards the melt nozzle edge.

As the particle mass concentration increases, the number of particles entering the expanding gas jets also increase. The particles that enter the expanding gas jets without reaching the melt nozzle surface join the expanding gas jets before the second oblique shock wave for all the flow

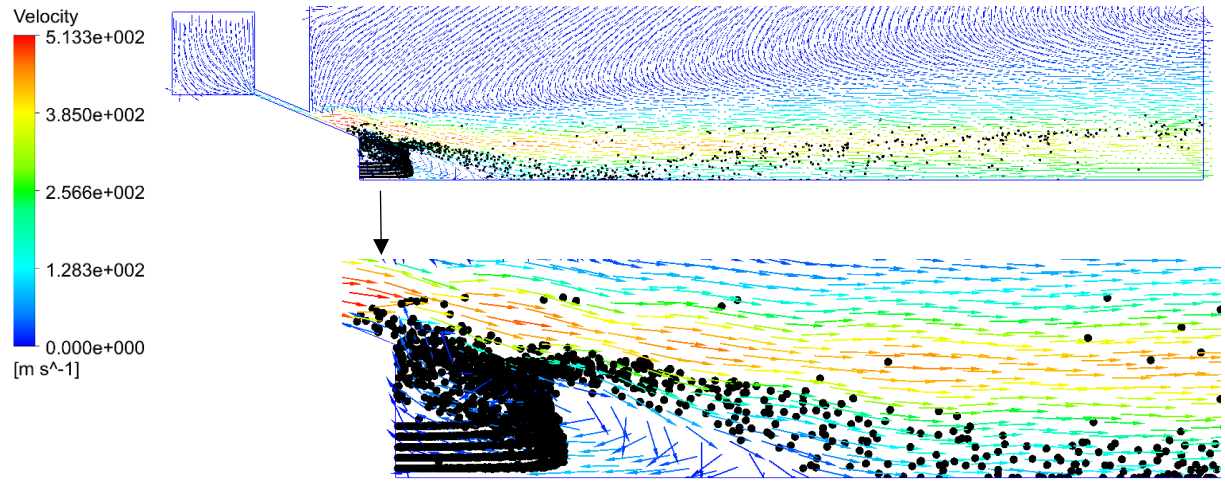

Flow time t = 18 ms

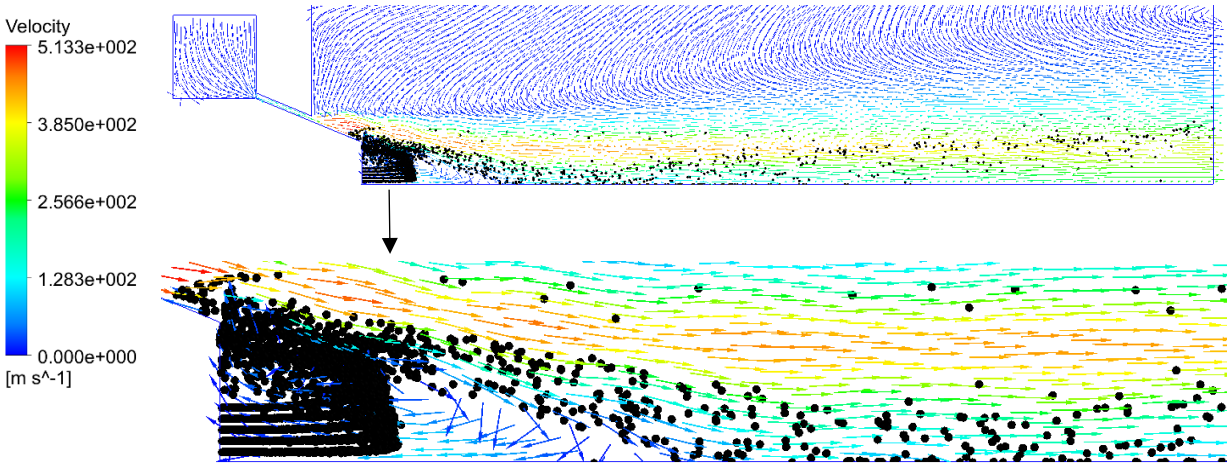

Flow time t = 20 ms

Figure 5.18 Velocity vector plots and particle trajectories at various flow times t= 18 ms and 20 ms

times through 20 milliseconds. As the gases along with the particles come across the oblique shock, gases begin expanding downstream the shock resulting in spreading of particle trajectories.

The particles move along with the expanding gas jets and converge at the stagnation point. The particles continue to move further downstream after bouncing off from the axis boundary. The spread of the particle trajectories moves away from the axis as they move closer to the outlet.

Flow time 21-30 milliseconds

Figure 5.19 and Figure 5.20 shows the particle trajectories and velocity vector plots for flow times t=22 ms, 25 ms, 28 ms and 30 ms. It can be observed from the Figure 5.7 that the particle mass concentration steadily increases through 30 milliseconds which indicates that the difference between the mass of the dispersed phase entering and exiting the recirculation zone

is increasing. The particles from the three injection closest to the axis (Injection I, II, III) continue to flow against the recirculating gases further downstream before reaching the zero-velocity state. The particles from the other two injection do not move further downstream as much as the former three injections due to the interaction with the eye of the recirculation zone. These particles reach their zero-velocity state on reaching the eye of the recirculation zone and enter the gas jets without reaching the melt nozzle surface. This leads to particles from each injection moving downstream to different lengths before attaining the zero-velocity state and gives rise to a tapered spread of particles in the recirculation zone.

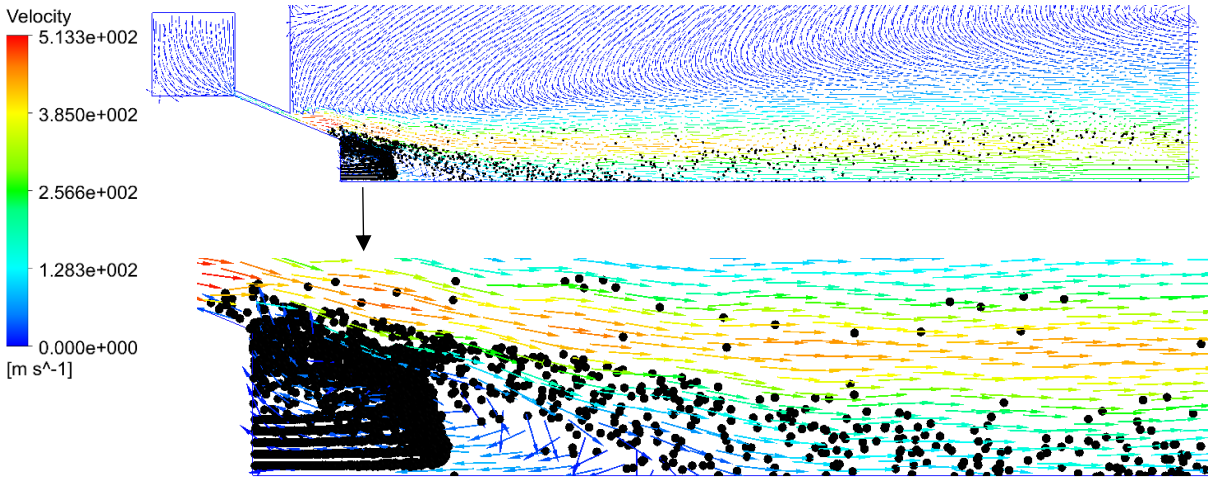

Flow time t = 22 ms

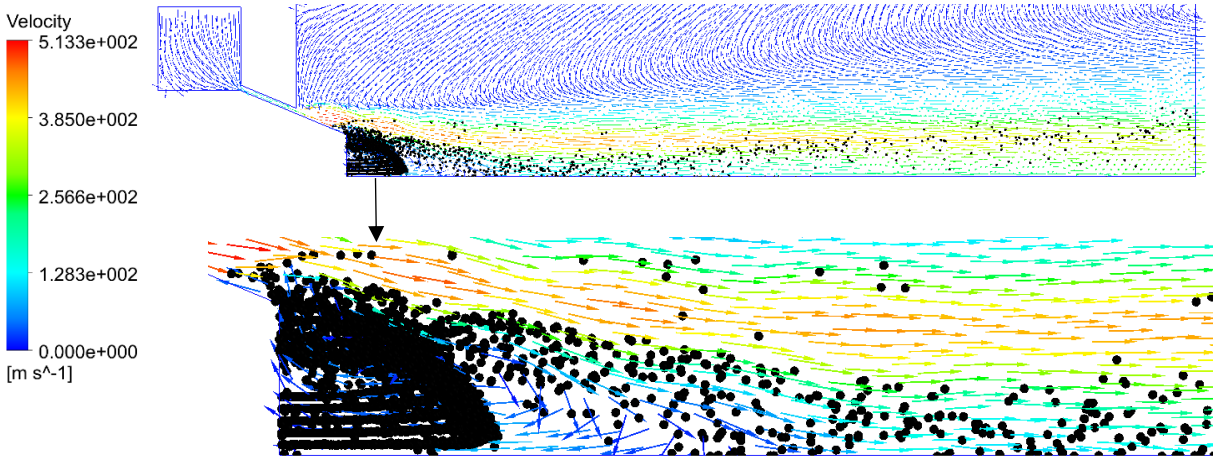

Flow time t = 25 ms

Figure 5.19 Velocity vector plots and particle trajectories for various flow times t =22 ms and t =25 ms

The few of the particles from the group that reaches the melt nozzle surface are drawn into the adverse flow pocket and those particles on crossing the oblique shock wave begin spreading and travel along with the expanding gas jets on the near side of the wall boundary

As the number of the particles exiting the recirculation zone increases, the spread of the particle trajectories along the boundary of the recirculation zone thickens. This thickening of the spread results in particles straying inside the recirculation zone. Also, the particles from the injections I & II continue to move further downstream as the flow time increases. This is observed in Figure 5.19 and Figure 5.20 as the increase in flow distance and number of particles straying into the recirculation zone. As the gases in the recirculation zone flow towards the melt nozzle, they encounter the stray particles first and then the incoming particles. The gases in the recirculation zone loses energy on interaction with these particles and this could enable the incoming particles to overcome the opposing the gases (that already spent the energy before due to the stray particles) and flow further downstream.

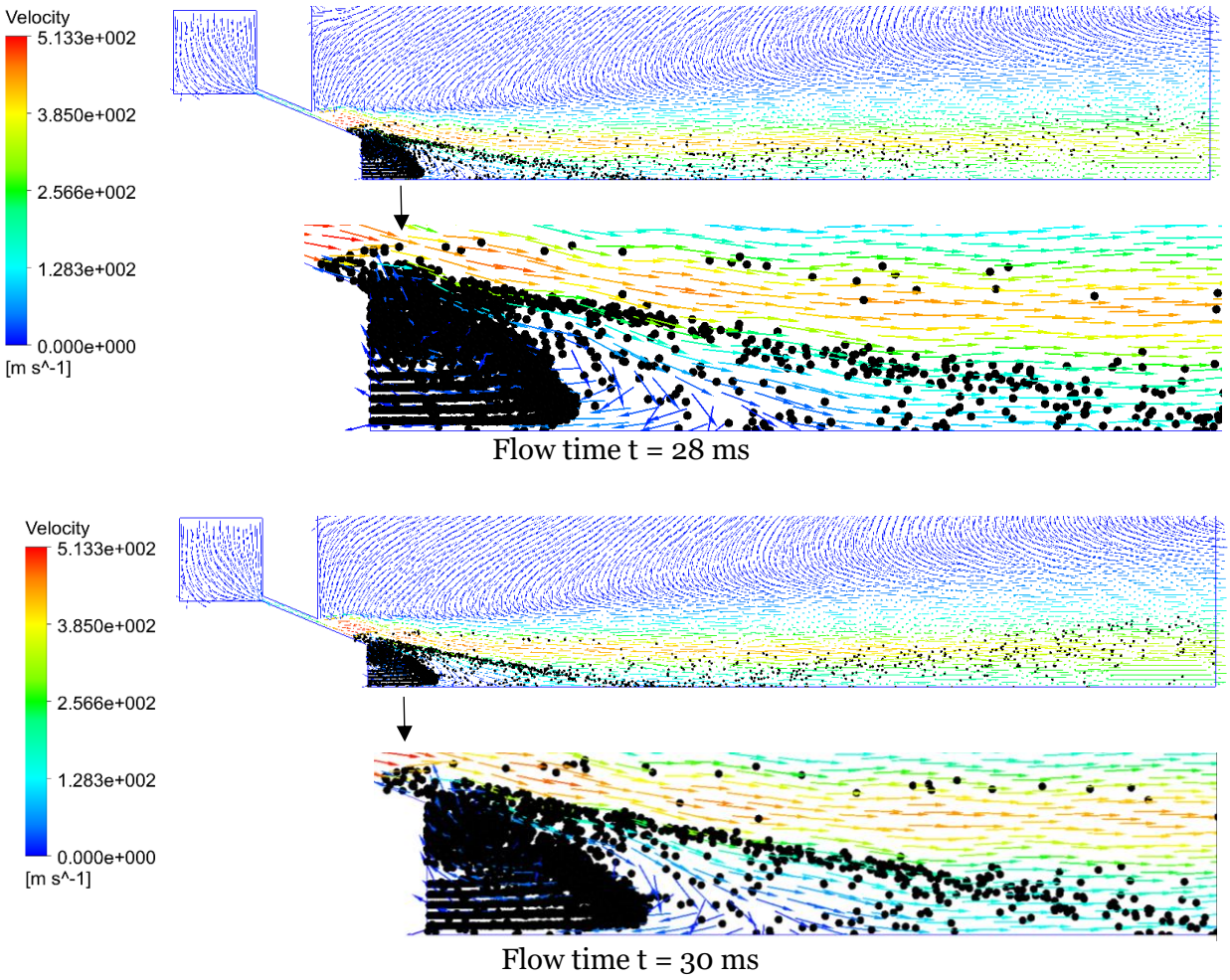

Figure 5.20 Velocity vector plots and particle trajectories for various flow times t=28 ms and t= 30 ms

The particles move along with the expanding gases, converge along the axis, and bounce off from the axis boundary. The spread of the particle trajectories moves away from the axis as they move closer to the outlet.

Flow time 31-40 milliseconds

The particle mass concentration maintains steadily through 40 milliseconds. Figure 5.21 and Figure 5.22 shows the particle trajectories and velocity vector plots for flow times t= 32 ms, 35 ms, 38 ms and 40 ms. As the number of particles stagnating in the recirculation zone saturate it, the number of particles entering the high-speed gas jets increases. This can be seen as the thinning followed by thickening of the spread of particle trajectories. The thinning of the spread is caused due to the increasing number of particles stagnating in the recirculation zone.

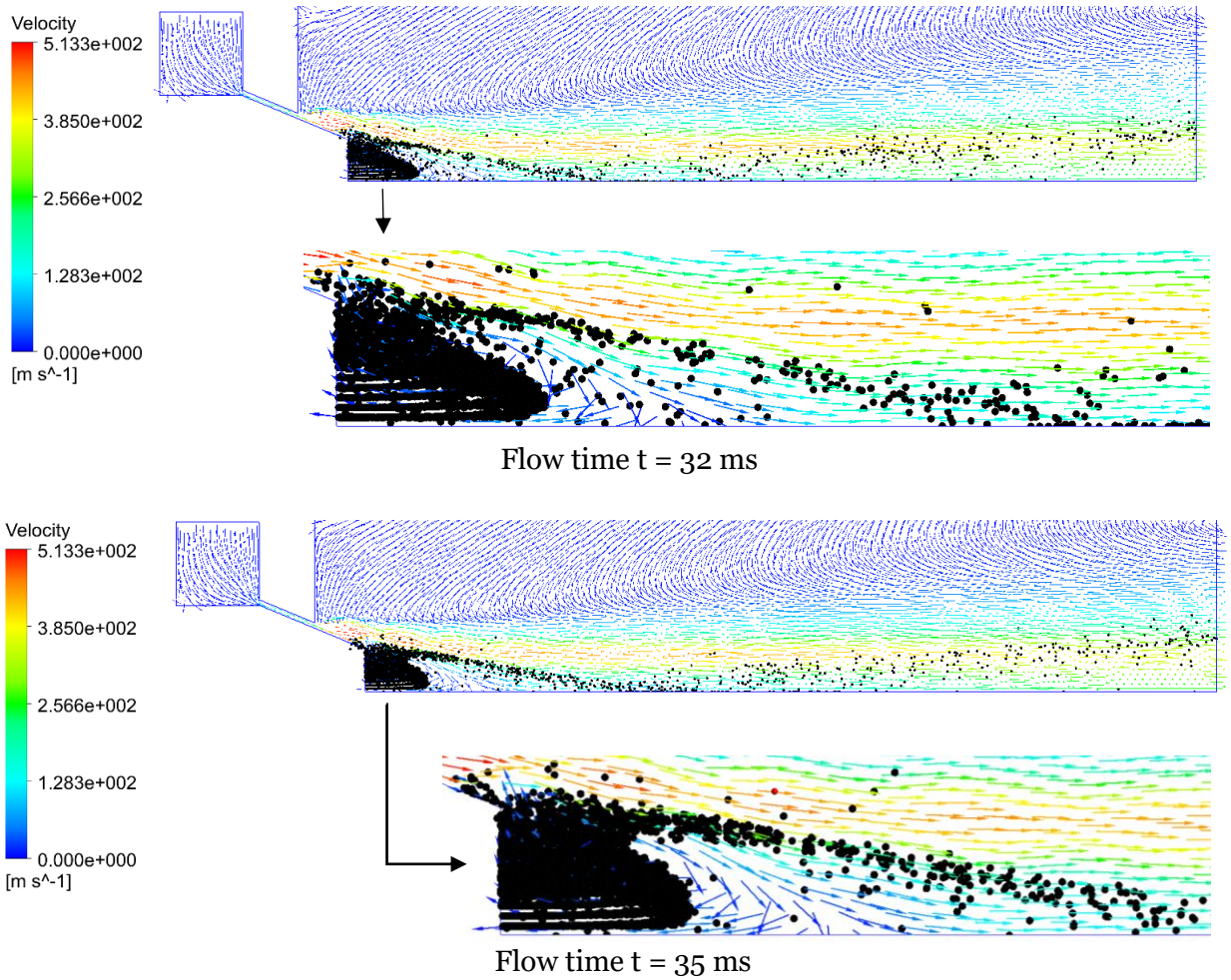

Figure 5.21 Velocity vector plots and particle trajectories for various flow times t=32 ms and t= 35 ms

Another consequence of thinning of the spread is that the number of particles straying into the recirculation zone is reduced. This reduction decreases the interaction between the

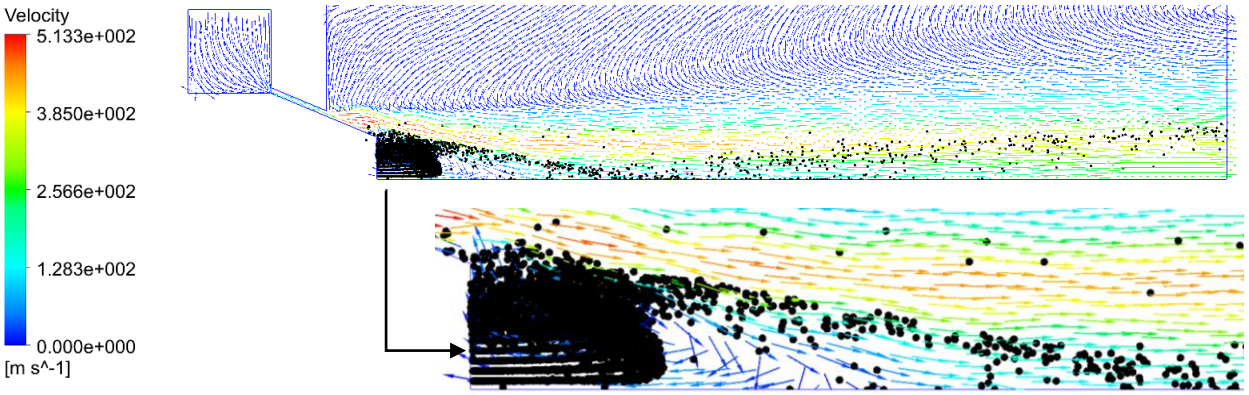

Flow time t = 38 ms

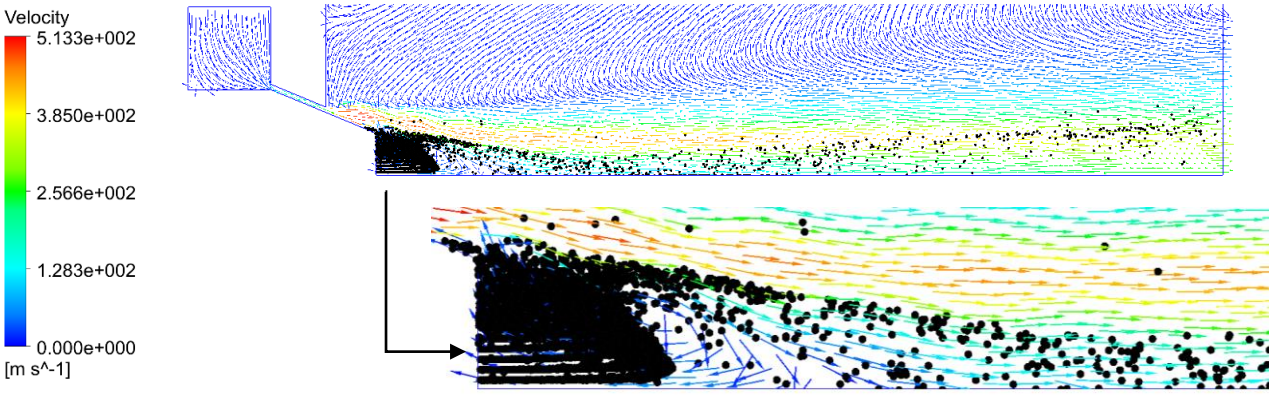

Flow time t = 40 ms

Figure 5.22 Velocity vector plots and particle trajectories for various flow times t=38 ms and t= 40 ms

particles and the recirculating gases and in turn decreases the energy losses the recirculating gases experience before reaching the incoming particles. This decrease in energy loss leads to incoming particles reaching their zero-velocity state sooner. (at a shorter distance) This can be seen in the Figure 5.21 and Figure 5.22 as reduction in the length of the particles moving forward.

As the number of particles stagnating in the recirculation zone increase and saturates, the number of particles entering the high-speed gas jets increase leading to thickening of the spread along the boundary of the recirculation zone.

The particles entering the adverse flow pocket come across the first oblique shock and few of these particles travel along the gases in the outer layer of the expansion waves on the near side of the wall. The particles move along with the expanding gases, converge along the axis and bounce off from the axis boundary. The spread of the particle trajectories moves away from the axis as they move closer to the outlet.

Flow time 41-50 milliseconds

The particle mass concentration increases gradually through 50 milliseconds. The thickening of the spread continues and this in turn leads to particles entering the recirculation zone to move further downstream before reaching the zero-velocity state. As the number of particles stagnating in the recirculation zone increase and saturate it, the spread of particle trajectories along the boundary of the recirculation zone thins. This thinning of the spread enables

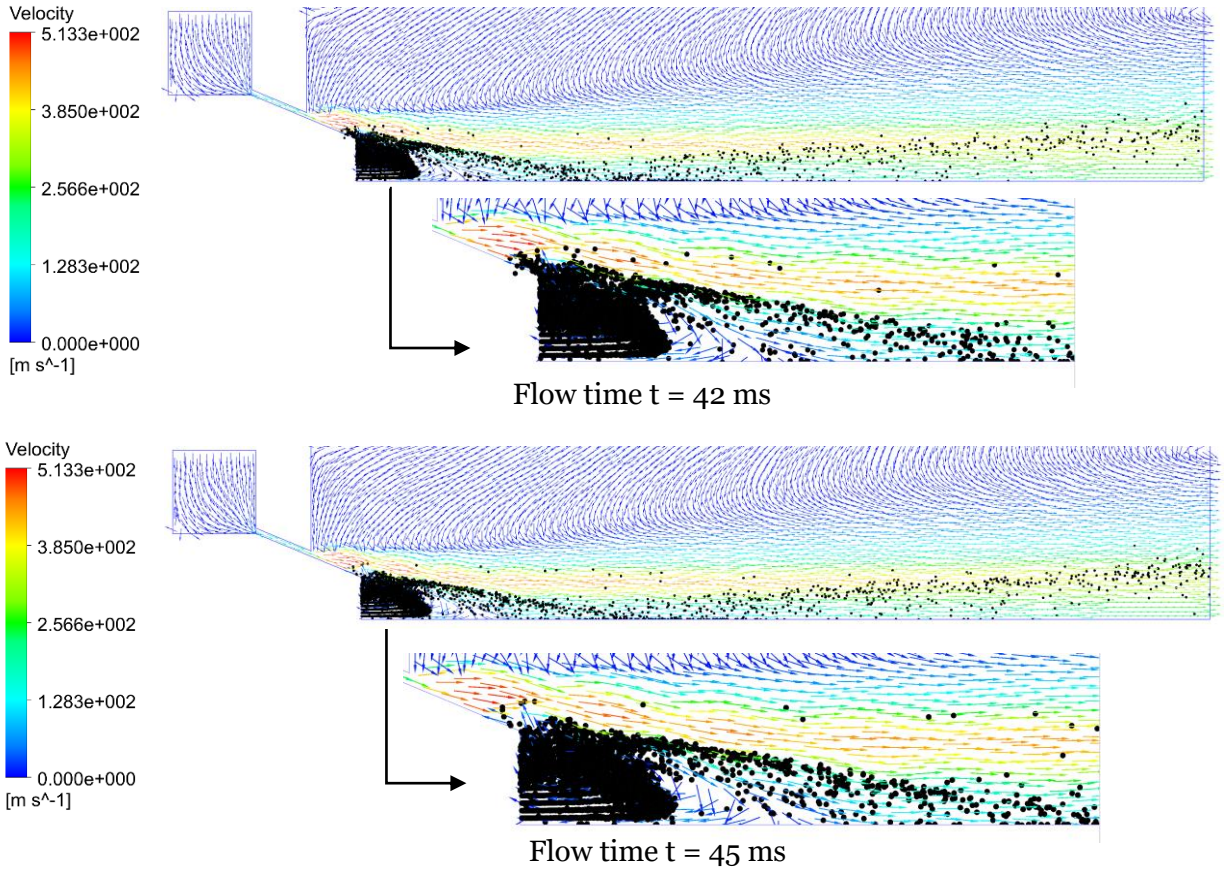

Figure 5.23 Particle trajectories and velocity vectors plots for flow time t= 42 ms and t= 45 ms

particles entering the recirculation zone to reach zero-velocity state sooner. Figure 5.23 and Figure 5.24 shows particle trajectories for flow time t= 42 ms, 45 ms, 48 ms and 50 ms. The particles entering the adverse flow pocket come across the first oblique shock and few of these particles travel along the gases in the outer layer of the expansion waves on the near side of the wall. The particles move along with the expanding gases, converge along the axis and bounce off from the axis boundary. The spread of the particle trajectories moves away from the axis as they move closer to the outlet.

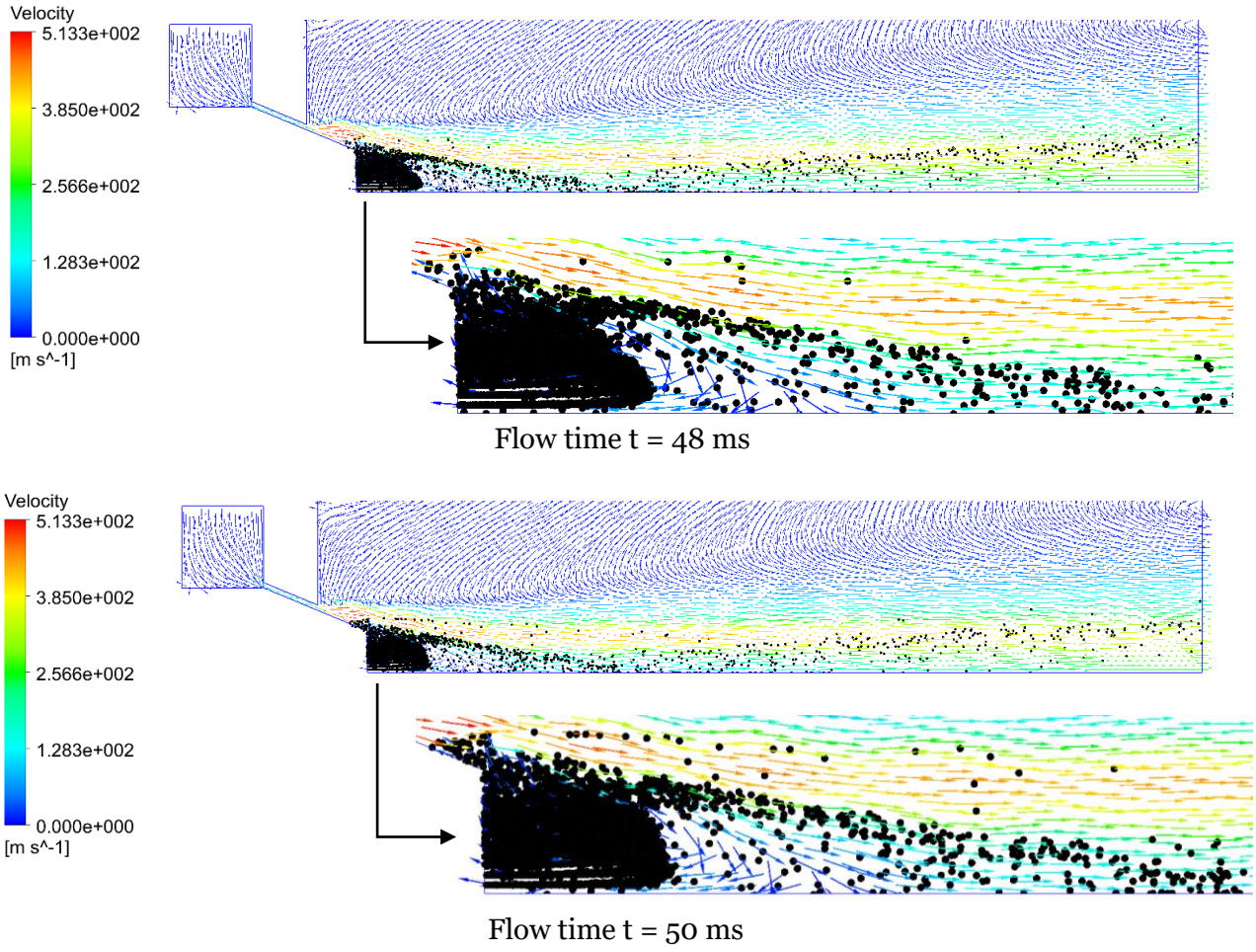

Figure 5.24 particle trajectories and velocity vector plots for flow time t= 48ms and t= 50ms

CASE 2: 3 MPa

The operating pressure 3 MPa produced an open wake. This is the commonly used operating pressure in industry. The particles flowed towards the recirculation zone's eye, reached zero-velocity state and changed their flow direction as observed in 1.5 MPa case. On reaching the nozzle circumference, the particles travelled through the high-speed gas layers towards the outlet. This case has been extensively discussed in the Appendix.

CASE 3: 4.5 MPa

The operating pressure 4.5 MPa produced a closed wake. Figure 5.25 shows the flow field with the closed wake highlighted. The GMR for this case was found to be 0.533.

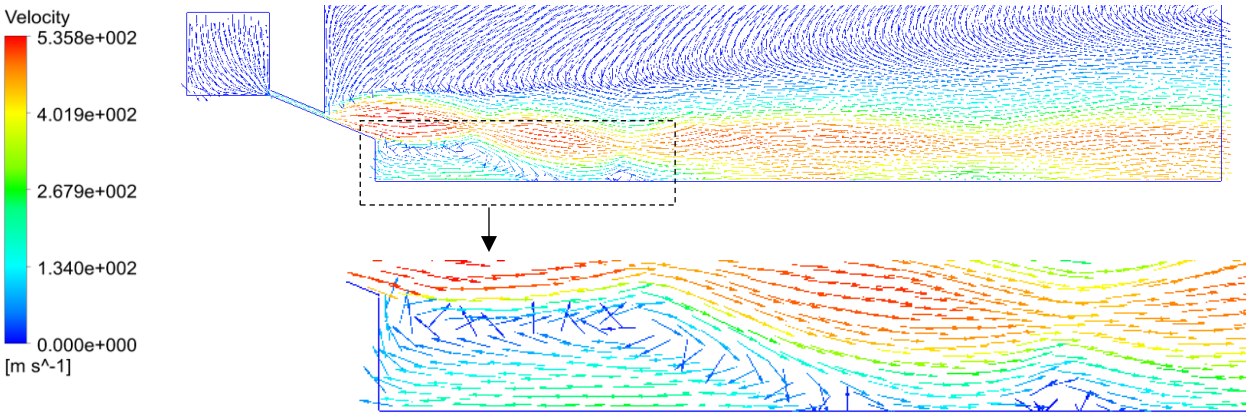

Figure 5.25 Velocity vector plots for flow time t= 0 ms

Flowtime 0.1-10 ms

Figure 5.26 shows the particle trajectories at t=0.1 ms. It can be observed that the particles move against the recirculating gases.

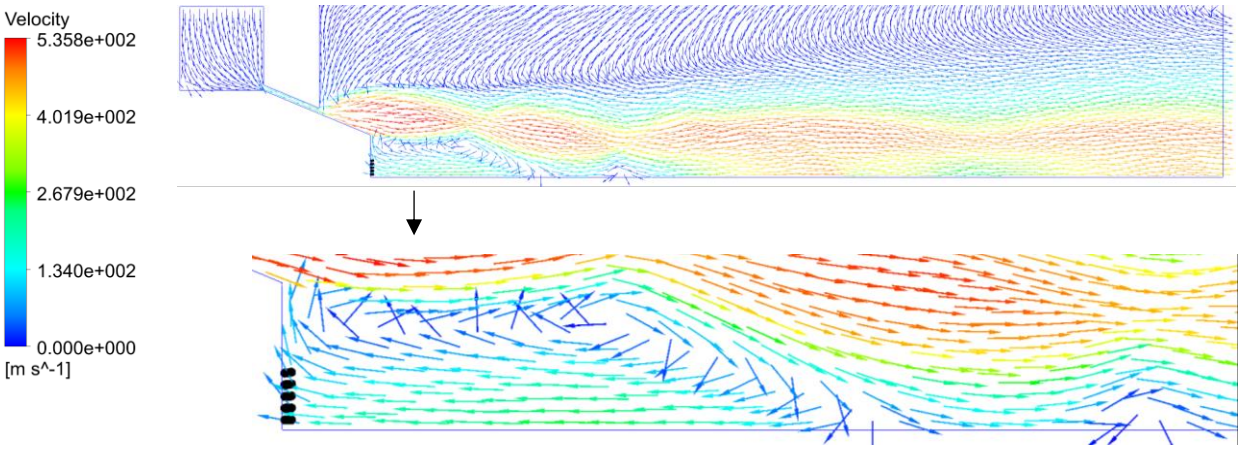

Figure 5.26 Particle trajectories and velocity vector plots for flow

Figure 5.27 shows the particle trajectories at t=0.5 ms. The particles begin changing their flow direction after expending their kinetic energy and flow along with the recirculating gases.

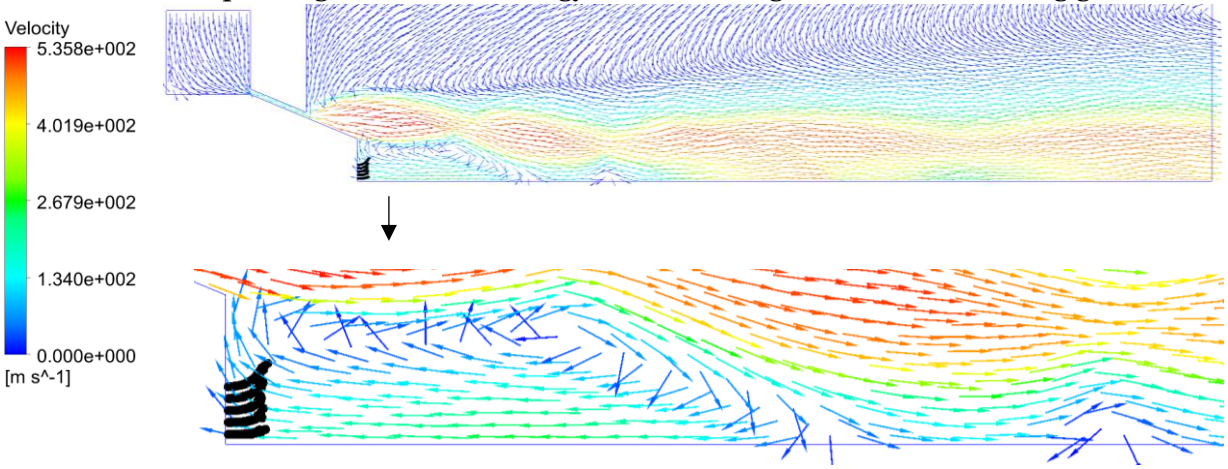

Figure 5.27 Particle trajectories and velocity vector plots for flow time t= 0.5 ms

Figure 5.28 shows the particle trajectories at t= 1 ms. It can be seen from the Figure 5.28 that the particles change their flow direction after reaching the zero-velocity state and begin moving along with the recirculating gases towards the high-speed gas jets. The gas flow rate into the atomizer increases with increasing operating pressure. An increase in the gas flow rate into the atomizing chamber leads to an increase in the gas flow rate into the recirculation zone. As the mass flow rate of dispersed phase into the recirculation zone is constant, this increased gas flow rate into the recirculation zone leads to particles entering the high-speed gas jets before reaching the melt nozzle surface.

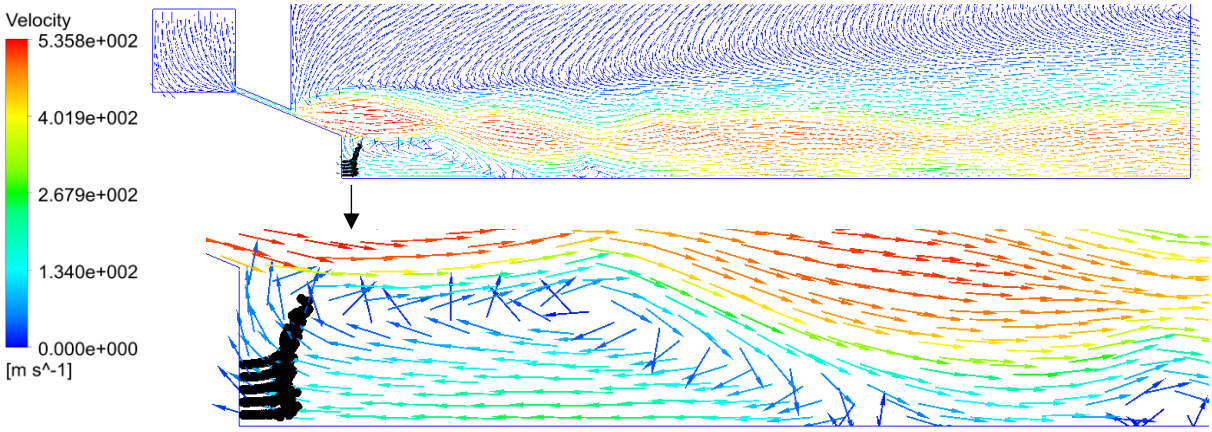

Figure 5.28 Particle trajectories and velocity vector plots for flow time t= 1 ms

It can be seen from the Figure 5.29 that the particles enter the high-speed gas jets before reaching the melt nozzle surface and begin moving along the boundary layer of recirculation zone towards the first oblique shock. Figure 5.29 shows the particle trajectories at t=1.5 ms.

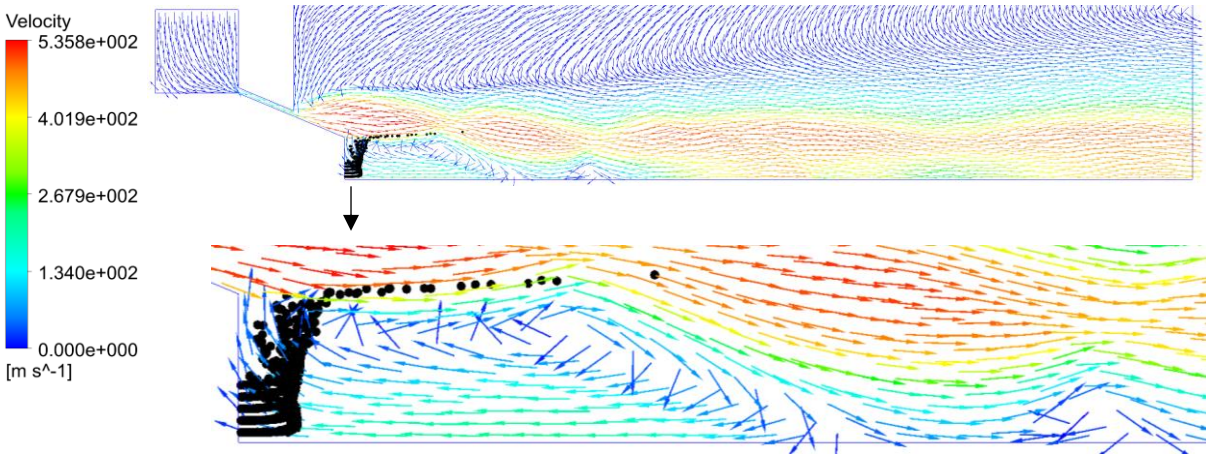

Figure 5.29 Particle trajectories and velocity vector plots for flow time t = 1.5 ms

Figure 5.30 shows the particle trajectories at t=2 ms. The particles exit the domain at 2 milliseconds.

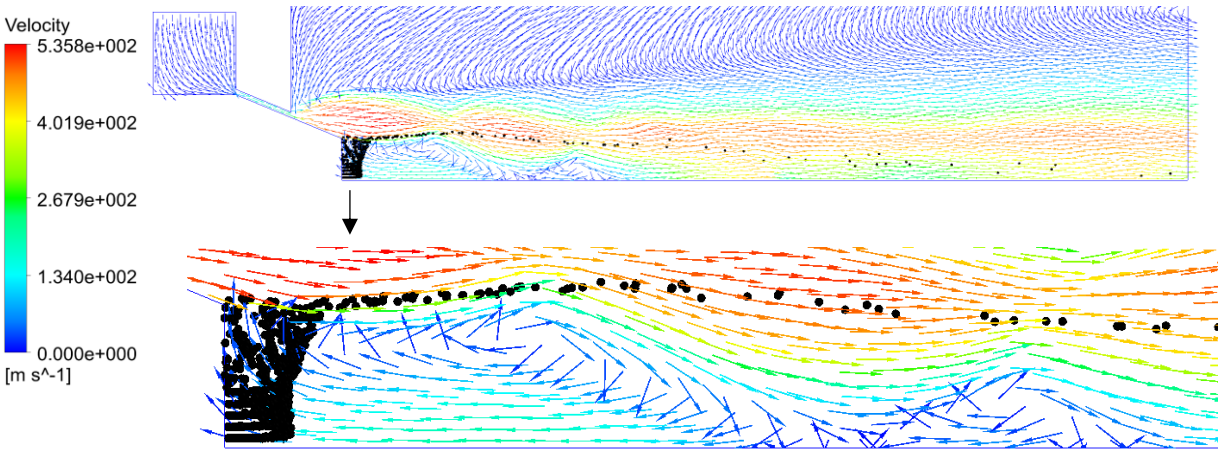

Figure 5.30 Particle trajectories and velocity vector plots for flow time t = 2 ms

The particle mass concentration increases as the particles can flow further downstream before reaching the zero-velocity state. The particles flow along with the recirculating gases towards the melt nozzle surface to enter the high-speed gas jets. The particles travel along the boundary of recirculation zone in the gas layers with low velocity towards the first oblique shock. The gases along with the particles undergo compression across the shock and begin expanding downstream the shock. The particles begin travelling along the high velocity layers of expanding gas jets downstream the shock towards the outlet.

Figure 5.31 shows the particle trajectories through 10 milliseconds. Particle mass concentration increases steadily through 10 milliseconds. As the flow time increases, the particles move further downstream before reaching the zero-velocity. As seen in Figure 5.7, the particle mass concentration increases steadily through 10 milliseconds and this is due to the particles moving further downstream against the gases. On reaching the zero-velocity state, particles begin moving towards the high-speed gas jets. A group of particles enter the expanding gases without reaching the melt nozzle surface. The rest of the particles move towards the melt nozzle edge and join the high-speed gas jets.

The particles travel along the boundary of the recirculation zone towards the first oblique shock. It can be seen from the Figure 5.31 that as the number of particles entering the expanding gas jets increase, few particles enter the outer layer of the recirculation zone.

The compressed gases on interaction with the oblique shock undergo expansion downstream of it. The spread of the trajectories of the particles carried by these gases will also increase. It can be seen in the Figure 5.31 that the spread of the particle trajectories thickens with increasing flow time. The particles travel towards the outlet through a series of expansion waves and oblique shocks. The strength of the shock decreases with increasing distance from

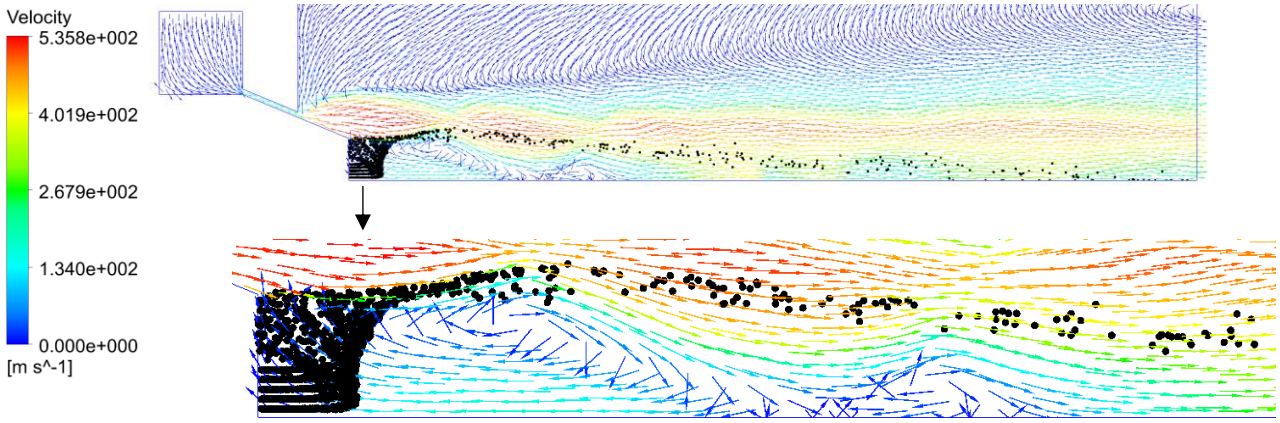

Flow time t = 5 ms

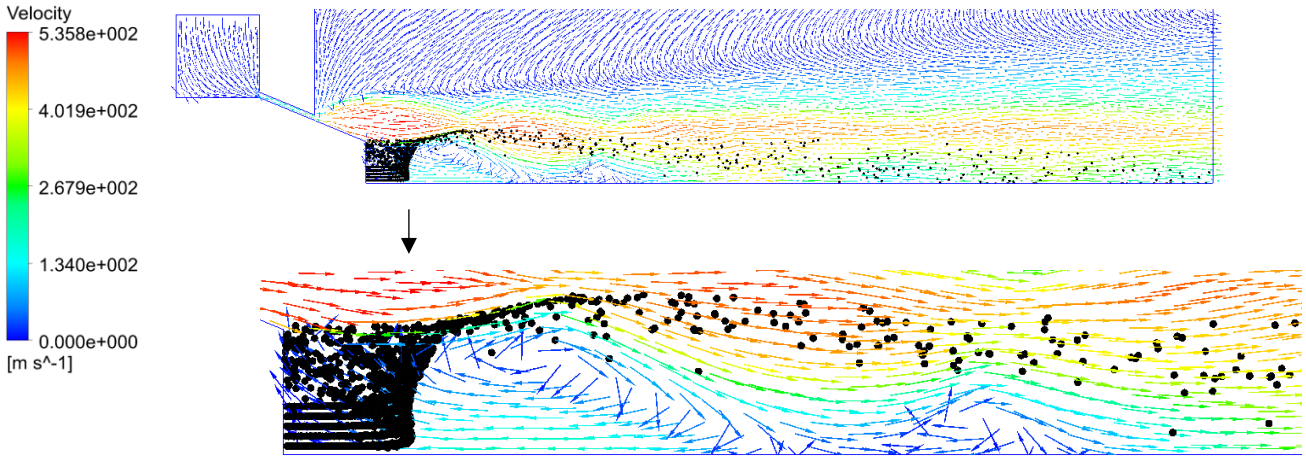

Flow time t = 8 ms

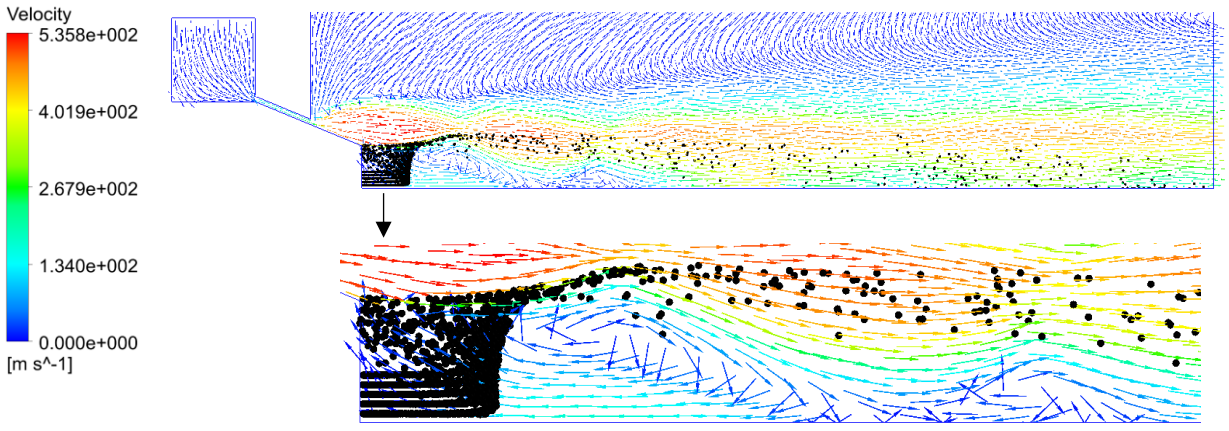

Flow time t = 10 ms

Figure 5.31 Particle trajectories and velocity vector plots for flow time t = 5ms, t = 8 ms and t =10 ms

the melt nozzle. Due to this, the particle trajectories begin spreading as they move towards the outlet. The particles on crossing the first oblique shock move towards the second oblique shock. As this is a closed wake case, a second recirculation zone is formed downstream the first recirculation zone. The spread of the particle trajectories begins increasing after the

second oblique shock. On crossing the second oblique shock, the particle trajectories converge along the axis. The particle trajectories begin converging along the axis further away from the outlet with increasing flow time. A small group of particles travelling along the outer layers of second recirculation zone (downstream the closed wake) enter it, recirculate and join the expanding gas jets along with the other particle trajectories.

Flowtime: 11-20 milliseconds

Figure 5.32 and Figure 5.33 show the particle trajectories for flow times between 11ms to 20 ms. The particles move further downstream inside the recirculation zone before reaching the zero-velocity state. The particles begin flowing towards melt nozzle edge along with the recirculating gases. As discussed previously, a group of particles enter the expanding gas jets without reaching the melt nozzle surface. The particles continue flowing along the boundary of the recirculation zone in a condensed manner as the gases undergo compression across the oblique shock.

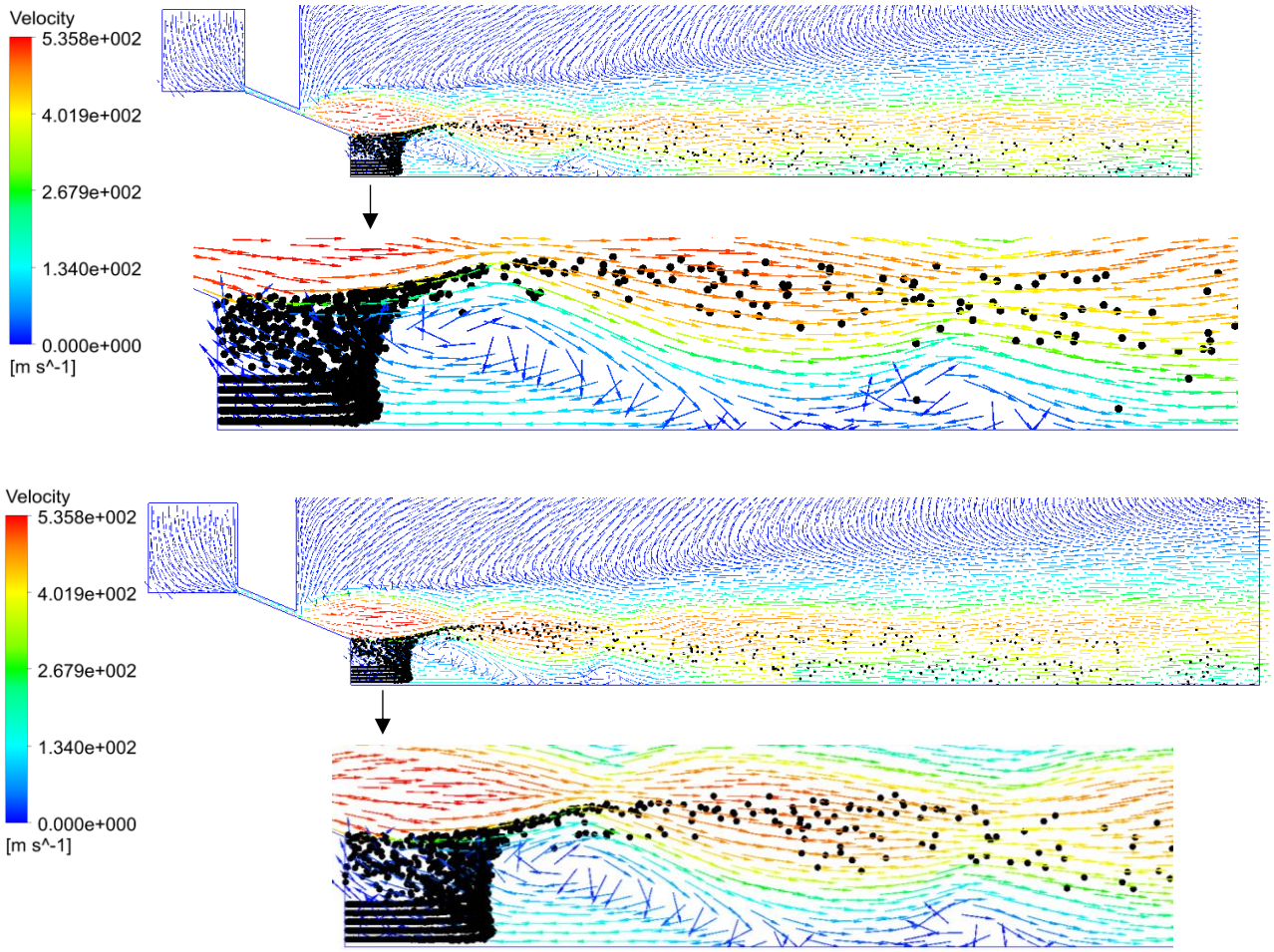

Figure 5.32 Particle trajectories and velocity vector plots for flow time t= 12 ms

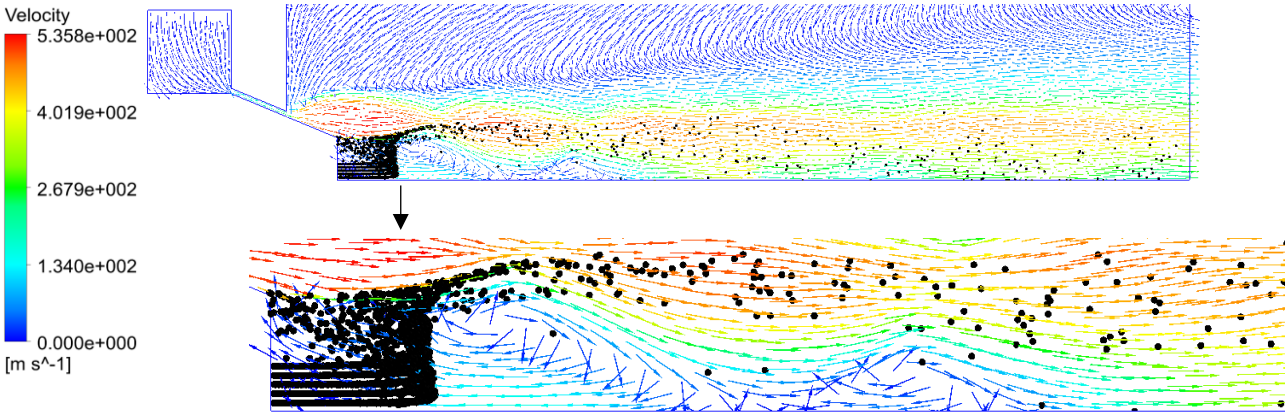

Flow time t = 18 ms

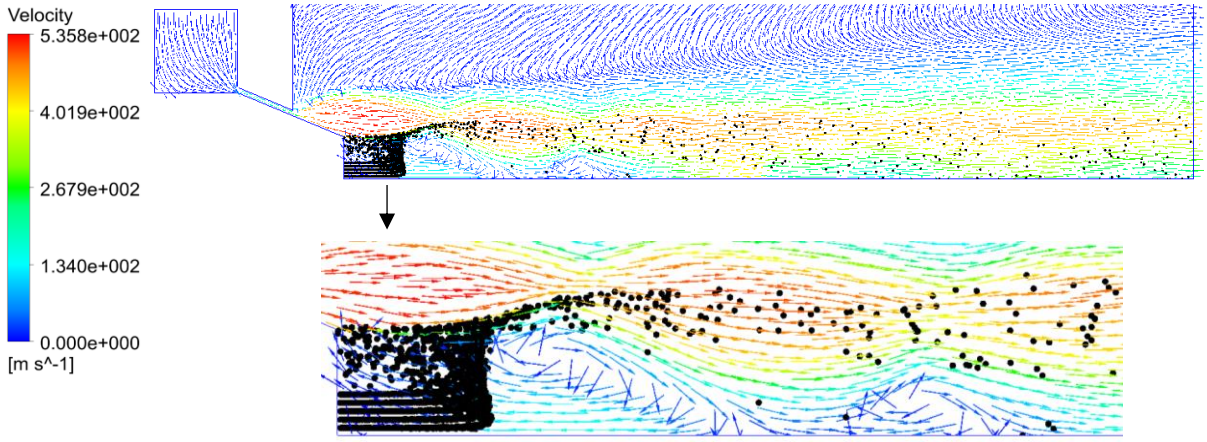

Flow time t = 20 ms

Figure 5.33 Particle trajectories and velocity vector plots for t= 15 ms, t = 18 ms and 20 ms

It can be seen from the Figure 5.33 that few of the particles enter the recirculation zone, recirculate along with the gases and other the expanding gases. The spread of the particle trajectories remains qualitatively same between the two oblique shocks. Few of the particles travelling along the low velocity layers (<150 ms^{-1}**)** travel along the boundary of both the recirculation zones and their trajectories converge along the axis

Flowtime: 21-30 milliseconds

Figure 5.34 and Figure 5.35 shows the particle trajectories for flow time till 30 ms. The particles entering the recirculation zone continue to move further downstream till 25 ms towards the eye of the recirculation zone. The particles do not move further downstream due to presence of the eye of the recirculation zone. As seen from the Figure 5.7, the particle mass concentration increases slightly till 25 ms and becomes constant through 30 ms. This constant particle mass concentration is due to the particles not moving further downstream the eye of the recirculation zone.

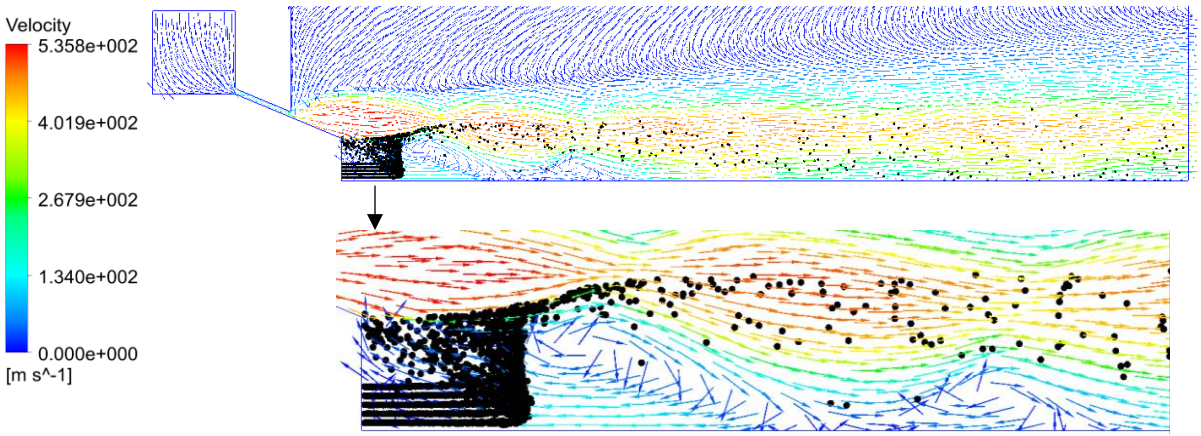

Flow time t = 22 ms

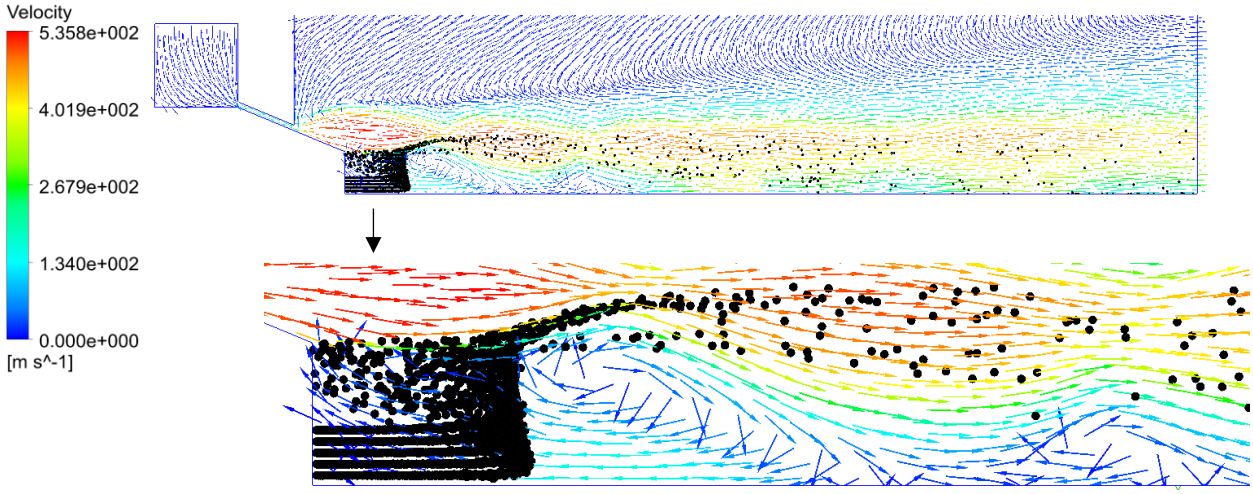

Flow time t = 25 ms

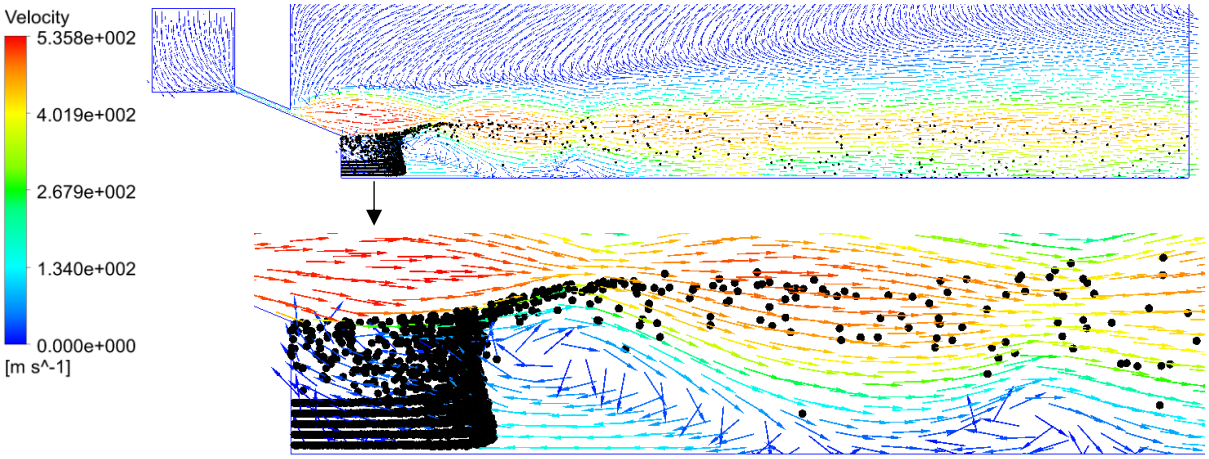

Flow time t = 28 ms

Figure 5.34 particle trajectories and velocity vector plots for t= 22 ms, t=25 ms and t= 28 ms

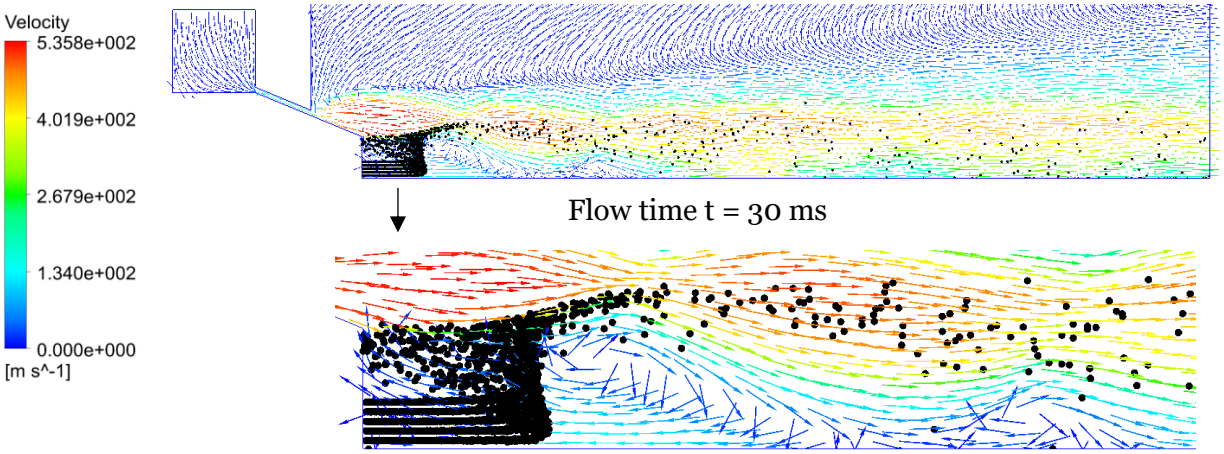

Figure 5.35 Particle trajectories and velocity vector plots for flow time t= 30 ms

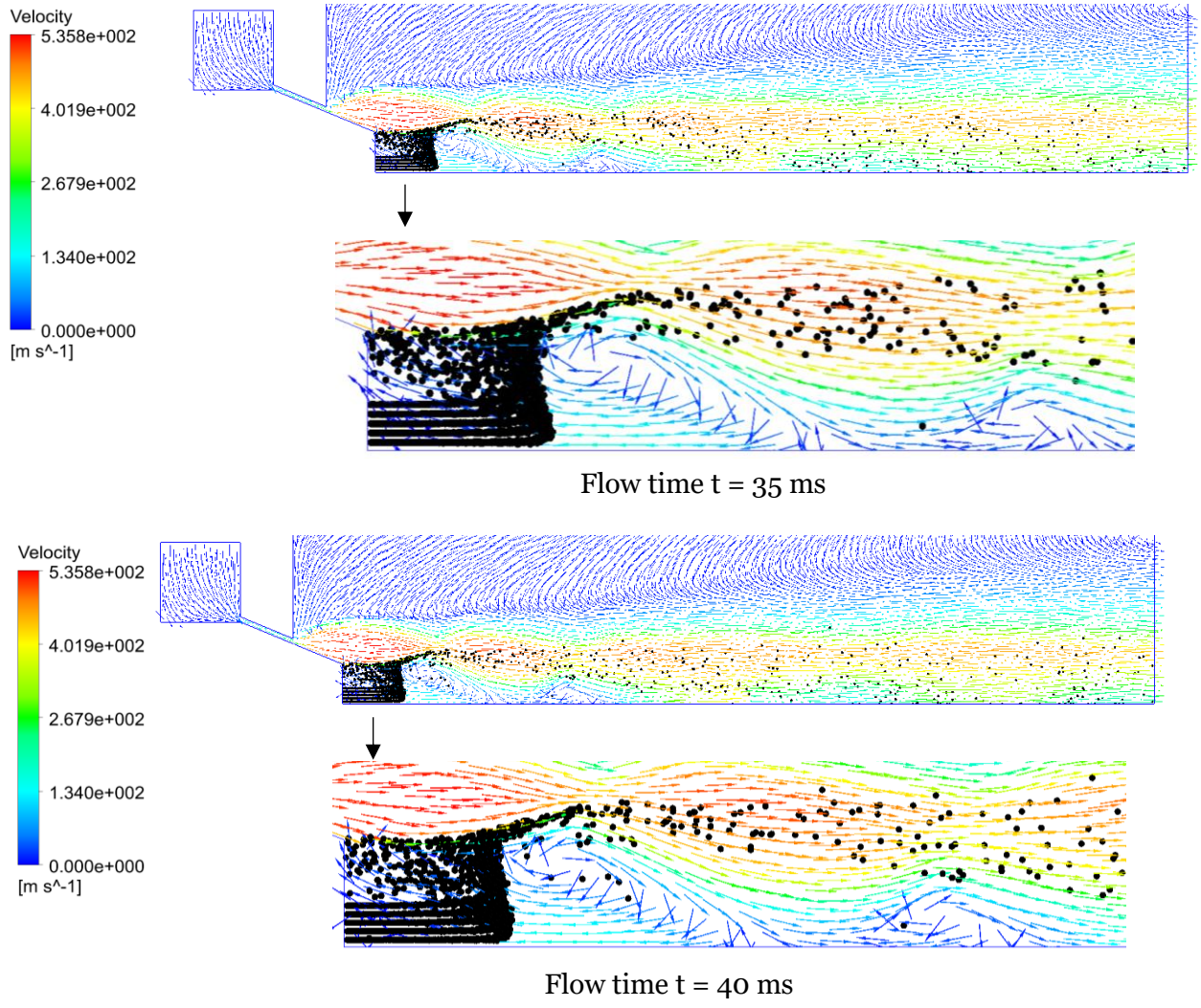

Figure 5.36 Particle trajectories and velocity vector plots for flow time t=35 ms and t=40 ms

Flowtime: 31-40 milliseconds

Figure 5.36 shows the particle trajectories for flow time till 40 ms. The particle mass concentration is constant through 40 ms. The particles entering the recirculation zone move against the gases till the eye of the recirculation zone and flow towards the high-speed gas jets.

Flowtime: 41-50 milliseconds

Figure 5.37 shows the particle trajectories for the flow time till 50 ms. The particle mass concentration is constant through 50 ms. The particles entering the recirculation zone move against the gases till the eye of the recirculation zone and flow towards the high-speed gas jets.

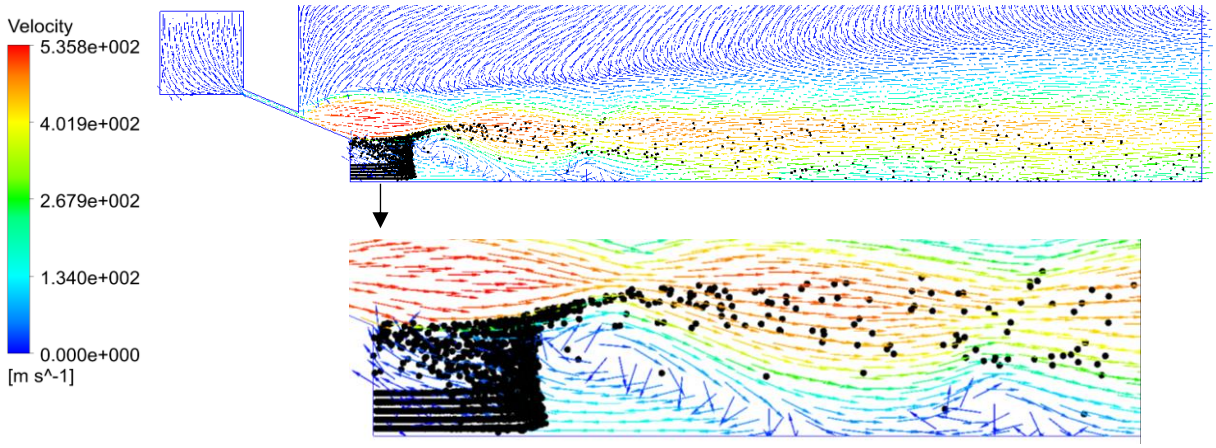

Flow time t = 45 ms

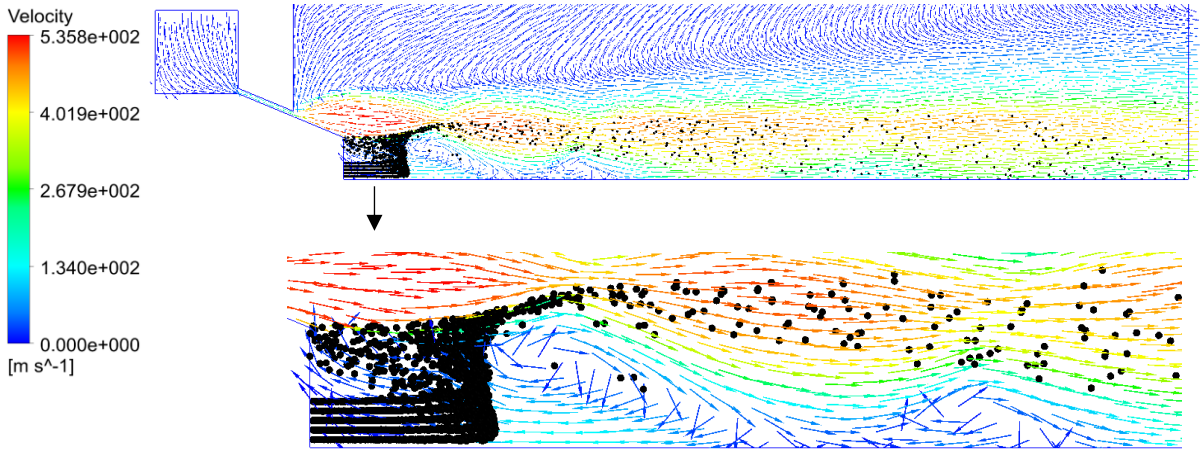

Flow time t = 50 ms

Figure 5.37 Particle trajectories and velocity vector plots for flow time t= 45 ms and t= 50 ms

CASE: 5 MPa

This is a closed wake case. The particles follow the same pattern as the 4.5 MPa case and the results are presented in the appendix.

5.2.4 Changes in flow field

The two-phase study was carried out in a two-way coupled model and therefore the Eulerian gas flow field changes every timestep on interaction with the Lagrangian particles. The particle trajectories were analysed in the section **5.2.3** and the changes in the gas flow field are discussed below.

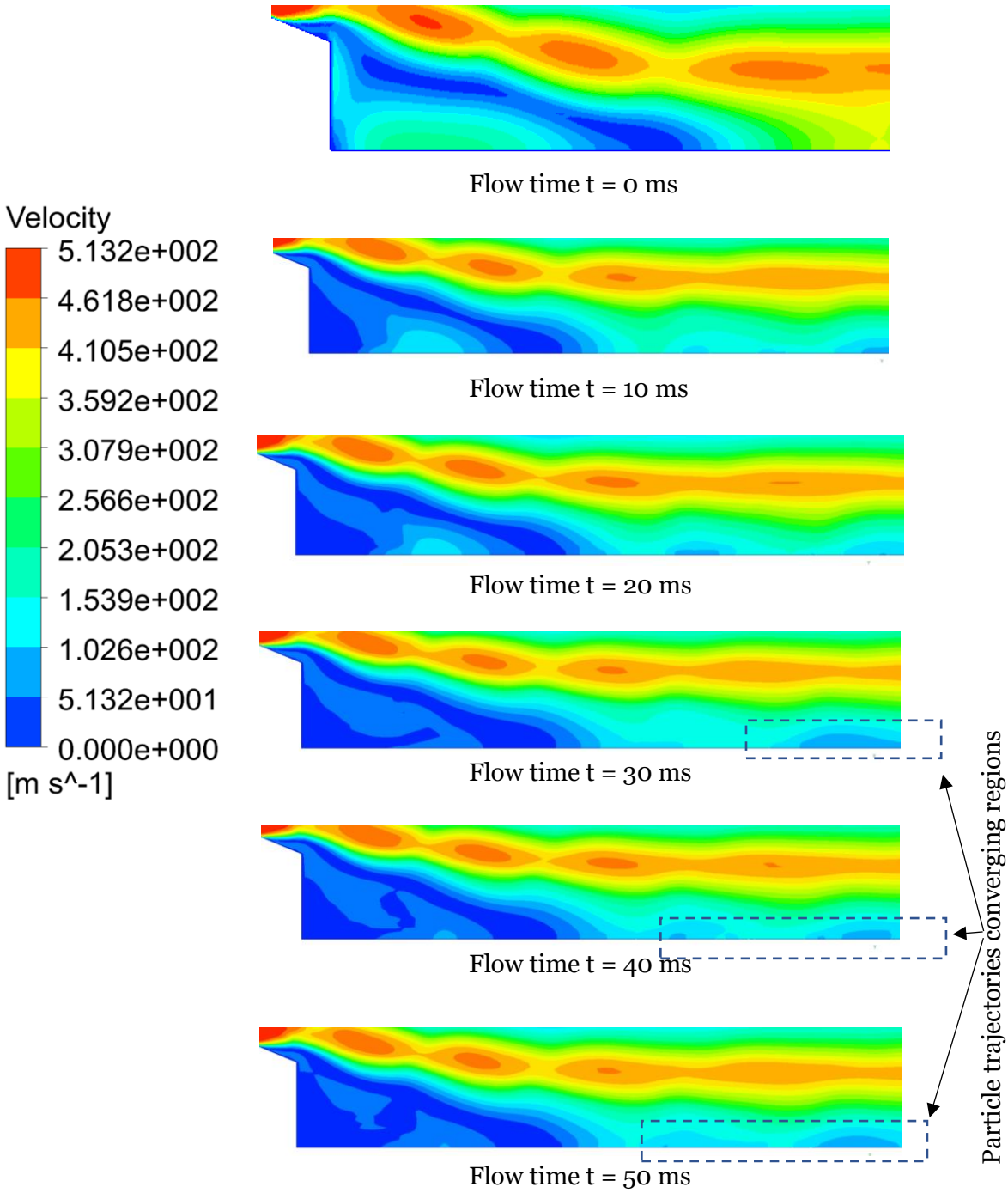

Figure 5.38 Velocity contour plots of the recirculation zone for flow times from t= 0 ms to t= 50 ms for 1.5 MPa operating pressure

CASE 1: 1.5 MPa

The operating pressure 1.5 MPa produced an open wake. The atomizer design considered in this study produced an adverse flow pocket on the melt nozzle surface. Figure 5.38 shows the velocity contour plots of the recirculation zone at various timesteps through 50 milliseconds.

The stagnation point where the expanding gases converge along the axis does not change throughout the 50 milliseconds. At t= 0 ms, the gases in the recirculation zone attain the maximum velocity of about 250 ms^{-1}.

It can be seen from the Figure 5.7 that the particle mass concentration increases throughout 50 milliseconds and this indicates that the recirculating gases are not sufficient to carry the particles to the high-speed gas jets leading to stagnation of particles in recirculation zone. The number of particles stagnating in the recirculation zone increases through 50 milliseconds. This increase in the number of particles stagnating leads to a steady decrease in the maximum velocity attained by the recirculating gases. This can be seen in the Figure 5.7. The particles moving with the high-speed gas jets converge along the axis and this leads to low velocities in the region of converging. This can be seen in the Figure 5.38

CASE 2: 3 MPa

The operating pressure 3 MPa produced an open wake. The particle mass concentration increases till flow time t = 25 ms and becomes a constant till t = 50 ms. The stagnation point does not move through the 50 milliseconds. At t = 0ms, the gases in the recirculation zone attains the maximum velocity of about 260 ms^{-1}. As discussed in the previous case (1.5 MPa), particles reach a zero-velocity state and flow along with the recirculating gases. The Eulerian flow field is shown at various timesteps in Figure 5.39

The particle mass concentration increases till 25 milliseconds and then becomes constant through 50 milliseconds. As the number of the particles in the recirculation zone increases, the maximum velocity attained by the recirculating gases decreases steadily. Once the particle mass concentration becomes constant, the flow-field does not undergo any major changes and the maximum velocity attained by the recirculating gases does not decrease anymore.

The particles moved against the recirculating gases till the eye of the recirculation zone and does not move further downstream. The maximum velocity of the recirculating gases decreases through t = 25ms as the particles continue to flow against the gases. The maximum velocity of the gases does not change till t = 50ms as the particles have reached eye of the recirculation zone by t= 25 ms

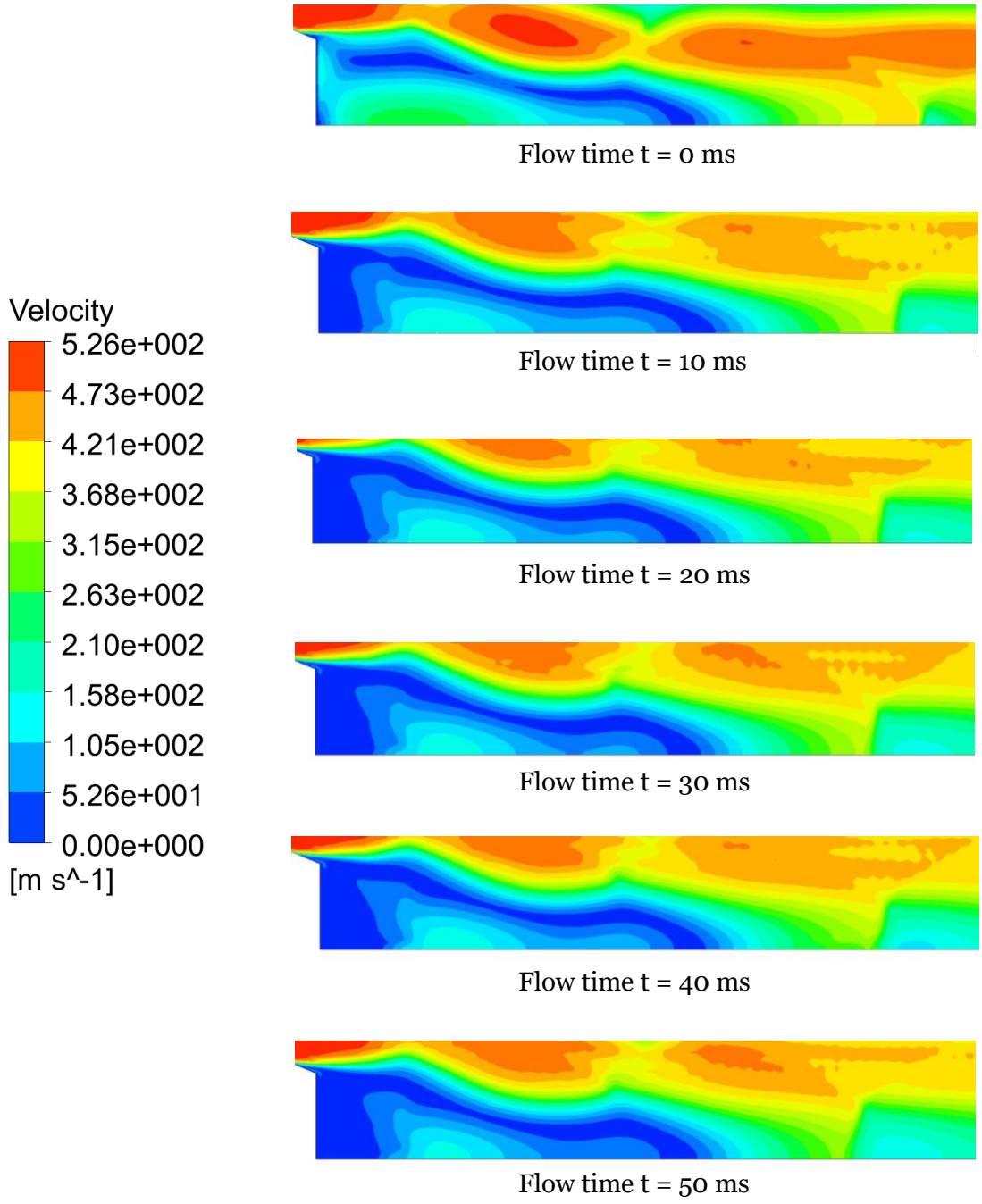

Figure 5.39 Velocity contour plots of the recirculation zone for flow times from t= 0 ms to t= 50 ms for 3MPa operating pressure

Case 3: 4.5 MPa

The operating pressure 4.5 MPa produced a closed wake and is the wake closure pressure. As mentioned previously, a closed wake is characterised by a normal shock in front of the nozzle.

Figure 5.40 shows various velocity contour plots for various timesteps. In this case, a recirculation zone is formed downstream the normal shock. The expanding gas jets reattaches twice in closed wake cases. The stagnation point where the expanding gases converge along

the axis after the normal shock does not change throughout the 50 milliseconds. At t= 0 ms, the gases in the recirculation zone attain the maximum velocity of about 270 ms^{-1}.

The particle mass concentration increases till 30 milliseconds and becomes constant till 50 milliseconds. As discussed in the previous cases, the maximum velocity attained by the gases decreases till 30 milliseconds and does not exhibit any notable changes till 50 milliseconds. It

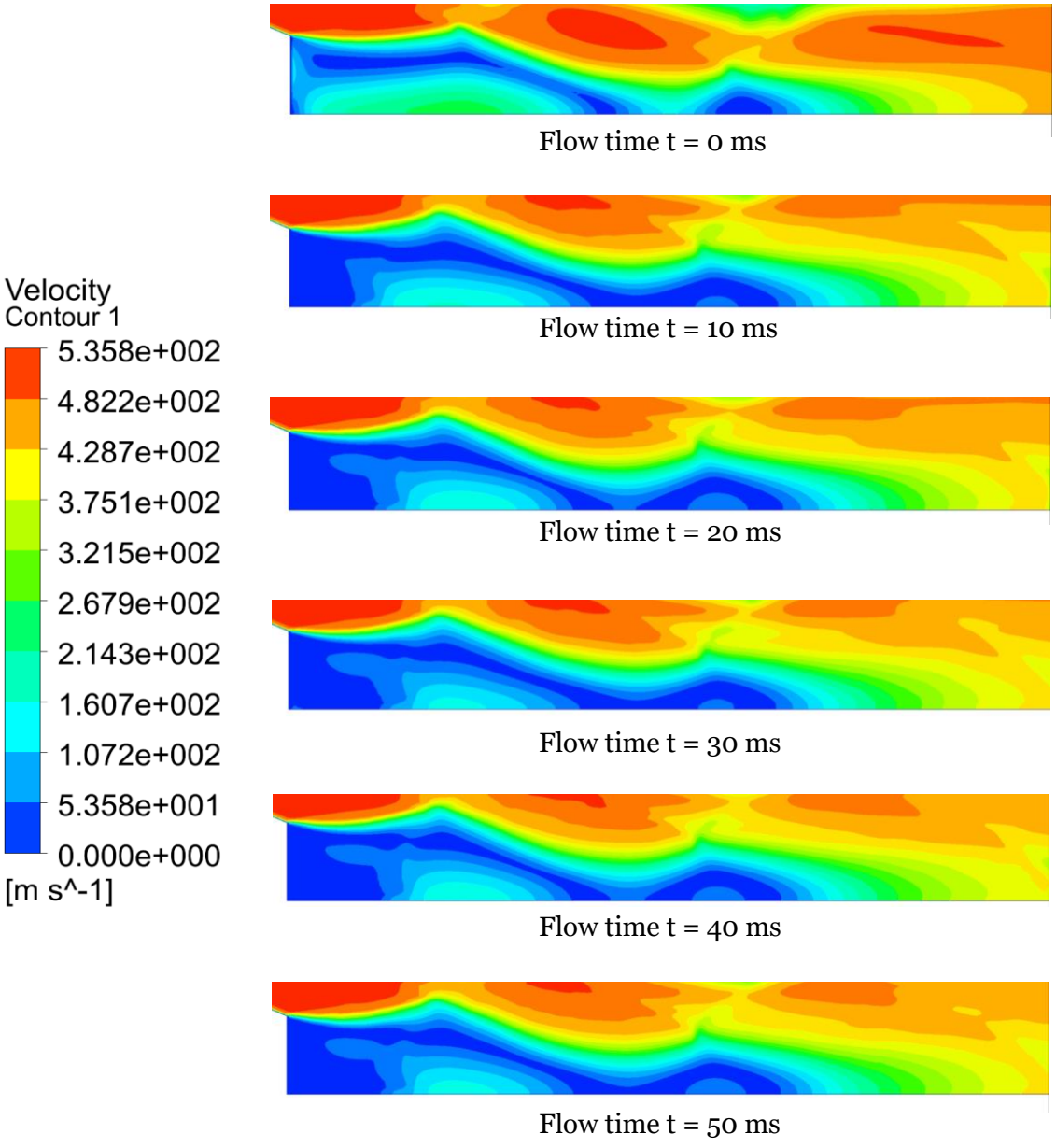

Figure 5.40 Velocity contour plots of the recirculation zone for flow times from t= 0 ms to t= 50 ms for 4.5 MPa operating pressure

can be seen from the Figure 5.40 that the Mach disk is disrupted to form an open wake condition.

Case 4: 5 MPa

The operating pressure 5 MPa produced a closed wake. The normal shock formed further downstream compared to the 4.5 MPa case. The particles move towards and until the eye of the recirculation zone till 40 milliseconds leading to increase in particle mass concentration. The particles do not move further downstream, and the particle mass concentration becomes

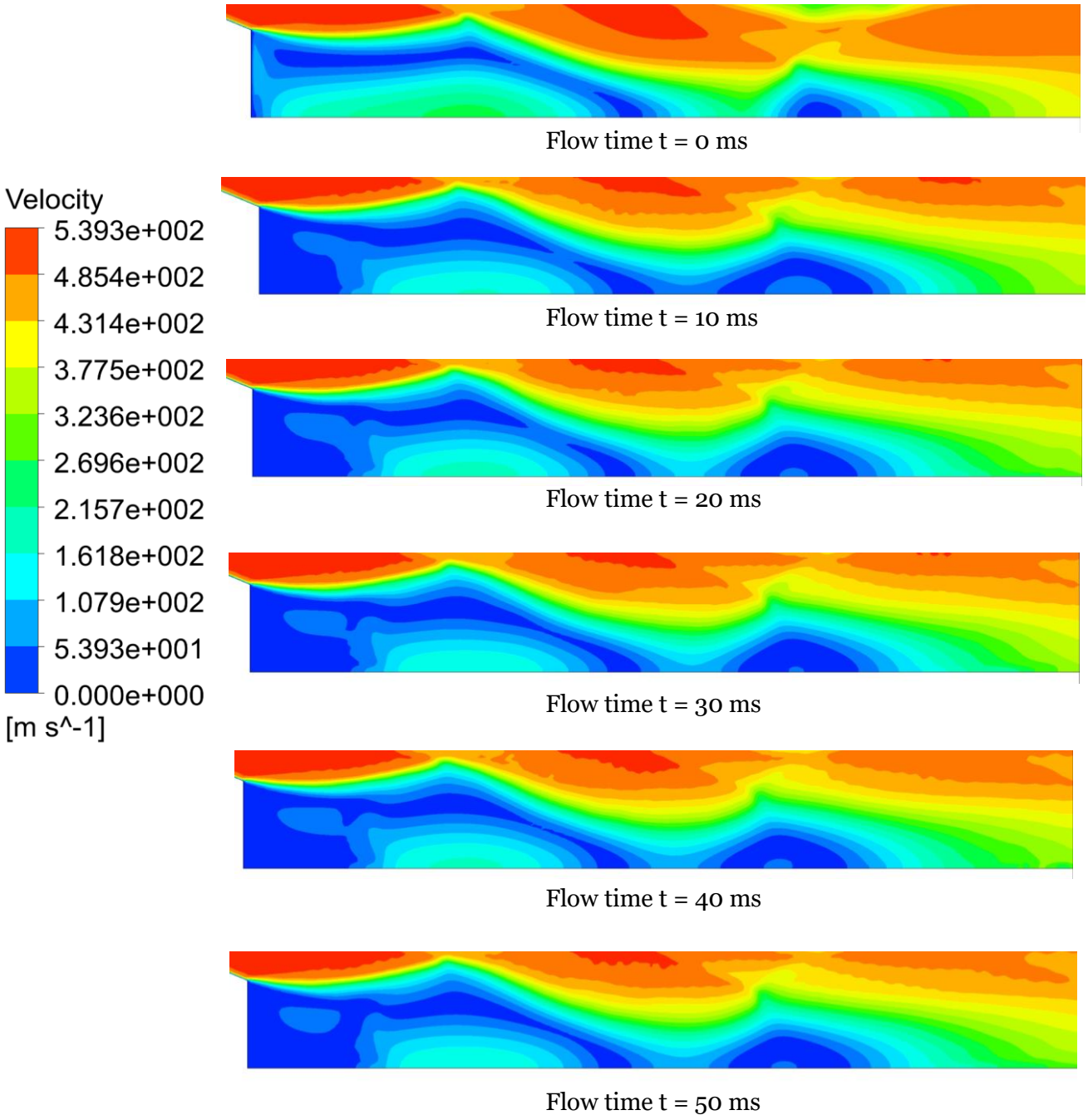

Figure 5.41 Velocity contour plots of the recirculation zone for flow times from t= 0 ms to t= 50 ms for 5 MPa operating pressure

constant in the last 10 milliseconds. At t= 0 ms, the gases in the recirculation zone attain the maximum velocity of about 270 ms^{-1}.

Figure 5.41 shows the velocity contour plots for various timesteps. The stagnation point where the expanding gases converge along the axis after the normal shock does not change throughout the 50 milliseconds. Also, the closed wake is disrupted as the oblique shocks forming the Mach disk lose their strength through 50 ms. The gases in the recirculation zone lose their velocity on interaction with the particles as the particles continue to move downstream. The velocity of the gases in the recirculation zone downstream the normal shock also loses their velocities as the particles enter it.

5.2.5 Residence time of particles

The residence time of a particle in the domain is the total time spent by the particle in the domain. The particles travel through the domain at various velocities leading to a range of residence times. On being released, the particles flow against the recirculating gases on being released into the recirculation zone. The particles travel further downstream with increasing timesteps towards the eye of the recirculation zone. The particles do not move further across

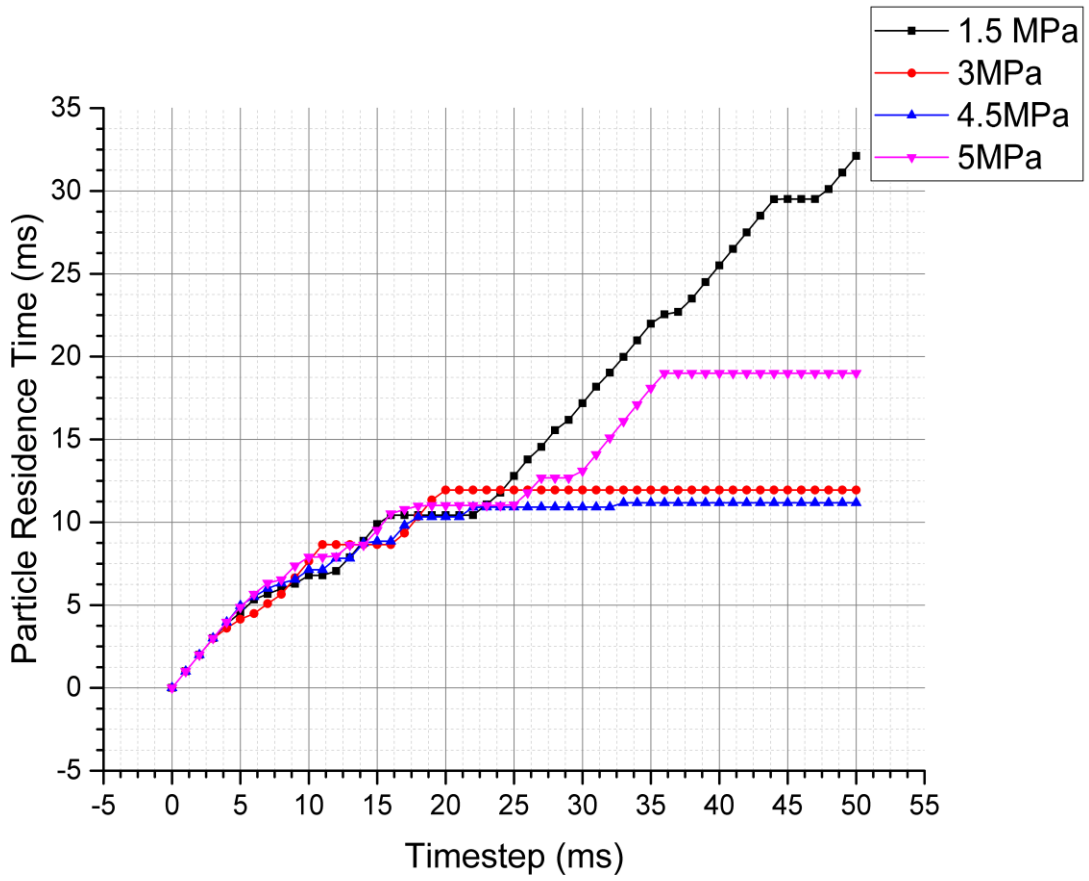

Figure 5.42 Graph showing the Maximum Particle Residence Time (ms) vs Timesteps (ms)

the recirculation zone in all the cases analysed in this study except the case with 1.5 MPa operating pressure.

Figure 5.42 shows the maximum residence time of the particles for every timestep. The residence time plotted in this graph is the maximum value observed at the particular timestep.

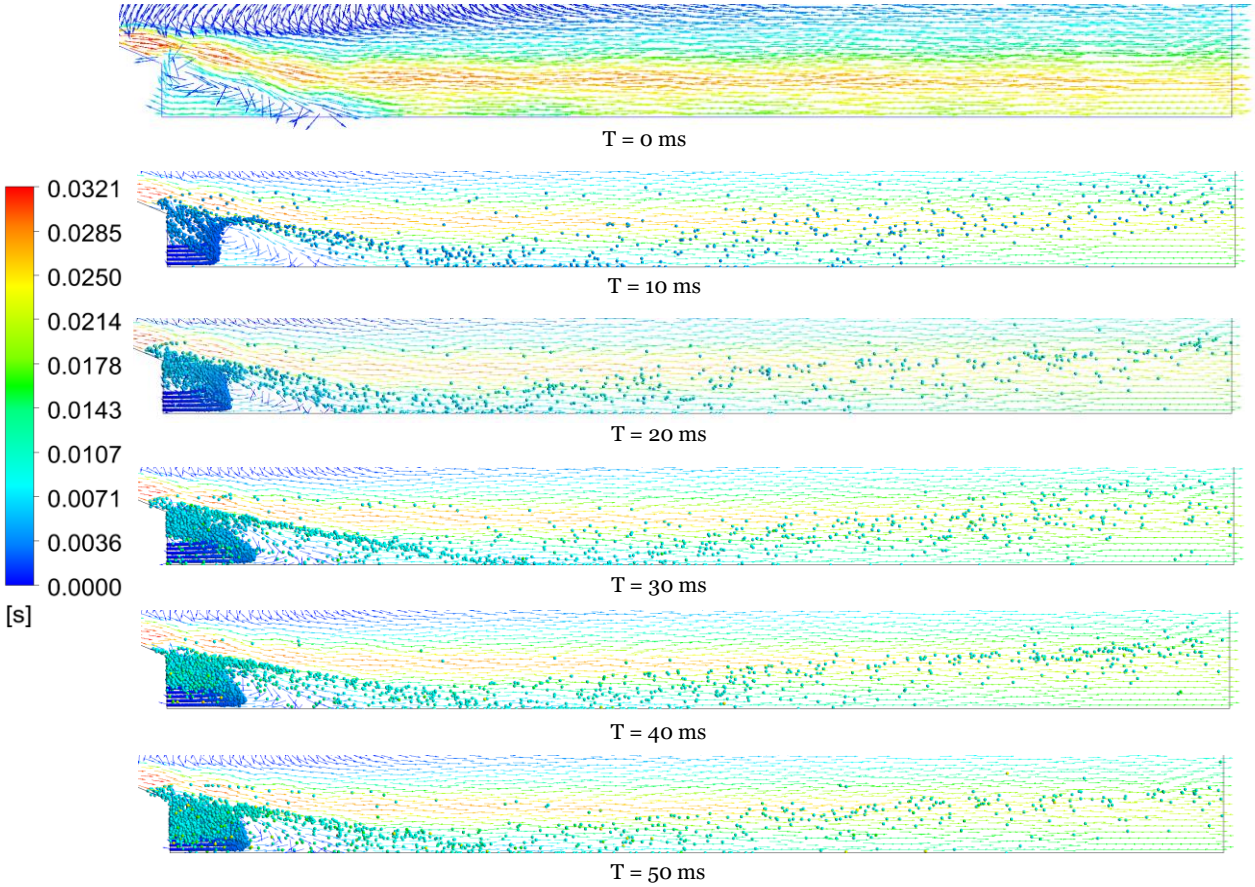

Figure 5.43 Particles coloured according to their residence time in a velocity vector plots at 1.5 MPa pressure

Figure 5.43 shows the particles coloured by their residence times on the velocity vector plots at 1.5 MPa for flow times t = 0 ms, 10 ms, 20 ms, 30 ms, 40 ms and 50 ms.

In this case, the GMR is high, and the particles move across the eye of the recirculation zone. It can be seen that residence time of majority of the particles remain in the low to lower-middle range throughout 50 milliseconds (0-0.01s). The particle mass concentration increases throughout 50 milliseconds as observed in the Figure 5.7. The stagnation of particles in the recirculation zone can be seen by the increasing residence time (plot colour) in the recirculation zone.

The maximum residence time of the particles also continues to increase as seen in the Figure 5.42**.** The gas flow rate in this case is not sufficient to carry the particles to the high-speed gas jets leading to stagnation of particles in the recirculation zone. This increasing stagnation leads to high particle residence times. Also, the maximum velocity achieved by the expanding gas

jets is the least of all the cases considered and this also contributes to the high particle residence times.

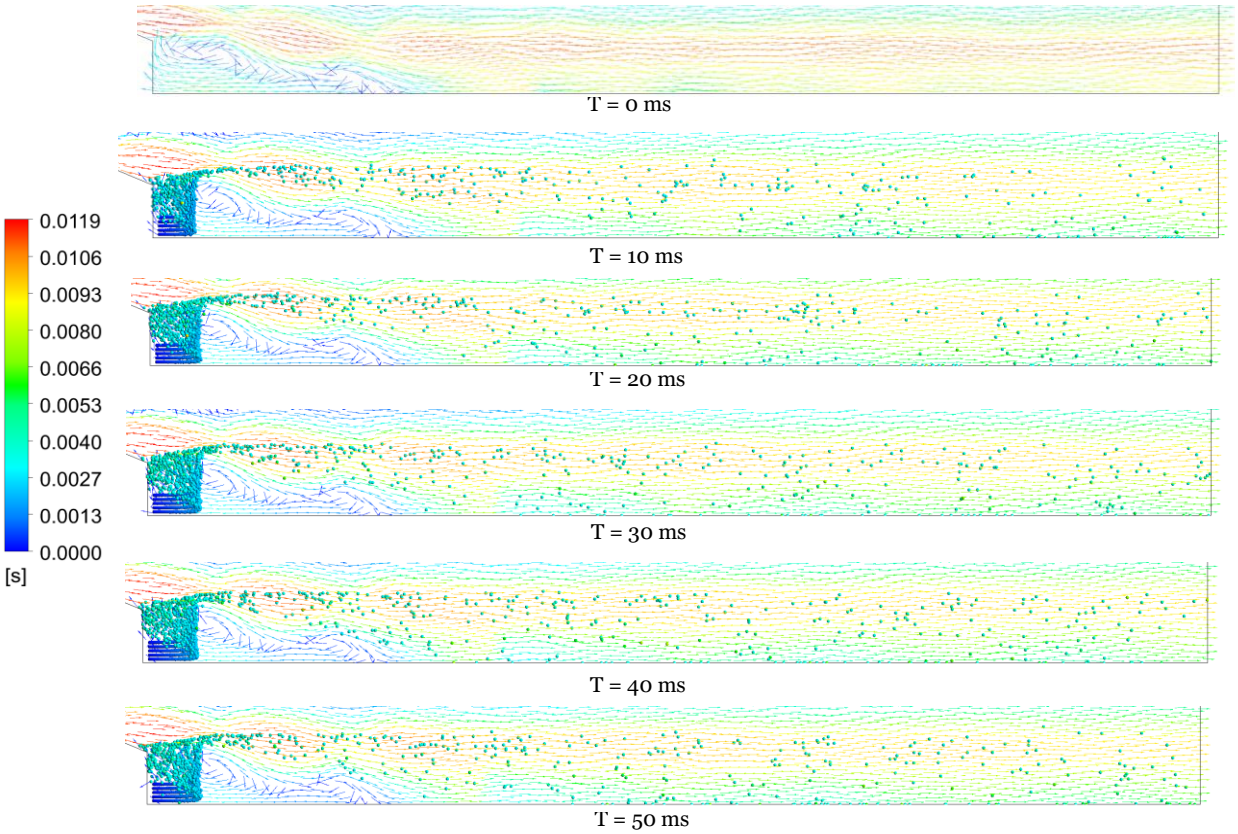

Figure 5.44 Particles coloured according to their residence time in a velocity vector plots at 3 MPa pressure

Figure 5.44 shows the particles coloured by their residence times on the velocity vector plots at 3 MPa for flow times t = 0 ms, 10 ms, 20 ms, 30 ms, 40 ms and 50 ms. Similar to the previous case, majority of particles' residence times remain in the lower-mid range (0- ~0.005 s).

In this case, the maximum residence time increases till 20 milliseconds and becomes a constant till 50 milliseconds. As discussed in the previous sections, the particles flow against the recirculating gases and reach the eye of the recirculation zone by 20 milliseconds leading to an increase in maximum residence time at every timestep. The particles do not move further downstream till 50 milliseconds resulting in a constant particle mass concentration. This can be seen in the Figure 5.7. The constant particle mass concentration indicates that the number of particles exiting the recirculation zone is constant. This leads to a constant maximum residence time between 20 milliseconds and 50 ms in this case as seen by Figure 5.42 Another consequence of constant particle mass concentration in the recirculation zone is that the residence time of the particles lie in the narrow range (~50-60 **µs).**

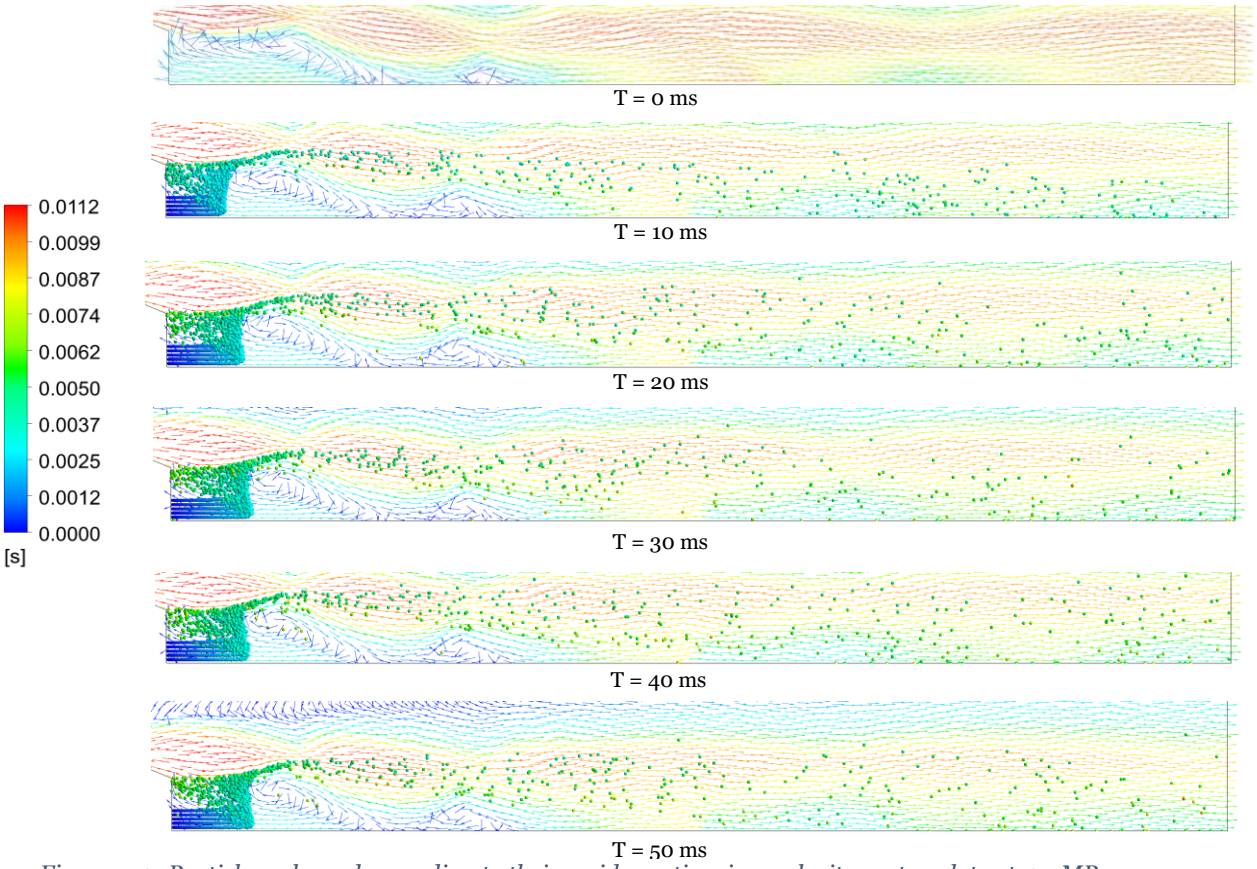

Figure 5.45 Particles coloured according to their residence time in a velocity vector plots at 4.5 MPa pressure

Figure 5.45 shows the particles coloured by their residence times on the velocity vector plots at 4.5 MPa for flow times t = 0 ms, 10 ms, 20 ms, 30 ms, 40 ms and 50 ms. It can be seen from the Figure 5.45 that the residence time of majority of particles remain in the higher-mid range (0-~0.006 s).

In this case, the maximum residence time of the particles increases till 23 ms and becomes constant till 32 ms at 10.91 ms as seen in Figure 5.42. The particle mass concentration increases rapidly till 23 ms and begins to increase very gradually till 30 ms as seen in Figure 5.7. As this is a closed wake case, the pressure in the recirculation zone is subambient and the particles have to overcome this pressure to exit the recirculation zone leading to stagnation of particles. This results in a constant maximum residence time before the particles can overcome the subambient pressure and exit the recirculation zone. The maximum residence time of the particles increases till the constant particle mass concentration is achieved. The particle mass concentration becomes constant between 30 ms and 50 ms and the particle residence time is constant between 30 ms and 50 ms. Also, another effect of the subambient pressure is that the average particle residence time in the recirculation zone remains in the higher-mid range.

Figure 5.46 shows the particles coloured by their residence times on the velocity vector plots at 5 MPa for flow times t = 0 ms, 10 ms, 20 ms, 30 ms, 40 ms and 50 ms. It can be seen from

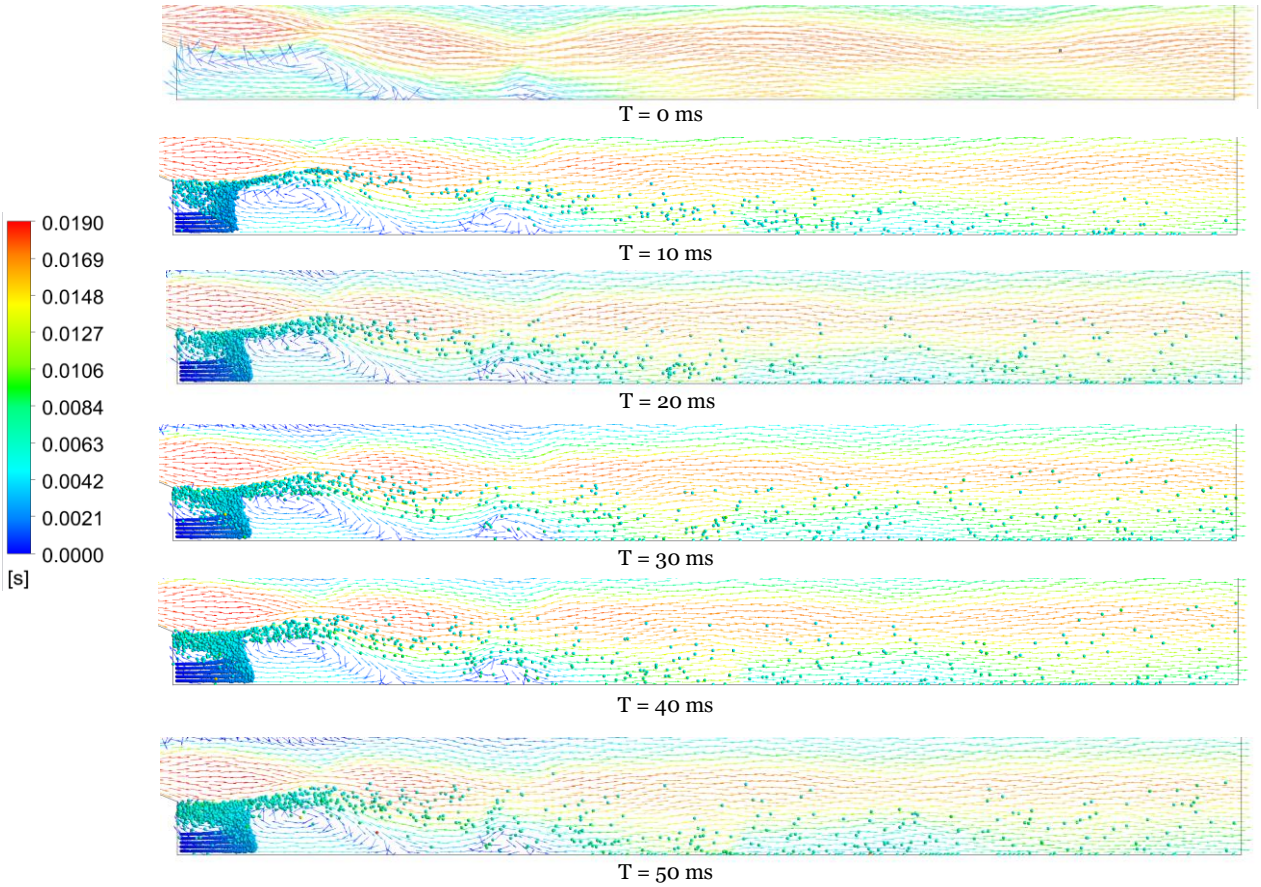

Figure 5.46 Particles coloured according to their residence time in a velocity vector plots at 5 MPa pressure

the Figure 5.46 that the residence time of the majority of the particles remain in the midrange (0~0.006s).

In this case, the maximum residence time of particles increases till 19 milliseconds and maintains constant till 25 milliseconds at 11.02 ms. As discussed in the previous case, this is a closed wake case, and the particles have to overcome the subambient pressure to exit the recirculation zone. This results in constant maximum particle residence time between 19 milliseconds and 25 milliseconds. The particle mass concentration increases till 39 milliseconds and the maximum residence time of particles increases due to stagnation of the particles in the recirculation zone. The particle mass concentration and hence the maximum residence time of the particles becomes constant between 39 milliseconds and 50 milliseconds. As in the previous case, the subambient pressure in the recirculation zone leads to increased residence time in it.

5.2.6 Velocity of the particles

The particle velocity is greatly influenced by the gases carrying it. The particles in the recirculation zone possess low velocities due to the gases acting against the flow direction of particles. On the other hand, the particles entering the expanding gas jets acquire high velocity. The gases lose their velocity on interaction with the shock waves and move towards

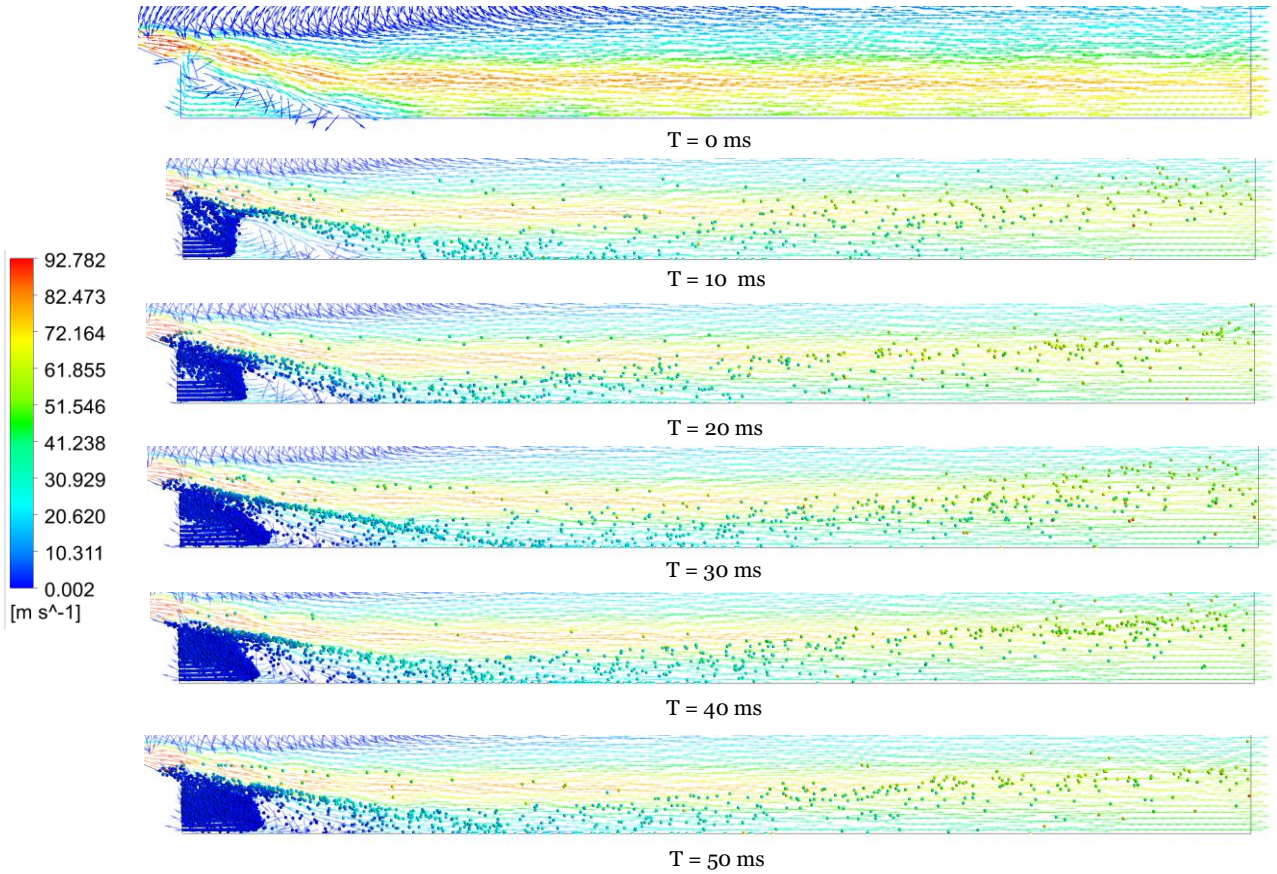

Figure 5.47 Particles coloured according to their velocities in a velocity vector plots at 1.5 MPa operating pressure

the next shock wave through expansion where they acquire high velocities. The strength of the shock waves decreases with increasing distance from the melt nozzle. Therefore, the losses in velocity possessed by the gases become less appreciable as the distance from the nozzle increases. This in turn leads to particles gaining velocity towards the outlet of the domain. It has been observed in the analysis that the particles gain velocity at the end of the domain.

Figure 5.47 shows the the velocity of the particles for flowtime t= 0ms, 10 ms, 20 ms, 30 ms, 40 ms and 50 ms at 1.5 MPa case. It can be seen that the particles move with low velocities in the recirculation zone and begin acquiring velocity as they travel towards the outlet. As the particles converge along the axis much closer to melt nozzle than the other three cases. The particles converge and bounce away into high velocity layers of atomizing gas. Therefore, a large number of particles travel in a low velocities range as seen in the Figure 5.47.

Figure 5.48 shows the velocity vector plots and the particles for the flowtime t= 0ms, 10 ms, 20 ms, 30 ms, 40 ms and 50 ms at 3 MPa pressure. A group of particle trajectories begin converging along the axis much further away that the 1 MPa case and the rest of the trajectories move towards the outlet through high speed layers. The particles travel at much higher velocities than the 1.5 MPa case as the gases achieve higher velocities at 3 MPa.

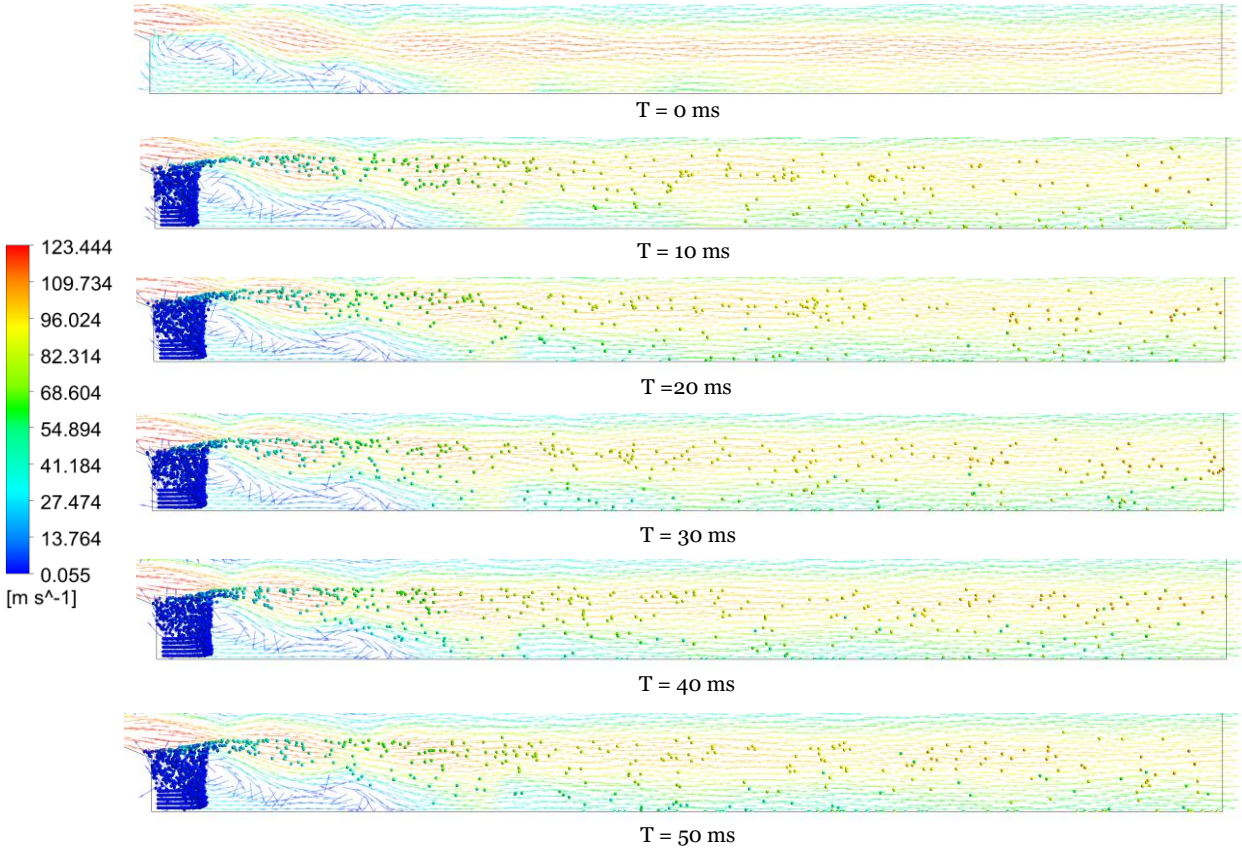

Figure 5.48 Particles coloured according to their velocities in a velocity vector plots at 3 MPa operating pressure

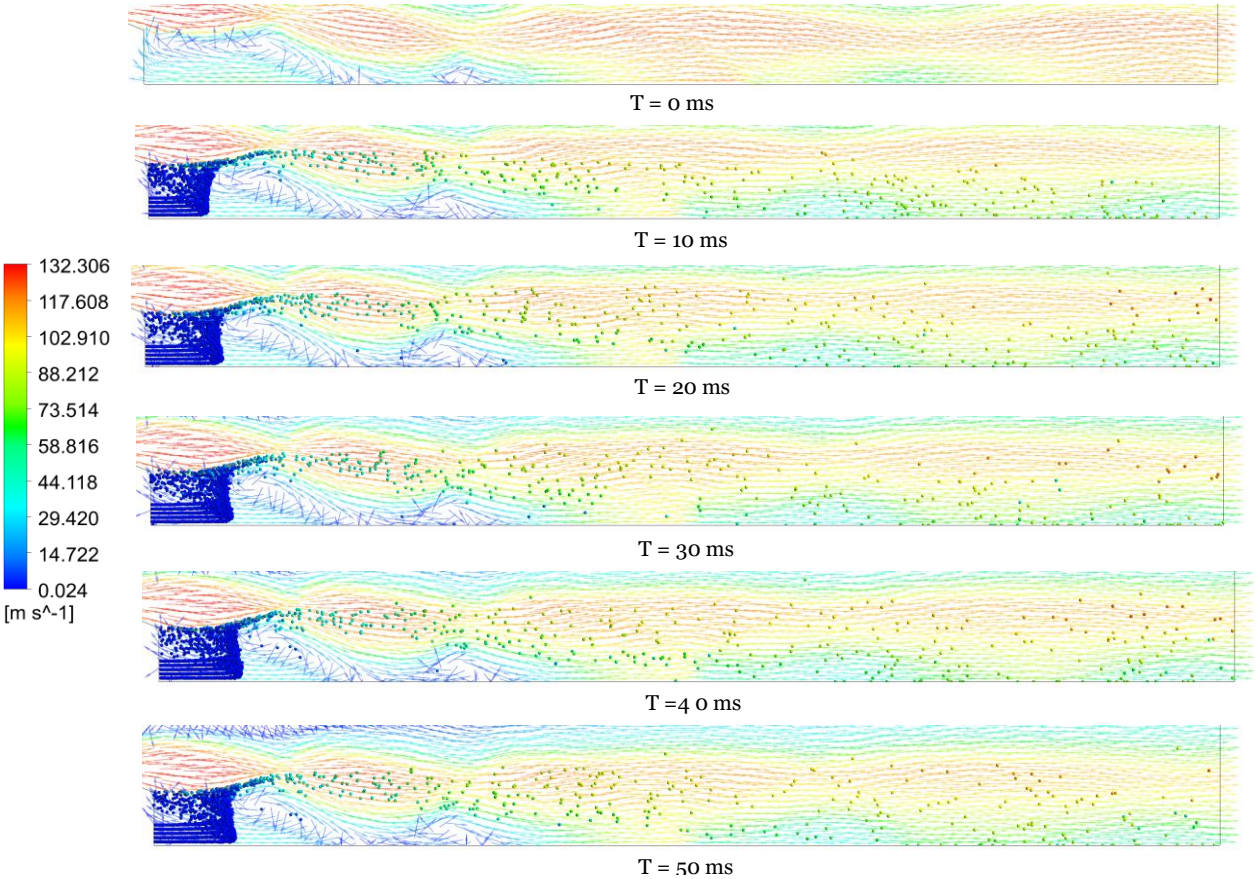

Figure 5.49 Particles coloured according to their velocities in a velocity vector plots at 4.5 MPa operating pressure

Figure 5.49 shows the velocity vector plots and the particles for the flowtime t= 0ms, 10 ms, 20 ms, 30 ms, 40 ms and 50 ms at 4.5 MPa pressure. Similar to 3 MPa case, a group of particle trajectories converge along the axis while the rest travel towards the outlet in high-velocity layers. The particle acquire velocities higher than the previous two cases. It can be seen from the Figure 5.49 that a large number of particles achieve the maximum velocity in this case as they travel through high velocity layers.

Figure 5.50 shows the velocity vector plots and the particles for the flowtime t= 0ms, 10 ms, 20 ms, 30 ms, 40 ms and 50 ms at 5 MPa pressure. A group of particle trajectories converge along the axis while the rest travel towards the outlet without converging. Particles achieve their maximum velocity as they near the otulet as the strength of the shocks decreases as the distance from the melt nozzle increases.

In all the cases, the particles travel at much lower range of velocities compared to the gases. In physical reality, this difference in velocities give raise to shearing of melt droplets which results in further atomization of melt.

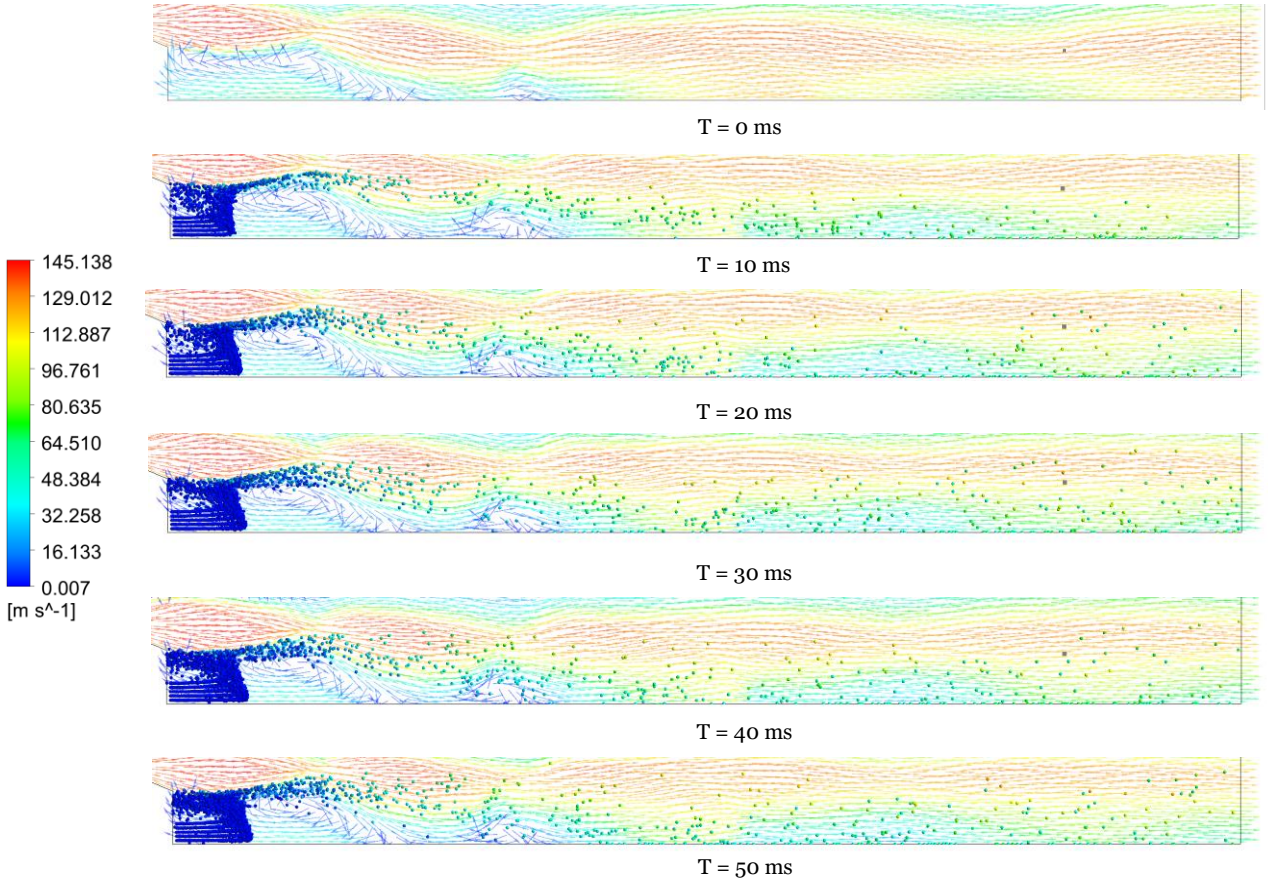

Figure 5.50 Particles coloured according to their velocities in a velocity vector plots at 5 MPa operating pressure

Figure 5.51 shows the maximum velocity attained by the particles inside the domain for every timestep. The maximum velocity of the expanding gas jets increases with increasing operating

pressure and the consequence of this increase in the maximum velocity of the expanding gas jets is the increase in the maximum velocity attained by the particles.

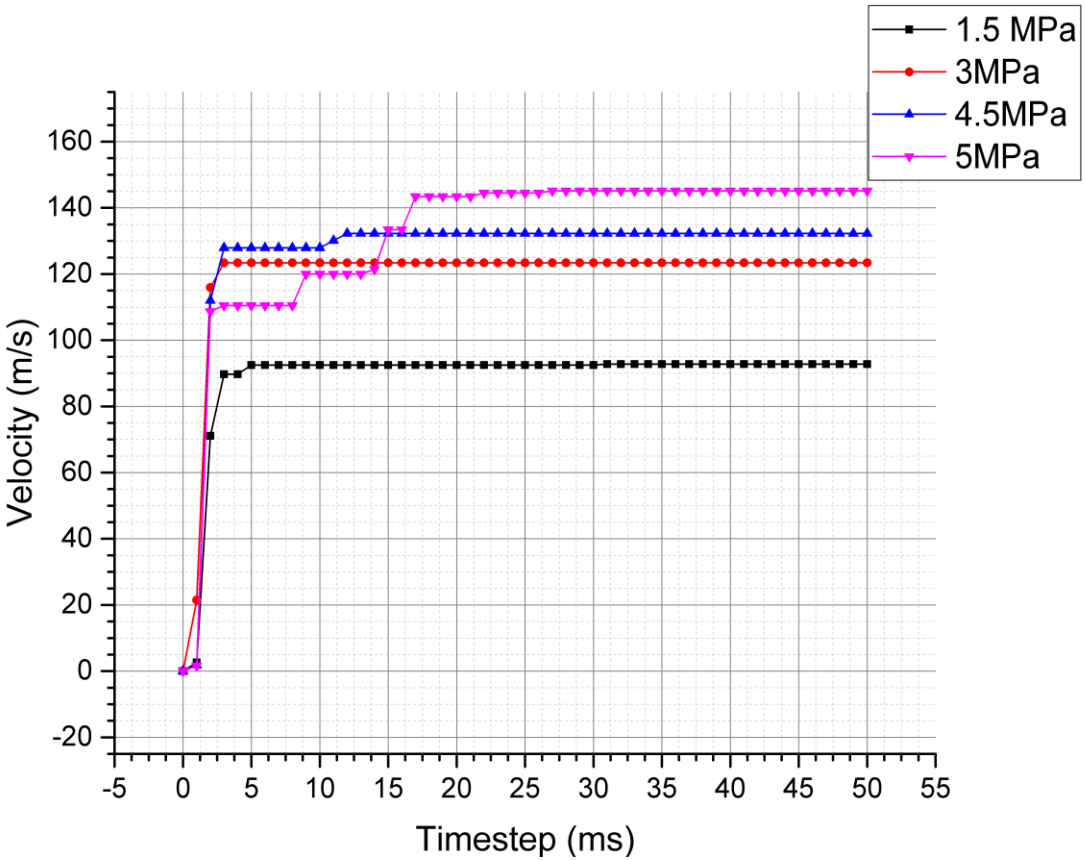

Figure 5.51 Graph showing the maximum velocity of the particles (ms^{-1}) vs Timesteps (ms)

It can be seen from the Figure 5.51 that the maximum velocity of the particles increases with the increase in operating pressure.

In the case with 1.5 MPa operating pressure, the velocity is constant from t = 5ms. The particles converge along the axis and bounce off in this case. As the particles move towards the outlet after the bounce-off, few of the particles begin travelling along the high-speed layers of the expanding gas jets with the maximum velocity. (constant maximum velocity = 92.51 ms^{-1})

In the case with 3 MPa operating pressure, the velocity is constant from t = 3 ms. In this case, the particles begin travelling along the high-speed layers before converging along the axis. Few of the particles travel along high-speed layers of expanding gas jets towards the result with the maximum velocity. (constant maximum velocity = 123.4 ms^{-1})

In the case with 4.5 MPa operating pressure, the maximum velocity is constant from t =3 ms to t = 10 ms. The trajectories of the particles are directed towards the axis. Initially, the particles travel along the high velocity gas layers and as the particle trajectories are directed towards the axis, the particles move towards the lesser velocity gas layers as they move towards

the outlet. Figure 5.47, Figure 5.48, Figure 5.49 and Figure 5.50 shows the velocity vectors and particles. The maximum velocity increases and becomes constant between the t = 12 ms to t= 50 ms. The increase in the maximum velocity is due to the spreading of the particle trajectories and few of the particles entering the high-speed gas layers in the expansion waves near the outlet. The particles travel at the maximum velocity near the outlet. (constant maximum velocity = 132.3 ms^{-1})

In the case with 5 MPa operating pressure, the trajectories of the particles are directed towards the axis. The maximum velocity increases till t = 3 ms and becomes constant till t = 8 ms. The maximum velocity increases and becomes a constant between t= 9 ms to t = 13 ms. The maximum velocity increases again till t =15 ms and becomes constant till t =16 ms. Finally, the maximum velocity increases and becomes constant till t =17 ms to t =50 ms. The particles begin moving along the high-speed gas layers and as the particle trajectories are directed towards the axis, the particles begin moving along the lower velocity gas layers as they near the outlet. The particle trajectories begin spreading and entering the high-speed layers as the flow time increases. As the particles enters the gas layers with increasing velocity, the maximum velocity of the particles also increases. (constant maximum velocity =145.138 ms^{-1})

5.2.7 Aspiration pressure

Aspiration pressure is an important process parameter in the process of CCGA. Aspiration pressure influences the movement of melt in the recirculation zone and hence the GMR of the process. A subambient aspiration pressure encourages the melt movement into the recirculation zone whereas an over ambient pressure discourages the melt movement into the recirculation zone. Also, a high sub ambient pressure results in high GMR leading to bigger particle size. On the other hand, a high over ambient pressure results in low GMR leading freeze-off during the process. Therefore, establishing an appropriate aspiration pressure is essential for efficient atomization.

In this analysis, the aspiration pressure was measured along the wall where the particles were released for every microsecond. Figure 5.6 shows the location where the aspiration pressure is measured. A rake with 20 points was set up at this location and average pressure over the rake was calculated for every microsecond. The pressure measured at this location is not absolute pressure and is relative to the surrounding gases.

Figure 5.53 shows variation in the aspiration pressure for every millisecond of the flow and it can be seen that the aspiration pressure changes rapidly in the first five millisecond. Figure 5.52 shows the variation in the aspiration pressure for every microsecond till t =5ms.

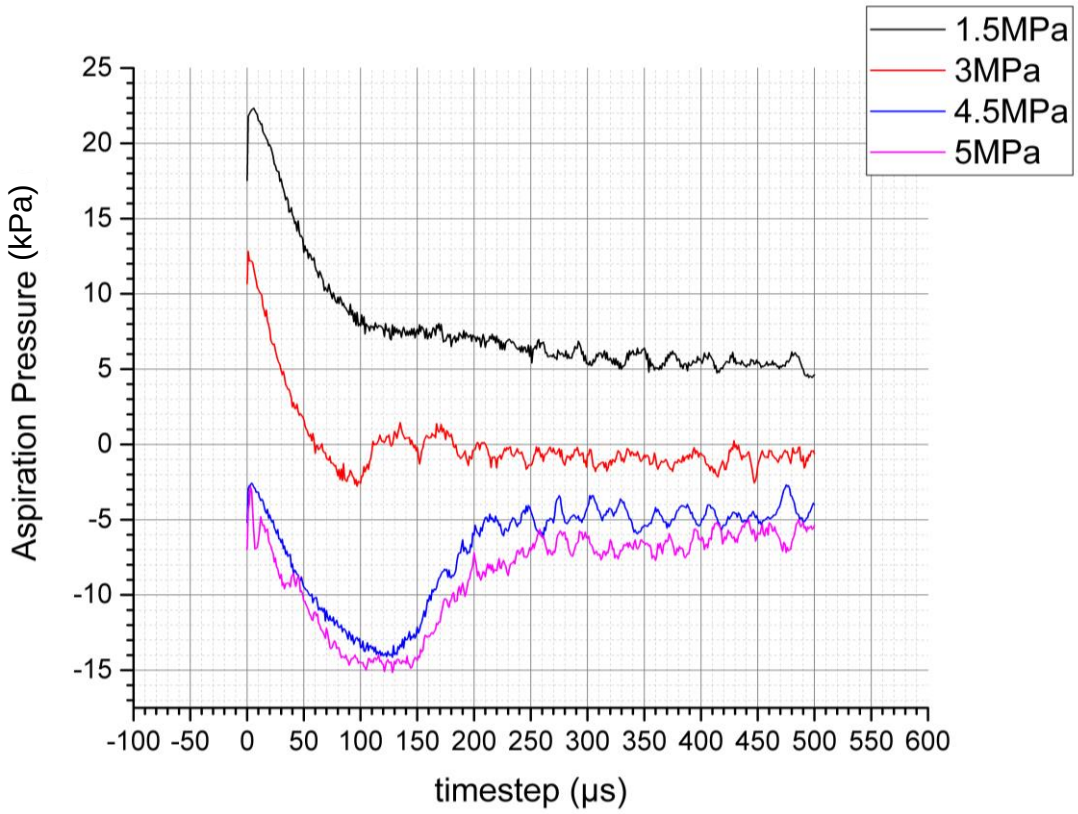

Figure 5.52 Graph showing the Aspiration pressure (kPa) vs Timesteps (µs)

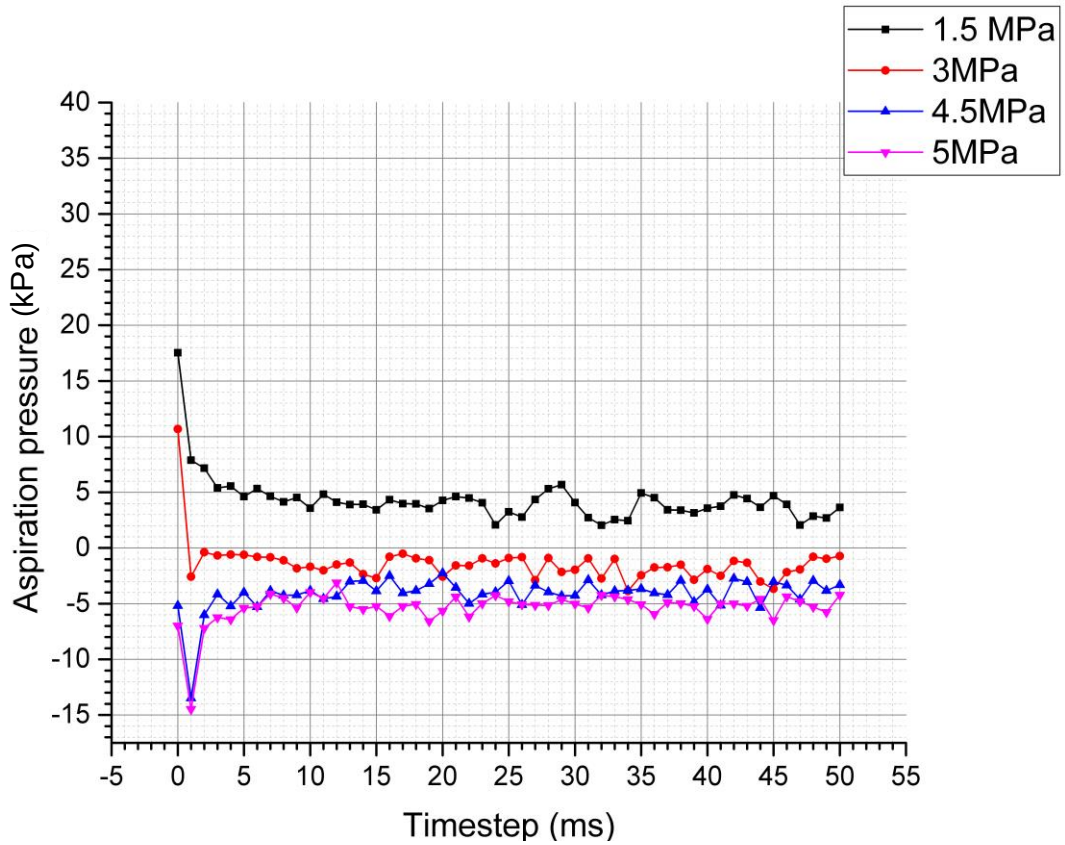

Figure 5.53 Graph showing the Aspiration pressure (kPa) vs Timesteps (ms)

In the case with 1.5 MPa operating pressure, the aspiration measure is overambient at t=0 ms. As the particles begin entering the recirculation zone, the aspiration pressure changes rapidly in the first five milliseconds. It can be seen from the Figure 5.52 that the aspiration pressure increases initially and decreases. The aspiration pressure decreases rapidly till t = 1 ms and gradually till t = 5 ms. It can be seen from the Figure 5.53 that the aspiration pressure fluctuates slightly around 4 kPa till t = 23 ms. As the particle mass concentration increases, the aspiration pressures begin fluctuating considerably around 4 kPa.

In the case with 3 MPa operating pressure, the aspiration pressure is overambient at t= 0 ms. As the particles begin entering the recirculation zone, the aspiration pressure decreases and becomes sub-ambient till t = 1ms to about -3 kPa. The aspiration pressure begins increasing from t= 1ms and fluctuates around 0 kPa till t = 2ms as seen in the Figure 5.52. The aspiration pressures decrease at this point and begin fluctuating around a constant subambient value till t= 50 ms. Also, the particles begin exiting the domain at t= 2ms. It can be seen from the Figure 5.53 that the aspiration pressure decreases till t =12 ms and begins to fluctuate around the constant subambient value of -1 kPa till t =50 ms.

In the case with 4.5 MPa operating pressure, the aspiration pressure is subambient (-5.138 kPa) at t= 0 ms. It can be seen from the Figure 5.52 that the aspiration pressure falls till t= 1.2 ms to about -14 kPa and increases till t = 2ms to about -5 kPa. The particles begin exiting the flow domain by t = 2ms and the aspiration pressure begins fluctuating from t= 12 ms to t =50 ms. It can be seen from the Figure 5.53 the aspiration pressure fluctuates slightly till t =12 ms and considerably till t = 50 ms around -4 kPa.

In the case with 5 MPa operating pressure, the aspiration pressure is subambient (-6.982 kPa) at t= 0 ms. It can be seen in the Figure 5.52 the aspiration pressure falls to -15 kPa till t = 1ms and fluctuates about -15 kPa till t= 1.5 ms. The aspiration pressure begins increasing till t=2.5 ms to -6 kPa. The particles begin exiting the flow domain by t= 3ms and the aspiration pressure fluctuates around -6 kPa till t= 5 ms. It can be seen from the Figure 5.53 that the aspiration pressure fluctuates considerably around -5 kPa till t=50 ms.

SUMMARY

The trajectories of particles and the changes in the flow field was analysed in a two-way coupled model. Two open wake cases (1.5 MPa, 3 MPa,) and two closed wake cases (4.5 MPa, 5 MPa) have been considered and the changes in the process parameters also considered. Particle mass concentration, Aspiration pressure, Maximum residence time of the particles and maximum velocity of the particles has been studied. All the results have been presented and discussed.

6 THREE-DIMENSIONAL SINGLE PHASE (GAS) ANALYSIS

Methodology, research and discussion.

Nozzle designs play a major role in influencing the development of the flow once the gas jets exit the gas tube. In the previous chapters, a two-dimensional model was utilized to analyse the flow features and the particle movement in an annular-slit atomizer. Generally, a two-dimensional model will not be sufficient to analyse the flow features in a discrete jet atomizer due to the lack of axisymmetry and might require certain approximations to simulate the atomization process. A three-dimensional model has been developed in this study to analyse the flow features in a discrete jet atomizer. Two different gas die designs have been analysed in this study and the results are tabulated. Both the nozzle designs have 18 discrete holes and a 45-degree apex angle. An advantage of DJ-CF atomizer is the reduced gas consumption, but these atomizers are sensitive to changes in geometrical parameters such as offset distance (i.e. space between the discrete jets) and intermittent spacing (distance between the melt nozzle and the gas delivery system).

The first design considered is a conventional discrete jet nozzle design in which the holes are located at a distance from the melt nozzle. This design utilized choked gas die to deliver the gas into the atomization chamber. It is based on the full-scale metal atomizer used in a powder manufacturing company and was used in the experimental works of Motaman [101]. Figure 6.1 shows the front view and the isometric view of the conventional discrete jet atomizer.

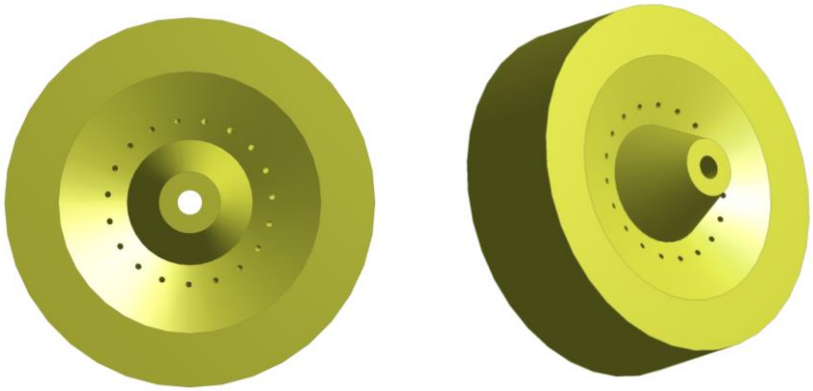

Figure 6.1 three-dimensional rendering of the conventional discrete jet atomizer in bottom view and isometric view

The second design is a novel design that combines the annular slit and discrete jet nozzle designs. In this design, the annular slit is replaced by a set of discrete holes. The offset distance was eliminated, and the shape of the discrete hole was changed from a circle to a semi-circle. This design also utilized choked gas die to deliver the gas into the atomization chamber.

Figure 6.2 shows front view and the isometric view of the novel discrete jet atomizer.

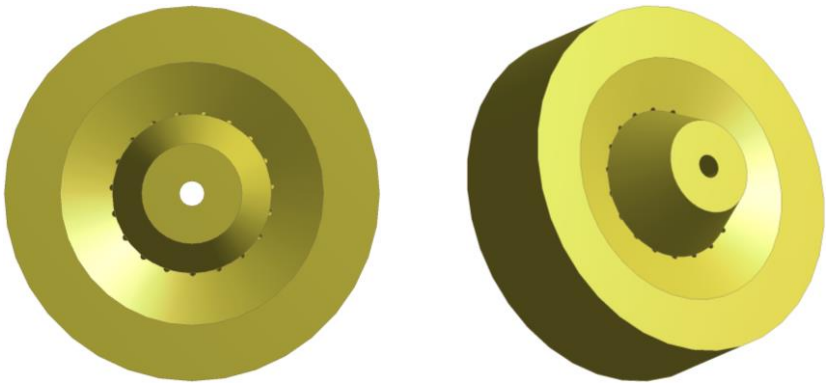

Figure 6.2 three-dimensional rendering of the novel discrete jet atomizer in bottom view and isometric view

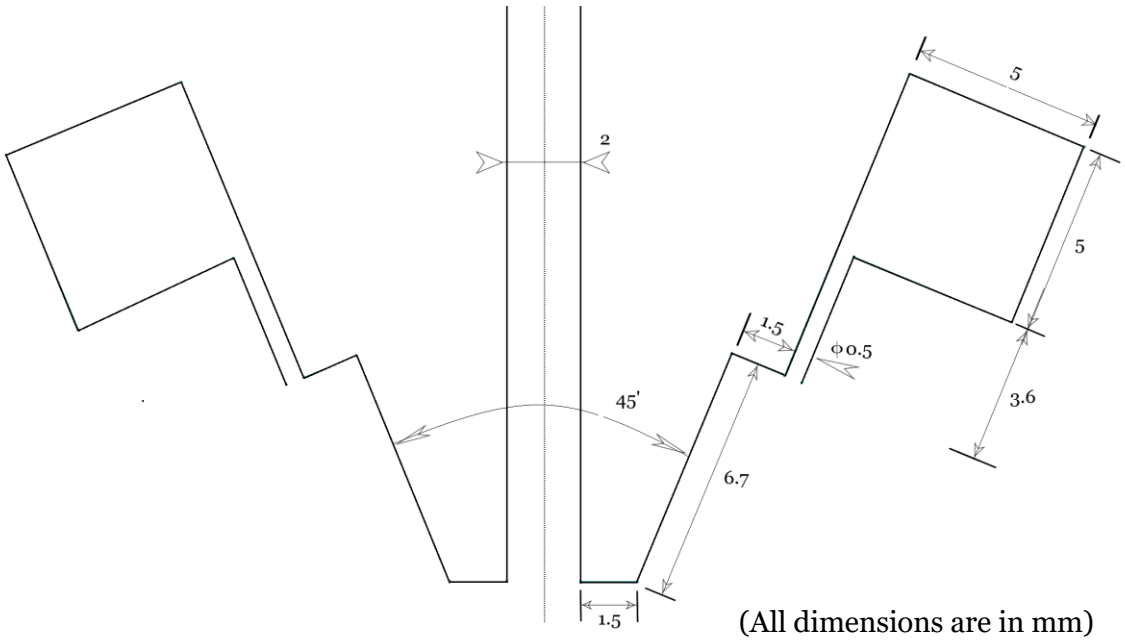

Figure 6.3 Schematic representation of conventional discrete jet atomizer with all dimensions

Figure 6.3 shows the various dimensions of conventional discrete-jet atomizer. The discrete-jets are 0.5 mm in diameter and located at a distance of 1.5 mm from the melt nozzle. The apex angle of this atomizer nozzle is 45 degrees.

Figure 6.4 shows the various dimensions of novel discrete-jet atomizer. The radius of the semicircle is 0.25 mm, and the offset-distance is eliminated. The apex angle in this design is

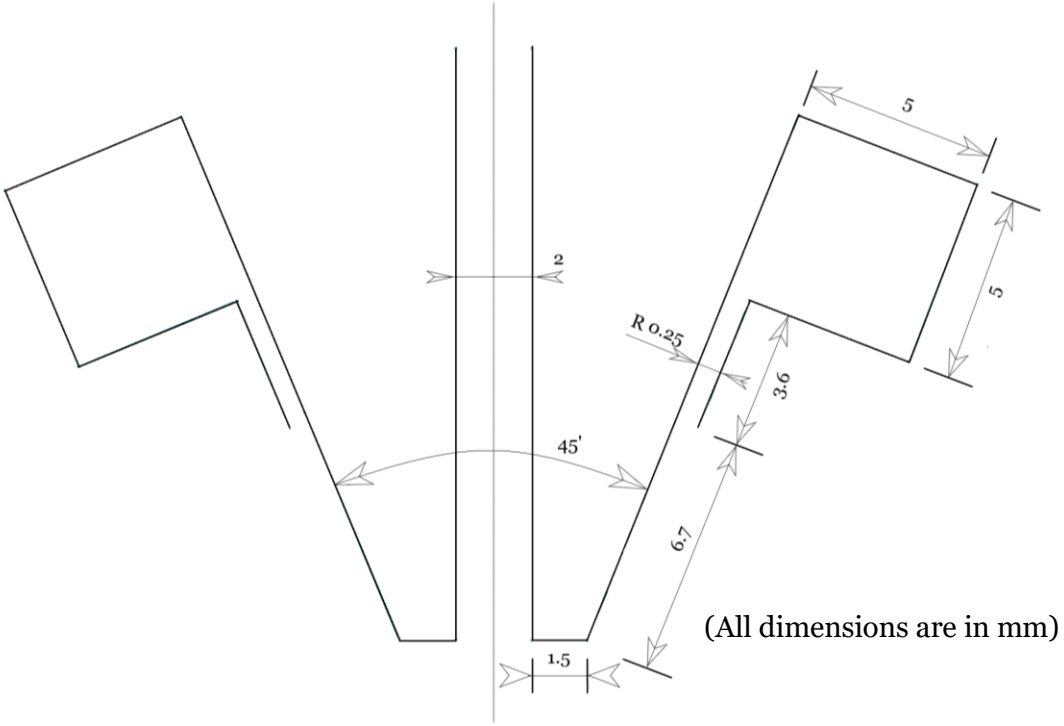

Figure 6.4 Schematic representation of novel discrete jet atomizer with all dimensions

also 45 degree. The methodology involved in developing a single-phase three-dimensional model and results obtained from it are discussed here.

6.1 METHODOLOGY

The process of developing a numerical model of CCGA involves establishing the flow domain, meshing the flow domain, applying the boundary condition, solving the governing equations and post-processing the results obtained.

6.1.1 Establishing the numerical domain

One of the main limitations in the three-dimensional models of CCGA is the computational requirement and a large number of numerical models of CCGA developed are in two-dimension. A full three-dimensional model of a discrete jet atomizer with domain dimensions of 60*24 will result in around 40 million cells with 0.1 mm element size. This is a huge requirement and pose a serious limitation on developing a three-dimensional model. In order to circumvent this issue, a periodic model has been used in this study. Three dimensional periodic models are extremely useful for simulating the behaviour of macro-scale systems of fluids and solids by reducing the computational requirement. Also, in a periodic model, the linear momentum of the system is conserved whereas the angular momentum is not.

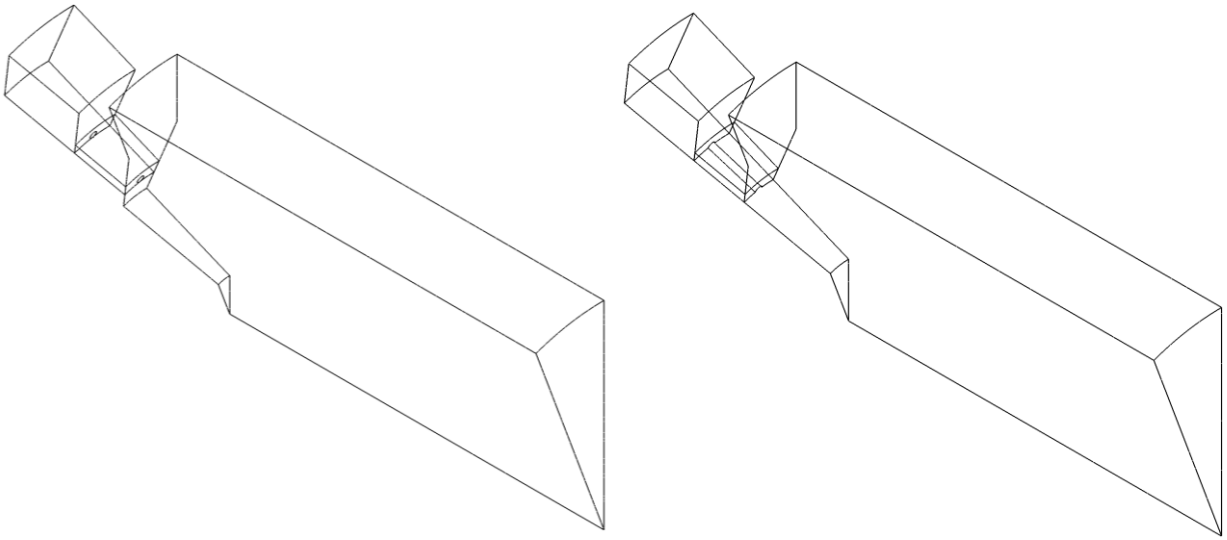

Conventional DJ atomizer Novel DJ atomizer

Figure 6.5 Schematic representation of the flow domain for both the designs in isometric view.

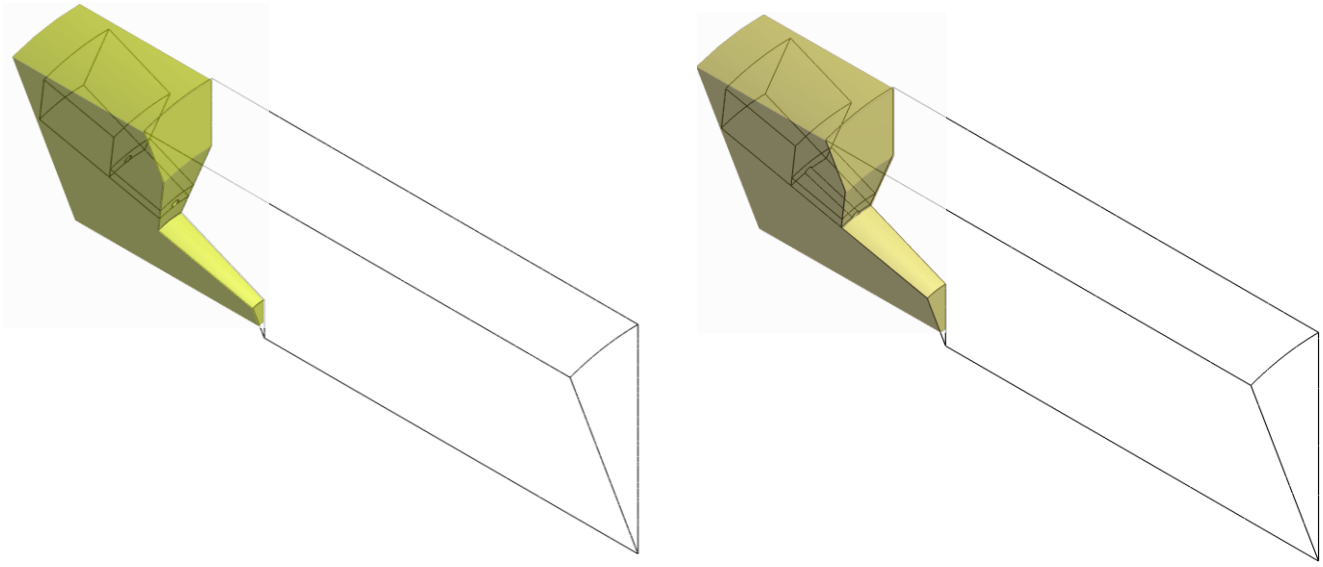

Conventional DJ atomizer Novel DJ atomizer

Figure 6.6 Schematic representation of the flow domain overlapped with a period of the nozzles

Periodic models are utilized to solve those flows that have a periodically repeating pattern. There are two types of periodic boundary conditions available in ANSYS fluent. The first type does not allow pressure drop across the periodic planes and the only one input required for this boundary condition is whether the geometry is rotationally or translationally periodic. The second type allows a pressure drop to occur across the periodic planes and requires the value of the pressure jump along with the type of periodicity.

Both the discrete-jet atomizer designs have 18 equispaced discrete holes and are periodic in nature. A rotational periodic boundary condition can be used in both these cases in order to

reduce the computational requirement. As there are 18 discrete holes, the domain can be divided into 18 periods with periodic angle of 20 degree. No pressure jump condition has utilized in this study.

The domain dimensions of the two-dimensional model were 60*24 mm, and the same dimensions are adopted for the three-dimensional periodic models. The domains were created in polar cylindrical coordinate system. Figure 6.5 shows the isometric view of the rotational domain considered.

Figure 6.6 shows a period of the nozzle and the domain considered in the isometric view. As discussed in chapter 4 (section 4.1), the melt delivery tube is eliminated in this study as this is a single-phase analysis.

6.1.2 Mesh Generation

In order to determine the grid independence, four different meshes with uniformly sized tetrahedral elements were considered. Figure 6.7 shows the cross-section of the mesh through the gas-chamber, gas delivery tube and the area surrounding the melt nozzle.

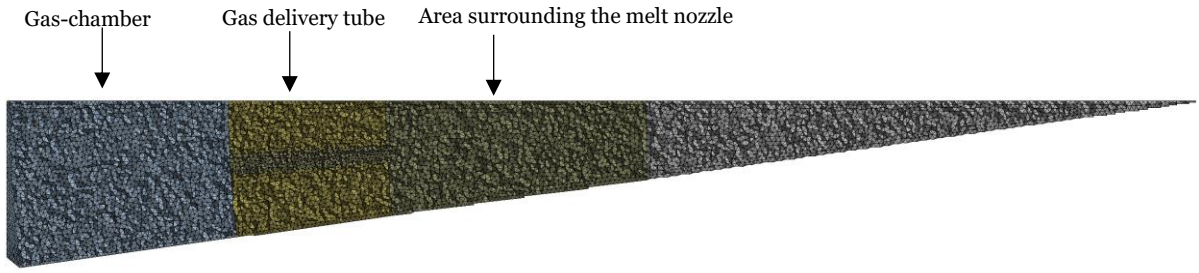

Figure 6.7 cross-section of mesh through the gas-chamber, gas delivery tube and area surrounding the melt nozzle

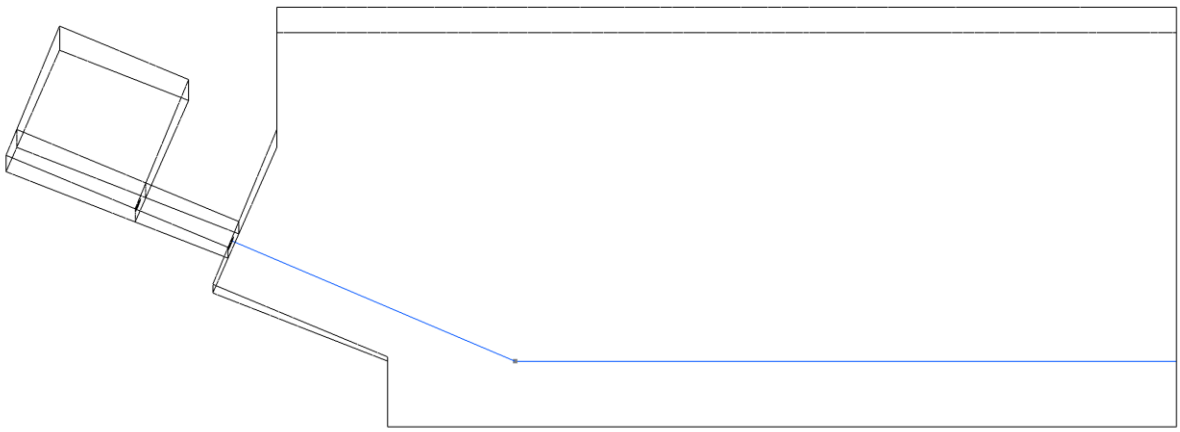

Figure 6.8 Schematic representation of the side-view of the flow domain and the location of the rake

A rake with 150 points passing through the region of high gradients was set up as shown in the Figure 6.8 and the velocity along the rake was analysed.

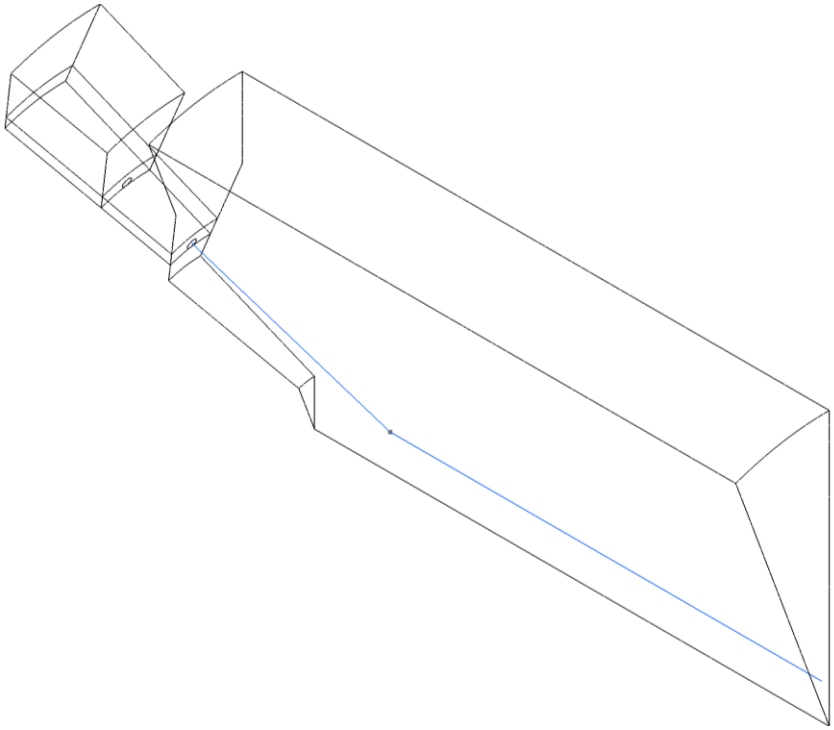

Figure 6.9 Schematic representation of the side-view of the flow domain and the location of the rake

Figure 6.9 shows the isometric view of the rake in the flow domain. A part of the rake passes through the cross-section shown in the Figure 6.7.

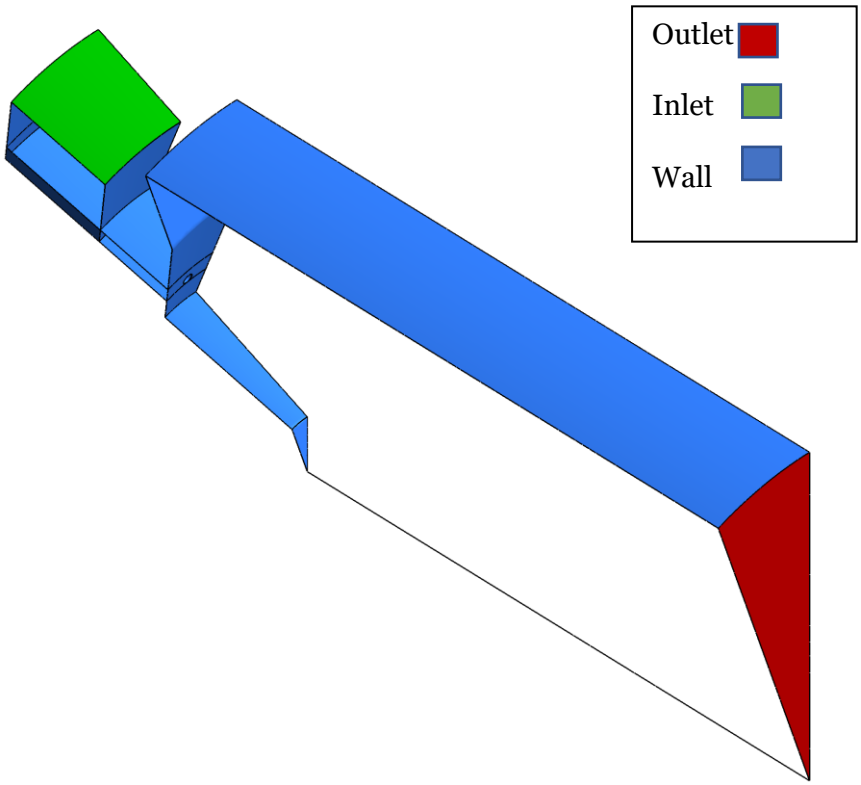

Figure 6.10 Schematic representation showing different boundaries used in this study

6.1.3 Material used:

Argon has been used in this study as the CERAM atomizer uses argon to atomize Raney nickel. The usage of argon has been discussed in section 4.1.3

6.1.4 Boundary conditions:

The boundary conditions used in the two-dimensional studies has been adopted in this study too. Figure 6.10 shows the boundary conditions used to define both the domains. The periodic boundaries are defined as periodic and shadow regions.

6.1.5 General Setup

The two-dimensional gas-only model was solved with standard k-ω model and second order discretization. Therefore, the same has been utilized in this study also.

The analysis is based on the following assumptions in order to simplify the calculations:

- Flow is considered to be steady state.
- Flow is considered 3D periodic.
- The fluid is considered as argon and modelled as a compressible ideal gas with specific heat ratio $\gamma = 1.66$.
- The impact of the molten metal is not considered.
- For presentation purpose, the model is rotated 90 degree anticlockwise so that the atomization direction is changed from vertically downwards to horizontal as seen in Figure 4.2.

6.2 RESULTS AND DISCUSSION

The process of developing a robust three-dimensional model to simulate CCGA involves grid convergence study, choosing appropriate boundary condition and domain dimensions. The mesh independence study is discussed in the first section followed by the results obtained for both the atomizer nozzles.

6.2.1 Mesh Independence study.

Four different meshes was considered in this study. All the meshes had tetrahedral elements of uniform size. The mesh independence was carried out with standard k-ω model and second order discretization at 3 MPa operating pressure. Table 6.1 shows the element size, number of elements and degree of fineness of all the meshes considered.

Table 6.1 Element size and the corresponding number of elements and the degree of fineness of all the meshes considered in this study

Element size	Number of elements	Degree of fineness
0.1 mm	9580734	Finest
0.15 mm	2964980	Finer
0.22 mm	1331331	Coarser
0.44 mm	230695	coarsest

Figure 6.9 shows the rake along which the mesh independence study was carried out. The variation in velocity along the rake was calculated for all the meshes considered and plotted in a graph. Figure 6.11 shows the variation of velocity along the rake vs the x-position. The mesh with element size 0.15 mm (finer mesh) produces a solution that does not change much with reduction in element size. The velocities vary between 0.05-7% between the finer and the finest mesh. Finer mesh (element size 0.15 mm) has been chosen for this study, in order to reduce the computational requirement.

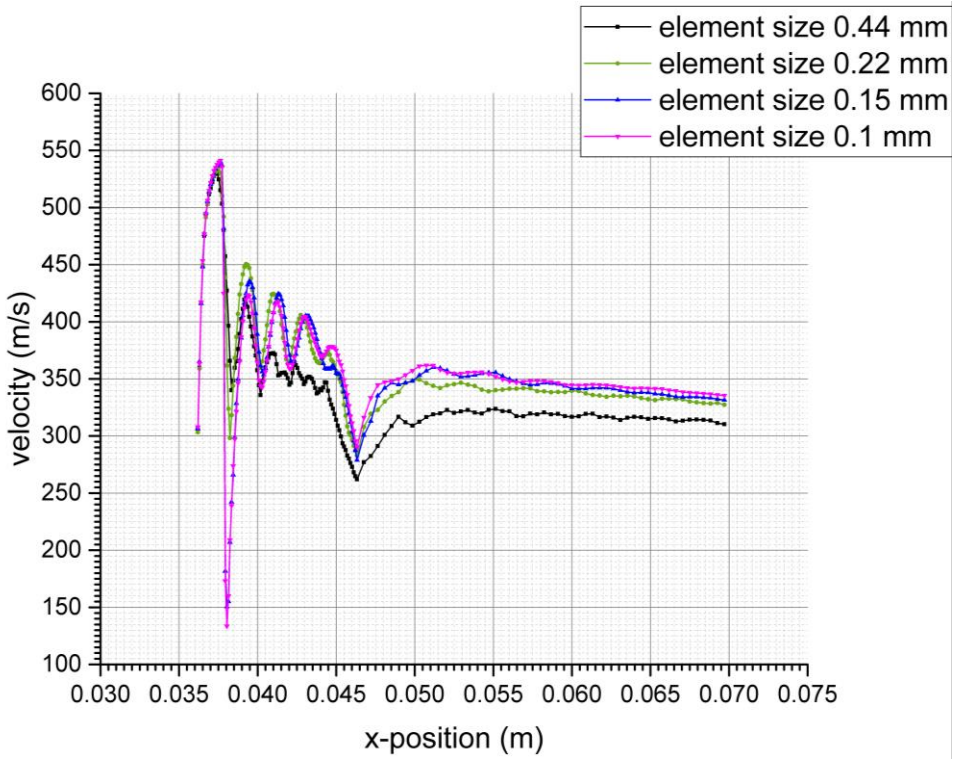

Figure 6.11 Graph showing the variation of velocity along the rake in all the four meshes.

All the simulations were carried out using Ansys 17.1 in a workstation with 32 GB RAM and 64-bit Operating system. Typical run time for each case was about 168 hours. All settings used to generate results are shown in Table 6.2.

Table 6.2 Settings used to generate results in this study

Setting	**Option**
Solver type	Density-based
Velocity formulation	Absolute
Time	Steady
Energy	On
Turbulence models	Standard k-ω
Formulation	Implicit
Flux type	Roe-FDS
Spatial Discretization	Second Order Upwind
URF Turbulent kinetic energy	0.8
Specific dissipation rate	0.8
Turbulent viscosity	1
Solid	1
Initialization	Hybrid

6.2.2 Flow dynamics for the conventional discrete jet atomizer

The first nozzle considered in this study is the conventional discrete jet atomizer. As the flow is choked in the gas tube in the conventional discrete jet atomizer, the flow develops as a Poiseuille flow and begins expanding into intermittent spacing and offset distance.

The same range of operating pressure used in two-dimensional analysis is adopted in this study also. The various flow features related to different operating pressures are discussed here.

1 MPa operating pressure:

The first pressure discussed in this study is 1MPa operating pressure. This pressure produces an open wake. Figure 6.12 shows the velocity contour plots in cross-sectional view and isometric view. The gases travel through sonic velocity in the gas tube. On exiting the gas tube, the gases begin travelling towards the outlet through a series of expansion waves and oblique shocks. The gases acquire velocity through expansion waves and lose velocity on interaction with the oblique shocks.

The gases attain sonic velocity as they reach the melt nozzle edge and therefore do not form any additional shocks downstream the melt nozzle. The gases travel with velocities equal to or lesser than the sonic velocity towards the outlet.

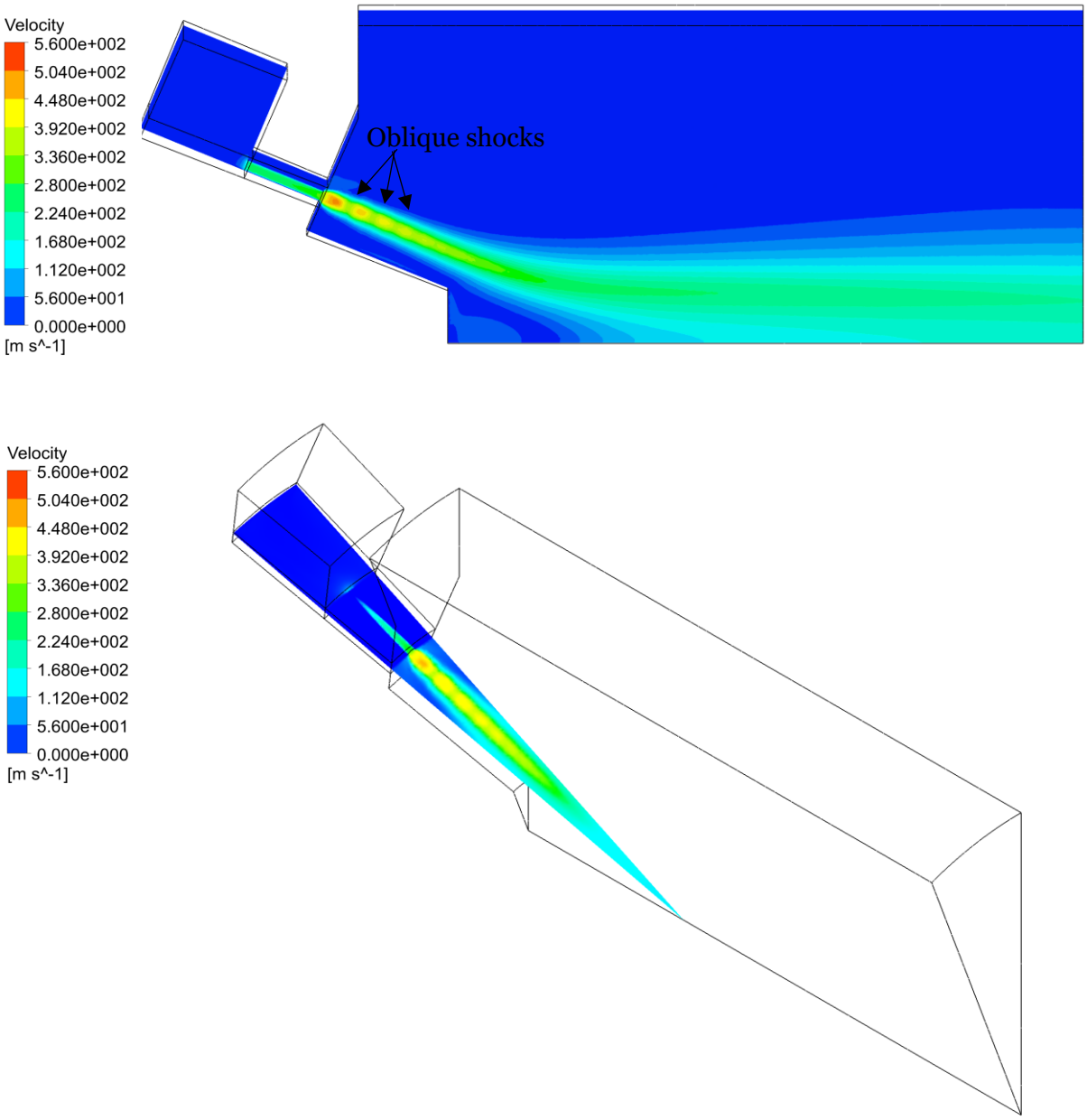

Figure 6.12 Velocity contour plots for 1MPa atomizing pressure in side-view and isometric view

Also, the expanding gases converge along the axis and form a recirculation zone in front of the melt nozzle as seen in the Figure 6.12. Also, the expanding gases from a discrete jet begin interacting with the expanding gases from the neighbouring jets from the fourth oblique shock.

Figure 6.13 shows the velocity vector plots for the 1MPa operating pressure. The recirculation zone is highlighted.

The aspiration pressure is calculated along the wall replacing the melt delivery tube by measuring the average pressure across the surface. The pressure calculated is a relative pressure (to the surrounding gases) and not absolute pressure at the point. The aspiration pressure is 7.178 kPa. This is an over ambient pressure and the common practice in the

industry is to maintain the melt at a pressure higher than the aspiration pressure to facilitate its entrance into the atomizing chamber.

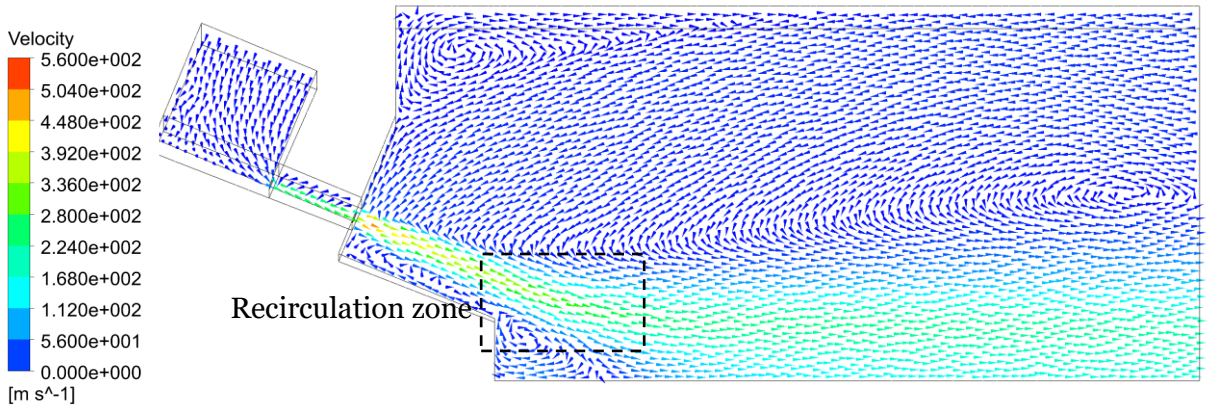

Figure 6.13 Velocity vector plots for 1MPa atomizing pressure in side- view

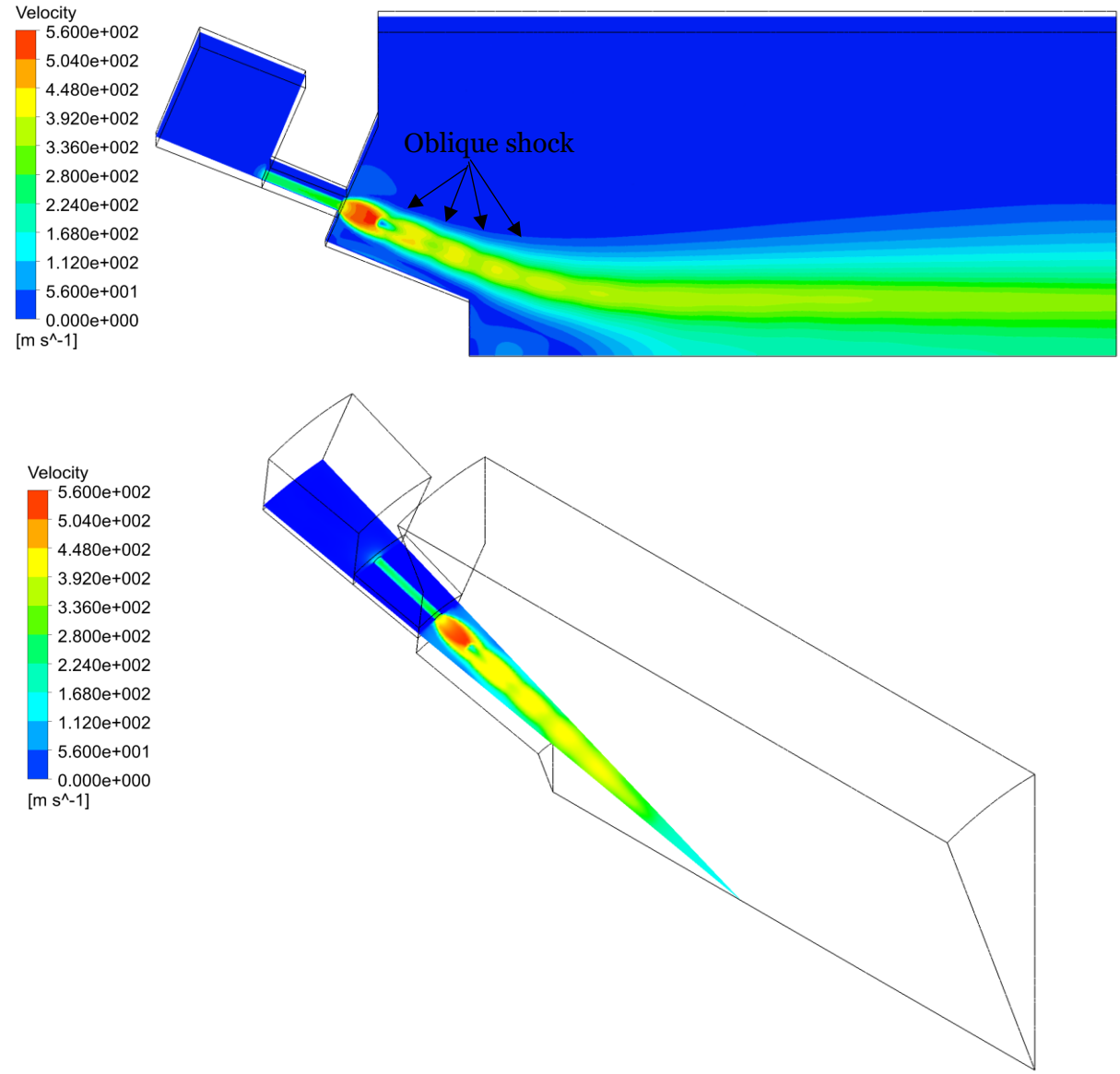

Figure 6.14 Velocity contour plots for 3MPa atomizing pressure in side- view and isometric view

3MPa operating pressure

The next pressure considered in this study is 3MPa operating pressure. This is a commonly used industrial pressure. This pressure forms an open wake. Figure 6.14 shows the velocity contour plots in cross-sectional view and isometric view. As the difference between the operating pressure and the ambient pressure is higher than the previous pressure (1MPa), the gases undergo increased expansion, and it can be seen from the Figure 6.14. The gases travel further downstream the melt nozzle as compared to the 1MPa operating pressure before reaching the sonic velocity.

The increased expansion of the gases can be seen in both the cross-sectional view and isometric view. The gases travel towards the outlet without forming any shocks on reaching the sonic velocity. The gases on the outermost layer of expansion waves on the near side of the melt nozzle form a recirculation zone on converging along the axis.

The expanding gases begin interacting with the other expanding gases from the neighbouring jets from the second oblique shock. Figure 6.15.

Aspiration pressure is calculated for this case too and is found to be 19.264 kPa which is over ambient. The melt has to be maintained at a pressure higher than the aspiration pressure so that it enters the atomizing chamber.

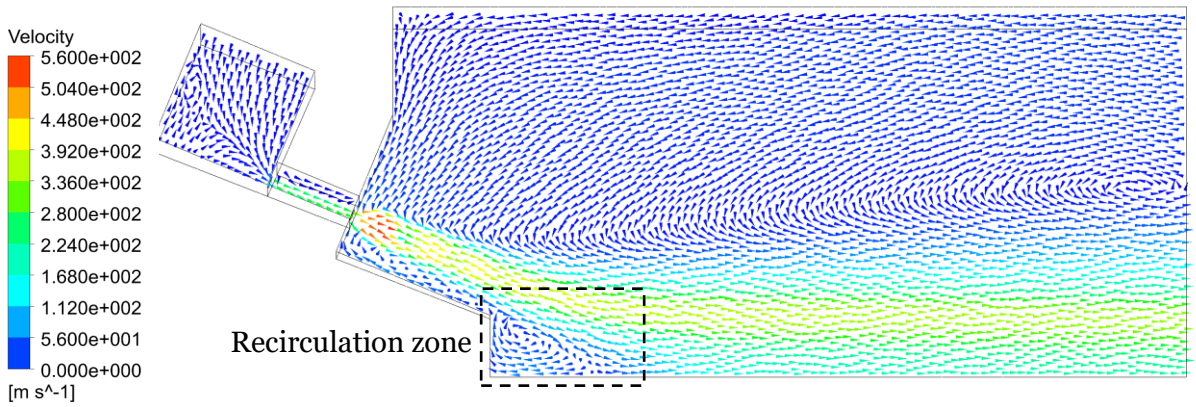

Figure 6.15 Velocity vector plots for 3 MPa atomizing pressure in side- view

4.5 MPa operating pressure

The third pressure considered in this study is 4.5 MPa operating pressure. A closed wake is observed, and a Mach disk is formed in front of the melt nozzle as the flow forms oblique shocks with sufficient strength to form a normal shock on interaction with other oblique shocks. Figure 6.16 shows the cross-sectional view and the isometric view of the velocity contour plots.

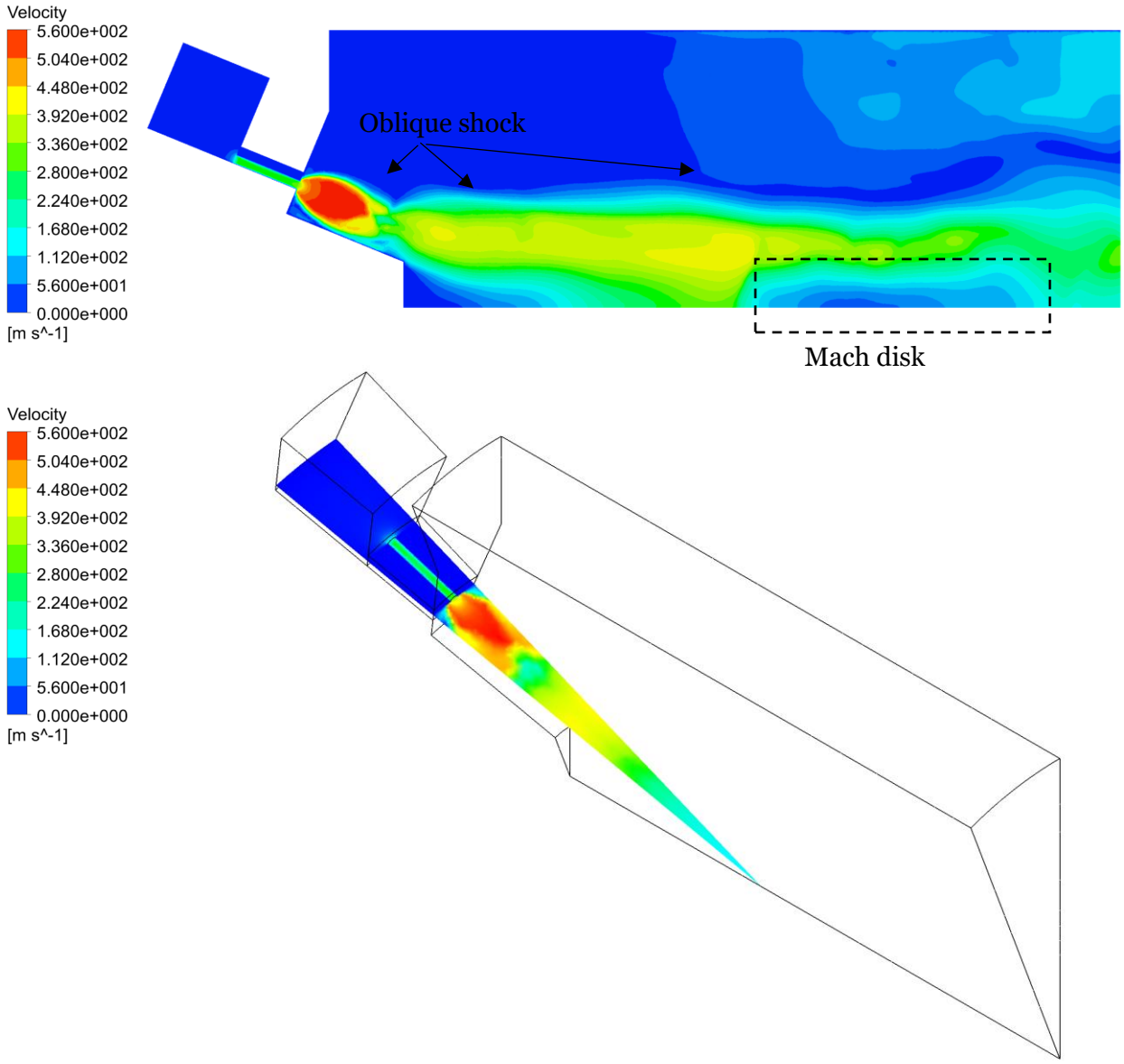

Figure 6.16 Velocity contour plots for 4.5 MPa atomizing pressure in side-view and isometric view

The expanding gases begin interacting with the other expanding gases within the first oblique shock. Figure 6.17 shows the velocity vector plots in the cross-sectional view. The gases begin expanding on exiting the gas delivery tube. The aspiration pressure is measured as -40.21 kPa. This is a sub ambient pressure and results in melt being drawn into the recirculation zone. In the two-dimensional gas-only study (chapter 4), a range of pressures were considered, and the wake closure pressure was found. Due to computational requirements, a limited range of pressures were only considered and hence 4.5 MPa cannot be assumed as wake closure pressure as no pressure between 3 MPa and 4.5 MPa were not analysed. Also, the non-zero velocities on the upper boundary wall are due to the computational resource limitation.

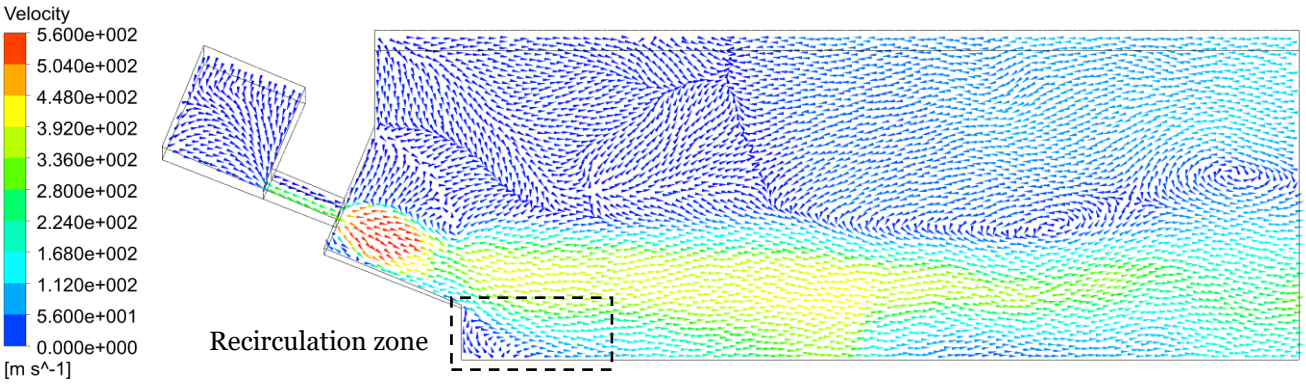

Figure 6.17 velocity vector plots for 4.5 MPa atomizing pressure in side-view

5 MPa operating pressure

This case is also a closed wake case, and a strong Mach disk is formed in front of the melt nozzle. A Mach disk is formed in front of the recirculation zone. The Mach disk is formed

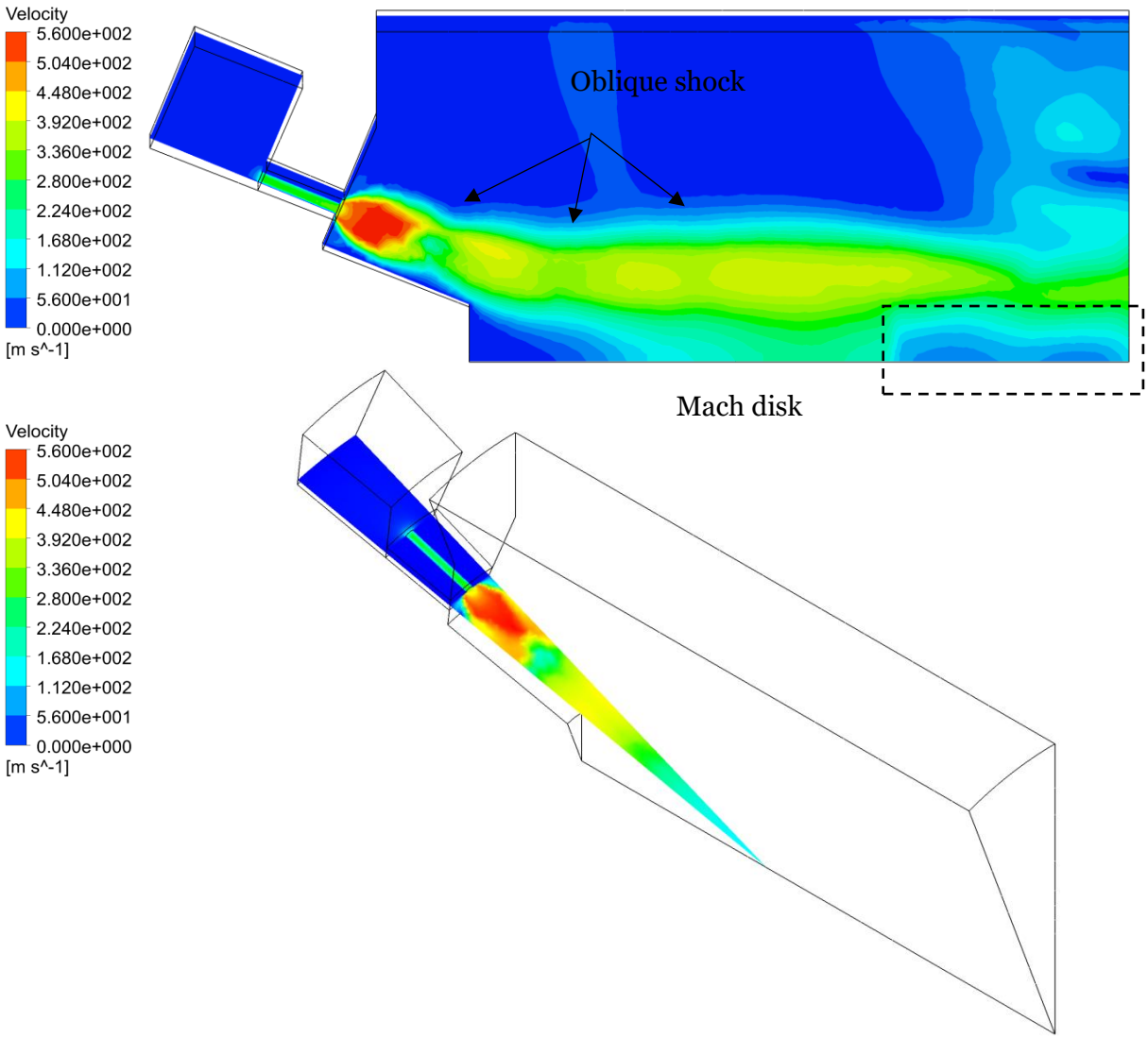

Figure 6.18 Velocity contour plots for 5 MPa atomizing pressure in side- view and isometric view

further downstream than the 4.5 MPa case as gases have more energy to over the resistance posed by the free boundary. The expanding gases begin interacting with the other expanding gases within the first oblique shock.

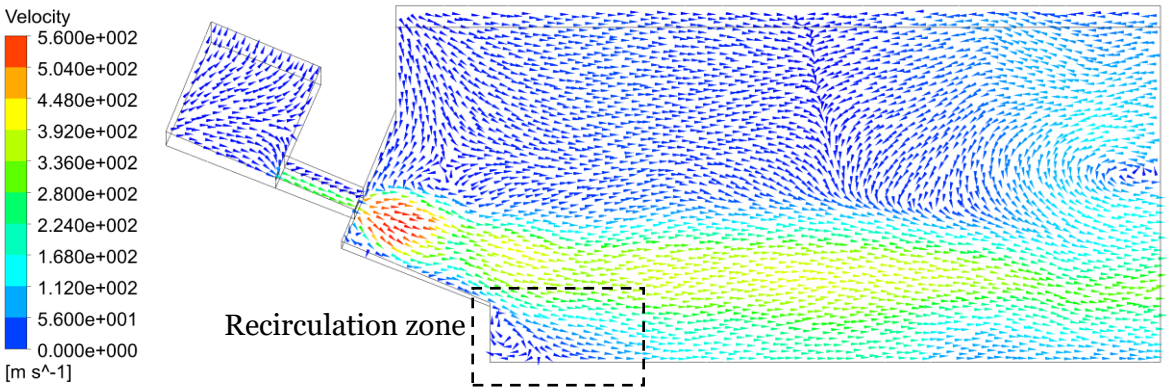

Figure 6.19 velocity vector plots for 5 MPa atomizing pressure in side- view

Figure 6.18 shows the cross-sectional view and the isometric view of the velocity contour plots. The expanding gases begin inte4racting with the other expanding gases with the first oblique shock. Figure 6.19 shows velocity vector plots for 5 MPa operating pressure. The aspiration pressure is measured as -51.879 kPa. This is a sub ambient pressure and results in melt being drawn into the recirculation zone. Figure 6.19 shows the velocity vector plots in the cross-sectional view. Also, the non-zero velocities on the upper boundary wall are due to the computational resource limitation.

6.2.3 Flow dynamics for the novel discrete jet atomizer

The second design considered in this study is the novel discrete jet atomizer as shown in Figure 6.2. The shape of the gas tube is semi-circular in this case and this affects the way the flow develops. The boundary layer developed in this flow can be divided into three – boundary layer developed on the melt nozzle surface (BL on flat plate), boundary layer developed across the curved surface of the pipe and the boundary layer formed in the corners. The BL interaction in the corners is passive in nature as they do not affect the flow structure, but the gases lose their velocity in this region.

The same range of pressures was adopted in this case also. As the exit area was reduced, the gas flow rate is also lesser than that observed in the previous design.

1MPa atomizing pressure

The first pressure considered is 1 MPa operating pressure. Figure 6.20 shows the isometric and cross-sectional view of the velocity contour plots.

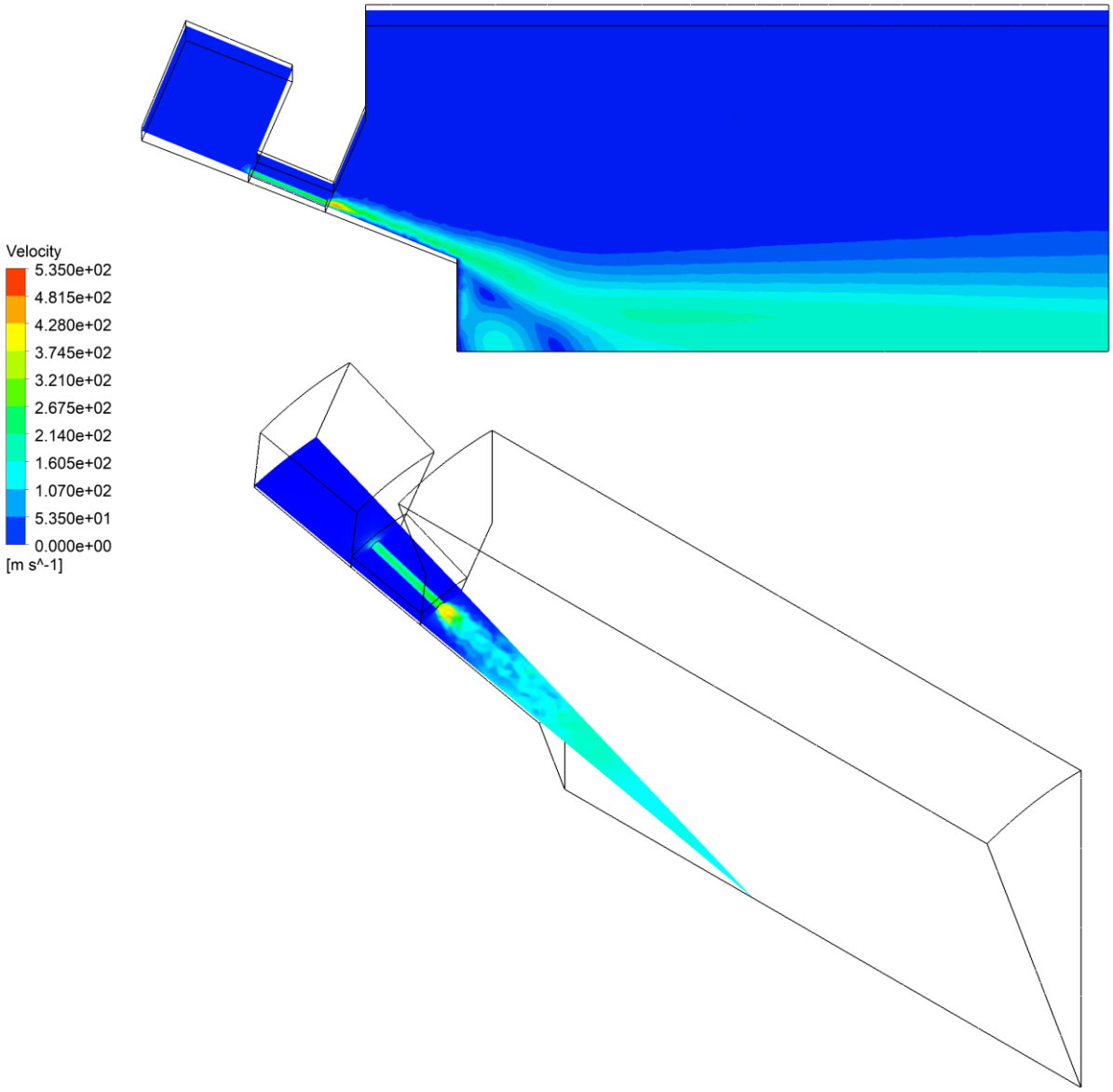

Figure 6.20 Velocity contour plots for 1 MPa atomizing pressure in cross-sectional and isometric view

The gases reach sonic velocities within a short distance due to the reduction in gas flow rate, intermittent spacing and boundary layer growth on the melt nozzle surface. On exiting the gas delivery tube, the gases begin expanding through expansion waves and reach sonic velocities rapidly. The gas flows along the melt nozzle and converge along the axis to form the recirculation zone. The gases travel towards the outlet without any significant expansion waves and oblique shocks. The aspiration pressure is found to be 8.9 kPa. This is an over ambient pressure that the melt needs to overcome to enter the aspiration pressure. Figure 6.21 shows the velocity vector plots for 1 MPa atomizing pressure in side-view.

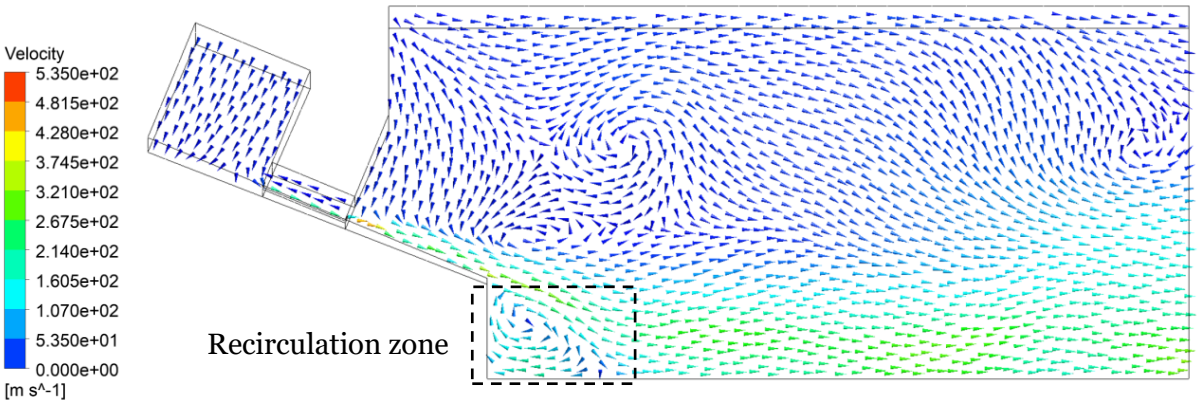

Figure 6.21 Velocity vector plots for 1 MPa atomizing pressure in side-view

3MPa atomizing pressure

The second pressure in this study is a 3 MPa operating pressure. The flow mechanism is similar to the previous pressure as this is also an open wake case. Figure 6.22 shows the cross-sectional and isometric view of the velocity contour plots. The gases undergo increased

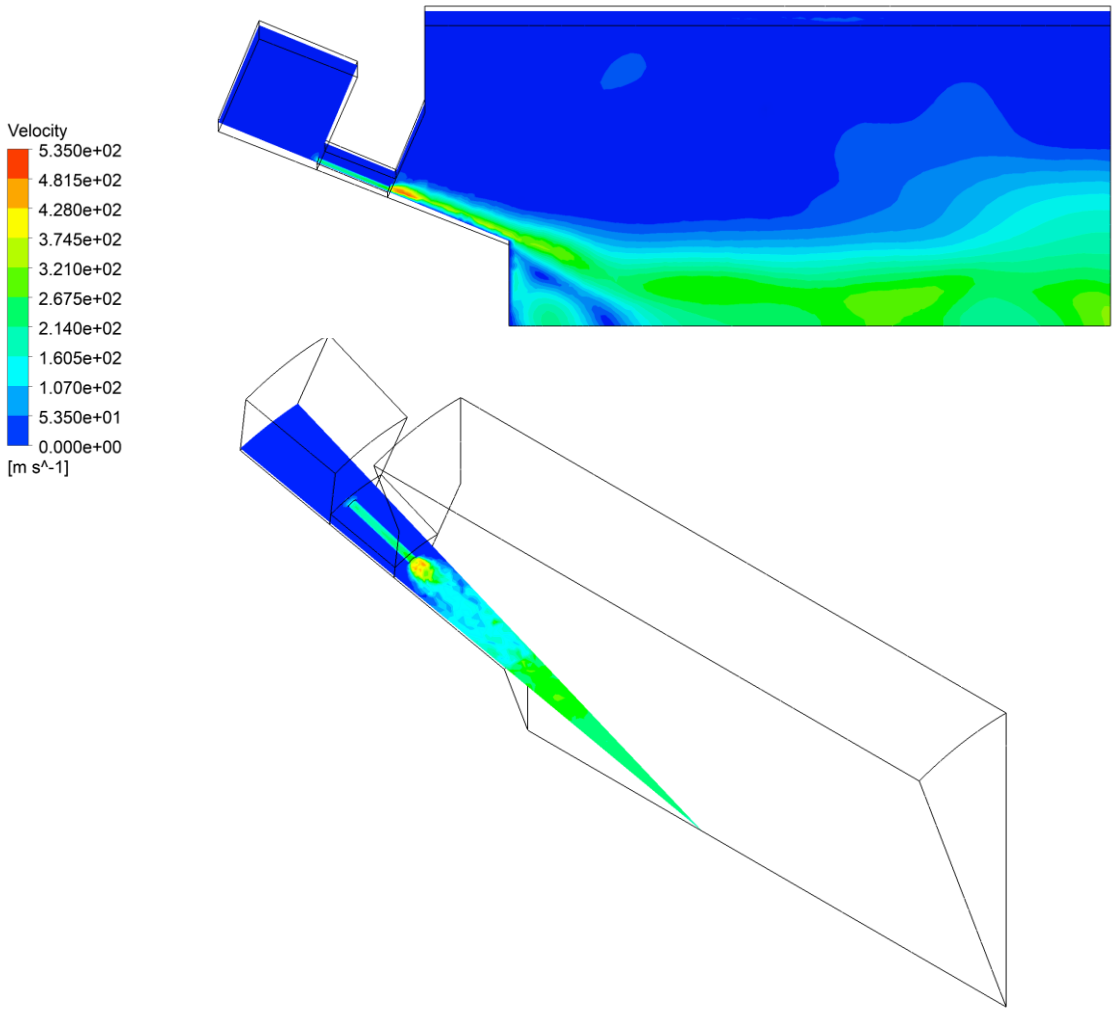

Figure 6.22 Velocity contour plots for 3 MPa atomizing pressure in cross-sectional and isometric view

expansion than those observed in 1MPa operating pressure case. The gases reach their sonic velocities along the melt nozzle and converge along the axis to form the recirculation zone. The gases travel towards the outlet through expansion waves and oblique shocks. The aspiration pressure is found to be 61.25 kPa. This is an over-ambient pressure and requires the melt to be maintained at a pressure higher than 61.25 kPa for the movement of melt into the atomization chamber. Figure 6.23 shows the velocity vector plots for 3MPa atomizing pressure.

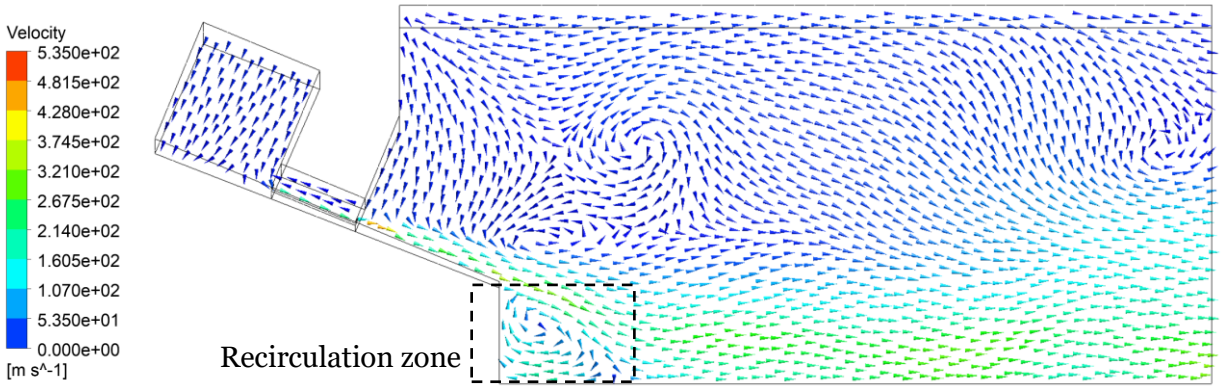

Figure 6.23 Velocity vector plots for 1 MPa atomizing pressure in side-view

4.5 MPa atomizing pressure

This pressure is a closed-wake case, and a Mach disk is observed in front of the melt nozzle. As in the previous case, the limitation of computational resources prevents a wide range of operating pressures (3 < P < 4.5) being analysed. The gases expand on exiting the gas die through a series of expansion waves and oblique shocks. Figure 6.25 shows the isometric view and the cross-sectional view of the velocity contour plots. The gases expand initially (1st expansion waves) to high velocities and come across the first oblique shocks. The gases

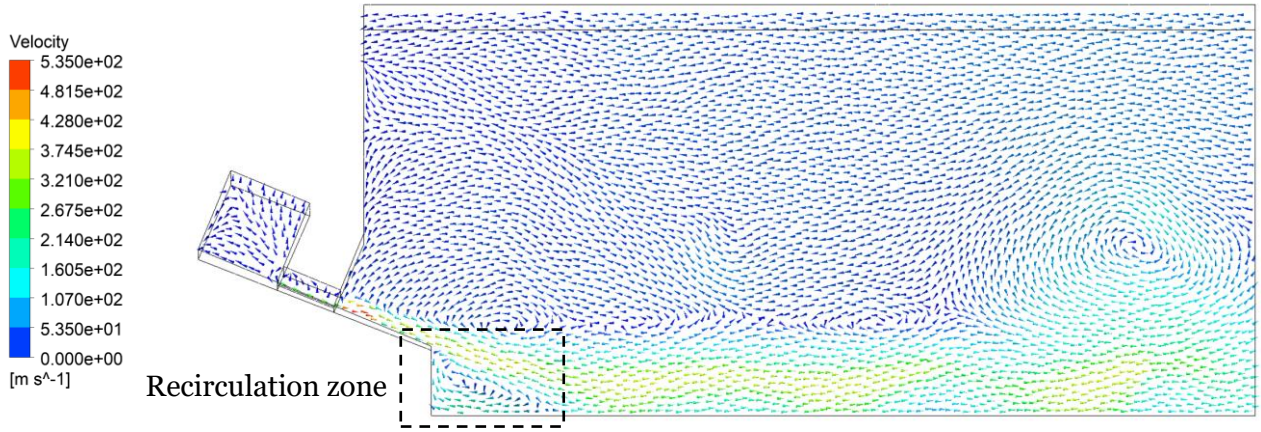

Figure 6.24 Velocity vector plots for 4.5 MPa operating pressure in side-view

undergo compression and lose their velocities. On crossing the oblique shock, the gases begin accelerating as seen in the Figure 6.25. The gases converge along the axis to form the recirculation zone. The gases travel towards the outlet through series of expansion waves and

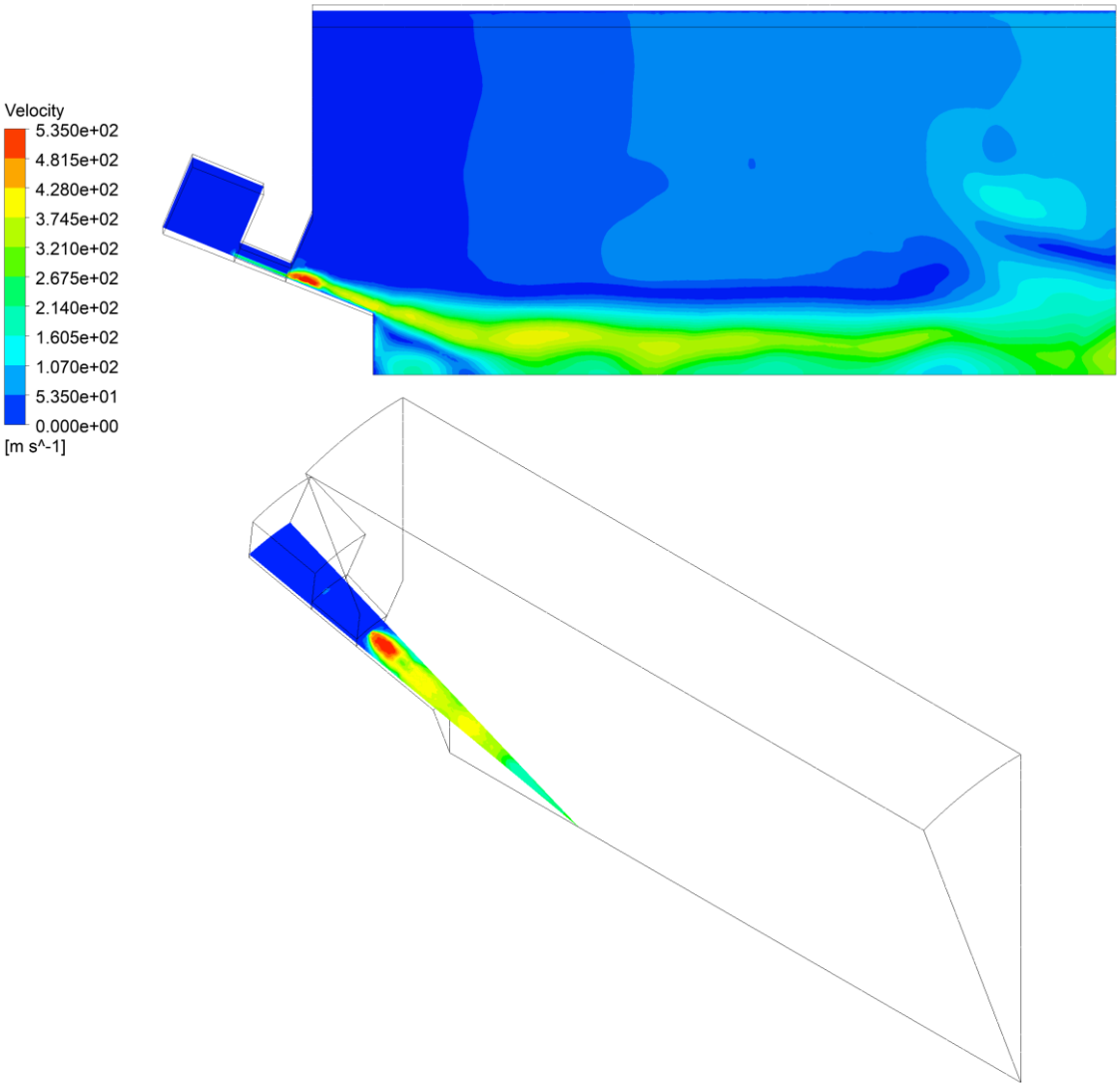

Figure 6.25 Velocity contour plots for 4.5 MPa atomizing pressure in cross-sectional and isometric view

oblique shocks leading to the formation of Mach disk in front of the melt nozzle downstream the recirculation zone. The aspiration pressure is found to be -13.588 kPa. This is sub-ambient, and the melt will be drawn into the recirculation zone. Figure 6.24 shows the velocity vector plots for 4.5 MPa atomizing pressure.

5 MPa atomizing pressure

This pressure is also a closed-wake case. Two Mach disks are observed in this case. A Mach disk is formed as a result of strong oblique shocks converging to form a single normal shock. The gases reach their highest velocities in the first expansion wave. The gases lose their velocity on reaching the first oblique shock but begin gaining velocity on crossing the oblique shock.

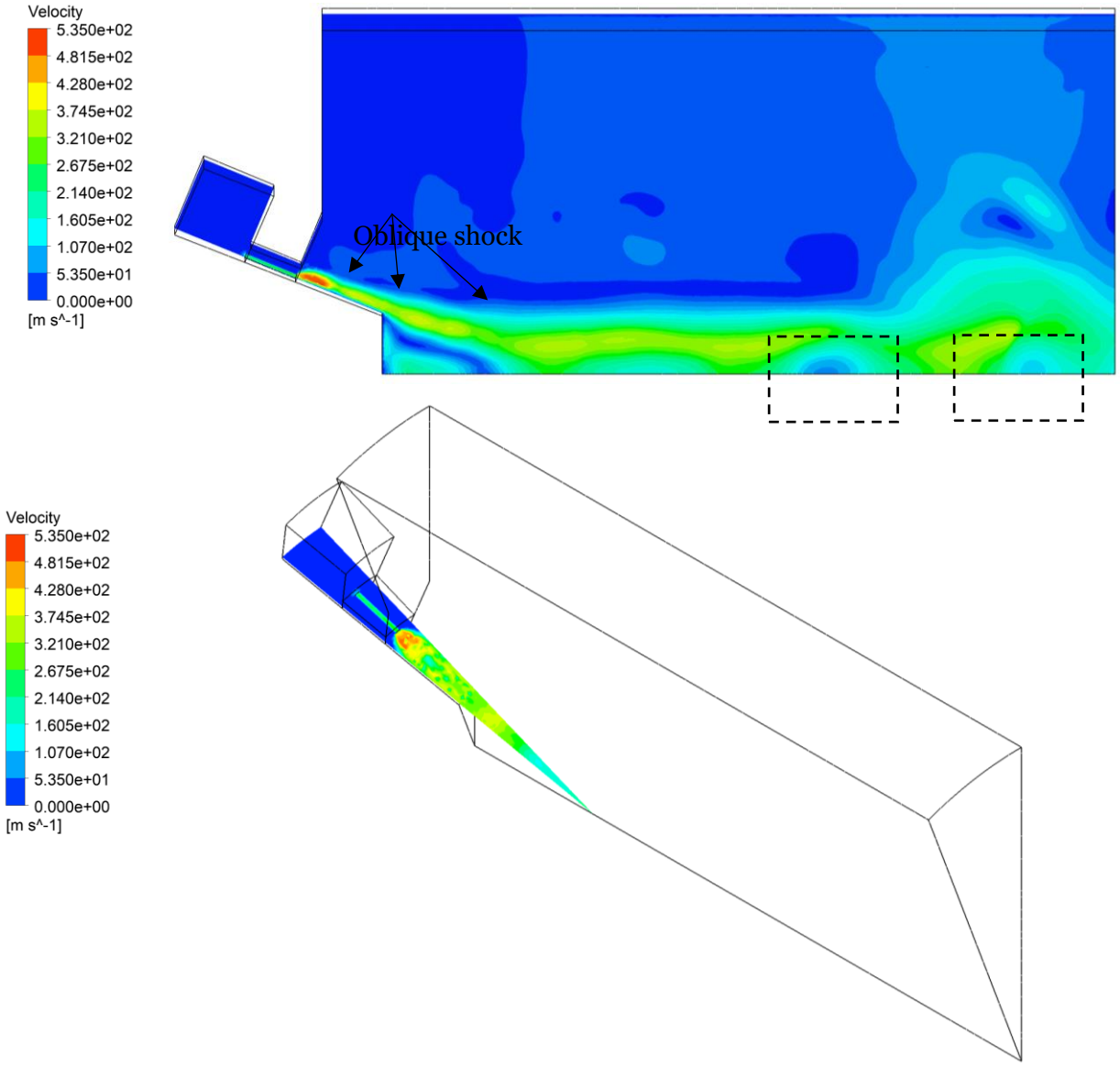

Figure 6.26 Velocity contour plots for 5 MPa atomizing pressure in cross-sectional and isometric view

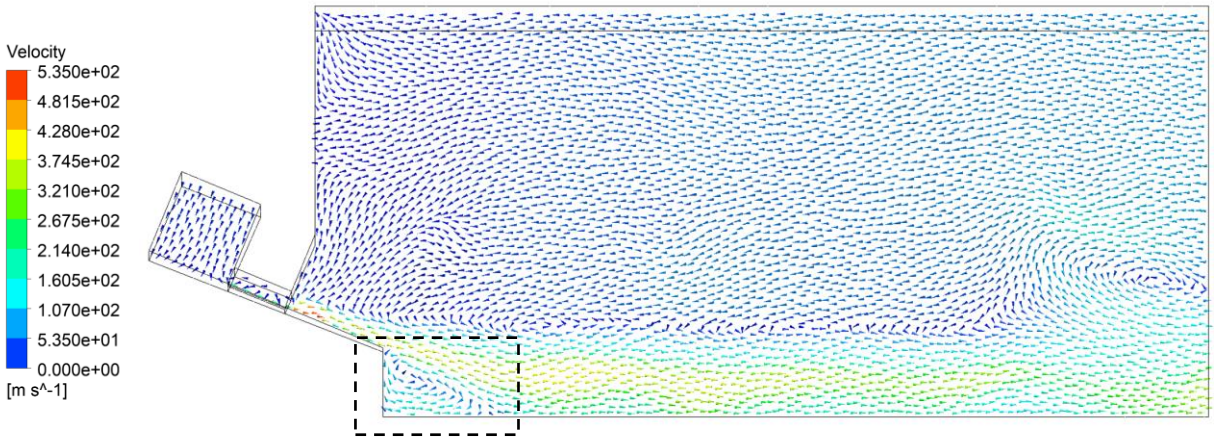

Figure 6.27 Velocity vector plots for 5 MPa operating pressure in side-view

The gases form a recirculation zone on converging along the axis. The gases travel towards the outlet through a series of expansion waves and oblique shocks.

A Mach disk is formed as seen in the Figure 6.26. The gases overcome the Mach disk and form the next Mach disk as seen in the Figure 6.26. A sub ambient aspiration pressure of -17.49 kPa is observed in this case facilitating the melt movement into the atomization chamber. Figure 6.27 shows the velocity vector plots for 5MPa atomizing pressure.

Summary

Two atomizer designs were considered in this study. A periodic flow domain with dimensions 60*15 mm was adopted, and a mesh independent study was carried out. A mesh with 0.165 mm elements was found to be produce results independent of element size. A range of pressures was analysed and wake conditions for all considered pressures in each case have been found. The aspiration pressure for every pressure was also found. The steady state was found when the residuals oscillated around a specific value as they did not converge.

7 NEED FOR THREE-DIMENSIONAL MODEL

Methodology, Research and Discussion

Three-dimensional periodic models have been developed in the chapter 6 to analyse the flow features in discrete-jet atomizers. Two-dimensional axisymmetric model was developed in chapter 4 to analyse the flow features in annular-slit atomizers. Figure 7.1 shows the bottom view of annular slit and discrete jet atomizer. The annular slit designs are axisymmetric in nature. The gas jets exiting the gas die will also expand axisymmetrically. Therefore, a two-dimensional model was sufficient to simulate the gas only flow field to capture the flow features in annular slit designs.

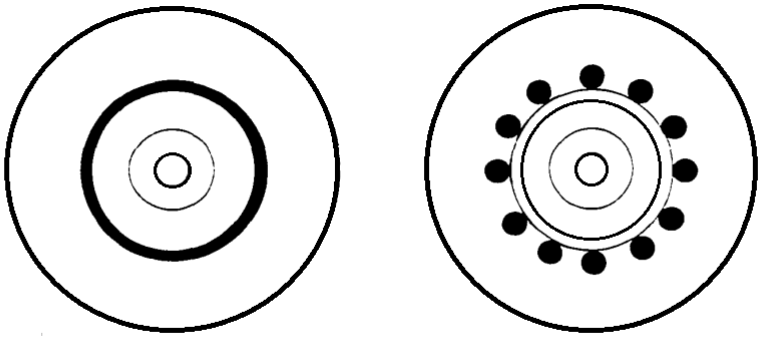

Figure 7.1 Bottom view of annular-slit design and discrete-jet design

In a discrete jet atomizer, the absence of axisymmetry due to the set of discrete gas jet holes spaced equally around the melt nozzle through which the gas exits. A two-dimensional model to represent this atomizer will have to be based on approximations as the geometry is not axisymmetric like annular slit atomizer. The various approximations were considered in this chapter and the results were compared with the results obtained in chapter 6.

7.1 METHODOLOGY

In a discrete jet atomizer, the holes through which the gases exit are located at a distance from the melt nozzle and this offset must be incorporated into the model. The flow domain for this study was created in cylindrical coordinate system. The dimensions of the domain are same as the domain used in single phase flow analyses with the incorporated offset length. Figure 7.2 Schematic representation of the numerical domain used in this study. shows the numerical domain used in this study.

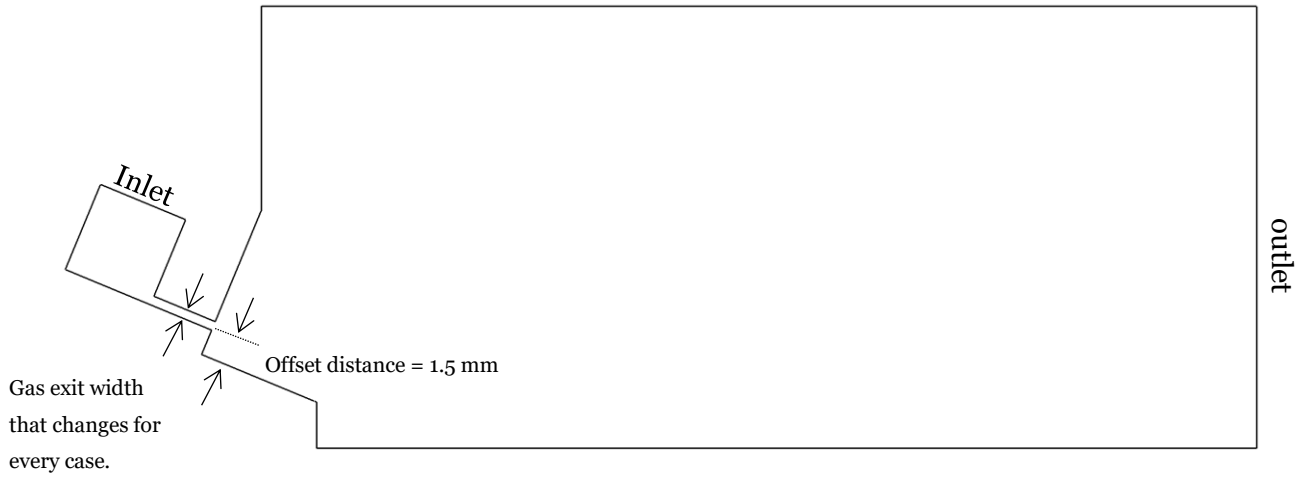

Figure 7.2 Schematic representation of the numerical domain used in this study.

A structured mesh is used in this study. A grid independence study was not taken for this specific analysis as the dimensions are same throughout except for the gas exit width and the mesh used previously was found to be sufficient to capture the changes in the flow. The standard k-ω turbulence model and air were chosen for this study. A density-based solver was used to generate results.

The assumptions for this model are:

- Flow is considered to be steady state.
- Flow is considered 2D axis-symmetric.
- The fluid is considered as argon and modelled as a compressible ideal gas with specific heat ratio $\gamma = 1.66$.
- The impact of the molten metal is not considered.
- For presentation purpose, the model is rotated 90 degree anticlockwise so that the atomization direction is changed from vertically downwards to horizontal.

All the simulations were carried out using Ansys 17.1 in a workstation with 32 GB RAM and 64-bit Operating system. All settings used to generate results are shown in Table 7.1

Table 7.1 Settings used to generate results in this study

Setting	**Option**
Solver type	Density-based
Velocity formulation	Absolute
2D space	Axisymmetric
Time	Steady
Energy	On

Turbulence models	Standard k-w
Formulation	Implicit
Flux type	Roe-FDS
Spatial Discretization	Second Order Upwind
URF Turbulent kinetic energy	0.8
Specific dissipation rate	0.8
Turbulent viscosity	1
Solid	1
Initialization	Hybrid

7.2 RESULTS AND DISCUSSION

As the discrete jet atomizers are not axisymmetric like annular slit atomizer, the two-dimensional model of such atomizers must include approximations to simulate the intermittent spacing between the discrete jets. Three different cases of approximations were considered in this study. In each case, either a geometrical parameter or process parameter was approximated to match that of the discrete jet atomizer's parameter.

Case 1: Width approximation

In the first case, the width of the gas jet tube was set at 0.5 mm which is the diameter of the discrete-jet holes. Figure 7.3 shows the velocity contour plots for the periodic model and the annulus model [2D model] with width of 0.5 mm at the operating pressure 3 MPa.

It can be seen from the Figure 7.3 that the gases expand markedly different in the two cases and the shocks are located further downstream in the axisymmetric model than in the periodic model. Also, this model produced closed wake whereas periodic model did not. The mass flow rate of the gas entering the atomizing chamber depends on the exit area of the gas die. The gas flow rate for this case was measured at 0.1690651 kgs^{-1}. As the slit width was set to be equal to the diameter of the discrete holes (0.5 mm), the exit area of this case is much higher than the exit area of the discrete jet atomizer. This increase in the exit area leads to an increase in the mass of the gas entering the atomization chamber (0.04167 kgs^{-1}) and thereby affects the flow features and the GMR of the process. Therefore, this is not a feasible approximation to simulate the flow features in discrete jet atomizer.

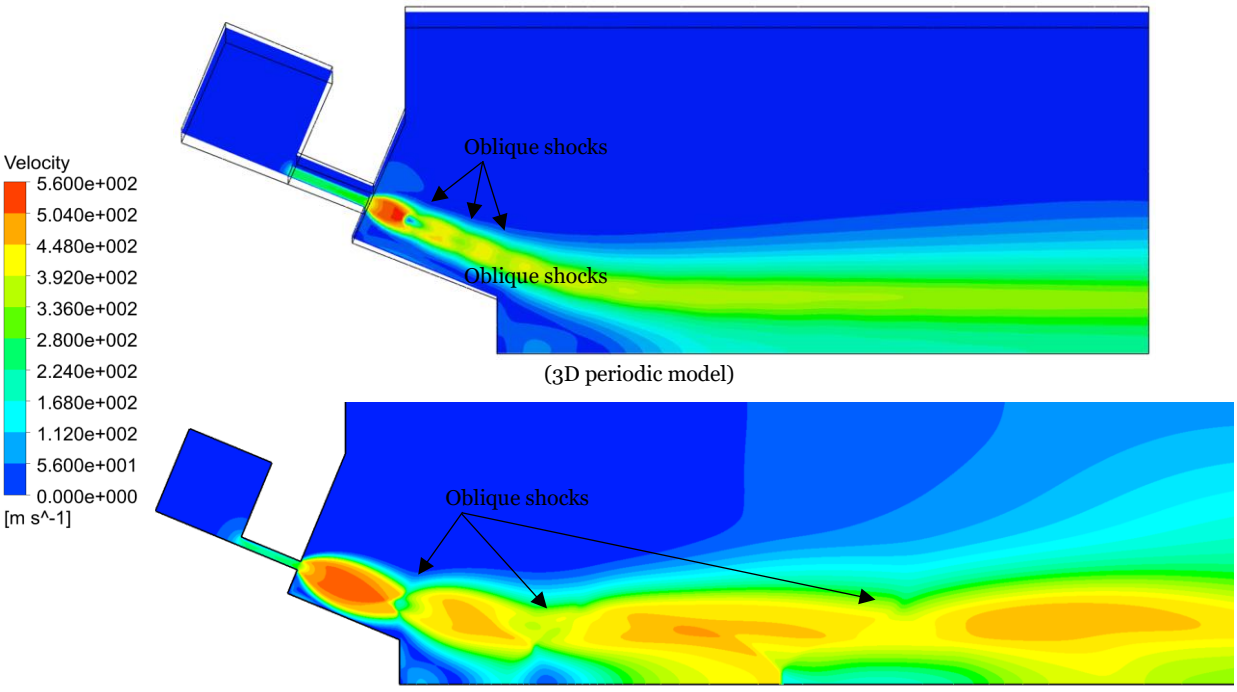

Figure 7.3 Velocity contour plots for the (a) periodic model and (b) axisymmetric model with gas tube width = 0.5 mm at 3 MPa operating pressure

Case 2: Area approximation

The second case considered in this study approximated the exit area. The surface area of the annular slit was matched to the total exit area of the discrete jets and the flow field was analysed.

Total surface area of the discrete jet delivery system is given by

$$A_{dJ} = 18 * \pi r^2$$

As the radius is 0.25 mm, $A_{dJ} = 1 \cdot 125\pi$ (mm²)

Total surface area of the annulus is given by

$$A_{AS} = \pi[R^2 - r^2]$$

$$A_{dJ} = A_{As}$$

The inner radius of the annulus is 6.4 mm. Therefore, the outer radius of the annulus is obtained as 6.5 mm and the width is calculated as 0.1 mm. The diameter of the discrete jets is 0.5 mm. It can be seen that the width of the gas exit must be reduced to 0.1 mm in order to approximate the exit area in the two-dimensional model.

Figure 7.4 shows the velocity contour plots for the periodic model and the axisymmetric model with width of 0.1 mm at the operating pressure 3 MPa. Though the gas exit area is the same as the discrete jet atomizer, the absence of the intermittent spacing in this model leads to reduction in the width of the exit. This in turn influences the mass flow rate of the gas entering the atomizing chamber. The gas flow rate was found to be 0.0104379 kgs^{-1} and this low gas flow rate affects the Gas Melt Ratio of the process. It can be seen from the Figure 7.4 that the flow features are different in this case and the shocks are located much closer to each other in the axisymmetric model than in the periodic model. Therefore, this model is also not a feasible approximation to simulate the discrete jet atomizer.

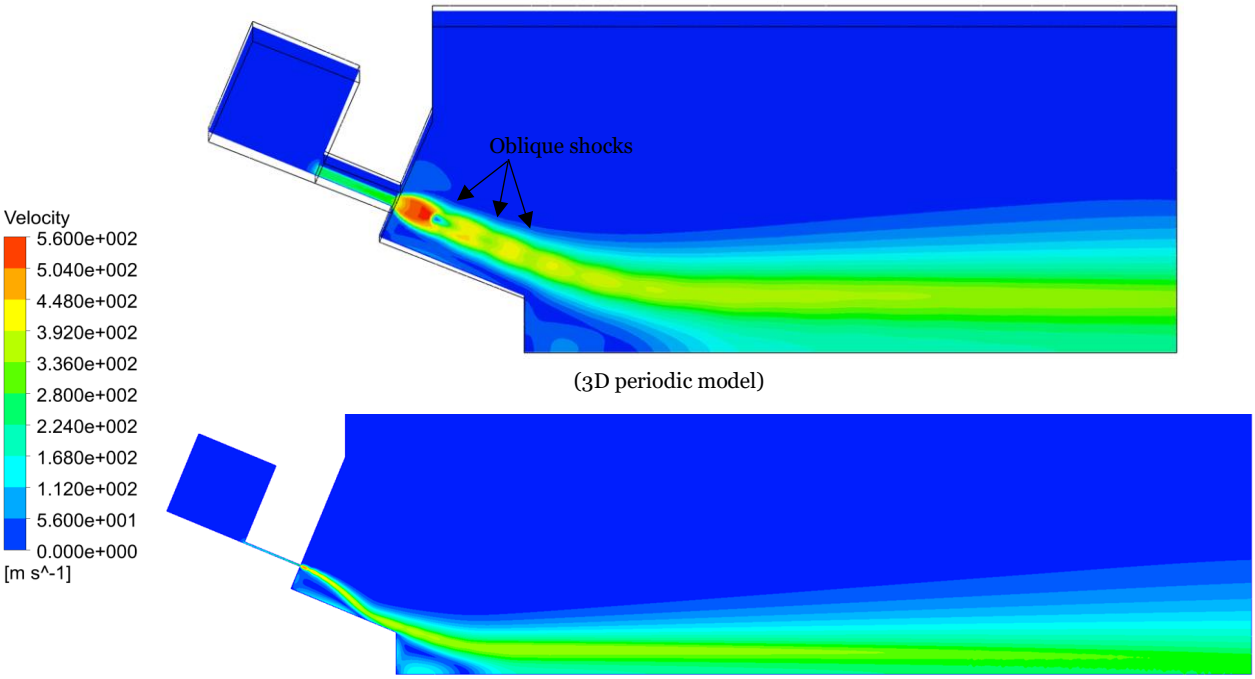

Figure 7.4 Velocity contour plots for the (a) periodic model and (b) axisymmetric model with gas tube width = 0.1 mm at 3 MPa operating pressure

Case 3: Volume flow rate approximation

The third case considered in this study deals with the mass flow rate. In the single-phase analysis (gas-only phase) and two-phase analysis, the atomizing gas was argon. The gas flow rate discrete-jet atomizer (CERAM) was found to be 2502 $gmin^{-1}$ (0.0417 kgs^{-1}), and this was matched in this case. The width of the annular slit in the model was found to be 0.21 mm for this case.

Figure 7.5 shows the velocity contour plots for the periodic model and the axisymmetric model with gas tube width 0.21 mm at 3 MPa operating pressure. Though the mass flow rate is matched, the expansion of the gas exiting through an annular slit is different from that of a discrete jet atomizer. The intermittent spacing in a discrete jet atomizer enables the gas to

undergo increased expansion compared to the annular slit atomizer. This difference in expansion influences the interaction of the gases with the free boundary and thus affects the location of shocks formed. This model predicts the shocks further downstream than it would be observed in the experimental work.

Gas flow rate is an important process parameter and impacts the GMR of the process. This is an interesting approximation as this can be utilized to an extent to simulate discrete jet atomizers and quantify the parameters depending on the mass flow rate (e.g. aspiration pressure) but the limitation of this model is in capturing the gas expansion accurately and its interaction with the free boundary. Therefore, this model is also not a feasible approximation to capture the flow features accurately.

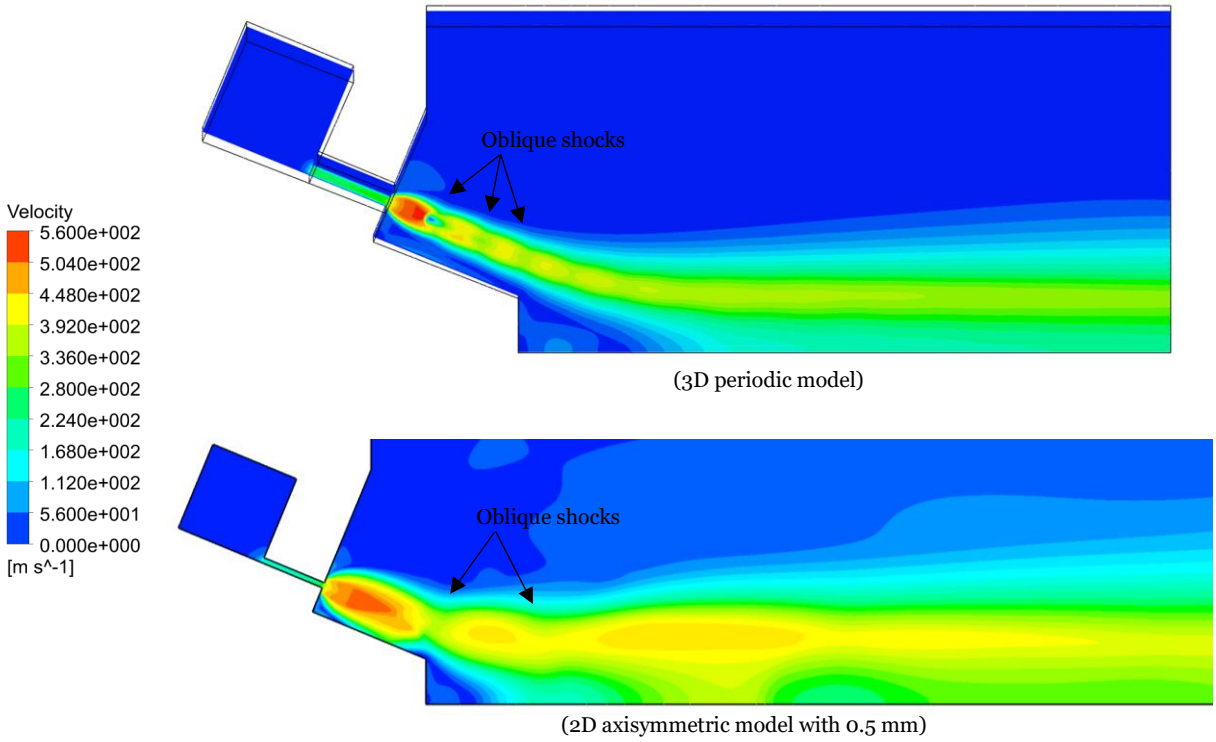

Figure 7.5 Velocity contour plots for the (a) periodic model and (b) axisymmetric model with gas tube width = 0.21 mm at 3 MPa operating pressure

CONCLUSION

Three different approximations were considered in this study. The case with width approximation (case 1) resulted in a gas flow rate higher than the discrete-jet atomizer's gas flow rate. The case with area approximation (case 2) resulted in a gas flow rate lower than the discrete-jet atomizer's gas flow rate. Though the volumetric flow rate approximation (case 3) can be used to analyse parameters depending on the gas flow rate, but it fails to capture the expansion of the gas jets accurately. Also, intermittent spacing in the nozzle results in higher energy dissipation which is not captured in a two-dimensional model. In order to understand

the flow mechanism of a discrete jet atomizer, it is essential to capture the oblique shocks and the expansion waves accurately. Hence, the intermittent spacing between the discrete jets must be preserved to simulate the flow features of the discrete jet atomizers and a three-dimensional periodic model is essential for analysis.

8 DISCUSSION

The aim of the project is to develop various two-dimensional and three-dimensional models to simulate the close-coupled gas atomization. The methodologies and the results have been given in the previous chapters. The overall discussion of the thesis is presented here. The gas flow dynamics, particle movement, velocity and the residence time of particles and the changes in the aspiration pressure for the considered range of operating pressure are discussed below.

8.1 Flow features

In all the atomizer designs considered in this study, the gases travel at choked velocity through the gas tube and on exiting it, they begin expanding. The gases travel towards the outlet through a series of expansion waves and oblique shocks. The expanding gases converge along the axis to form the recirculation zone. The flow features produced by the nozzles for each pressure considered in this study have been discussed here.

1 MPa atomizing pressure

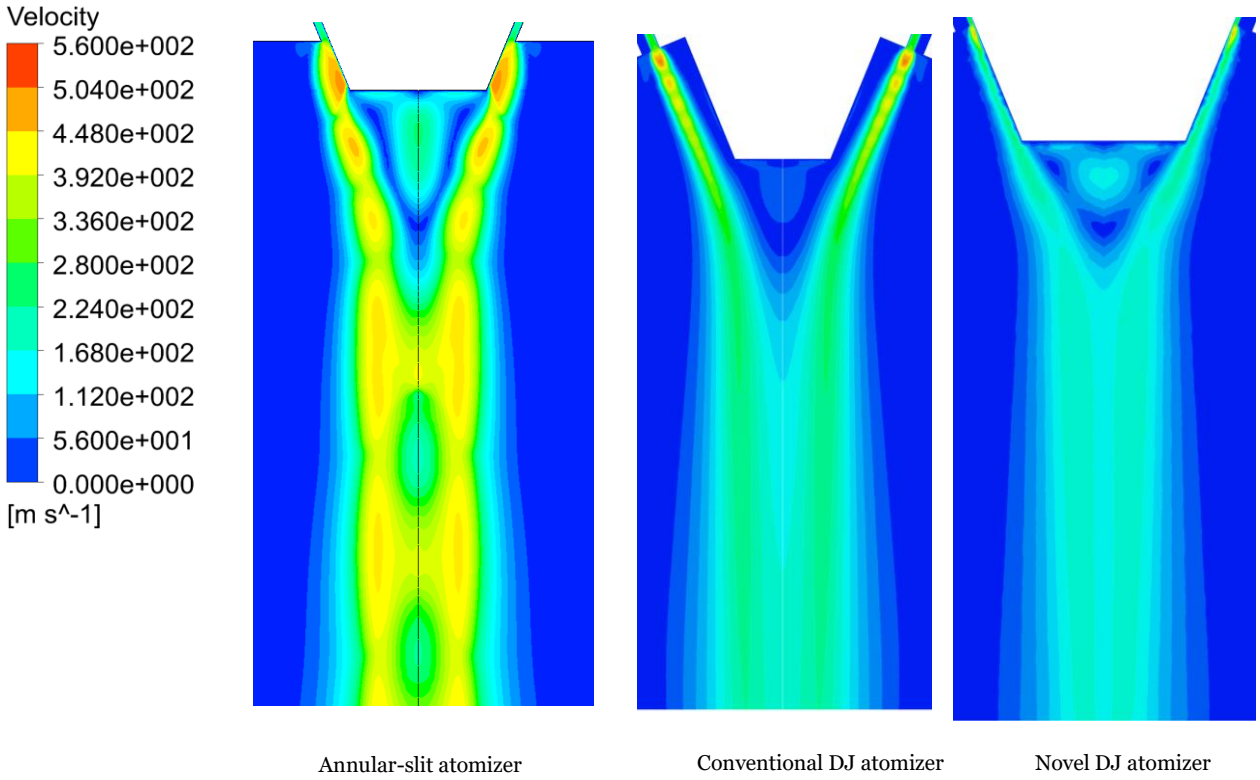

Figure 8.1 Velocity contour plots for all the three nozzle at 1 MPa operating pressure

Figure 8.1 shows the recirculation zones produced in all three nozzles at 1MPa atomizing pressure.

In the annular-slit atomizer, the gases travel the maximum distance at high velocities due to the lack of offset-distance and intermittent spacing which prevents the energy losses due to these geometrical parameters and also due to high gas flow rate (among these three designs). This also causes the shocks to be formed further downstream than the other two cases. Three shocks with two regions of expansions are formed before the flow reaches the stagnation point. It can be seen from the Figure 8.1 that the boundary of the recirculation zone is slightly concave along the regions of expansion. Also, the first oblique shock is located much closer to the nozzle (among all the pressures considered for this design) and it leads to a partially convex region in the recirculation zone due to thinning of the flow as it approaches the first oblique shock.

In the conventional Discrete-Jet atomizer, the gases expand into the intermittent spacing and offset distance and converge to form the recirculation zone. The gases expend their energy to overcome the shocks, and this leads to the gases undergoing reduced expansion as they move further away from the gas tube as seen in the Figure 8.1. It can be seen from the Figure 8.1 and Figure 8.2 that the velocities attained by the gases as they travel beyond the melt nozzle are below their sonic velocity leading to no strong shocks. The gases come across five shocks formed between the gas exit and the melt nozzle edge. The shape of the recirculation zone is not affected by the high-speed gases at this pressure. Also, the velocity of gases in the recirculation zone is the minimum among the three designs. The offset distance between the melt nozzle and the gas jets give rise to layers of gases with low velocity along the melt nozzle surface. Also, as this design has intermittent spacing between the discrete jets, the gases expand in the space in front of the melt nozzle where the gases do not exit. Figure 8.2 shows the cross-sectional view of the expansion. It can be seen from the Figure 8.2that the expanding gas from a discrete jet do not interact with the expanding gases from the neighbouring discrete jets during the initial expansion. The distance between the expansion waves of the gases from the neighbouring jets reduces as they flow forward, and they begin travelling through each other on interaction (as discussed in background science) from the fourth oblique shocks. As the gases flow through each other, the gases in the low velocity layers acquire velocity on interacting with gases in high velocity layers and vice versa.

In the novel Discrete-Jet atomizer, the gases undergo the least expansion. It can be seen from the Figure 8.3 that the gases expand rapidly to high velocity (>400 ms^{-1}) in the first expansion wave does not undergo any considerable expansion downstream. The expanding gases interact with the free boundary and begin losing velocity as it moves forward. As the gases flow over the melt nozzle surface, a boundary layer develops, and this affects the velocity of the gases in

the region as seen in the Figure 8.1. Also, the intermittent spacing between the discrete jets in this design allows the gases to expand in it and gases lose velocity on interaction with the free boundary in this region too. Due to all these reasons, the gases lose their energy rapidly within

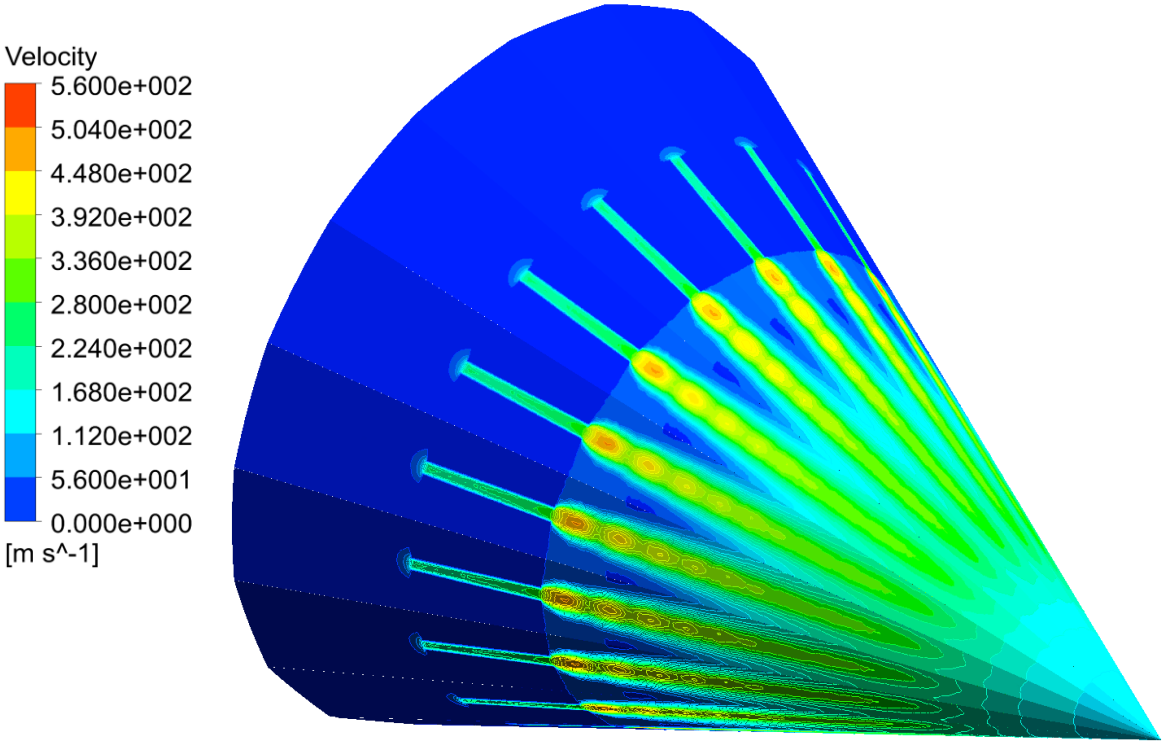

Figure 8.2 Cross-sectional velocity contour plots for 1 MPa atomizing pressure in the conventional discrete-jet atomizer

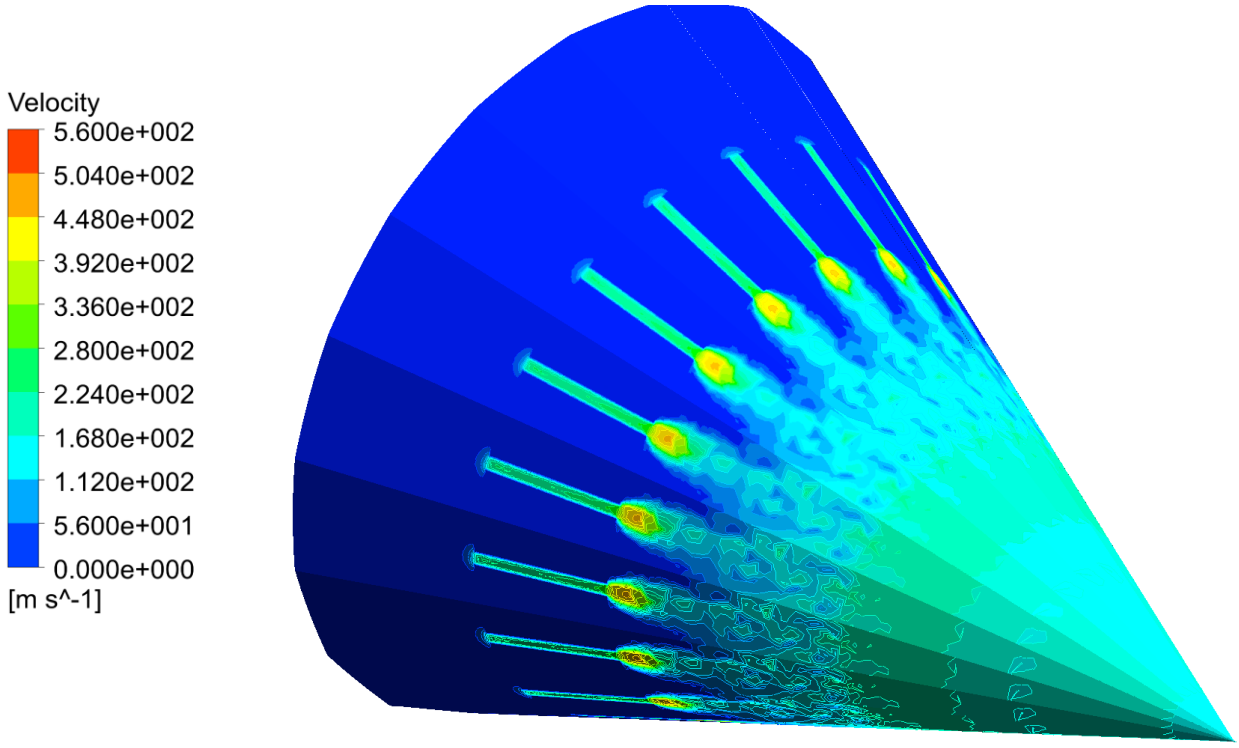

Figure 8.3 Cross-sectional velocity contour plots for 1 MPa atomizing pressure in the novel discrete-jet atomizer

the first expansion and does not form any considerable expansion or strong oblique shocks downstream. The gases flow along the melt nozzle edge and converge along the axis to form the recirculation zone. The shape of the recirculation zone is not influenced by the gases. An open wake is observed at this pressure. The expanding gases begin interacting with the neighbouring expanding gases downstream the first expansion. Figure 8.3 shows the crossectional velocity contour plots for 1 MPa.

3 MPa atomizing pressure

The next pressure considered in this study is 3 MPa. This is a commonly used atomizing pressure in the industry. At 3 MPa operating pressure, the gases undergo increased expansion compared to 1MPa case and forms an open wake.

It can be seen form the Figure 8.4 that the flow undergoes two shocks before reaching the stagnation point in the annular slit atomizer. The boundary of the recirculation zone is more concave than the 1 MPa case as the gases are expanding more in this nozzle design and a tiny partial convex region can be seen around the nozzle due to thinning of flow.

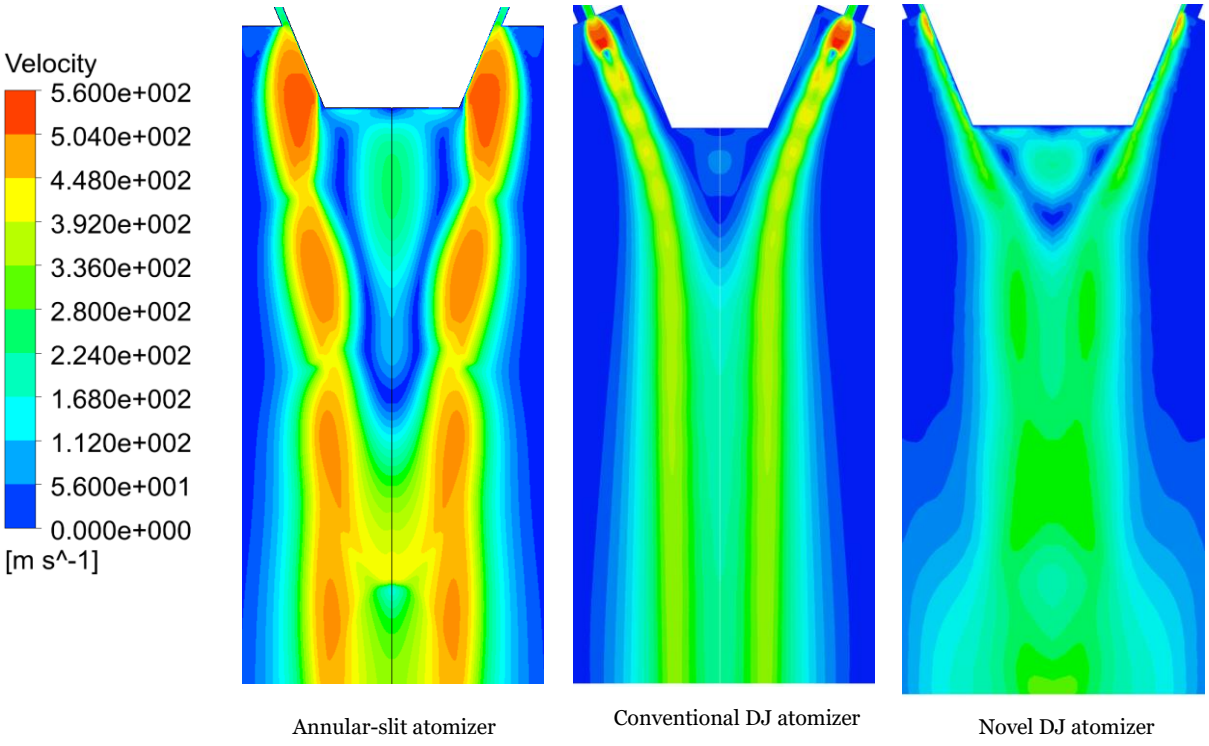

Figure 8.4 Velocity contour plots for all the three nozzles at 3 MPa operating pressure

In the conventional Discrete-Jet atomizer, the gases expand in the same pattern as seen in 1 MPa. As the flow possess more energy, it undergoes increased expansion and forms shocks further downstream than observed at 1MPa. It can be seen from the Figure 8.4 that the flow undergoes three shocks between the gas exit and the melt nozzle edge. Also, the flow continues

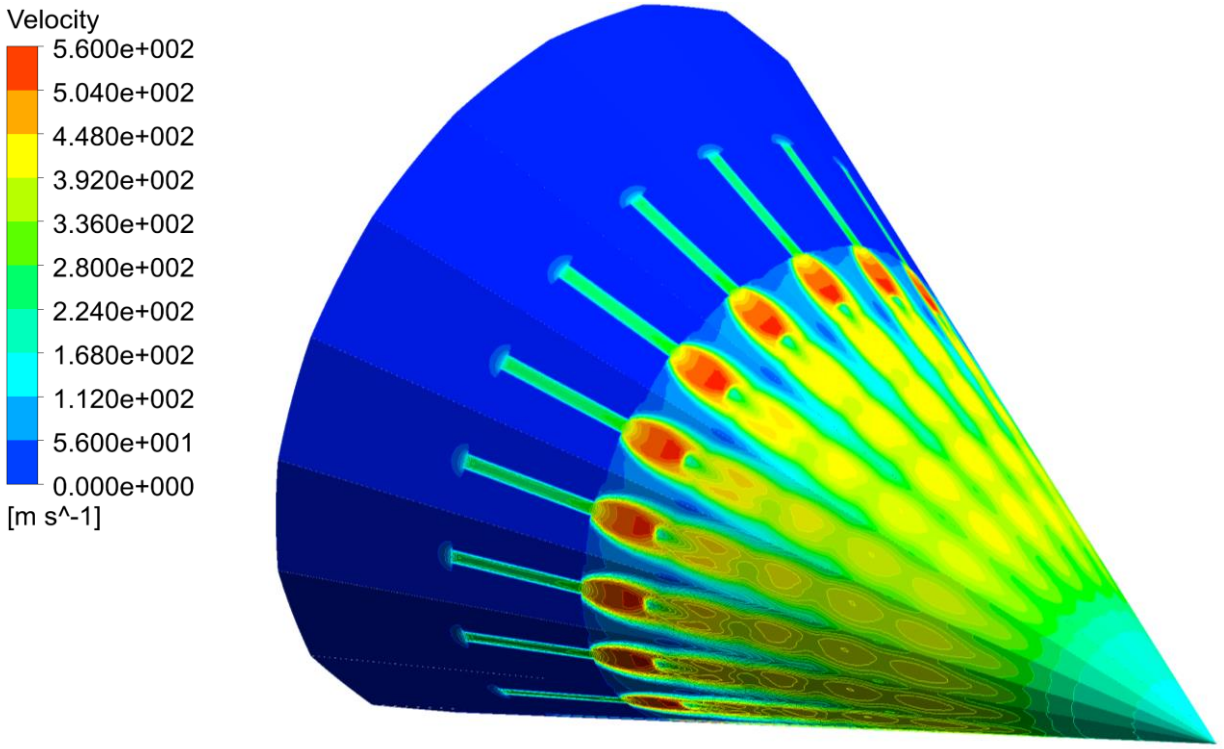

Figure 8.5 Cross-sectional velocity contour plots for 3 MPa atomizing pressure in the conventional discrete-jet atomizer

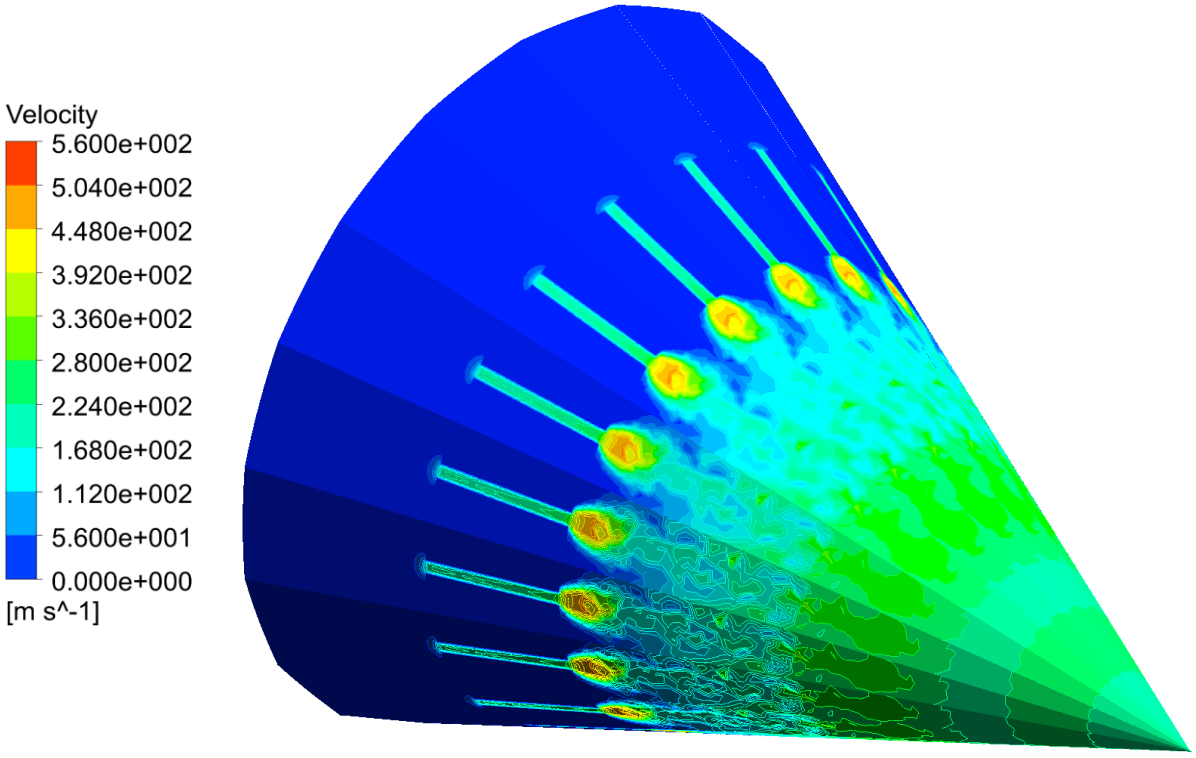

Figure 8.6 Cross-sectional velocity contour plots for 3 MPa atomizing pressure in the novel discrete-jet atomizer

to travel towards the outlet through expansion waves and oblique shocks but the maximum velocity achieved by the gases decreases as the gas moves further away from the melt nozzle towards the outlet. The shape of the recirculation zone is not affected by the expansion as no

significant expansion occurs around the recirculation zone at this pressure and the velocity of gases in the recirculation zone is the minimum among the three designs. Also, it can be seen from the Figure 8.5 that the gases that expand in the intermittent spacing begin interacting with the gases from the neighbouring jets from the second oblique shock. As the expansion waves interact with each other, they continue to flow through each other with slight deviation. The gases in the outer layers of expansion waves acquire velocity on interaction with gases in the inner layers of expansion waves of the neighbouring gas jets and vice versa.

In the novel Discrete-Jet atomizer, the gases flow in the same mechanism as observed for 1MPa operating pressure. The gases undergo expansion on exiting the gas tube and reach their maximum velocities in the first expansion wave as seen in Figure 8.4. As the gas possess more energy, the first oblique shock is formed further downstream than the 1 MPa case. The gases do not undergo significant expansion downstream the first expansion and continues to flow towards the outlet through weak oblique shocks and expansion. The shape of the recirculation zone is not influenced by the gases flowing around it. The expanding gases begin interacting with the neighbouring expanding gases downstream the first expansion and it can be seen from the Figure 8.6.

4.5 MPa atomizing pressure

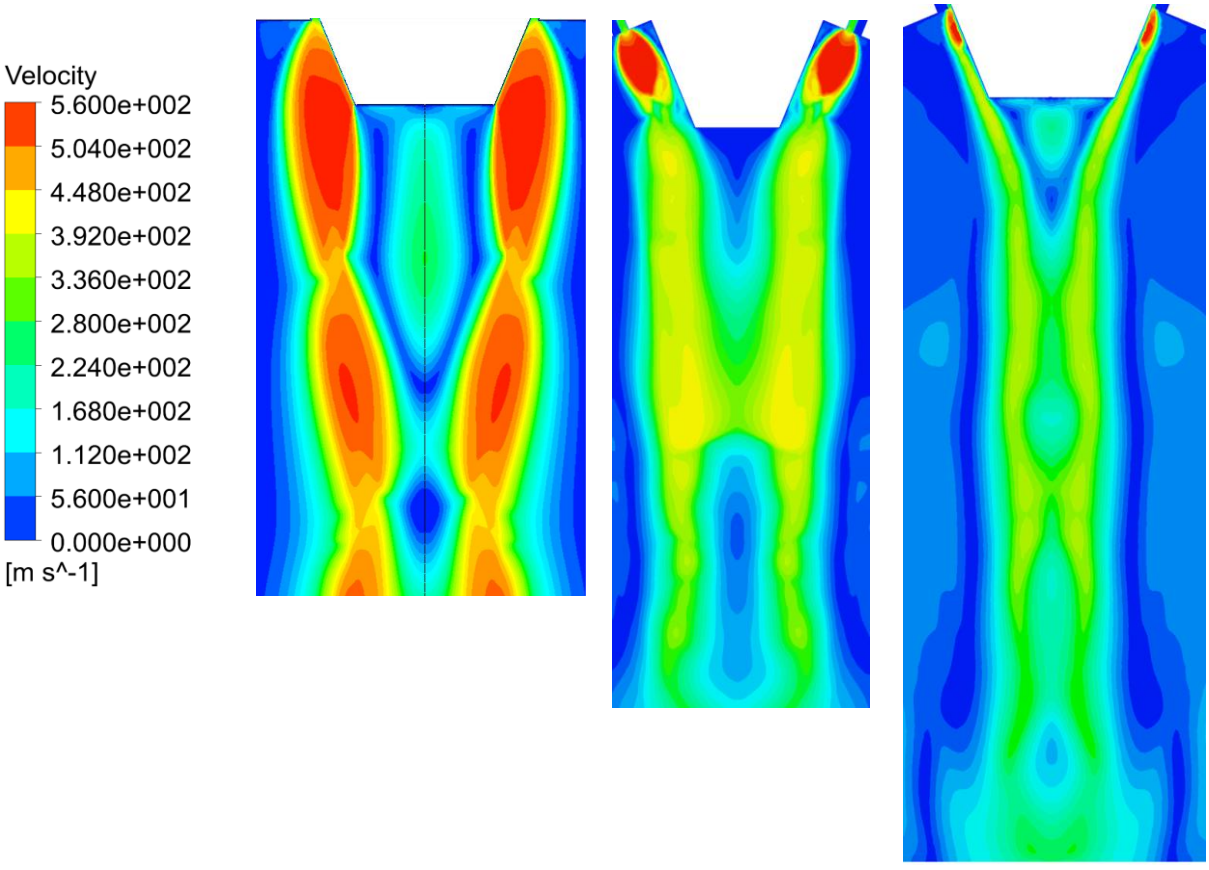

Figure 8.7 Velocity contour plots for all the three nozzles at 4.5 MPa operating pressure

At 4.5 MPa operating pressure, the gases expand more than the previous two operating pressures, and a closed wake is formed. A closed wake is characterised by the Mach disk downstream the recirculation zone. The expanding gas jets lose their velocity as they interact with the free boundary and oblique shocks are formed in the process. When the oblique shocks possess sufficient strength, they interact and form a normal shock on converging along the axis. A recirculation zone is formed downstream the Mach disk. The partial concave regions seen in previous pressures are not observed in this pressure.

This is the wake-closure pressure (WCP) for the annular-slit atomizer. It can be seen from the Figure 8.7 that two shocks are formed before the flow reaches the stagnation point. The gases undergo increased expansion compared to the previous two pressures and a Mach disk is formed along the gas expansion between the two oblique shocks. As this is the wake closure pressure, the oblique shocks are just strong enough to form a Mach disk and therefore, the distance between the two recirculation zones is nearer to each other.

In the conventional discrete-jet atomizer, the Mach disk is formed further downstream to recirculation zone than the annular-slit atomizer. The gas begins expanding on exiting the gas die and forms the first oblique shock. It can be seen from the Figure 8.7 that only one shock is formed between the gas exit and the melt nozzle edge and additional three shocks are formed before the formation of Mach disk. Also, the gas expands for a longer distance between the third oblique shock and fourth oblique shock i.e. just before the Mach disk. This is due to the fact that the strength of the shocks decreases as they move away from the melt nozzle and the gas can flow for longer distance before undergoing a shock. As mentioned before, a Mach disk is formed when the oblique shocks of sufficient strength interact with each other. The flow possesses sufficient energy at 4.5 MPa inlet pressure to form strong oblique shocks of sufficient strength (on interaction with free boundary) to give rise to a Mach disk as seen in Figure 8.7. Also, the expanding gases interact with those from the neighbouring discrete jets in the intermittent spacing within the first oblique shock as seen in Figure 8.8. The gases in the expansion waves from each discrete jet continues to flow towards the outlet through expansion waves of other discrete jets through interaction as discussed in the previous pressures. The expanding gases converge along the axis to form a recirculation zone. It can be seen from the Figure 8.7 that the gases in the outer layer of the expansion wave come in contact with melt nozzle surface and continue to flow along it. Also, the shape of the recirculation zone is concave due to the expansion waves surrounding it and the velocity of gases in the recirculation zone is the minimum. In the novel Discrete-Jet atomizer, the gas follows the same mechanism as seen in 3 MPa pressure. A small Mach disk is formed much further downstream than the other two designs. Figure 8.7 shows the Mach disk. The gases do not accelerate to the high velocities

as observed in the first expansion but continue to flow towards the outlet through series of expansion waves and oblique shocks. The oblique shocks form a Mach disk downstream the

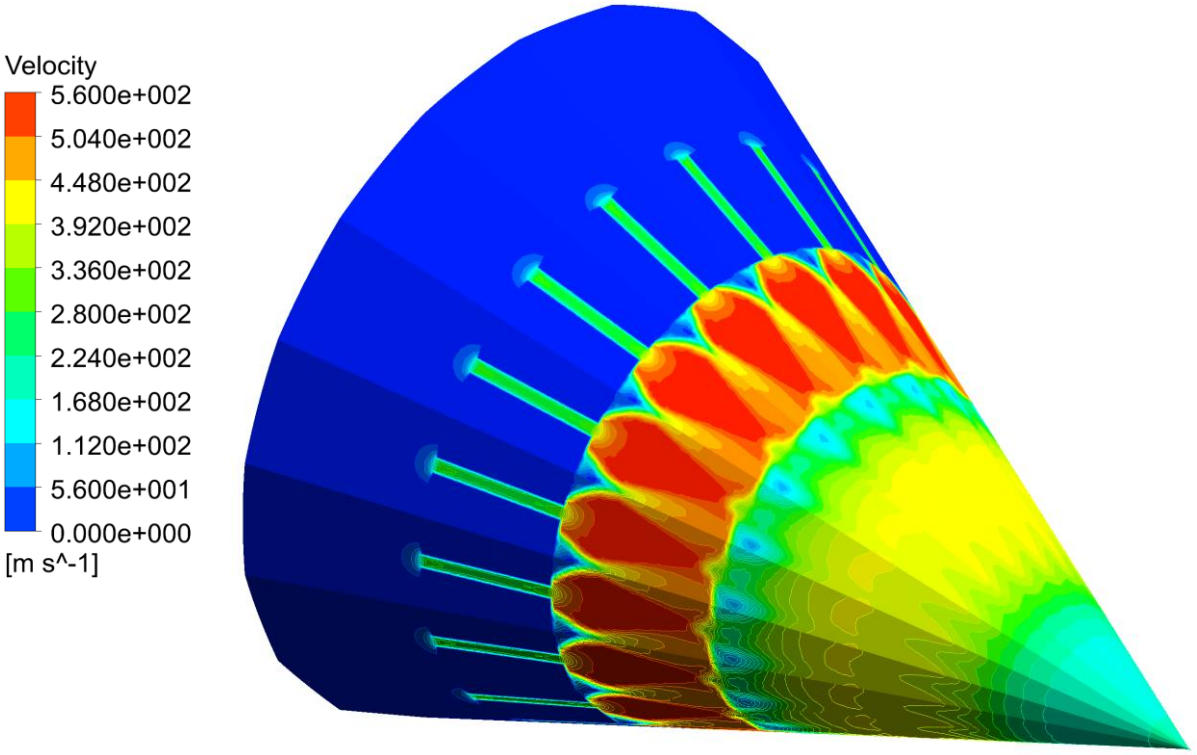

Figure 8.8 Cross-sectional velocity contour plots for 4.5 MPa atomizing pressure in the conventional discrete-jet atomizer

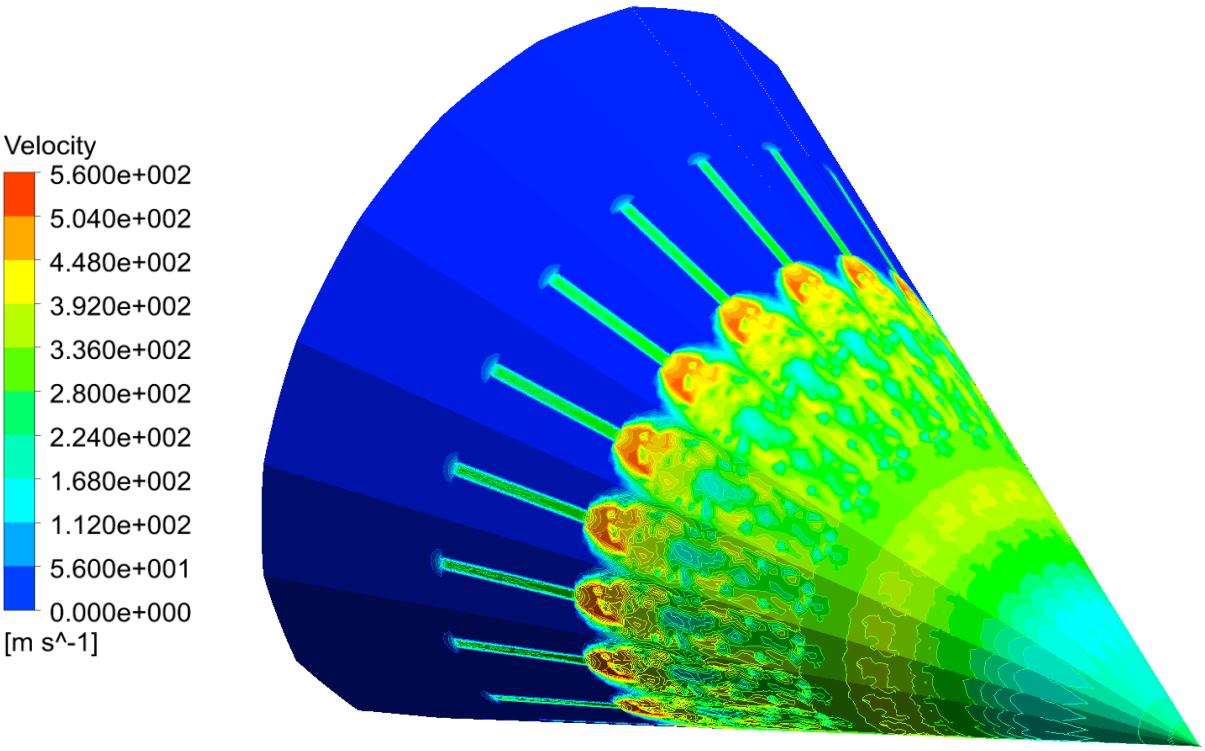

Figure 8.9 Cross-sectional velocity contour plots for 4.5 MPa atomizing pressure in the novel discrete-jet atomizer

recirculation zone. The flow overcomes this Mach disk and continues to flow towards the outlet. The expanding gases converge along the axis to form the recirculation zone. The shape of the recirculation zone is influenced by the surrounding gas expansion resulting in slightly concave boundaries along the expansions. The expanding gases begin interacting with the neighbouring expanding gases along the first expansion. Figure 8.9 shows the velocity contour plots in cross-section.

5 MPa atomizing pressure

The final pressure in this study is 5 MPa operating pressure. It can be seen from the Figure 8.10 that all the designs produced a Mach disk.

In the annular-slit atomizer, the gases undergo two shocks before reaching the stagnation point. The Mach disk is formed along the expansion between two oblique shocks. As the gas possess more energy than the previous pressures, it can flow further downstream against the free boundary. It can be seen from the Figure 8.10 that the Mach disk is formed further downstream than that seen in 4.5 MPa due to this reason. The partial concave regions seen in previous open wake pressures are not observed in this pressure.

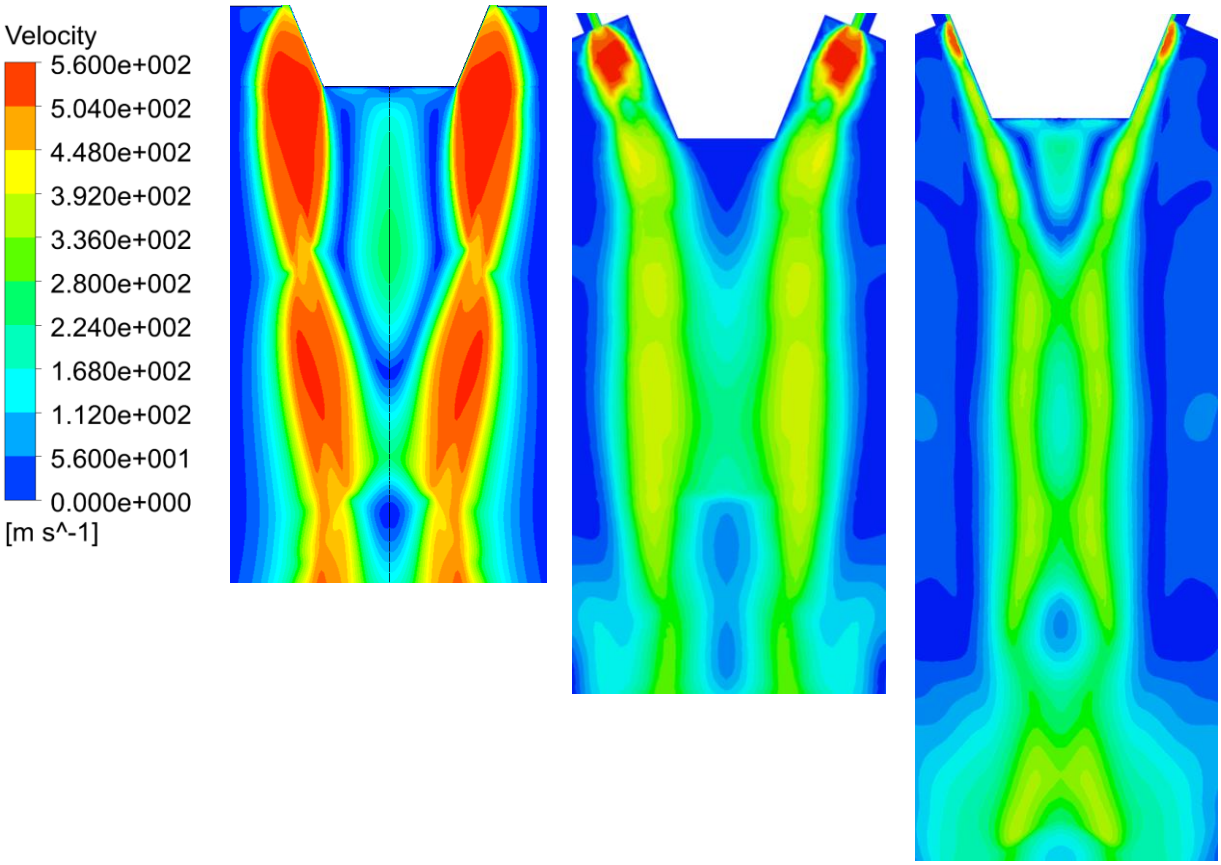

Figure 8.10 Velocity contour plots for all the three nozzle at 5 MPa operating pressure

In the conventional discrete-jet atomizer, the flow pattern follows the same mechanism as seen in 4.5 MPa. It can be seen from the Figure 8.10 that only one shock is formed between

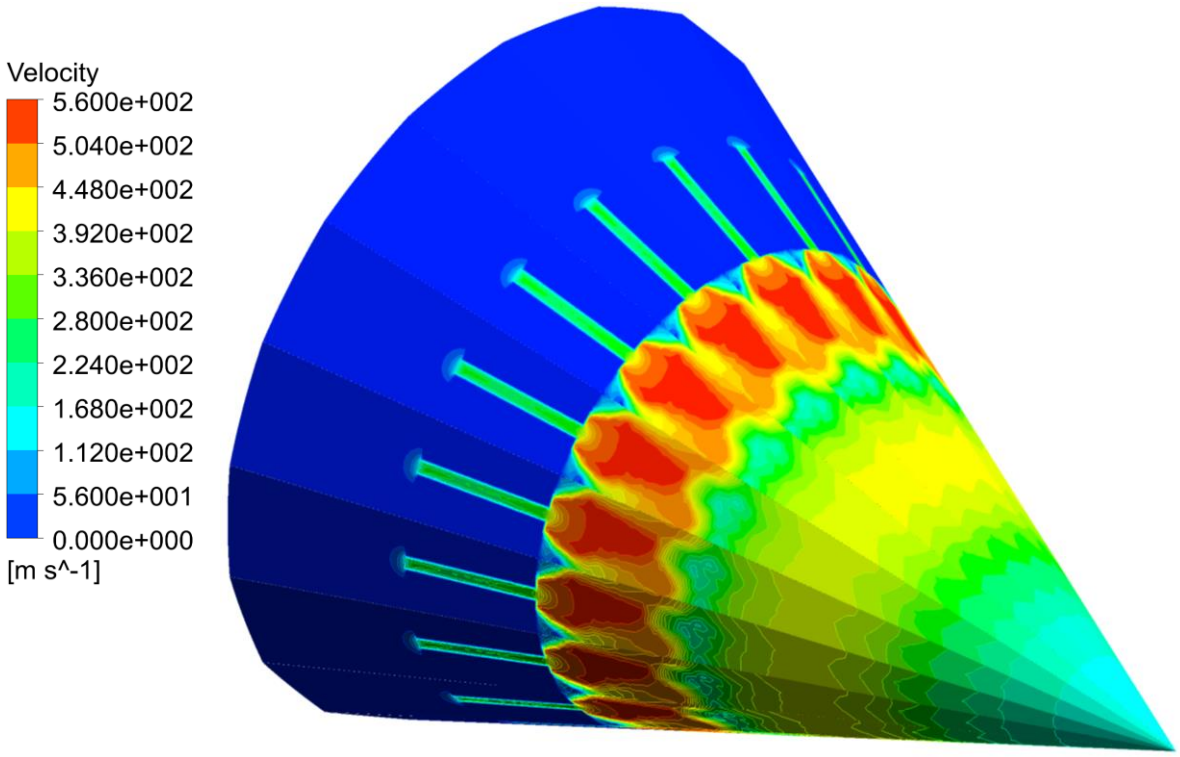

Figure 8.11 Cross-sectional velocity contour plots for 5 MPa atomizing pressure in the conventional discrete-jet atomizer

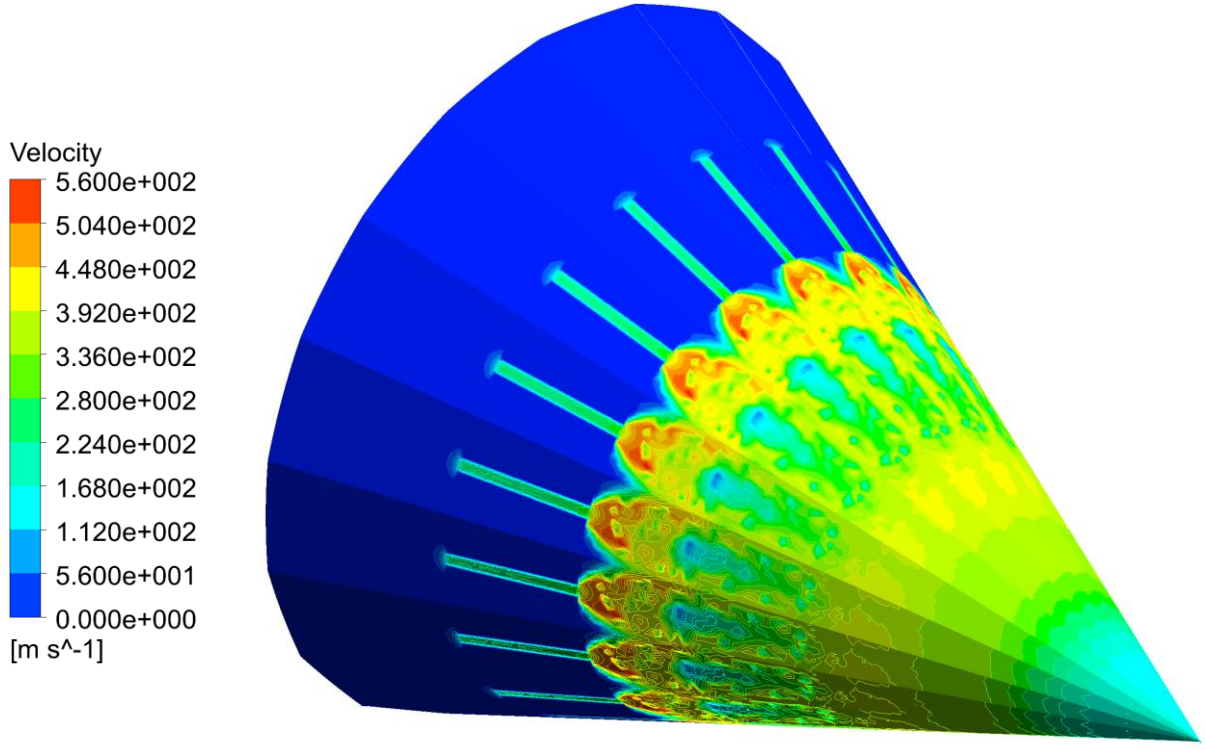

Figure 8.12 Cross-sectional velocity contour plots for 5 MPa atomizing pressure in the novel discrete-jet atomizer

the gas exit and the melt nozzle. The gases continue to flow towards the outlet through a series of expansion waves and oblique shocks. A Mach disk is formed after fourth oblique shock. The expanding gases begin interaction with neighbouring expanding gases within the first oblique shocks. The boundary of the recirculation zone is concave between the first and the second oblique shocks due to the gas expansion as seen in Figure 8.10. Also, the velocity of gases in the recirculation zone is the minimum among the three designs. Figure 8.11 shows the cross-section of velocity contour plots at 5 MPa. The expansion and areas of velocity loss (shocks) can be seen Figure 8.11

In the novel discrete-jet atomizer, the flow follows the same mechanism as seen in 4.5 MPa. The gases undergo an increased expansion, and this leads to formation of shocks further downstream than those observed in the previous pressures. The gases travel towards the outlet through a series of expansion waves and shocks. As observed before, the gases do not accelerate downstream the first oblique shock as much as they accelerate in the first expansion. The gases converge along the axis to form the recirculation zone. The shape of the recirculation zone is influenced slightly as compared to the other two designs by the expanding gases surrounding it and it can be seen in the Figure 8.10 as concave boundary along expansion. Also, two Mach disks are observed at this pressure as seen in the Figure 8.10. The gases flow towards the outlet and forms Mach disk on interaction with other oblique shocks. The flow overcomes this Mach disk to form a smaller Mach disk downstream it. This can be seen from the Figure 8.10. The flow continues towards the outlet beyond the Mach disks. Figure 8.12 shows the velocity contour plots in cross-section.

8.2 Influence of geometrical parameters

The geometry of the nozzle affects the flow features developed around it. Design parameters such as apex angle, intermittent spacing and offset distance in a nozzle play an important role in determining the flow features and the particle size.

8.2.1 Intermittent spacing

In annular slit atomizer, the gas is delivered into the atomization chamber through a slit whereas in a discrete jet atomizer, the gas is delivered through a set of discrete jets separated by intermittent spacing.

The presence of intermittent spacing affects the gas consumption for the same operating pressure. Also, it influences the flow features and the way the gas loses energy in the flow. This is because the intermittent spacing in the discrete-jet atomizers allow the gas to expand

radially and in sideways but the lack of intermittent spacing in annular slit atomizers allow the gas to expand only radially.

In an ideal scenario, the efficiency of the process can be increased by minimizing the energy loses. The gases exiting the AS nozzle expand in forward direction but in the DJ nozzle, the gases expand sideways in intermittent spacing and in forward direction. This additional expansion in the intermittent spacing could cause an increased energy loses in DJ nozzles compared to AS nozzles. The annular slit atomizer is widely used in industry despite the high gas consumption rate due to minimum energy loses and ease in manufacturing the nozzle.

An ideal nozzle design must strike a balance between the gas consumption and energy losses. It can be seen from the cross-sections of flows in Figure 8.2, 8.3, 8.5, 8.6, 8.8, 8.9 that the gases undergo increased expansion as the operating pressure increases. The consequence of this increased expansion is that the gases begin interacting with the gases from the neighbouring jets at higher velocities as the operating pressure is increased and this reduces the energy loses due to expansion at high operating pressures. Every nozzle design must have an optimum intermittent spacing for the operating pressure beyond which the gas loses their energy on expanding in the intermittent spacing. Therefore, an appropriate intermittent spacing between the discrete jets play an important role in minimizing the energy loses.

This is an important observation in this study. Generally, the number of discrete-jets incorporated in an atomizer depends on the gas flow rate required for the process but this observation allows us to conclude that each operating pressure has an “design” intermittent spacing below which the gases experience energy loses.

In chapter 6, various approximations were considered to simulate the intermittent spacing in two-dimension. It was found that the intermittent spacing must be preserved in the model to simulate the flow features accurately. In all the cross-sectional figures Figure 8.2, 8.3, 8.5, 8.6, 8.8 & 8.9) presented in this chapter, velocity losses can be seen clearly in the intermittent spacing which will not be possible to simulate in two-dimensional models. Therefore, a three-dimensional model is essential to analyse discrete-jet atomizers.

8.2.2 Offset distance

Generally, gas exit is at an offset distance from the melt exit in discrete jet atomizers and the offset distance is absent in annular slit atomizers. Figure 8.13 shows the expansion around the melt nozzle with and without the offset distance.

The scope of the project is limited in terms of offset distance as different offset distances were not investigated but the fixed offset distance in conventional Discrete-Jet atomizer is sufficient to analyse the effects of the offset space in the nozzle.

The offset space in the nozzle design allows the gases to expand more than that observed in those designs without the offset space. This expansion in the region of the offset distance results in flow undergoing energy loses. A large offset distance in the nozzle leads to adverse flow around it leading to lick-back. It can be seen from the Figure 8.13 that the flow in the nozzles without the offset distance does not have adverse flow around them at low pressures. The ideal offset distance in a nozzle should not produce any adverse flow on it for the operating pressure.

The melt moves across the nozzle surface towards the circumference through prefilming and this movement is influenced by the velocity of the gases forcing the melt towards the nozzle edge. It can be seen from the figures 8.1, 8.4, 8.7 and 8.10 that the velocity of gas in front of the melt nozzle is higher in designs without the offset distance. These high velocity gases bring the melt to the circumference quicker, resulting in a thinner films and smaller ligands. On the other hand, the low velocity recirculating gases in the conventional discrete-jet atomizer results in thicker films and larger ligands. The scope of the thesis in terms of offset-distance is limited and prefilming cannot be investigated thoroughly.

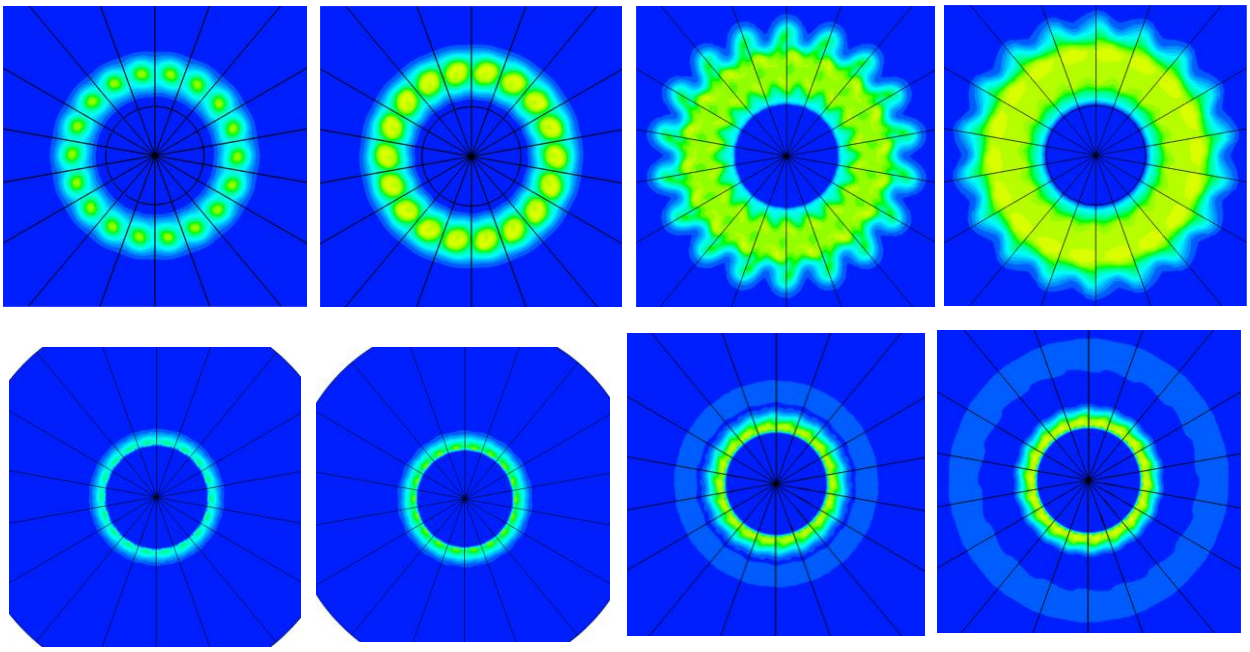

Figure 8.13 Velocity contour plots of expansion around the nozzle for both the discrete jet designs

(Top: conventional discrete-jet atomizer Bottom: Novel discrete-jet atomizer)

8.3 The particle movement and GMR dependence

The movement of particles has been presented in detail in chapter 5. The movement of melt in the recirculation zone is influenced by the GMR of the process. The annular-slit nozzle design was optimized for 3 MPa which is a commonly used pressure in industry. When the operating pressure was reduced (<3 MPa), particles was drawn over the nozzle surface. It can be seen in the Figure 5.10-5.23. Though the simulation was carried out for 50 milliseconds with the particles being continuously flowing in and out of the adverse flow pocket on the nozzle surface, this will not be observed in the physical process as the "lick-back" will deform the melt nozzle surface. The particles converge downstream the stagnation point and bounce off towards the outlet. This is due to the shape of the recirculation zone. A very high GMR at 1.5 MPa leads to stagnation of particles in the recirculation zone and the process will fail eventually when it is run more than 50 milliseconds. Another consequence of this GMR is the particles stagnating along the axis leading to low velocity pockets downstream the recirculation zone.

In the other three cases, the particle tracks are determined mainly by the first set of oblique shocks. In the 3 MPa case, the particles begin travelling through the outer layer of the gases on the near side of the wall. The particle tracks begin spreading towards the axis as the flow time increases. In the two cases with closed wake, the particle tracks converge along the axis and spread towards the upper wall. This is due to the flow around the closed wake directing the particle tracks towards the axis. The lack of closed wake in 3 MPa case enables the particles to travel on the outer layers of expansion waves. The introduction of particles in the 3 MPa case gives rise to barely sub ambient pressure and this leads to the particle movement in the recirculation zone reaching a steady-state at 15 milliseconds.

The common feature observed in all the three cases is that the particles do not move further downstream the eye of the recirculation zone through 50 milliseconds. In the cases with closed wake (4.5 MPa & 5 MPa), the particles from the injections I, II & III move further down (than those from injections IV, V) before reaching the zero-velocity state. This is due to the sub ambient aspiration pressure in the recirculation zone causes the particles to stagnate in it before entering the high-speed gas jets.

Every atomizer nozzle design has a range of GMR beyond which the process fails. A very low GMR leads to melt freezing in the melt tube and a very high GMR distorts the nozzle. As the melt breakup and solidification is not modelled, the ideal range of GMR is difficult to calculate. In order to run the atomizer at 1.5 MPa, the protuberance length must be reduced, and the

melt flow rate must also be reduced. The other three pressures can be run in this nozzle design without nozzle deformation.

8.4 Velocity of the particles

The velocity of the particles through the flow domain and maximum particle velocity observed at every timestep was analysed in this study. Figure 5.51 shows the maximum velocity vs the time step**.** It can be seen from the Figure 8.14 that the velocity at which the particles travel is greatly affected by the gases carrying it and therefore the compression across the shockwaves leads to losses in particle velocity.

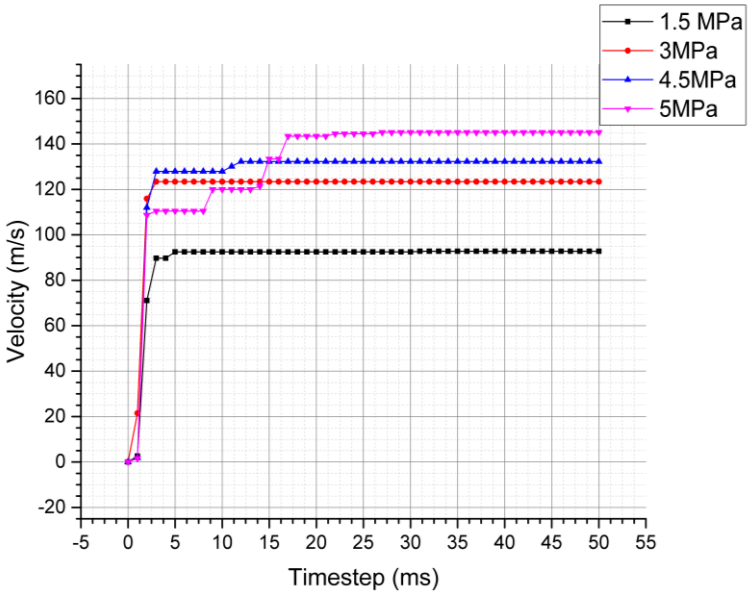

Figure 5.51 Graph showing the maximum velocity of the particles (ms^{-1}) vs Timesteps (ms)

The maximum gas velocity depends on the operating pressure of the atomizer, shape of the recirculation zone and location of shocks around it. As the operating pressure is increased, the gases travel much longer in high velocity range due to the available gas momentum. As the particles move across the flow domain, a large number of particles begin travelling in the high velocity layers. This allows those particles to reach higher maximum particle velocities.

The shape of the recirculation zone affects the flow direction of the particles. Figure 8.14 shows the particles and the velocity vector plots for 1.5 MPa at 50 milliseconds. A small recirculation zone as observed at 1.5 MPa operating pressure leads to particle tracks converging downstream the stagnation point and diverging from the axis as they move towards the outlet. This diverging of particle tracks leads to particles entering the high velocity layers of the expansion wave and the particles acquire the maximum velocity at this point. Also, this converging and diverging trajectories of the particles leads to a majority of particles travelling

in the low velocity gas layers resulting in lower range of particle velocity through 50 milliseconds.

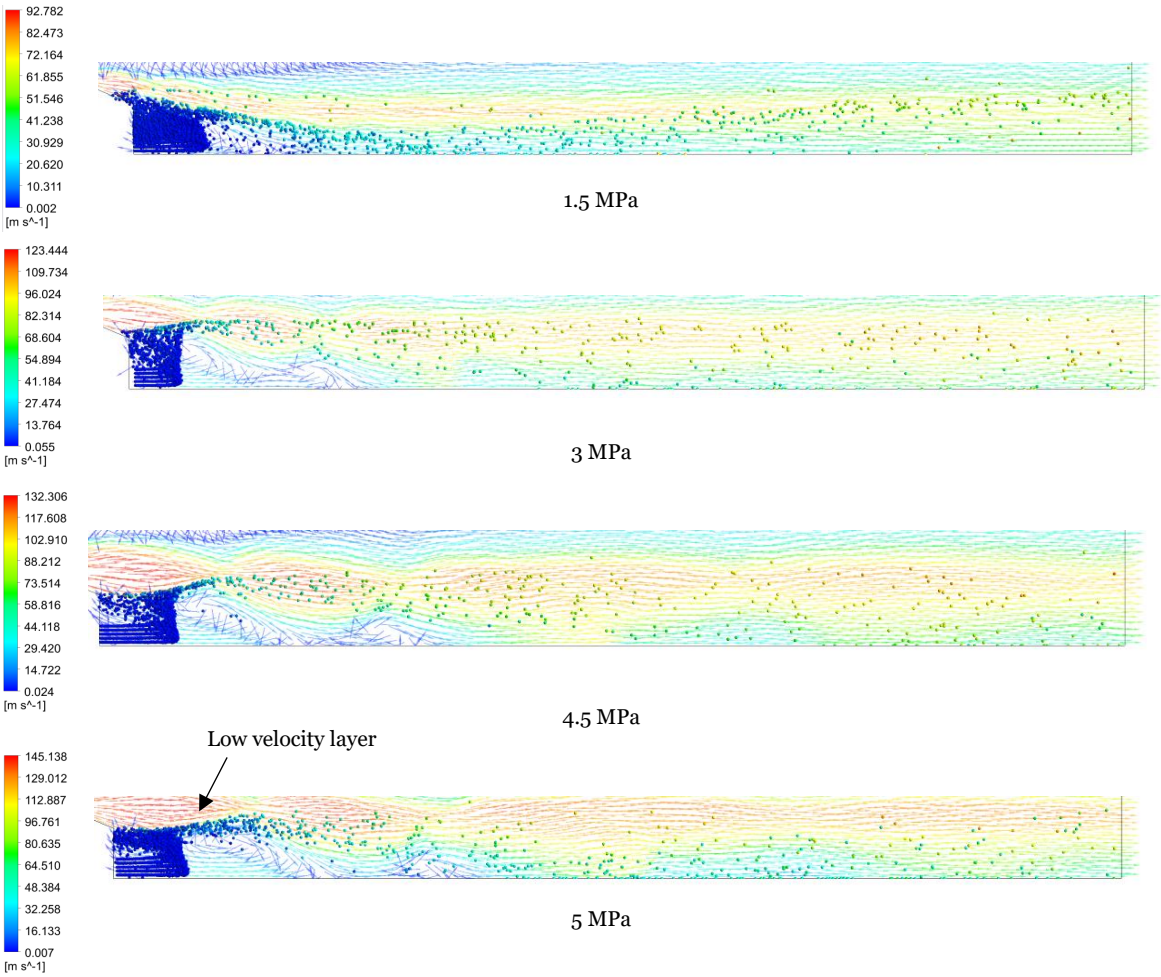

Figure 8.14 Particles coloured by velocity and velocity vector plots.

In other pressures (>1.5 MPa), the recirculation zone is greatly influenced by the gas expansion around it. The particles reach maximum velocity within the first three milliseconds in 3 MPa case as the location of the first shock leads to particles travelling along the high velocity layers towards the outlet from the first oblique shock. In the 3MPa case, the particles travel in the high velocity layers downstream the first oblique shock due to its location as seen in Figure 8.14 Particles coloured by velocity and velocity vector plots. This enables a large number of particles to travel in the higher range velocities.

In the cases with closed wake (4.5 MPa and 5 MPa), the particle tracks converge downstream the stagnation point of the closed wake. On converging, the particles begin travelling along the low velocity layers initially and as the flow time increases, the particles begin travelling through high velocity layers as they begin spreading across the expansion waves as seen in

Figure 5.25-5.66. This spreading of the particles leads to them achieving maximum velocities as they enter high velocity layers.

The location of the second shockwave (closed wake) also influences the velocity of the particles. The distance between the Mach disk and the recirculation zone is greater in 5 MPa case which leads to the particle tracks converging closer to the outlet (compared to 4.5 MPa case). The particles reach their maximum velocities when they travel along the high velocity gas layers. Generally, in these two cases, the particles enter these high velocity gas layers due to spreading of the particle tracks. In the 4.5 MPa case, the distance between the closed wake and the outlet is greater than the 5 MPa case and this increased distance enables the particles to spread further before reaching the outlet and this in turn allows the particles to reach their maximum velocities sooner. Similarly, in the 5 MPa case, the shorter distance between the closed wake and the outlet results in particle tracks not spreading as much as 4.5 MPa case before reaching the outlet in the initial timesteps. As the flow time increases, the spreading of particle tracks increases, and this leads to particles reaching maximum velocities (in high velocity layers) at later flow times. In both the cases, a great majority of particles travel in mid-higher range of velocity due to the location of Mach disk and the converging-diverging patter of trajectories as seen in Figure 8.14.

Also, the gases along with particles decelerate across the shocks. The strength of the shocks decreases as the distance from the nozzle increases. This decrease in the strength of the shock allows the particles to reach high velocities near the outlet. The velocities of the particles are different from the velocity of the gas layers in which it travels. It can be inferred that this difference in the velocities shears the ligands influencing the particle size.

Significant works have been carried out by Mullis in quantifying the melt movement and the range of velocities in which the droplets travel through the gases. Biggs et al analysed an annular slit atomizer at 2.6 MPa inlet pressure. They noticed that the droplet tracks begin spreading as the distance from the nozzle increased. They also found that the particles moved at velocities in the range of 30 ms^{-1} in their flow domain (about 7 nozzle diameters downstream). This velocity is in agreement with the velocities estimated by Mullis et al. The velocity of the particles at 3 MPa was also around 30-40 ms^{-1} through the length of 7 nozzle diameters downstream from melt nozzle. They utilized high speed imaging and calculated the velocity by determining the density gradient caused by the melt movement.

8.5 Residence time of the particles

The residence time of the particles at every timestep was also analysed. The particles are given an initial velocity of 1.5 ms^{-1}. The particles flow against the recirculating gases, reach their zero-

velocity state and begin flowing along with the gases. The residence time of the particles includes the time spent by the particles in the recirculation zone (low velocity region) and the time spent travelling along the high velocity gases. The time spent by the particles in the recirculation zone(s) play a major role in determining the maximum residence time.

Also, the residence time of the particles is greatly affected by the GMR of the process and the wake conditions. The location of the shocks affects the trajectories and velocities of particles. Figure 5.43-5.75 shows the residence time of particles for various flow times for all pressures considered in this study. Figure 5.42 shows the maximum residence time of the particles at every timestep. Figure 5.7 shows the mass concentration of the recirculation zone at every timestep.

At 1.5 MPa operating pressure, the GMR of the process is very high. A very high GMR results in melt stagnating in the recirculation zone as there is no sufficient gas available to carry the melt droplets. This leads to increase in melt concentration in the recirculation zone and in turn affects the residence time of the particles. The mass concentration in the recirculation zone and the maximum residence time of the particles increase through 50 milliseconds in this case

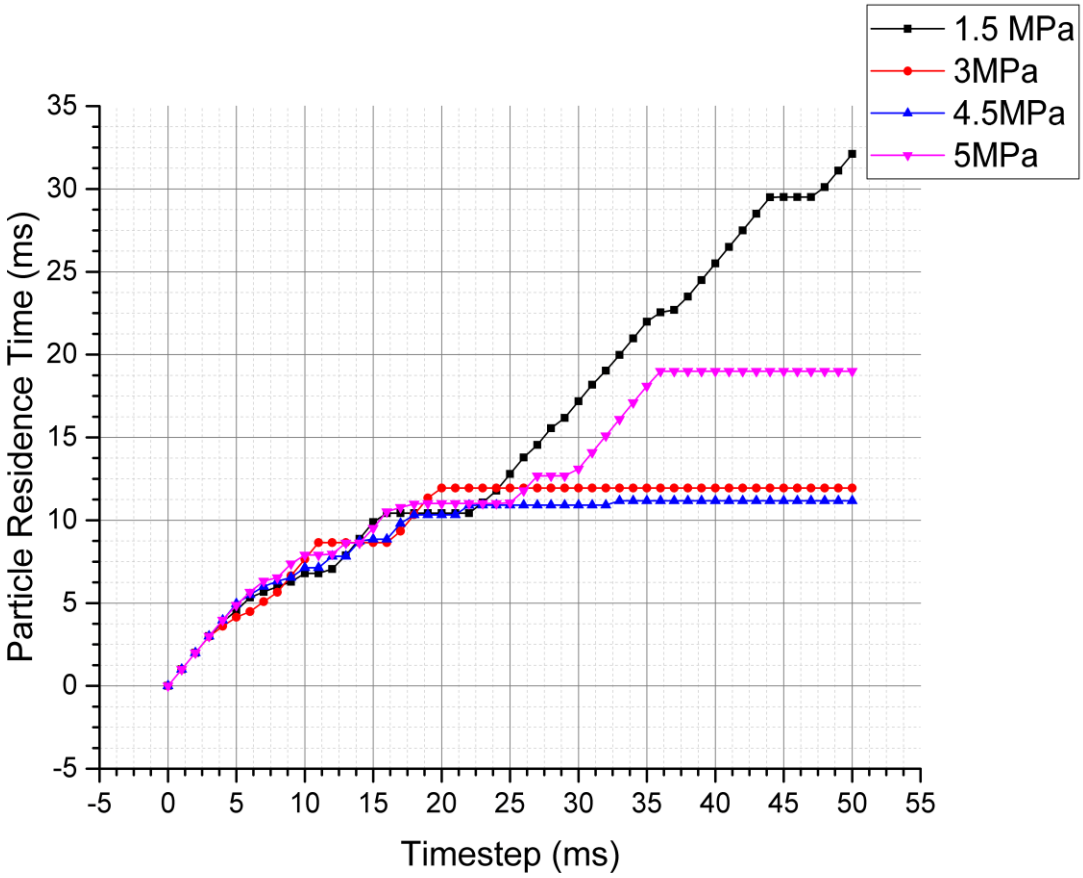

Figure 5.42 Graph showing the Maximum Particle Residence Time (ms) vs Timesteps (ms)

due to high GMR. As seen in chapter 5, the residence time of majority of the particles remain in lower-mid range (0.01 s) for this case but this is the maximum seen among the cases.

In all the cases (3-5 MPa) except 1.5 MPa, the maximum residence time increases in the initial timesteps and becomes constant. Though the 4.5 MPa case is a closed wake with a sub ambient aspiration pressure, the maximum residence time observed is the least. This is due to the location of the eye of the recirculation zone enabling the particles to flow more or less diagonally towards the nozzle edge. In the 3 MPa case, the particles reach the eye of the recirculation zone by 20 milliseconds (time taken to travel from melt nozzle to recirculation zone's eye is 2 ms). The residence time of the particles is higher than the 4.5 MPa case because the eye of the recirculation zone forces the particle to stagnate. Also, the particle residence time of most of the particles remains in lower-mid range. The location of the first oblique shock enables the particles to travel in the high velocity layers and this leads the low residence time. The case with the 5 MPa operating pressure has the maximum residence time. This is due to the sub ambient aspiration pressure and the location of the Mach disk. The particles stagnate in the recirculation zone, enter the high-speed gases and enter the second recirculation zone downstream the Mach disk. This results in a high residence time of the particles and the residence time of majority of particles remain in higher-mid range.

Various factors affect the residence time of particles. A sub ambient aspiration pressure (4.5 MPa & 5 MPa) pulls the particles into the recirculation zone resulting in stagnation of particles. This increases the residence time of particles in general, but the high velocity achieved by the atomizing gas due to increasing operating pressure results in the maximum residence time decreasing. Another factor affecting the high residence time is the shape of the recirculation zone and its eye. The shape of the recirculation zone and the eye of it determines how the particles enter the high-speed gas jets which in turn affects the number of particles travelling through the low velocity gas layers.

In the physical CCGA process, the melt is broken into ligands by the shearing forces due to atomizing gases. A very high maximum residence time results in melt freeze off leading to increase in particle size and the process gets terminated. A low maximum residence time results in particles exiting the primary atomization region too soon. Therefore, an appropriate operating pressure is one where the residence time of the melt is sufficient to deform the melt without leading to a melt freeze off.

8.6 Aspiration pressure

Aspiration pressure is an important process parameter in the CCGA process. Aspiration pressure is measured at the melt exit and is the pressure due to the average mass balance

across the melt exit in the recirculation zone. Aspiration pressure across the melt nozzle depends on the operating pressure and nozzle design parameters. It was measured for all the pressures in all the designs considered in this study. Generally, open wake cases produce an over-ambient aspiration pressure and the closed wake cases produce a sub-ambient aspiration pressure in this study. Figure 8.15 shows the variation in aspiration pressure for all the

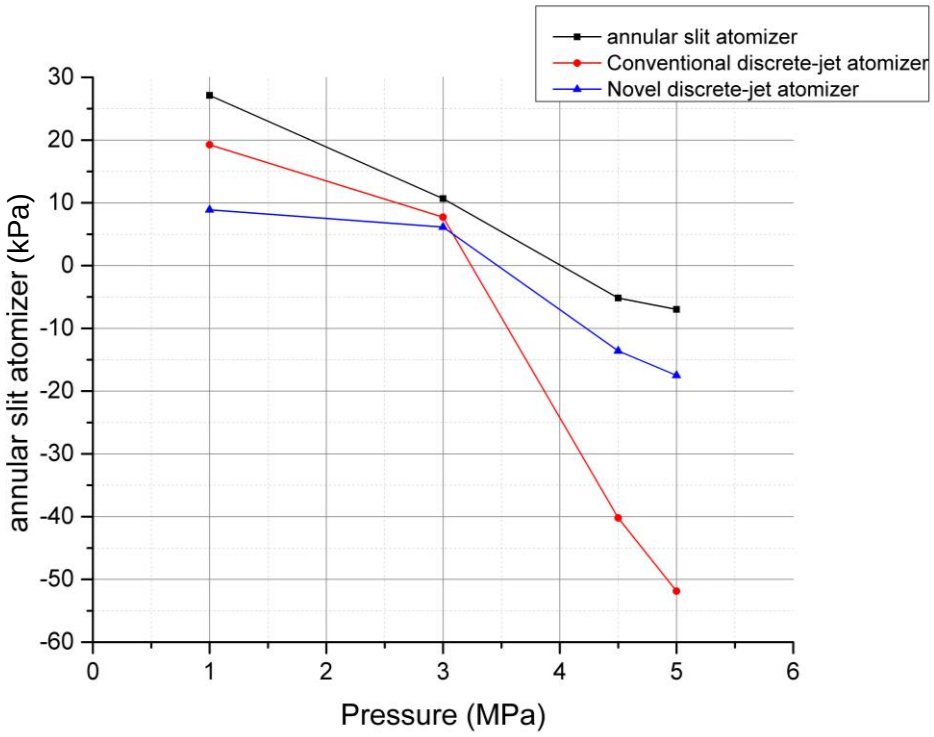

Figure 8.15 Variation of aspiration pressure (kPa) wrt operating pressures (MPa)

pressures considered. Table 8.1 shows the aspiration pressures corresponding to all operating pressures.

Table 8.1 Table containing aspiration pressures for all operating pressures.

Pressure	Annular slit atomizer (kPa)	Conventional discrete-jet atomizer (kPa)	Hybrid discrete-jet atomizer (kPa)
1 MPa	27.13	19.264	8.9
3 MPa	10.682	7.7178	6.125
4.5 MPa	- 5.178	-40.21	-13.588
5 MPa	-6.982	-51.879	-17.49

An important trend noticed in aspiration pressure changes in the gas-only flow field is the decrease in the aspiration pressure as the operating pressure increases. As discussed before, the energy and momentum possessed by the gas increases as the operating pressure increases. This leads to formation of shocks with increased strength which in turn affects the aspiration pressure (relative to the surrounding).

The nozzle design plays an important role in determining the flow features around the melt nozzle. The annular slit atomizer produces highest aspiration pressure among the three designs for every operating pressure due to the lack of offset distance and the intermittent spacing in the annular slit along with a shorter protuberance length. The discrete jet atomizer with the offset distance produces large variations in aspiration pressure. The longer melt nozzle along with the offset distance allows the gases to expand more and this leads to a recirculation zone with low velocities as seen in the Figure 8.15. Also, both the nozzle designs with no offset distance exhibit similar trends in changes in aspiration pressure.

The offset space in the discrete jet atomizer leads to increased expansion and this affects the mass flux in the recirculation zone. The increased area around the melt nozzle influences the aspiration pressure across the melt nozzle surface. Though the gas flow rate is the minimum in the design with no offset space, the lack of offset space reduces the area around the nozzle where the gases can expand, and this yields higher aspiration pressures.

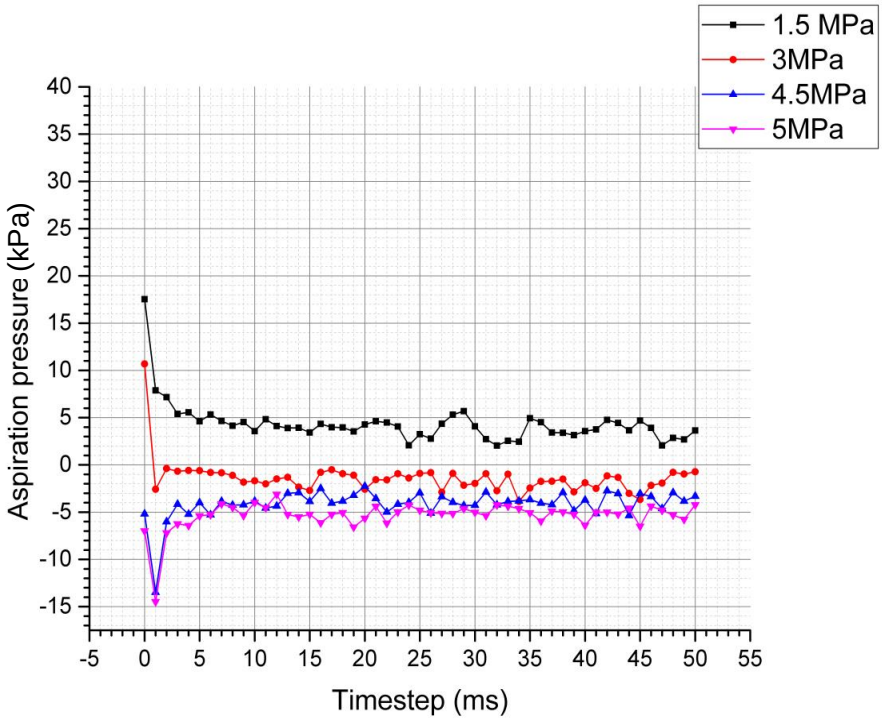

Figure 5.53 Graph showing the Aspiration pressure (kPa) vs Timesteps (ms)

An ideal nozzle must have an appropriate aspiration pressure i.e. the aspiration pressure should not be too deep to stagnate the melt in the recirculation zone or not too high to stop the melt flow.

The changes in aspiration pressure on introduction of melt has not been studied experimentally due to the high temperature factor. This model measures the aspiration pressure in front of the wall replacing the melt tube for every millisecond till 50 milliseconds. In this study, an over ambient aspiration pressure was observed throughout 50 milliseconds for 1.5 MPa pressure. The other three pressures encountered a sub-ambient aspiration pressure when the particles enter the recirculation zone. As discussed previously, a sub ambient pressure stagnates the particles in the recirculation zone and the particles exit it on overcoming this 'pulling' pressure.

A noteworthy observation in the Figure 5.53 is the sudden changes in the aspiration on introduction of particles into the recirculation zone. The particles are given a velocity of 1.5 ms^{-1} in the direction of outlet and as such the particles move forward and stagnate. The mass concentration of the particles in the recirculation zone increases and becomes nearly constant as seen in the Figure 5.53. This means the mass of the particle entering the recirculation zone is higher than the mass of the particles flowing towards the melt nozzle for exiting the recirculation zone. This stagnating mass in the recirculation zone influences the pressure exerted by the gas on the melt nozzle surface. The aspiration pressure measured in a relative pressure to the surrounding gases. The stagnation of particles in the recirculation zone downstream the melt exit reduces the over ambient pressure in the open wake cases and deepens the sub ambient pressure in the closed wake cases.

Most of the commercial atomizers use the single-phase aspiration pressure as the guide for usage. The rapid changes in the aspiration pressure in the initial timesteps indicates that the influence of melt is not negligible**.** Though the pressure is high at 3MPa (10.682 kPa) in the gas only flow field, it varies between 0 to -4 kPa throughout 50 milliseconds. This is due to the particles flowing against the gases and reaching zero-velocity state near the eye of the recirculation zone. Despite the aspiration pressure becoming sub ambient when the melt flow reaches a steady state, in order to initiate the process, the melt has to be maintained at a higher pressure than the gas-only aspiration pressure. This high pressure of melt will affect the velocity with which it enters the recirculation zone thereby affecting the mass entering it per unit time. A faster influx of melt will give rise to improperly atomized ligands which affects the particle size distribution.

Figure 8.16 shows the variation in aspiration pressure(kPa) wrt operating pressure (MPa) with and without the particles. The flow field without the particles is in the steady-state and hence

the aspiration pressure is constant. The flow field with particles is transient but the aspiration pressure varied around a constant value between 10 milliseconds and 50 milliseconds. Therefore, average aspiration pressure for the 40 milliseconds (10 ms-50 ms) was calculated for all the cases and plotted. It can be seen from the Figure 8.16 that the aspiration pressure does not change as steeply for the two-phase flow-field as seen in the gas-only flow field.

The difference in aspiration pressures with and without the particles is high in the over-ambient cases i.e. 1.5 MPa and 3 MPa. The aspiration pressure is a relative pressure and depends on the surrounding conditions. This is because the particles reach their zero-velocity state at the eye of the recirculation zone and stagnate, and stagnation of particles creates a region of high pressure. This leads to a relative low pressure in front of the melt nozzle. The aspiration pressure becomes subambient in the 3 MPa case. The difference in the aspiration pressures with and without the particles is low in the subambient cases i.e. 4.5 MPa and 5MPa. The subambience in this relative pressure (aspiration pressure) is reduced in these two cases as the movement of particles around the melt nozzle affects the aspiration pressure. It can be

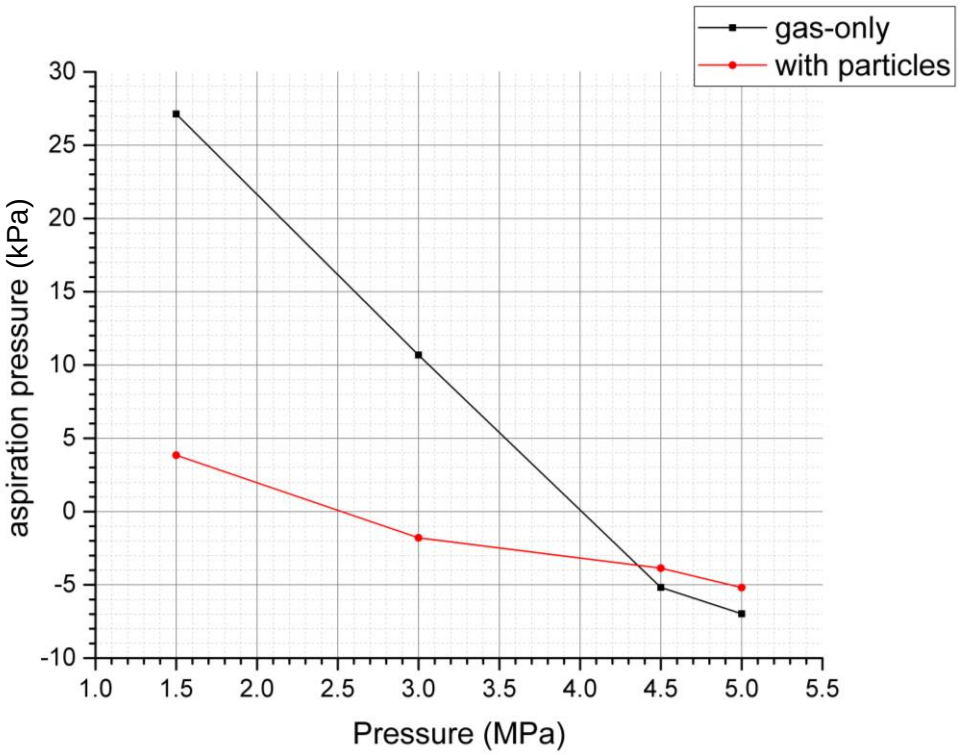

Figure 8.16 Variation in aspiration pressure(kPa) wrt operating pressure (MPa) with and without particles

safely concluded from the Figure 8.16 that the aspiration pressure predictions based on gas-only investigation are not reliable and a two-phase analysis is essential to establish correct guide for the industry.

8.7 Pulsatile model

The movement of melt inside the recirculation zone influences the interaction between the melt and the gas which in turn affects the particle size distribution. A pulsation model has been studied by a lot of researchers with prominent works carried out by Mullis et al and Ting et al. The pulsatile model has been discussed in chapter 3. In this model, the melt moves inside the recirculation zone in a pulsing fashion leading to oscillating flow features. The melt disrupts the Mach disk when it enters the recirculation zone of a closed wake flow field. The disruption of Mach disk enables the recirculating gas downstream the Mach disk to enter the recirculation zone and this forces the melt into the melt tube. The absence of melt results in Mach disk formation and the melt enters the recirculation zone again. This is the pulsation model.

The changes in the aspiration pressure while the melt is being atomized has not been studied in depth. The aspiration pressure in gas only flow field has been studied extensively. Generally, an open wake has an over ambient aspiration pressure, and the closed wake has a sub ambient aspiration pressure.

The pulsation model has two distinct components – the melt disrupting the Mach disk, the gas downstream the Mach disk disrupting the melt flow. The lack of melt tube in the model used in this study forces a constant melt supply into the recirculation zone as the particles are directly released into the recirculation zone. This makes it impossible to model the disruption of melt flow. In physical reality, the recirculating gases prevents the melt from entering the chamber from the melt delivery tube.

The first part of the pulsation model has been analysed in this study. A Mach disk is formed when oblique shocks of sufficient strength from different families of shocks interact to form a normal shock. The strength of the shock depends on the difference between the operating pressure and the ambient conditions and closed wake is observed at high operating pressures due to this reason. The disruption of Mach disk is brought about by the loss of strength in the oblique shocks (i.e. energy losses in the high-speed gas layers). The energy losses prevent the oblique shocks from forming the Mach disk despite their interaction with each other. This is the mechanism observed in open wake cases too.

The introduction of particles in the high-speed gas jets leads to energy losses due to interaction (aerodynamic losses). This energy loss affects the oblique shock formed which in turn affects the Mach disk formation. The velocity contour plots for various timesteps have been shown in Figure 5.38-5.70. The presence of particles in the recirculation zone results in velocity losses in it. As the particles travel along the outer layer of expansion waves (boundary of recirculation zone), the energy (velocity) losses result in weaker oblique shocks as compared to the gas only

flow field. Weaker oblique shocks do not form a Mach disk on interaction. This can be seen in the Figure 5.38-5.70.

The second component of the pulsatile model can be analysed by including a melt tube which couples the melt flow with flow features in front of the melt nozzle. The disruption of Mach disk will cause the recirculating gas downstream the Mach disk also to join the first recirculation zone. The constant influx of particles with a constant velocity creates a relative sub ambient pressure along the melt delivery wall as the particles flow forward and stagnate around the recirculation zone's eye. In the absence of this constraint, the melt flow will be coupled with the drawing or pushing pressure (aspiration pressure) due to the recirculating gases. In physical CCGA, the melt will be maintained at a pressure higher than the over ambient pressure to ensure constant melt flow into the recirculation zone. The constant melt influx constraint in this model prevents the pressure changes (sub-ambient to over ambient) and hence the second part of the pulsation model cannot be realised.

8.8 Critical assessment of the models.

The main research interests in the field of CCGA are wake closure pressure, aspiration pressure, velocity of melt and pulsation of melt in the recirculation zone as discussed in the above sections.

The two-dimensional AS nozzle flow domain is based on the model developed by Motaman. Experimental works available for validation are mostly based on DJ nozzles. Therefore, the model has been optimized with gas flow rate. This is a good approximation as this allows us to simulate the flow field produced by the discrete-jet nozzle to a certain extent and measure the process parameters depending on the mass flow rate. The major limitation of simulating the DJ nozzle in two-dimension is that the flow features cannot be captured accurately due to the intermittent spacing in DJ nozzle. The wake conditions and wake closure pressure have been analysed. The wake closure pressure is in agreement with the experimental WCP observed by Motaman. Similarly, the three-dimensional conventional DJ nozzle is based on the DJ nozzle in which the experimental works were carried out by Motaman and the wake conditions are agreement with his works.[101]

Aspiration pressure is another important process parameter. Figure 8.16 shows the comparison between the gas-only aspiration pressure and aspiration pressure with melt presence. It has been inferred that gas-only aspiration pressure cannot be used as an industrial guide. The aspiration pressure variation due to the presence of melt has been presented. This is a recent development in this field and there is no experimental data available to compare the results as it is difficult to measure the variation with hot melt present in physical scenario.

Pulsation model has been studied extensively by Mullis et al. [86] The high speed imaging works carried out by Mullis concluded that the melt pulsates at low intensity in open wake cases and is prominent in closed wake cases. The first part of pulsation model has been realized in this study. The Mach disk is disrupted by the melt flowing through the oblique shocks forming the Mach disk. The complete pulsation of the melt cannot be achieved in this model due to the absence of melt delivery tube.

The velocity of the particles at 3 MPa was also around 30-40 ms^{-1} in this study. Briggs et al analysed images obtained by high-speed imaging to quantify the velocity of the melt. [125] In the CCGA, the size of the droplets affects the velocity in which it travels in the gas. They found out that the particles travelled through the expansion waves around the recirculation zone as observed in this model. They also found that the particles moved at velocities in the range of 30 ms^{-1} in their flow domain (about 7 nozzle diameters downstream). This velocity and the velocity estimates of Mullis et al are in agreement with the velocity observed at 3 MPa in this study.

Certain approximations have been introduced in the models to reduce the computational power requirement and though the major results in this study have been found to be in agreement with experimental works, the trade-off is that few aspects of the CCGA cannot be analysed or realized. The future works in conclusion discusses the developments that can be implemented to the models.

Summary

The results of all the models have been discussed in this chapter. All the three nozzle designs considered in this study were analysed for the same range of pressure and closed wake was found in all pressures greater than 4.5 MPa. A strong Mach disk has been observed in both the conventional discrete jet atomizer and annular slit atomizer. A weak Mach disk has been observed in the novel discrete jet atomizer. The gas consumption rate is higher in annular slit which affects the production costs. The recirculation zones formed in the annular slit atomizer are characterised by high velocities compared to their counterparts due to lack of offset spacing and intermittent spacing.

The intermittent spacing in the nozzle design reduced the gas consumption rate, provided space for expansion and lead to energy losses. The cross-sectional view of the velocity contours shows the low velocity layers between two adjoining gas expansion. This energy loss does not happen in the annular slit and the gas has more energy to expend on their interaction with particles. Similarly, the offset distance in the atomizer leads to more expansion and increased energy losses. This also affects the energy available for particle interaction. These losses can

be overcome by operating the atomizer at a pressure higher than the ideal operating pressure which will increase the cost of powder production.

These geometrical parameters affect the aspiration pressure. Annular slit atomizer produces the highest aspiration pressure due to close proximity of gas and melt exits. The discrete jet with no offset has the minimum gas flow rates but the lack of offset space gives rise to minimum over ambient aspiration pressure and higher sub ambient pressures. The velocity contour plots of novel discrete-jet atomizer shows that the gases rapidly lose their energy due to expansion and boundary layer interaction. This affects the shocks formed downstream and the aspiration pressure relative to it.

The particles acquire velocity on interaction with the gases. The velocity of particles observed in the model was in agreement with works of Briggs et al and Mullis et al. The limitations of the model are constant particle sizing, lack of break-up modelling and absence of melt tube. All these limitations affect the gas energy available for the melt-gas interaction leading to high particle velocity.

Finally, the pulsatile model has been discussed. The oscillation of melt plume can be broken into two parts – melt disrupting the Mach disk and the gases downstream the Mach disk disrupting the melt flow. The first part of this model has been realised in this study. The lack of melt tube and constant influx of melt in this model prevent the coupling of melt and the aspiration pressure and thus the second part of the pulsatile model cannot be realised.

9 CONCLUSION

This thesis can be divided into two parts. The first deals with the analysis of the flow features and the interaction of melt with atomizing gas in an annular-slit nozzle. The second part deals with the flow feature analysis in two discrete-jet nozzles.

The main issue in developing robust numerical model of CCGA is the huge computational requirements. All the nozzles were studied for the same range of operating pressures. The flow domain was solved for one half of the axial section for the annular-slit nozzle due to its rotational symmetry. The results of the gas-only flow field analysis have been presented in the chapter 4. The interaction of melt with the atomizing gas has been analysed in chapter 5. In the case of the discrete-jet nozzles, a periodic model has been adopted. The results have been presented in the chapter 6. The overall discussion has been presented in the chapter 8.

The flow features of the annular slit nozzle were analysed, and the wake closure pressure was found to be 4.5 MPa. The rotational symmetry of this nozzle is maintained throughout the flow times in the gas-only flow.

In the DPM model, the melt was introduced as particles of same diameter and the flow field was solved for 50 milliseconds. This model is based on a number of assumptions such as constant melt flow rate and constant particle size. The trajectories of the particles were analysed for all the pressures ($1.5<P_{op}<5$ MPa). It was found that the movement of melt particles in the recirculation zone is influenced by its shape and the location of eye. The movement of melt particles in the high-speed jets is influenced by the location of the initial shocks and the size of gas expansion. The velocity and the residence time of the particles were analysed for every timestep. The maximum velocity and maximum residence time were also found.

The flow features of the discrete-jet nozzles were analysed, and the open-wake and closed-wake pressures were found. The wake closure pressure for these two designs has not been found as the pressures between 3 MPa and 4.5 MPa were not analysed due to the high computational requirement.

Finally, the aspiration pressure has been found for all the pressures analysed in this study. The aspiration pressures of the Annular-Slit and novel Discrete-Jet atomizers followed the same trend whereas the aspiration pressures of conventional Discrete-Jet atomizer fall steeply as the wake changes from being open to closed. The aspiration pressure of the steady state gas-

only flow and the average aspiration pressure of the two-phase flow (10-50 ms) were compared, and it was found that the aspiration pressure predictions based on gas-only investigation are not reliable and a two-phase analysis is essential to establish correct guide for the industry.

Future works

In the physical reality, the melt is broken into ligands of various diameters which is further atomized to melt droplets. A particle diameter function can be incorporated to introduce particles with various diameters in the flow domain to optimize the model. Another approximation is the elimination of melt delivery tube. The consequence of this elimination is that the second part of the pulsatile model cannot be realized. The model can be optimized by introducing the melt delivery tube. This will couple the aspiration pressure and the melt movement into the recirculation zone. This is an important optimization, as the pulsation of the melt can be investigated. The melt delivery tube will enable the process to reach the state of little to no melt in the flow domain (second part of pulsatile model).

The introduction of melt disrupts the rotational symmetry and in-order to simulate the melt movement accurately, a three-dimensional model is essential. In the physical reality, the melt moves across the nozzle surface (bottom surface), but the entire surface is not wetted leading to improper prefilming. In a two-dimensional model, this improper prefilming cannot be captured accurately. Therefore, a three-dimensional model is essential to simulate the melt movement around the nozzle. Also, the need for a three-dimensional model for discrete-jet nozzles due to lack of rotational symmetry has been discussed in chapter 6. Three-dimensional models can be developed to analyse the melt movement in order to understand it in depth.

REFERENCES

1. German, R.M., *Powder metallurgy science.* Metal Powder Industries Federation, 105 College Rd. E, Princeton, N. J. 08540, U. S. A, 1984. 279, 1984.
2. Poquillon, D., et al., *Cold compaction of iron powders—relations between powder morphology and mechanical properties: Part I: Powder preparation and compaction.* Powder Technology, 2002. **126**(1): p. 65-74.
3. Klar, E., *Powder metallurgy: applications, advantages, and limitations.* 1983.
4. White.D.G, *Powder metallurgy concept* Advances in Powder Metallurgy and Particulate Materials, 2002. **MPIF Ed, USA**: p. 1-12.
5. Lawley, A., *Atomization: the production of metal powders.* Metal Powder Industries Federation, 1105 College Rd. East, Princeton, New Jersey 08540-6692, USA, 1992. 159, 1992.
6. Singh, S., S. Ramakrishna, and R. Singh, *Material issues in additive manufacturing: A review.* Journal of Manufacturing Processes, 2017. **25**: p. 185-200.
7. Grant, N.J., *Rapid solidification of metallic particulates.* JOM, 1983. **35**(1): p. 20-27.
8. Grant, N.J., *Rapid Solidification Technology: Particulate Production and Consolidation Structure-properties relationships.* Industrial Materials Science and Engineering, 1984.
9. Buelow, N.L., *Microstructual investigation of mixed rar earth iron boron processed vis melt-spinning and high-pressure gas-atomization for isotrophic bonded permanent magnets*. 2005, Ames Lab., Ames, IA (United States).
10. Mais, B. and G.A. Mowbray, *UMT promises tight control of particle size.* Metal Powder Report, 1998. **53**(11): p. 30-33.
11. Hohmann, M., et al., *Modern Systems for Ceramic-Free Powder Production.* Advances in Powder Metallurgy & Particulate Materials--1992., 1992. **1**: p. 27-39.
12. Upadhyaya, G.S., *Powder metallurgy technology*. 1997: Cambridge Int Science Publishing.
13. Gutmanas, E.Y., *Materials with fine microstructures by advanced powder metallurgy.* Progress in Materials Science, 1990. **34**(4): p. 261-366.
14. Angelo, P. and R. Subramanian, *Powder metallurgy: science, technology and applications*. 2008: PHI Learning Pvt. Ltd.
15. Hirschhorn, J.S., *Introduction to powder metallurgy.* 1969, 341 P, 1970.
16. Klar, E., *Atomization.* Metals handbook, 1984: p. 25-51.
17. Aydin, O. and R. Unal, *Experimental and numerical modeling of the gas atomization nozzle for gas flow behavior.* Computers & Fluids, 2011. **42**(1): p. 37-43.
18. Li, B., et al., *Two dimensional modeling of momentum and thermal behavior during spray atomization of γ-TiAl.* Acta materialia, 1996. **44**(6): p. 2409-2420.
19. Kearns, M., *Development and applications of ultrafine aluminium powders.* Materials Science and Engineering A, 2004. **375-377**: p. 120-126.
20. Mullis, A.M., et al., *Estimation of cooling rates during close-coupled gas atomization using secondary dendrite arm spacing measurement.* Metallurgical and materials Transactions B, 2013. **44**(4): p. 992-999.
21. Ting, J., M.W. Peretti, and W.B. Eisen, *The effect of wake-closure phenomenon on gas atomization performance.* Materials Science and Engineering: A, 2002. **326**(1): p. 110-121.
22. Anderson, I., R. Figliola, and H. Morton, *Flow mechanisms in high pressure gas atomization.* Materials Science and Engineering: A, 1991. **148**(1): p. 101-114.
23. Ting, J., et al., *Design and testing of an improved convergent-divergent discrete-jet high pressure gas atomization nozzle.* Metal Powder Industries Federation, Advances in Powder Metallurgy & Particulate Materials- 1998, 1998. **3**: p. 10.
24. Grant, P., *Solidification in spray forming.* Metallurgical and Materials transactions A, 2007. **38**(7): p. 1520-1529.
25. Li, D., *Encyclopedia of microfluidics and nanofluidics*. 2008: Springer Science & Business Media.
26. Rathakrishnan, E., *Applied gas dynamics*. 2019: John Wiley & Sons.

27. White, F.M., *Fluid Mechanics, in SI Units*. 2016, McGraw-Hill, New York.
28. JD, A., *Fundamentals of aerodynamics*. 6 ed. 2017: McGraw-Hill.
29. Versteeg, H.K. and W. Malalasekera, *An introduction to computational fluid dynamics: the finite volume method*. 2007: Pearson education.
30. Wilcox, D.C., *Turbulence modeling for CFD. La Canada, CA: DCW Industries.* Inc, November, 2006.
31. ANSYS, A., *ANSYS Fluent User's Guide, 17.2.* Canonsburg: ANSYS, 2016.
32. Saiy, M., *Turbulent mixing of gas streams*. 1974, PhD Thesis, Imperial College, University of London.
33. Spalding, D.B., *Mathematical models of turbulent transport processes*. 1978: Imperial College of Science and Technology, Department of Mechanical Engineering.
34. Wilcox, D.C., *Reassessment of the scale-determining equation for advanced turbulence models.* AIAA journal, 1988. **26**(11): p. 1299-1310.
35. Speziale, C.G., R. Abid, and E. Anderson. *Clay: A Critical Evaluation of Two-Equation Models for Near Wall Turbulence*. in *AIAA elat Fluid Dynamics, Pluma Dynamics and Luers Conference, June*. 1990.
36. Menter, F., *Improved two-equation k-ω turbulence models for aerodynamic flows NASA Ames, CA.* NASA Technical Memorandum, 1992. **103975**.
37. Varaksin, A.Y., *Turbulent particle-laden gas flows*. 2007: Springer.
38. Gosman, A. and E.J.L. Ioannides, MO, *Aspects of Computer Simulation of Liquid-Fueled Combustors, AIAA Paper 81-0323; St.* 1981.
39. Ishii, M.J.N.S.r.T.R.A., *Thermo-fluid dynamic theory of two-phase flow.* 1975. **75**: p. 29657.
40. Ishii, M., *One-dimensional drift-flux model and constitutive equations for relative motion between phases in various two-phase flow regimes*. 1977, Argonne National Lab., Ill.(USA).
41. Ishii, M. and N.J.A.j. Zuber, *Drag coefficient and relative velocity in bubbly, droplet or particulate flows.* 1979. **25**(5): p. 843-855.
42. Ishii, M., K.J.N.E. Mishima, and design, *Two-fluid model and hydrodynamic constitutive relations.* 1984. **82**(2-3): p. 107-126.
43. Delhaye, J. and J. Achard, *On the averaging operators introduced in two-phase flow modeling*. 1976: Centre d'études nucléaires de Grenoble.
44. Drew, D.A.J.A.r.o.f.m., *Mathematical modeling of two-phase flow.* 1983. **15**(1): p. 261-291.
45. Drew, D.A.J.P.t.-p.f., *Analytical modeling of multiphase flow.* 1993.
46. Hirt, C.W. and B.D.J.J.o.c.p. Nichols, *Volume of fluid (VOF) method for the dynamics of free boundaries.* 1981. **39**(1): p. 201-225.
47. Enwald, H., E. Peirano, and A.-E. Almstedt, *Eulerian two-phase flow theory applied to fluidization.* International Journal of Multiphase Flow, 1996. **22**: p. 21-66.
48. Thompson, J.S., *A study of process variables in the production of aluminium powder by atomization.* Journal of the Institute of Metals, 1948. **74**: p. 101.
49. Klov, E. and W. Schfer, *High Pressure Gas Atomisation of Metal, 57, Syracuse*. 1972, Syracuse University Press.
50. Bradley, D., *On the atomization of liquids by high-velocity gases.* Journal of Physics D: Applied Physics, 1973. **6**(14): p. 1724.
51. Ünal, R., *The influence of the pressure formation at the tip of the melt delivery tube on tin powder size and gas/melt ratio in gas atomization method.* Journal of Materials Processing Technology, 2006. **180**(1-3): p. 291-295.
52. Jiang, G., H. Henein, and M. Siegel, *Intelligent sensors for atomization processing of molten metals and alloys*, in *Production and Processing of Fine Particles*. 1988, Elsevier. p. 497-506.
53. Zeoli, N., *Multiphase modelling of the characteristics of close coupled gas atomization*. 2011, Aston University.

54. Ouyang, H.-W., C. Xin, and B.-y. Huang, *Influence of melt superheat on breakup process of close-coupled gas atomization.* Transactions of Nonferrous Metals Society of China, 2007. **17**(5): p. 967-973.
55. Frazer RP, E.P., *Research into performance of atomization for liquids.* Imperial College Chemical Engineering Society Journal, 1953. **7**: p. 52-68.
56. Savart, F., *Annal.* Chim, 1833. **53**: p. 337.
57. Plateau, J., *Memoir on the Phenomena Presented by a Mass of Liquid Free and Removed from the Action of Gravity.* Mem. Acad. R. Belg, 1843. **16**.
58. Rayleigh, L., *On the instability of jets.* Proceedings of the London mathematical society, 1878. **1**(1): p. 4-13.
59. Eötvös, R., *Ueber den Zusammenhang der Oberflächenspannung der Flüssigkeiten mit ihrem Molecularvolumen.* Annalen der Physik, 1886. **263**(3): p. 448-459.
60. Quincke, G., *Wiedemann's Annalen.* 1877.
61. Lenard, P., *Ueber die schwingungen fallender tropfen.* Annalen der Physik, 1887. **266**(2): p. 209-243.
62. Bohr, N., *Xii. Determination of the surface-tension of water by the method of jet vibration.* Philosophical Transactions of the Royal Society of London. Series A, Containing Papers of a Mathematical or Physical Character, 1909. **209**(441-458): p. 281-317.
63. Dombrowski, N. and W. Johns, *The aerodynamic instability and disintegration of viscous liquid sheets.* Chemical Engineering Science, 1963. **18**(3): p. 203-214.
64. Bradley, D., *On the atomization of a liquid by high-velocity gases: II.* Journal of Physics D: Applied Physics, 1973. **6**(18): p. 2267.
65. See, J.B. and G.H. Johnston, *Interactions between nitrogen jets and liquid lead and tin streams.* Powder Technology, 1978. **21**(1): p. 119-133.
66. Kuehn, R., *Atomization of liquid fuels. Part II.* 1925.
67. Weber, C., *Zum zerfall eines flüssigkeitsstrahles.* ZAMM-Journal of Applied Mathematics and Mechanics/Zeitschrift für Angewandte Mathematik und Mechanik, 1931. **11**(2): p. 136-154.
68. DeJuhasz, K.J., *Dispersion of sprays in solid injection oil engines.* Trans. ASME (OGP), 1931. **53**: p. 65.
69. Laufer, J., *Investigation of turbulent flow in a 2D channel.* NACATN 2133, 1950.
70. Ranz, W., *On Sprays and Spraying. Department of Engineering Research. Pennsylvania State University*. 1956, Bulletin.
71. Tennekes, H., J.L. Lumley, and J.L. Lumley, *A first course in turbulence*. 1972: MIT press.
72. Hinze, J., *0. 1975 Turbulence*. 1972, McGraw-Hill.
73. Kowalewski, T.A., *On the separation of droplets from a liquid jet.* Fluid Dynamics Research, 1996. **17**(3): p. 121-145.
74. Chigier, N. and Z. Farago, *Morphological classification of disintegration of round liquid jets in a coaxial air stream.* Atomization and Sprays, 1992. **2**(2).
75. Mansour, A. and N. Chigier, *Disintegration of liquid sheets.* Physics of Fluids A: Fluid Dynamics, 1990. **2**(5): p. 706-719.
76. Carvalho, I. and M. Heitor, *Liquid film break-up in a model of a prefilming airblast nozzle.* Experiments in Fluids, 1998. **24**(5-6): p. 408-415.
77. El-Genk, M.S. and H.H. Saber, *Minimum thickness of a flowing down liquid film on a vertical surface.* International Journal of Heat and Mass Transfer, 2001. **44**(15): p. 2809-2825.
78. Senecal, P., et al., *Modeling high-speed viscous liquid sheet atomization.* International Journal of Multiphase Flow, 1999. **25**(6-7): p. 1073-1097.
79. Matsumoto, T., et al., *Measurement of surface tension of molten copper using the free-fall oscillating drop method.* Measurement Science and Technology, 2005. **16**(2): p. 432.
80. Hsiang, L.-P. and G.M. Faeth, *Near-limit drop deformation and secondary breakup.* International journal of multiphase flow, 1992. **18**(5): p. 635-652.

81. Anderson, I.E., D. Byrd, and J. Meyer, *Highly tuned gas atomization for controlled preparation of coarse powder.* Materialwissenschaft und Werkstofftechnik, 2010. **41**(7): p. 504-512.
82. Anderson, I.E. and R.L. Terpstra, *Progress toward gas atomization processing with increased uniformity and control.* Materials Science and Engineering: A, 2002. **326**(1): p. 101-109.
83. Miller, S.A., *Apparatus for melt atomization with a concave melt nozzle for gas deflection*. 1986, Google Patents.
84. Mates, S.P. and G.S. Settles, *A study of liquid metal atomization using close-coupled nozzles, Part 1: Gas dynamic behavior.* Atomization and Sprays, 2005. **15**(1).
85. Mates, S.P. and G.S. Settles, *A study of liquid metal atomization using close-coupled nozzles, part 2: atomization behavior.* Atomization and Sprays, 2005. **15**(1).
86. Mullis, A.M., et al., *Log-normal melt pulsation in close-coupled gas atomization.* Metallurgical and Materials Transactions B, 2013. **44**(4): p. 789-793.
87. Ting, J. and I.E. Anderson, *A computational fluid dynamics (CFD) investigation of the wake closure phenomenon.* Materials Science and Engineering: A, 2004. **379**(1-2): p. 264-276.
88. McCarthy, I., et al., *High speed imaging and Fourier analysis of the melt plume during close coupled gas atomisation.* Powder metallurgy, 2009. **52**(3): p. 205-212.
89. Anderson, I. and R. Figliola, *Observations of gas atomization process dynamics((in powder metallurgy)).* Modern developments in powder metallurgy, 1988: p. 205-223.
90. Ünal, A., *Influence of gas flow on performance of "confined" atomization nozzles.* Metallurgical and Materials Transactions B, 1989. **20**(6): p. 833-843.
91. Anderson, I., R. Terpstra, and R. Figliola, *Melt Feeding and Nozzle Design Modifications for Enhanced Control of Gas Atomization.* Advances in powder metallurgy and particulate materials, 2004: p. 26-36.
92. Ting, J., *Gas atomization processing of tin and silicon modified LaNi5 for nickel-metal hydride battery applications*. 1999, Ames Lab., IA (United States).
93. Ting, J., *Optimizing melt tip geometry for high-pressure gas atomization.* Metal Powder Report, 1998. **5**(53): p. 40.
94. Nilsson EOF, N.S., Hagelin EG, *US patent 2997245*, U. Patent, Editor. 1961.
95. Mates, S.P., S.D. Ridder, and F.S. Biancaniello. *Comparison of the supersonic length and dynamic pressure characteristics of discrete-jet and annular close-coupled nozzles used to produce fine metal powders*. in *TMS Annual Meeting and Symposium*. 2000.
96. Motaman, S., et al., *Numerical and experimental modelling of back stream flow during close-coupled gas atomization.* Computers & Fluids, 2013. **88**: p. 1-10.
97. Miller, S. and J. Strauss, *Use of two-phase flow aspiration pressure for improved close-coupled nozzle performance.* Metal Powder Report, 2002. **6**(57): p. 58.
98. McCarthy, I.N., *Optical investigations into close-coupled gas atomisation*. 2010, University of Leeds.
99. Cui, C., F. Cao, and Q. Li, *Formation mechanism of the pressure zone at the tip of the melt delivery tube during the spray forming process.* Journal of materials processing technology, 2003. **137**(1-3): p. 5-9.
100. Miller, S., *Global and midfield imaging of liquid metal atomization.* Advances in Powder Metallurgy & Particulate Materials--1993., 1993. **1**: p. 25-34.
101. Motaman, S., *High-speed imaging and computational modelling of close-coupled gas atomization*. 2013: University of Leeds.
102. Wigg, L., *Drop size prediction for twin-fluid atomizers*. 1960: NGTE.
103. Lubanska, H., *Correlation of spray ring data for gas atomization of liquid metals.* JOM, 1970. **22**(2): p. 45-49.
104. Sun, P., et al., *Review of the methods for production of spherical Ti and Ti alloy powder.* Jom, 2017. **69**(10): p. 1853-1860.
105. Strauss, J., *Close-coupled gas atomization using elevated temperature gas.* Advances in Powder Metallurgy and Particulate Materials, 1999. **1**(1/3): p. 1-23.

106. Slotwinski, J.A. and E.J. Garboczi, *Metrology needs for metal additive manufacturing powders.* Jom, 2015. **67**(3): p. 538-543.
107. Burgess, D.J., et al., *Particle size analysis: AAPS workshop report, cosponsored by the Food and Drug Administration and the United States Pharmacopeia.* The AAPS journal, 2004. **6**(3): p. 23-34.
108. Mi, J., R. Figliola, and I. Anderson, *A numerical simulation of gas flow field effects on high pressure gas atomization due to operating pressure variation.* Materials Science and Engineering: A, 1996. **208**(1): p. 20-29.
109. Espina, P. and U. Piomelli. *Numerical simulation of the gas flow in gas-metal atomizers*. in *Proceedings of FEDSM*. 1998.
110. Zhao, X., et al., *Effect of atomization gas pressure variation on gas flow field in supersonic gas atomization.* Science in China Series E: Technological Sciences, 2009. **52**(10): p. 3046-3053.
111. Xu, Q., et al. *Fundamental fluid dynamics during liquid metal atomization*. in *Liquid Metal Atomization: Fundamentals and Practice as held at the 2000 TMS Annual Meeting*. 2000.
112. Mi, J., R. Figliola, and I. Anderson, *A numerical investigation of gas flow effects on high-pressure gas atomization due to melt tip geometry variation.* Metallurgical and Materials transactions B, 1997. **28**(5): p. 935-941.
113. Zeoli, N. and S. Gu, *Computational validation of an isentropic plug nozzle design for gas atomisation.* Computational materials science, 2008. **42**(2): p. 245-258.
114. Ridder, S.D., et al. *Optimization of an Annular Jet Commercial Gas-Metal Atomizer*. in *TMS Annual Meeting and Symposium*. 2000.
115. Tong, M. and D.J. Browne, *Direct numerical simulation of melt–gas hydrodynamic interactions during the early stage of atomisation of liquid intermetallic.* Journal of Materials Processing Technology, 2008. **202**(1-3): p. 419-427.
116. Neumann, S., et al., *Influencing Parameter Study on Primary Breakup of Free Falling Steel Melt Jets Using Volume of Fluid Simulation.* steel research international, 2016. **87**(8): p. 1002-1013.
117. Kuntz, D.W. and J.L. Payne, *Simulation of powder metal fabrication with high pressure gas atomization.* Advances in Powder Metallurgy and Particulate Materials--1995., 1995. **1**: p. 1.
118. Figliola, R. and I. Anderson, *Characterization of high pressure gas atomization flow fields.* Computational & Numerical Techniques in Powder Metallurgy, 1992: p. 29-39.
119. Underhill, R., et al., *Modelling of droplet behaviour during spray forming using Fluent.* International Journal of Non-Equilibrium Processing, 1997. **10**(2).
120. Grant, P., B. Cantor, and L. Katgerman, *Modelling of droplet dynamic and thermal histories during spray forming—I. Individual droplet behaviour.* Acta Metallurgica et Materialia, 1993. **41**(11): p. 3097-3108.
121. Grant, P., B. Cantor, and L. Katgerman, *Modelling of droplet dynamic and thermal histories during spray forming—II. Effect of process parameters.* Acta metallurgica et materialia, 1993. **41**(11): p. 3109-3118.
122. Grant, P. and B. Cantor, *Modelling of droplet dynamic and thermal histories during spray forming—III. Analysis of spray solid fraction.* Acta metallurgica et materialia, 1995. **43**(3): p. 913-921.
123. Antipas, G., *Modelling of the break up mechanism in gas atomization of liquid metals. Part I: The surface wave formation model.* Computational Materials Science, 2006. **35**(4): p. 416-422.
124. Antipas, G.J.I.J.o.C.M.S. and S. Engineering, *Liquid column deformation and particle size distribution in gas atomisation.* 2011. **4**(3): p. 247-264.
125. Bigg, T., A.J.M. Mullis, and M.T. B, *Spatially Resolved Velocity Mapping of the Melt Plume During High-Pressure Gas Atomization of Liquid Metals.* 2020. **51**(5): p. 1973-1988.

A. APPENDIX

The trajectories of the particles for 50 milliseconds of flow time in this study. The 1.5 MPa (open wake case) and 4.5 MPa (closed wake case) have been discussed in chapter 5. The particle trajectories produced by other two pressures (3 MPa & 5 MPa) are discussed here.

CASE 1: 3MPa

Figure A.1 shows the flow field at 0 millisecond with the open wake highlighted. The gas jets exiting the gas die travel towards the outlet through a series of Prandtl Meyer expansion waves. The GMR for this case was found to be 0.791.

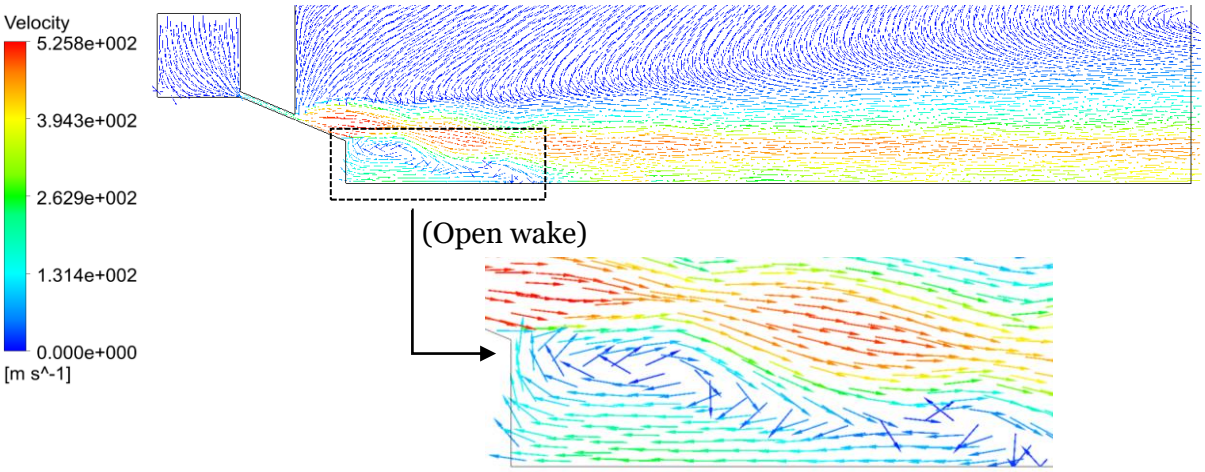

Figure A.1 Velocity vector plots for flow time t = 0 ms

Flow time 0.1-10 milliseconds

The particles are released into the recirculation zone due to the absence of melt delivery tube. Figure A.2 shows the particle trajectories at flow time t=0.1 ms. It can be observed that the particles begin move against the flow direction of recirculating gases.

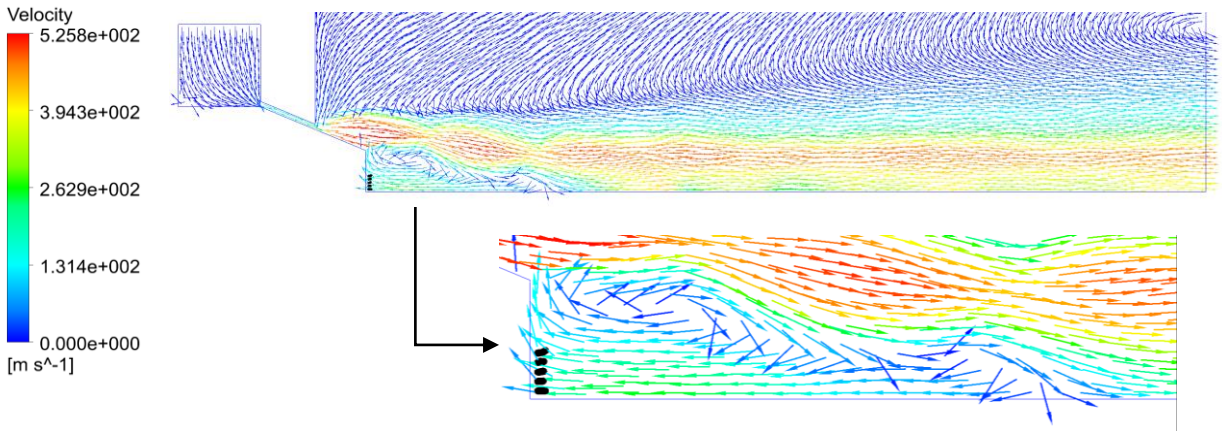

Figure A.2 particle trajectories and velocity vector plots for flow time t = 0.1 ms

Figure A.3 shows the particle trajectories at t=0.5 ms. The particles reach zero velocity state and begin changing flow direction.

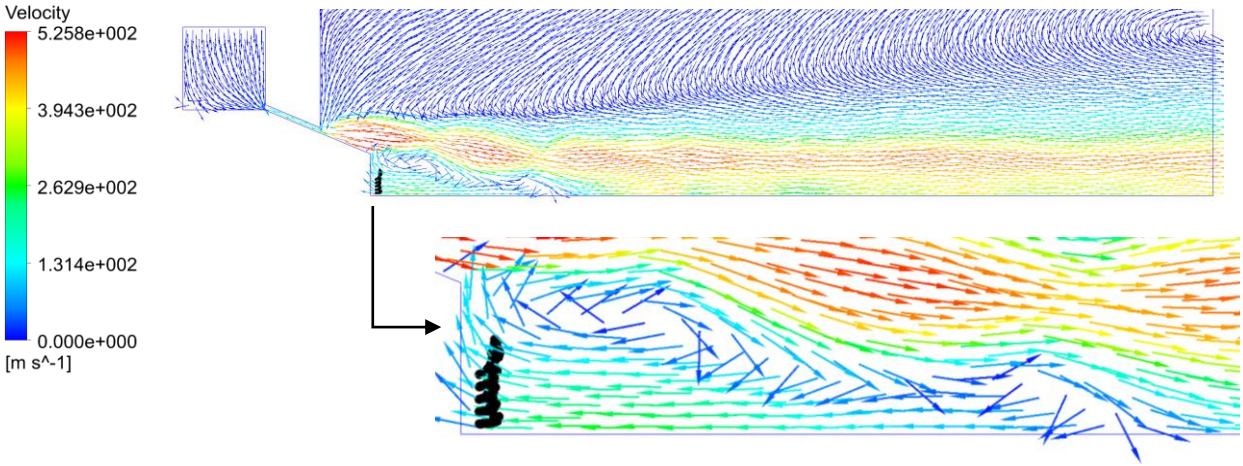

Figure A.3 particle trajectories and velocity vector plots for flow time t= 0.5 ms

Figure A.4 shows the particle trajectories at t=1 ms. The particles flow along with the recirculating gases towards the melt nozzle surface and begin moving towards the nozzle edge to enter the high-speed gas jets.

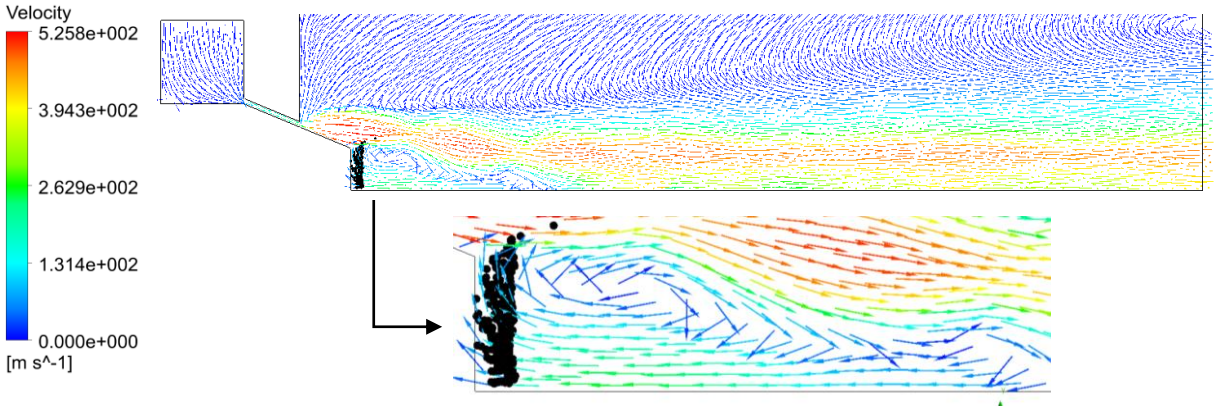

Figure A.4 particle trajectories and velocity vector plots for flow time t= 1ms

Figure A.5 shows the particle trajectories at flow time t=1.5 ms. The particles enter the gas jets and move towards the first oblique shock. The expanding gases undergo compression across the shock waves and begin expanding downstream the shock. The trajectories of the particles upstream of the oblique shock are compact due to the compression of the gases and begin spreading downstream the oblique shock with the expanding gases.

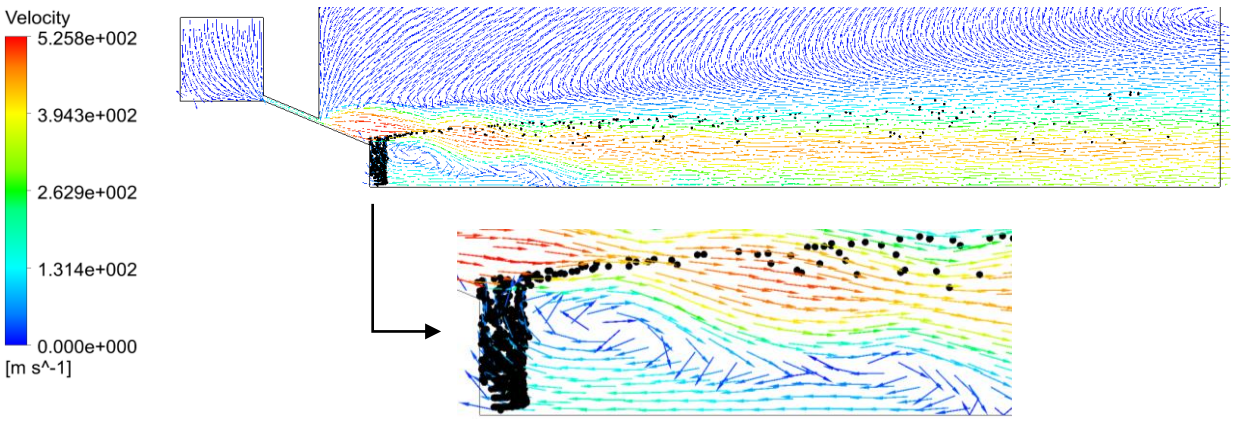

Figure A.5 particle trajectories and velocity vector plots for flow time t= 1.5 ms

Figure A.6 shows the particle trajectories at flow time t=2ms. The particles begin exiting the domain at t= 2ms along the outer layers of expanding gas jets on the near side of the wall boundary.

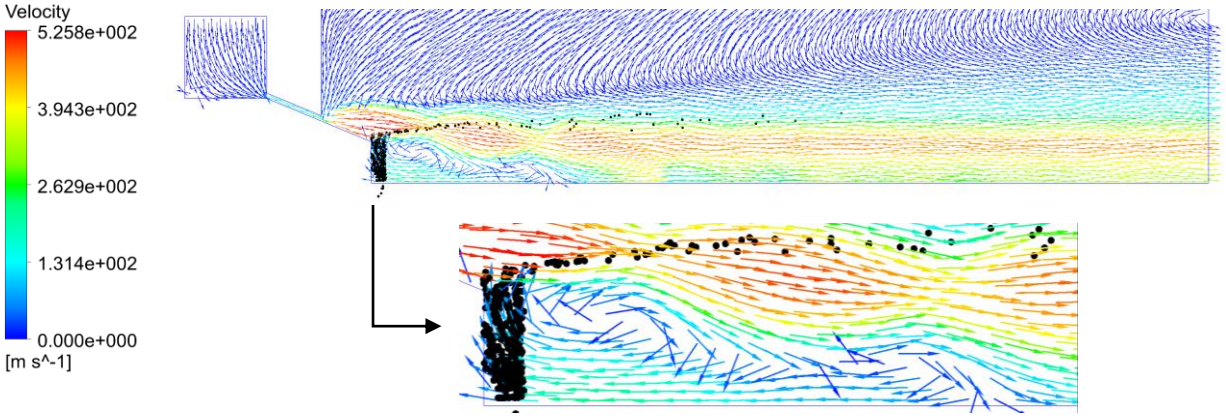

Figure A.6 Particle trajectories and velocity vector plots for flow time t = 2ms

As the particles mass concentration in the recirculation zone increases the particles move further downstream before reaching the zero-velocity state. The particles change their flow direction, move towards the melt nozzle edge and enter the expanding gas jets. It can be seen from comparing the Figure A.7 that the particles move further downstream inside the recirculation zone before reaching the zero-velocity state as the flow time increases.

The gas jets travel towards the outlet through a series of expansion waves and oblique shocks. The strength of the shocks decreases as the flow moves further downstream and this in turn results in gases undergoing reduced compression and increased expansion as the gases move towards the outlet. The spread of the particle trajectories increases as the flow moves towards the outlet due to the above-mentioned reason.

Figure A.7 shows the particle trajectories at flow times t= 5ms, t= 8ms and t= 10ms.

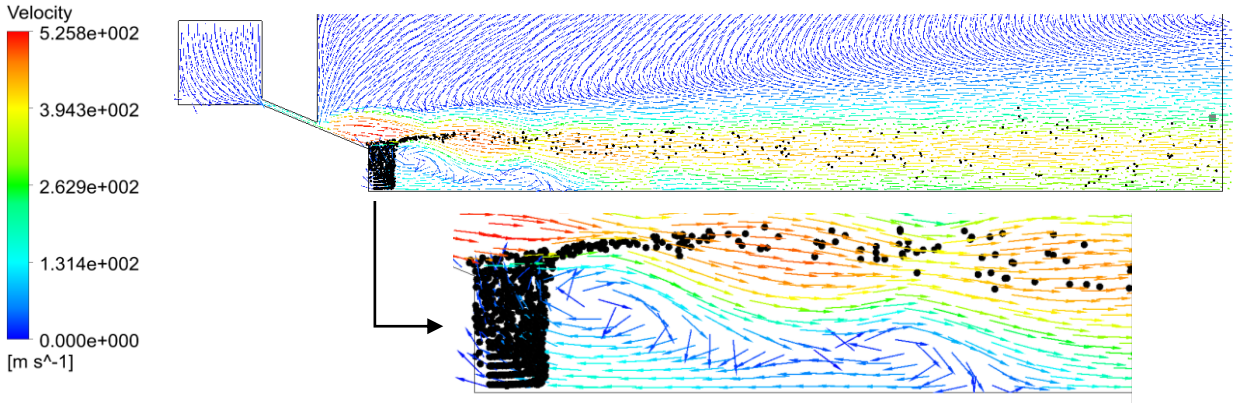

Flow time t = 5 ms

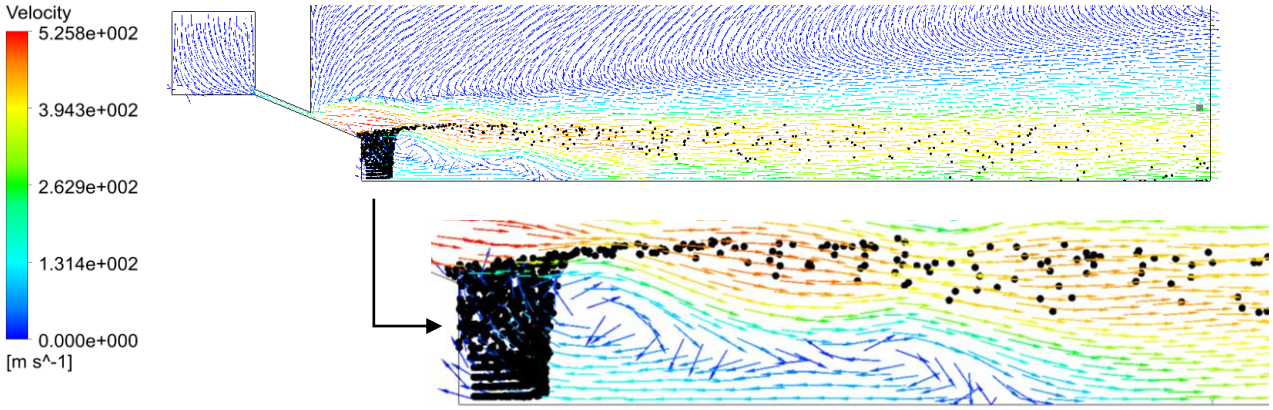

Flow time t = 8 ms

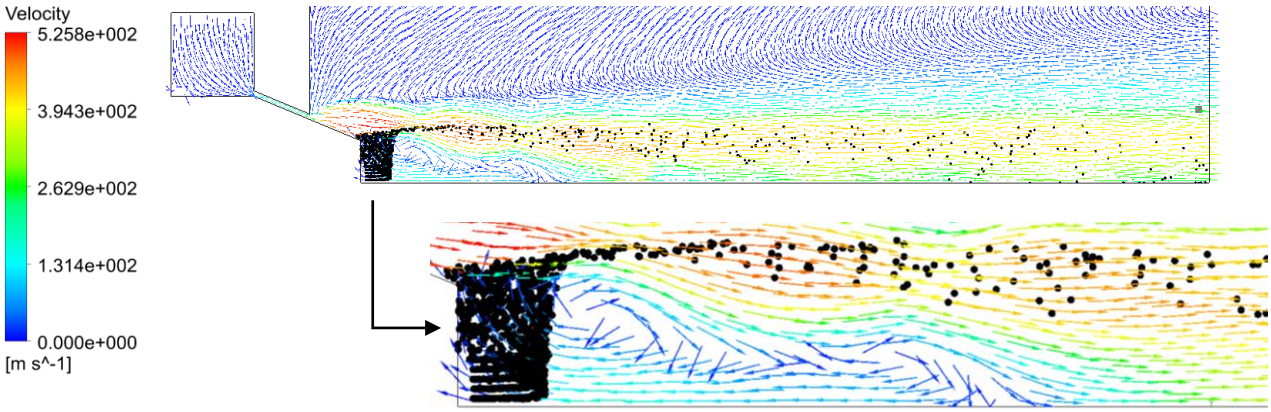

Flow time t = 10 ms

Figure A.7 Particle trajectories and velocity vector plots for flow times t= 5 ms, t = 8 ms and t =10 ms

The number of particles entering the expanding gas jets increases as the particle mass concentration in the recirculation zone increases. This leads to increase in the spread of the particle trajectories. Initially the particles travel along the outer layers of the expansion waves on the near side of the wall. It can be observed from the Figure A.7 that the particle trajectories begin increasingly directed towards the axis with increasing flow time. This is due to the

expanding gas jets converging at the stagnation point which drives the particles in them to be directed towards the axis.

Flow time: 11-20 milliseconds

Figure A.8 and Figure A.9 shows the particle trajectories for the flow time t=12 ms, t= 15ms, t= 18 ms and t= 20ms.

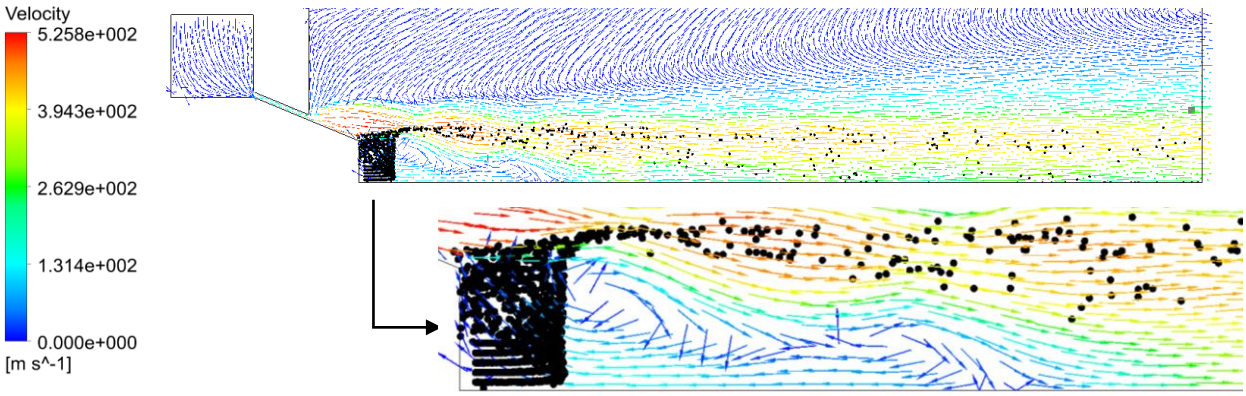

Figure A.8 Particle trajectories and velocity vector plots for flow time t= 12 ms

The particles continue to flow against the gases further downstream before reaching the zero-velocity state. As seen from the Figure 5.7 the particle mass concentration increases gradually through 20 milliseconds. As the number of particles entering the recirculation zone is constant, this gradual increase in the particle mass concentration means that the number of particles exiting the recirculation increases with increasing flow time.

The location of the eye of the recirculation zone and the shape of the recirculation zone influences the movement of particles inside it. The GMR for this particular case was found to be 0.791.

As the mass of gas entering the recirculation zone is higher in this case, the particles do not move downstream as much as observed in the 1.5 MPa case. The particles continue moving till the eye of recirculation zone as observed in Figure A.9 and enter the high-speed gas jets before the first oblique shock through 20 milliseconds. This leads to spread of particle trajectories being condensed upstream the shockwave and expanding downstream the shockwave.

The particle trajectories begin spreading as they move towards the outlet and becoming directed towards the axis. As the spreading of the trajectories increases, the trajectories begin converging along the axis much further away from the outlet. (closer to the melt nozzle).

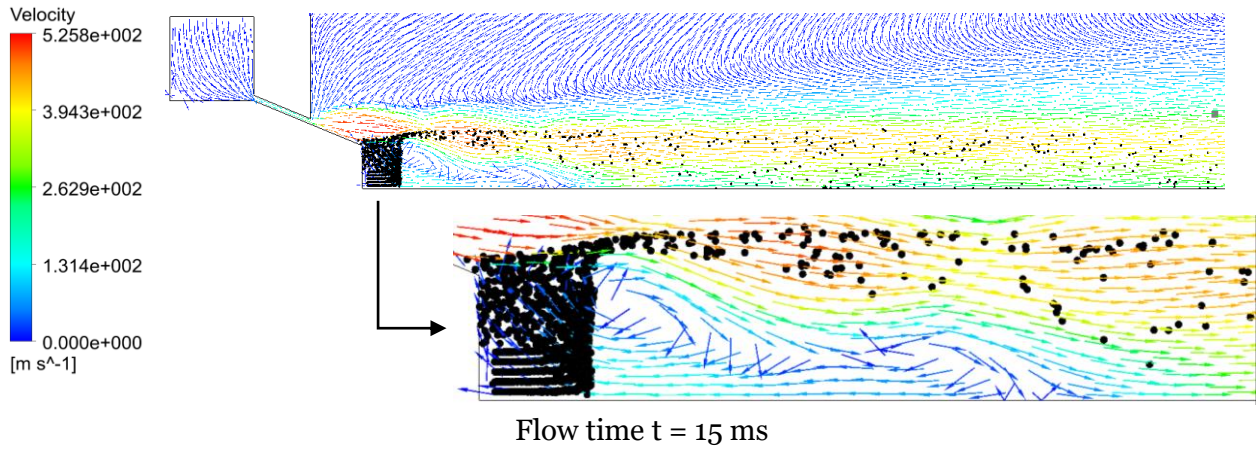

Flow time t = 15 ms

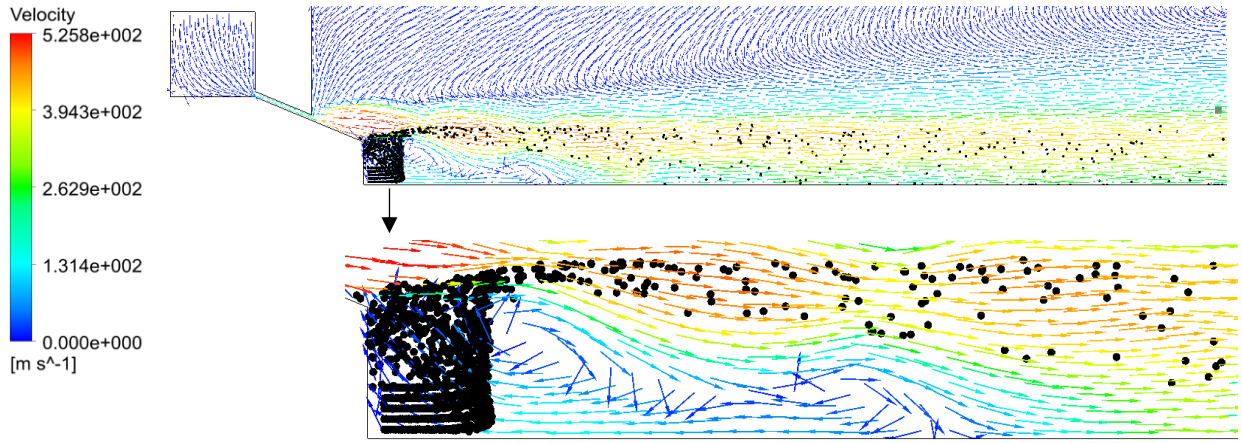

Flow time t = 18 ms

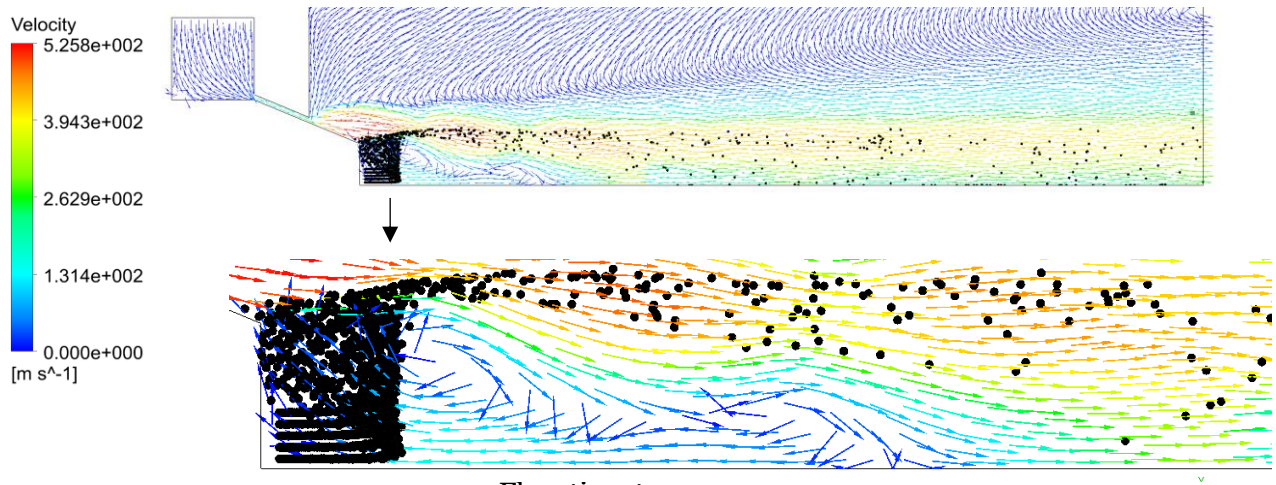

Flow time t = 20 ms

Figure A.9 Particle trajectories and velocity vector plots for flow times t= 15 ms, t= 18 ms and t= 20 ms

Flow time 21-30 milliseconds

Figure A.10 and Figure A.11 shows the particle trajectories till 30 milliseconds.

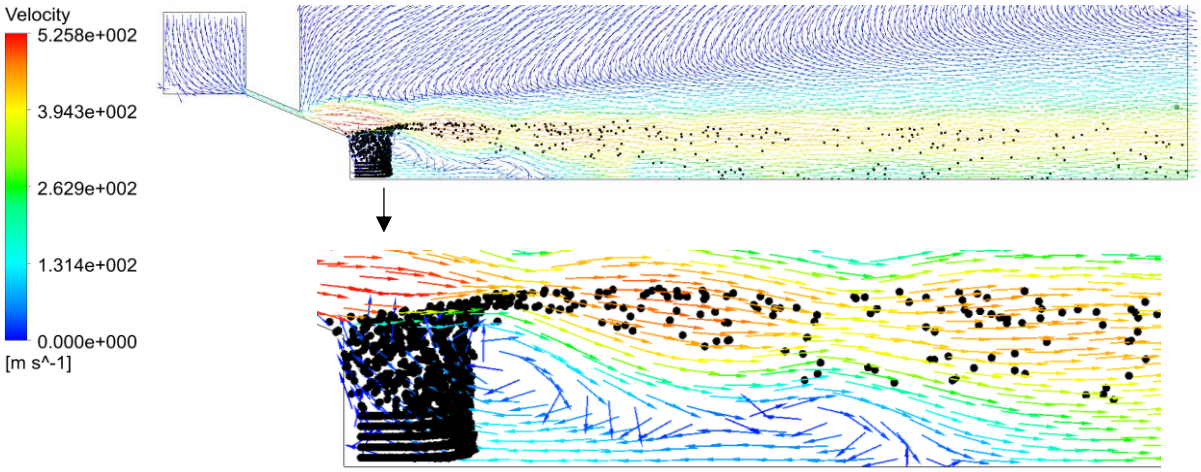

Flow time t = 22 ms

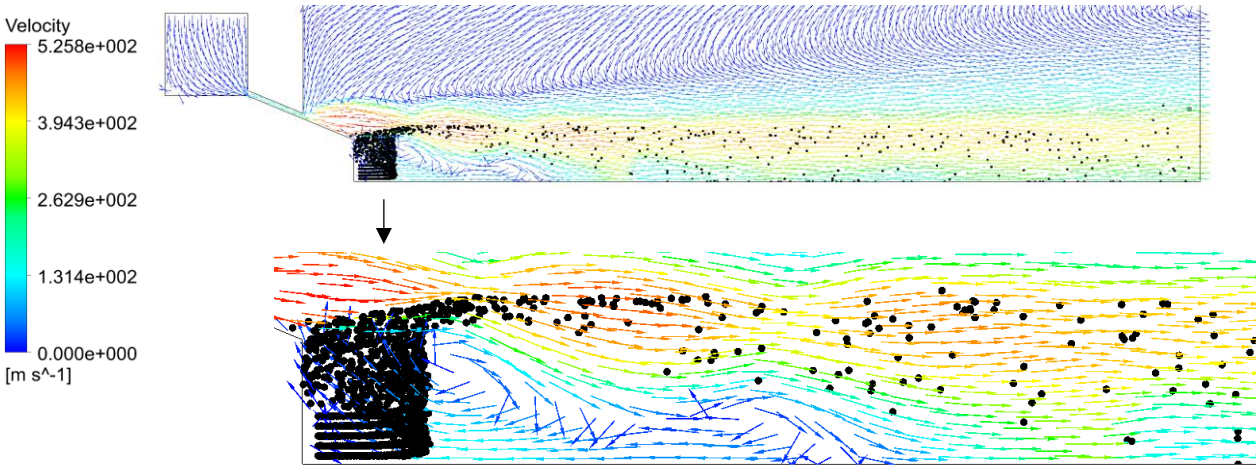

Flow time t = 25 ms

Figure A.10 Particle trajectories and velocity vector plots for flow time t= 22 ms and t=25 ms

The particle mass concentration reaches a near constant value through 30 milliseconds. The particles entering the recirculation zone move downstream, but the recirculating come across the eye of the recirculation zone. The particles do not move across the eye of the recirculation zone as the gases possess enough energy to direct the particles into the expanding gas jets. The eye of the recirculation zone is located just before the first oblique shock meaning the particles join the high-speed gas jets before the oblique shock. This enables the particles to travel along the high-speed gas layers after the first oblique shock wave. In the previous case (1.5 MPa), the particles move further downstream the eye of the recirculation zone as the recirculating gases do not possess sufficient energy to stop the particles.

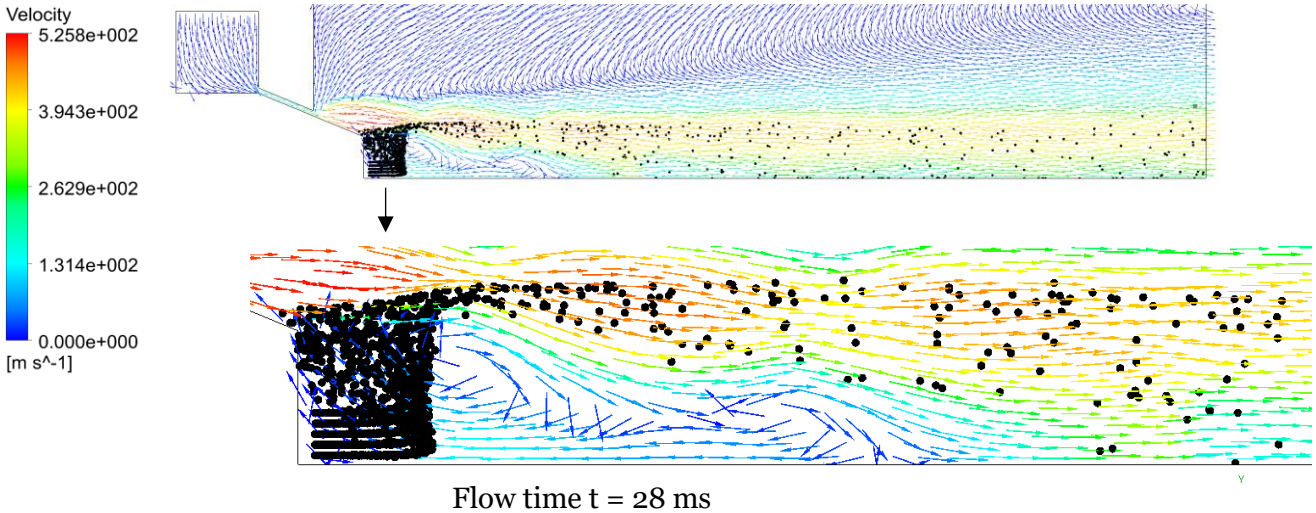

Flow time t = 28 ms

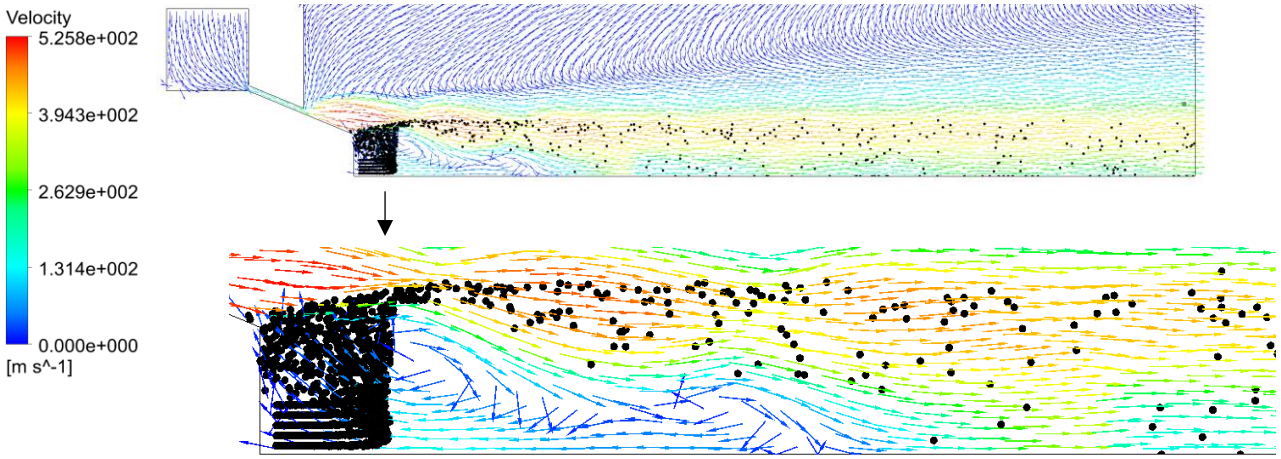

Flow time t = 30 ms

Figure A.11 Particle trajectories and velocity vector plots for flow times t = 28 ms and t= 30 ms

The particle trajectories begin spreading more as they move towards the outlet and becoming directed towards the axis. As the spreading of the trajectories increases, the trajectories begin

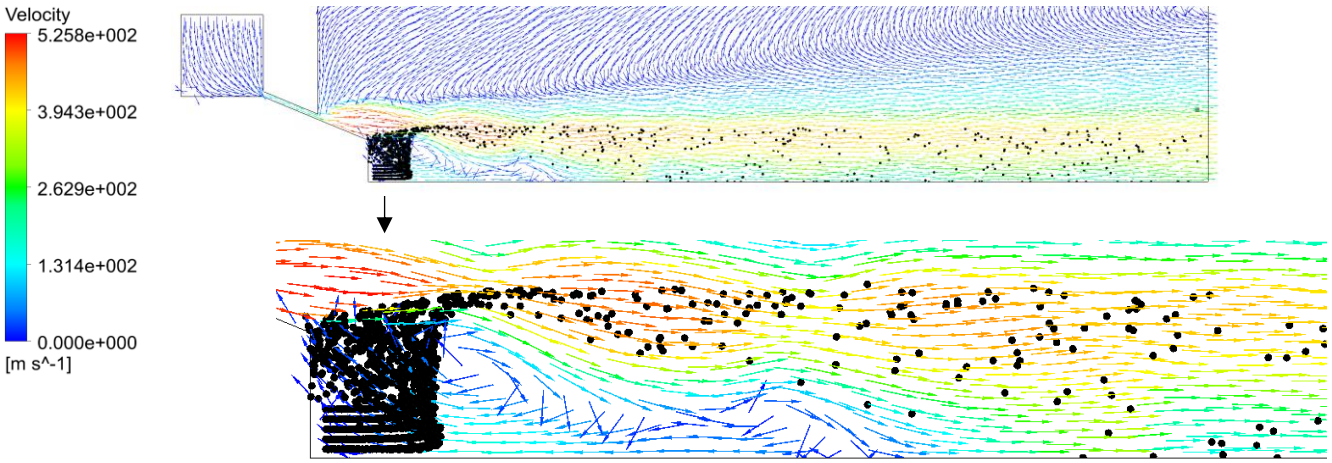

Flow time t = 32 ms

Figure A.12 Particle trajectories and velocity vector plots for t= 32 ms

converging along the axis much further away from the outlet. (closer to the melt nozzle).

Flow time 31-40 milliseconds

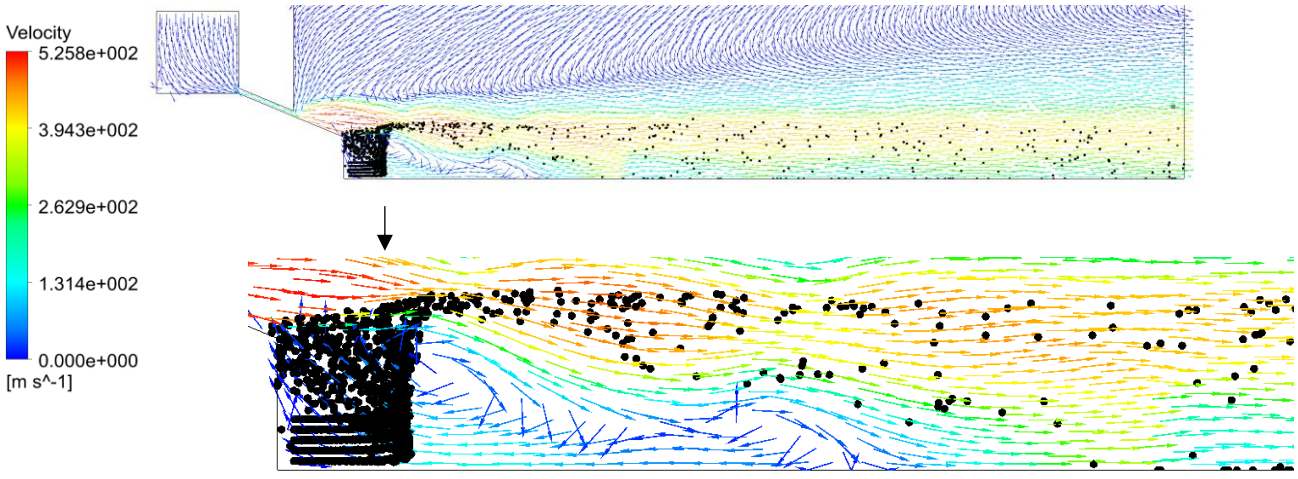

Flow time t = 35 ms

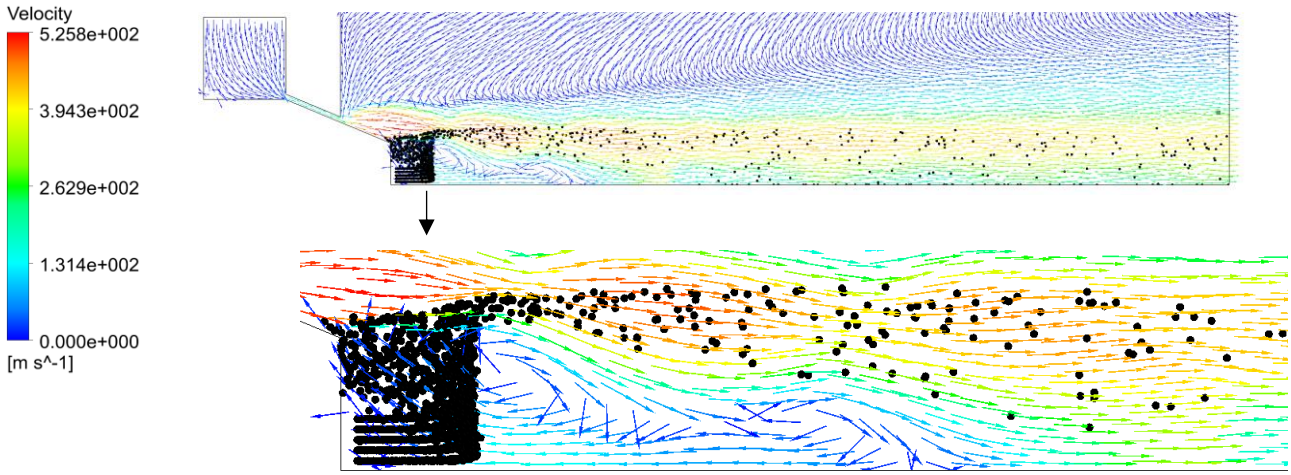

Flow time t = 38 ms

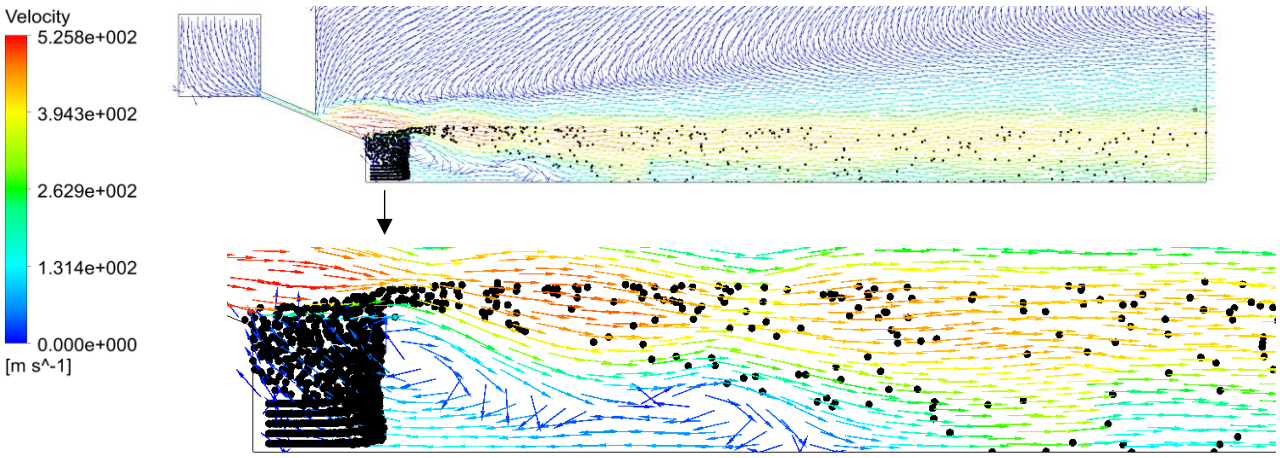

Flow time t = 40 ms

Figure A.13 Particle trajectories and velocity vector plots for t= 35 ms, t= 38 ms and t= 40 ms

Figure A.12 Particle trajectories and velocity vector plots for t= 32 ms and Figure A.13 shows the particle trajectories till 40 milliseconds.

The particle mass concentration becomes nearly constant through the 40 milliseconds as seen in Figure 5.7. The particles do not move downstream the eye of the recirculation zone. As the number of particles entering the recirculation zone is constant, this constant particle mass concentration indicates that the number of particles exiting the recirculation zone is constant i.e. the mass of the recirculating gases is sufficient to carry the particles into the gas jets.

The particles join the gas jets before the first oblique shock as the eye of the recirculation zone is located just before it. The spreading of the particle trajectories does not exhibit any notable change through 40 milliseconds. The spread of the particle trajectories increases as the flow move towards the outlet, particles travel along the boundary of the recirculation zone and the trajectories converge along the axis near the recirculation zone. The particles do not enter the recirculation zone throughout till 40 ms.

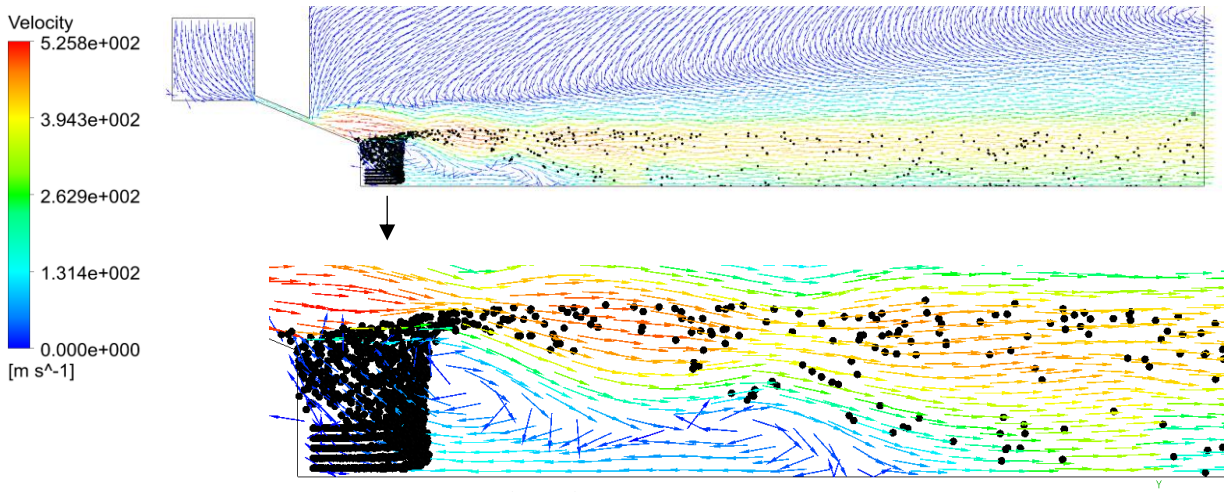

Flow time t = 42 ms

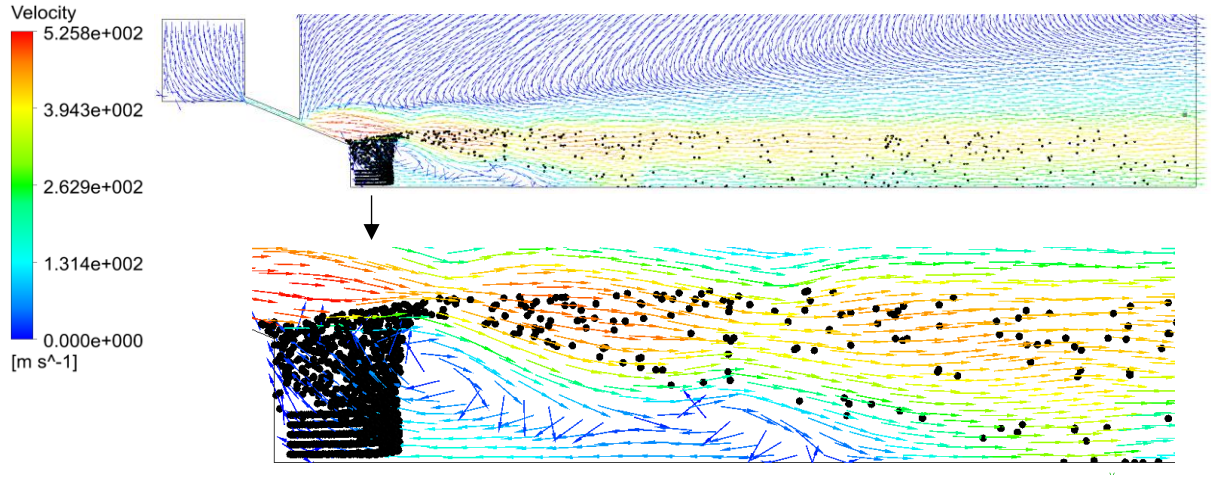

Flow time t = 45 ms

Figure A.14 Particle trajectories and velocity vector plots for t= 42 ms and, t= 45 ms

Flow time 41-50 milliseconds

The particle mass concentration is nearly constant till 50 milliseconds. There are no notable changes in the particle trajectories. The particles enter the recirculation zone, travel further downstream and reach the zero-velocity state at the eye of the recirculation zone. The particles then travel towards the melt nozzle surface and enter the high-speed gas jets. Figure A.14 and Figure A.15 shows the particle trajectories till 50 milliseconds.

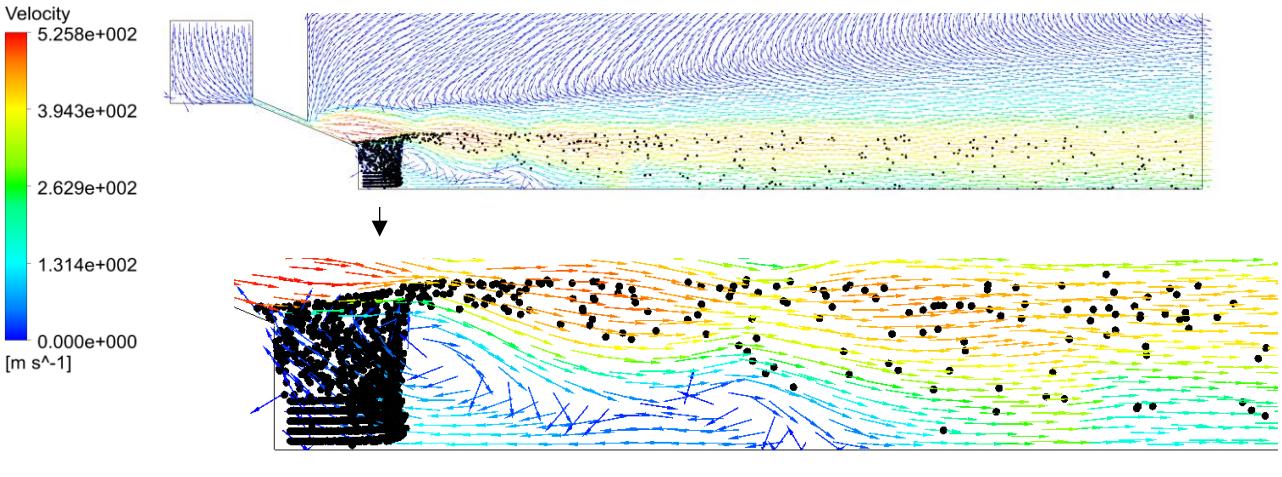

Flow time t = 50 ms

Figure A.15 Particle trajectories and velocity vector plots for t= 50 ms

CASE 4: 5 MPa

Figure A.16 shows the flow field with the closed wake highlighted. The GMR for this case was

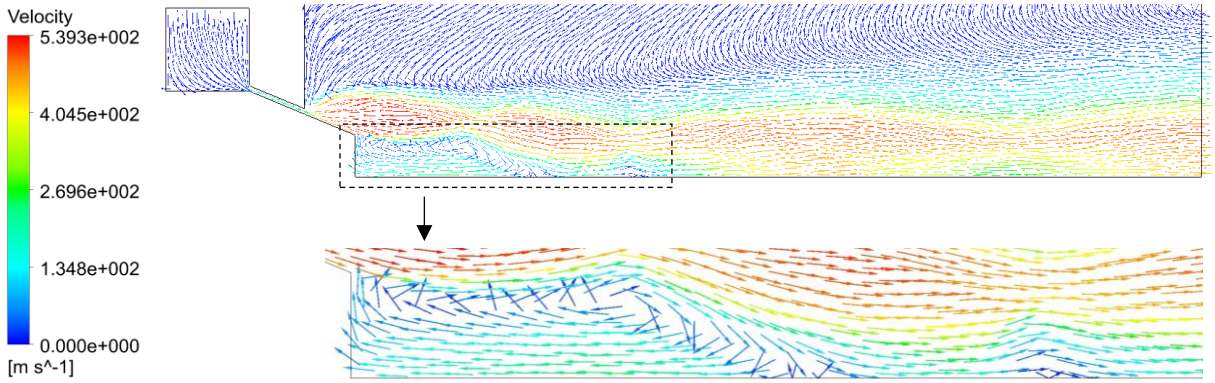

Figure A.16 Velocity vector plots for flow time t= 0 ms

found to be 0.478.

Figure A.17 shows the particle trajectories at time t=0.1ms. The particles flow against the recirculating gases.

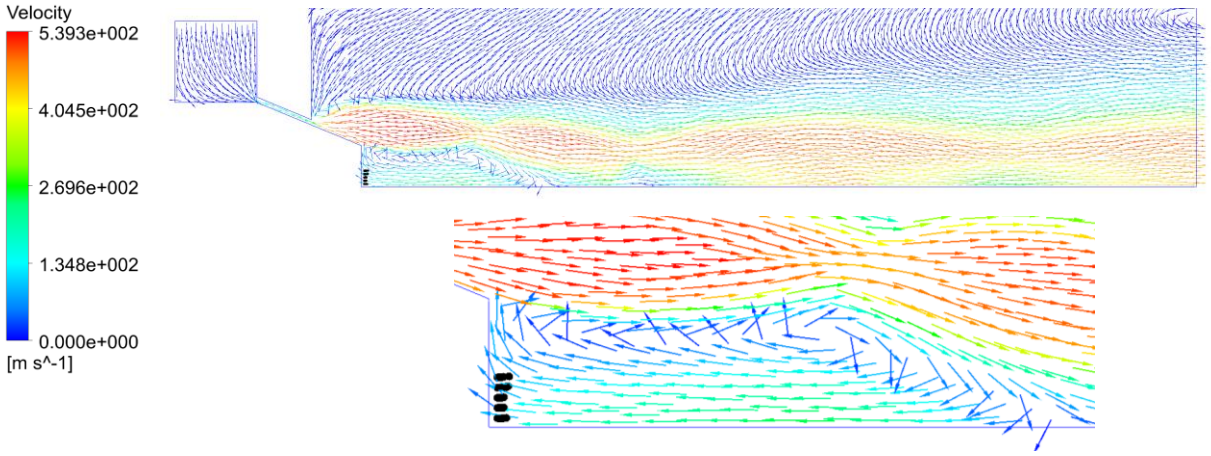

Figure A.17 Particle trajectories and velocity vector plots for flow time t= 0.1 ms

Figure A.18 shows the particle trajectories at time t= 0.5 ms. It can be seen from this figure that the particles have reached the zero-velocity state and is beginning to change their flow direction.

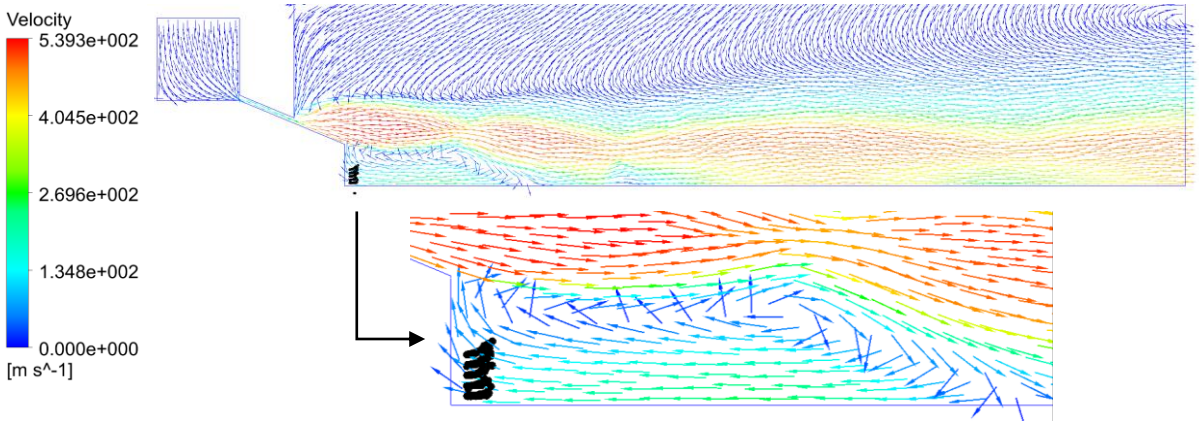

Figure A.18 Particle trajectories and velocity vector plots for flow time t =0.5 ms

Figure A.19 shows the particle trajectories at time t= 1 ms. It can be seen from this figure that the particles begin flowing with the recirculating gases towards the melt nozzle edge.

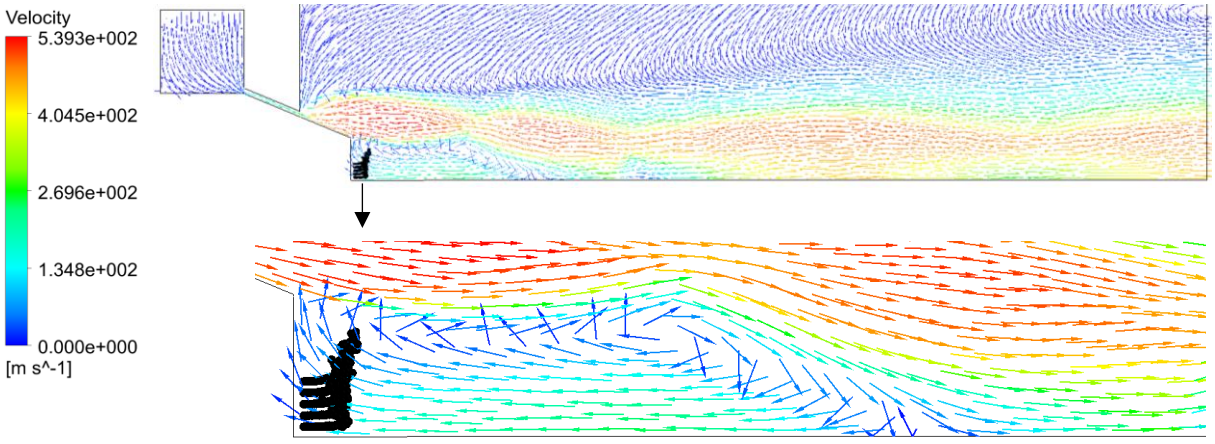

Figure A.19 Particle trajectories and velocity vector plots for flow time t= 1 ms

Figure A.20 shows the particle trajectories at time t=1.5 ms. The particles move along with the recirculating gases and enter the high-speed gas jets without reaching the melt nozzle surface. The gas flow rate increases with increasing atomizing pressure. As the gas flow rate into the atomizing chamber increases, the mass of the gas entering the recirculation zone also increases. As the number of the particles entering the recirculation zone is constant, this increased gas flow rate into the recirculation zone enables the particles to enter the recirculation zone without reaching the melt nozzle edge. The particles on reaching the high-speed gas jets begin travelling along the boundary of the recirculation zone towards the first oblique shock.

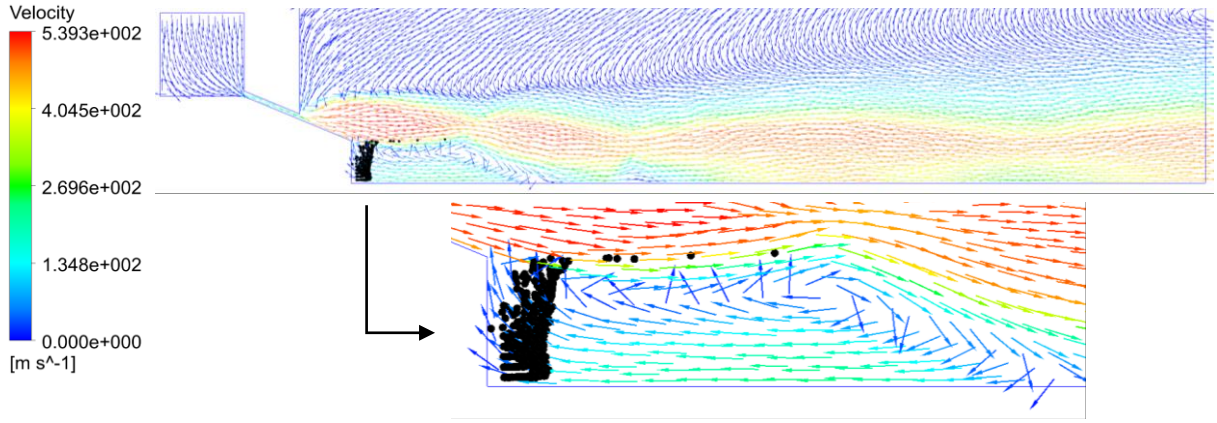

Figure A.20 Particle trajectories and velocity vector plots for flow time t= 1.5 ms

Figure A.21 shows the particle trajectories for flow time t= 2 milliseconds. As the particle mass concentration in the recirculation zone increases, the particles travel further downstream before reaching the zero-velocity state. The particles change their flow direction and travel.

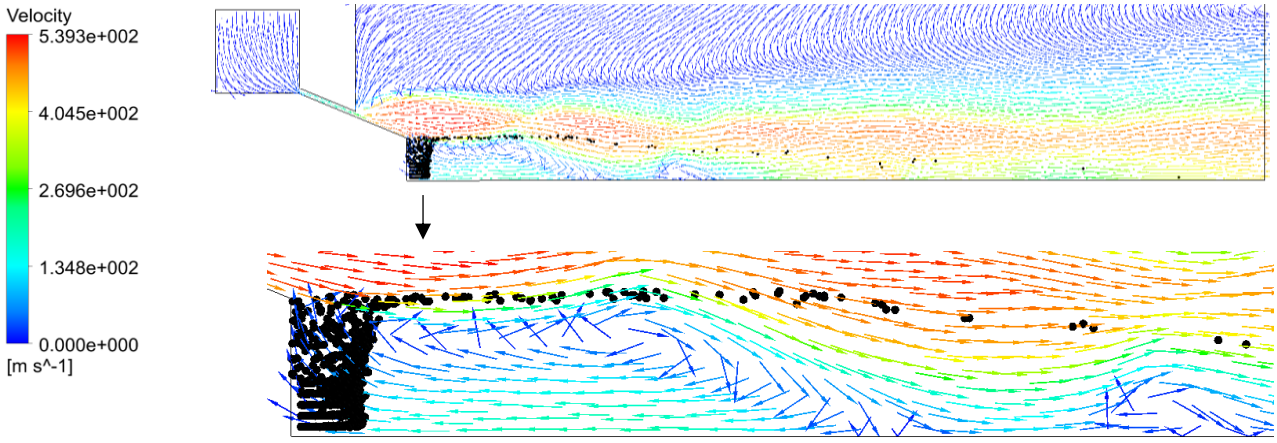

Figure A.21 Particle trajectories and velocity vector plots for flow time t = 2 ms

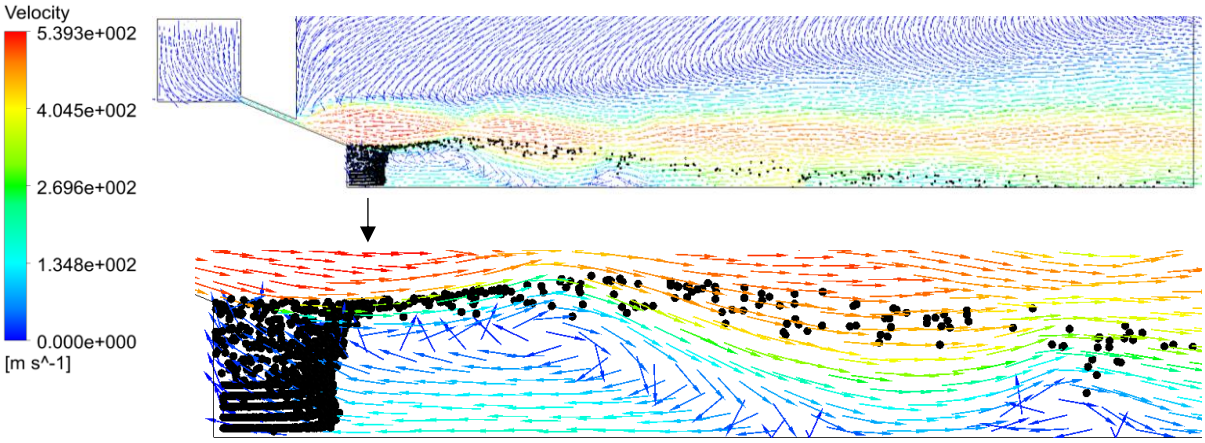

Flow time t = 5 ms

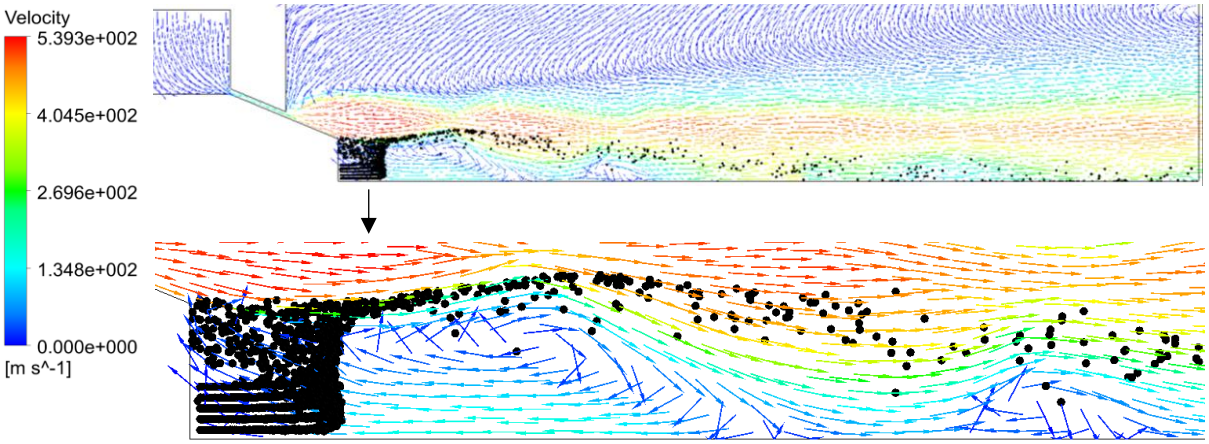

Flow time t = 8 ms

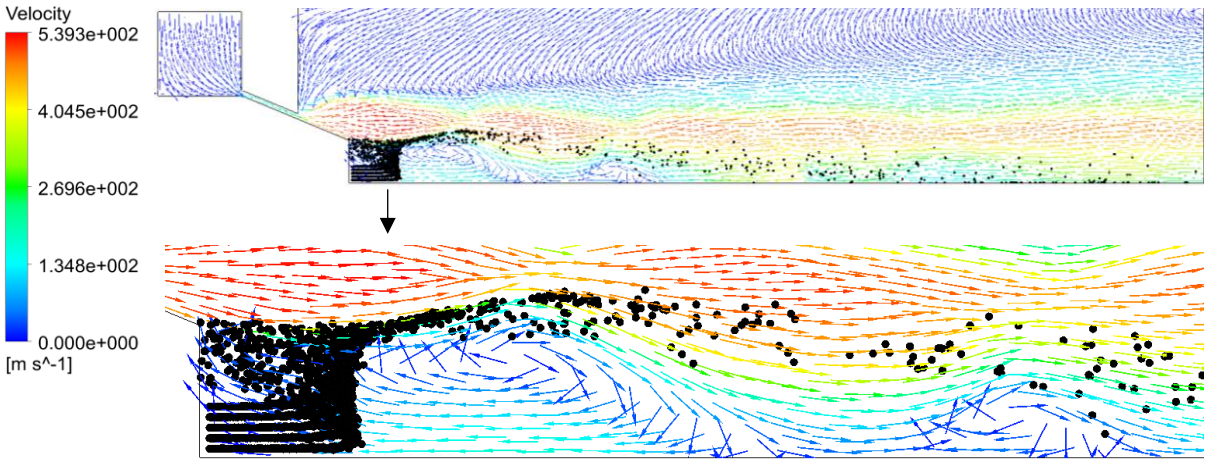

Flow time t = 10 ms

Figure A.22 Particle trajectories and velocity vector plots for t= 5 ms, t= 8 ms and t= 10 ms

before reaching the zero-velocity state. The particles change their flow direction and travel towards the melt nozzle surface to enter the expanding gas jets. The particles travel towards

the first oblique shock along the boundary of the recirculation zone.

The particles on reaching the first oblique shock enter the high velocity layers of the expansion waves and begin travelling towards the second oblique shock. On interaction with the second oblique shock, the particles begin moving towards the outlet along with the expanding gas jets. As seen from the Figure 5.8, the particle trajectories become directed towards axis as the particles move towards the outlet.

The particle mass concentration increases through 10 milliseconds. The particles begin exiting the domain at t= 3ms. As the flow time increases, the particles move further downstream towards the eye of the recirculation zone before reaching zero-velocity state. Figure A.22 shows the particle trajectories and velocity vector plots for various timesteps till 10 milliseconds.

The number of particles entering the high-speed gas jets increase as the particle mass concentration increases i.e. as the number of particles in the recirculation zone increases, the number of particles carried by the recirculating gas towards the melt nozzle and hence the number of particles entering the high-speed gas jets increase. This can be seen from the Figure A.22 as the thickening spread along the boundary of the recirculation zone.

The particles travel along the boundary of the recirculation zone towards the first oblique shock. As the gas jets expand downstream the first oblique shock and this results in spreading of particle trajectories along the high velocity layers of expanding gas jets. Also, this thickening of spread results in few particles entering the recirculation zone, recirculate along with the gases and travel along the boundary of the recirculation zone.

The 5 MPa operating pressure results in a closed wake. On crossing the first oblique shock, the particles travel towards the second oblique shock and the spread of the particle trajectories increases between the two oblique shocks. The second recirculation zone (due to closed wake) is located just before the second oblique shock. The gases and the particle trajectories undergo compression across the second oblique shock and begin expanding downstream it. Few particles travelling along the low velocity layers of the second recirculation zone enter into it, move along with the gases and join the expanding gases again.

The strength of the shock decreases with the increasing distance from the melt nozzle. Due to this, the spread of the particle trajectories increases, and they move towards the outlet. The expanding gas jets converge along the axis and move towards the axis. the trajectories of the particles carried by these gases also converge along the axis and bounce off from the axis boundary. The particle trajectories converge increasingly further away from the outlet as the flow time increases.

Flowtime 11-20 milliseconds

The particle mass concentration increases through 20 milliseconds. The particles entering the recirculation zone move further downstream increasingly closer towards the eye of the recirculation zone before reaching the zero-velocity state. The particles on reaching the zero-

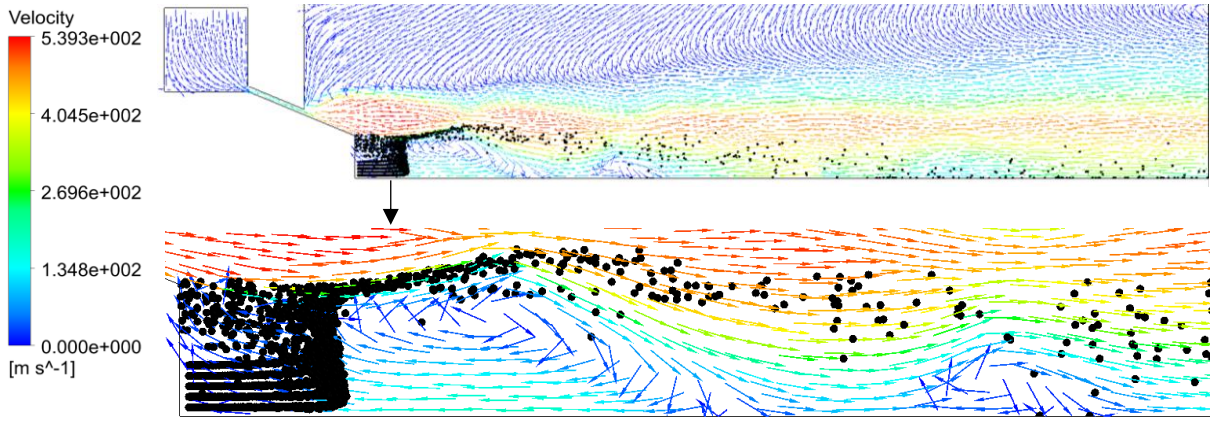

Figure A.23 Particle trajectories and velocity vector plots for flow time t= 12 ms

velocity state, change their flow directions and flow towards the melt nozzle surface where they enter the high-speed gas jets. The gas entering the atomizing chamber and hence the recirculation zone increases with the increasing operating pressure. It can be seen from the Figure A.23, Figure A.24 and Figure A.25 that a group of particles on reaching near the eye of the recirculation zone enter the high speed gas jets with the recirculating gases without reaching the melt nozzle surface. On the other hand, the rest of the particles travel towards the melt nozzle edge along with the recirculating gases and enter the high-speed gas jets.

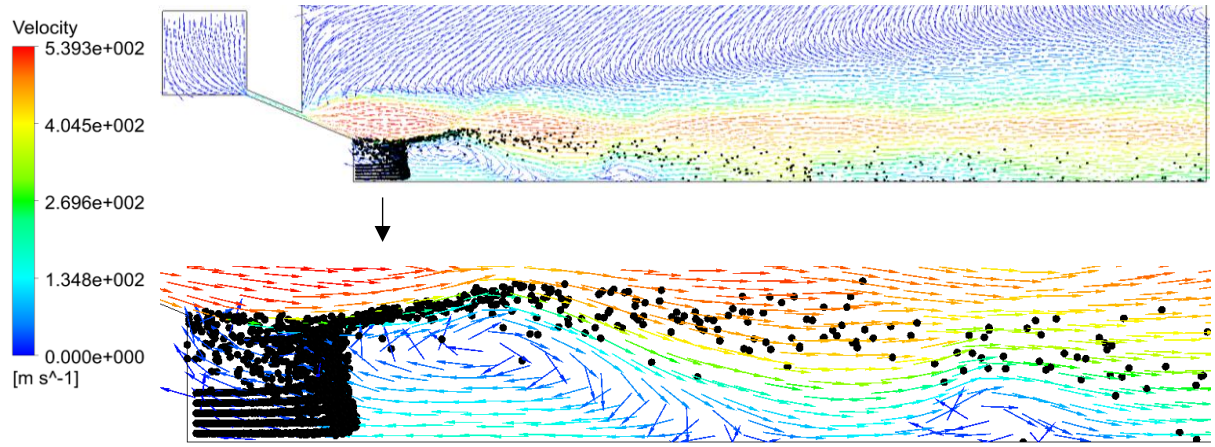

Figure A.24 Particle trajectories and velocity vector plots for flow tile t= 15 ms

The particles entering the high-speed gas jets move towards the first oblique shock along the boundary of the recirculation zone. As the number of particles entering the recirculation zone increases, the spread of the particle trajectories also increases along the low velocity layers of the expansion waves. Few of the particles bleed into the recirculation zone and recirculate along with the gases to re-join the high-speed gas jets again. The particle trajectories on crossing the first oblique shock begin spreading along the high velocity layers of the expansion waves towards the second oblique shock.

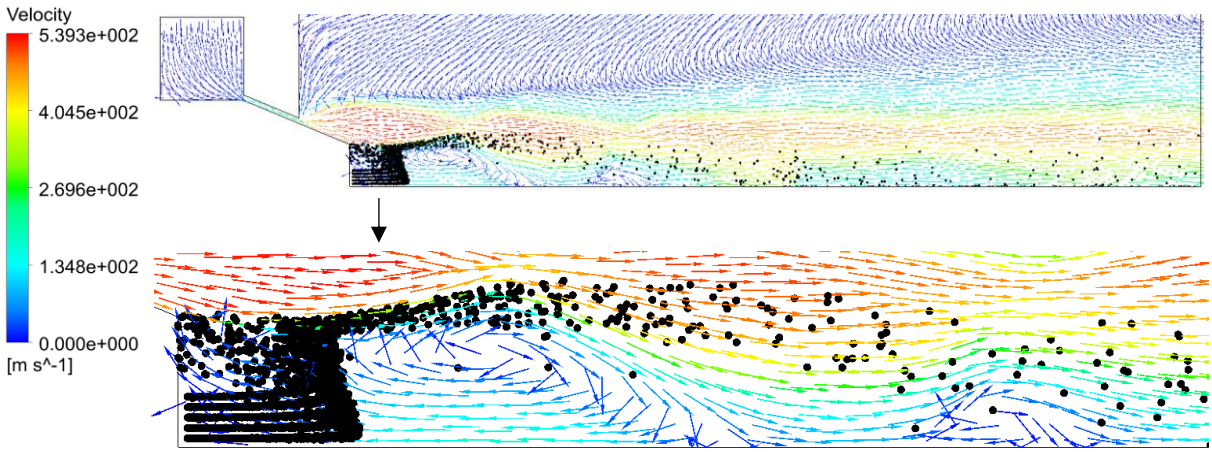

Flow time t = 18 ms

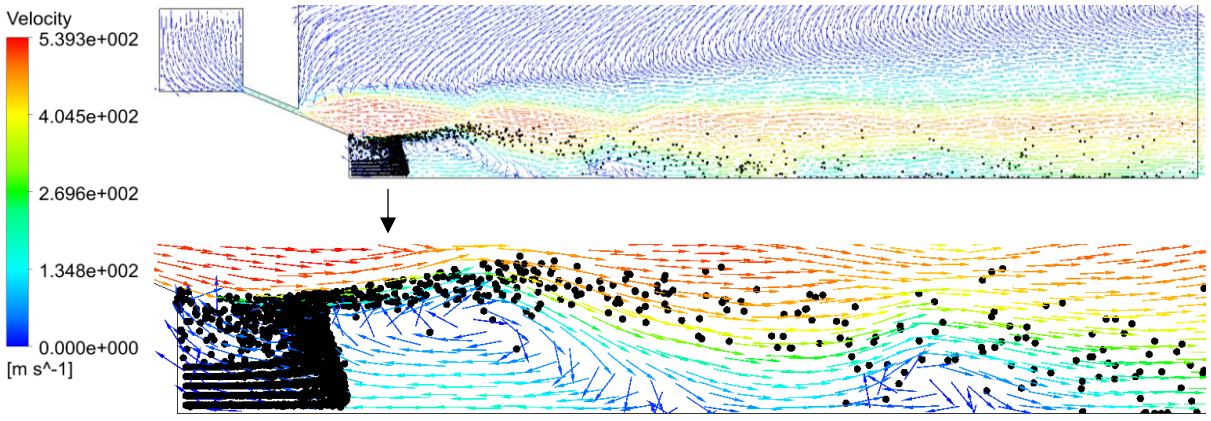

Flow time t = 20 ms

Figure A.25 Particle trajectories and velocity vector plots for flowtimes t= 18 ms and t= 20 ms

The second recirculation zone (due to closed wake) is located at the second oblique shock. The gases along with the particles undergo compression across the second oblique shock. The particles travelling along the boundary of the recirculation zone enter it, move along with the gases and join the expanding gases. The spread of the particle trajectories increases with the increasing flow time. This increasing spread leads to an increase in the number of particles entering the recirculation zone downstream the first recirculation zone.

The particles move towards the outlet on crossing the second oblique shock. The spread of the particle trajectories increases as the strength of the oblique shock decreases as they move towards the outlet. Figure A.23, Figure A.24 and Figure A.25 shows the particle trajectories and velocity vector plots for various timesteps between 11 milliseconds and 20 milliseconds.

Another consequence of this spreading of particle trajectories is that they converge along the axis further away from the outlet as the flow time (and the spreading) increases.

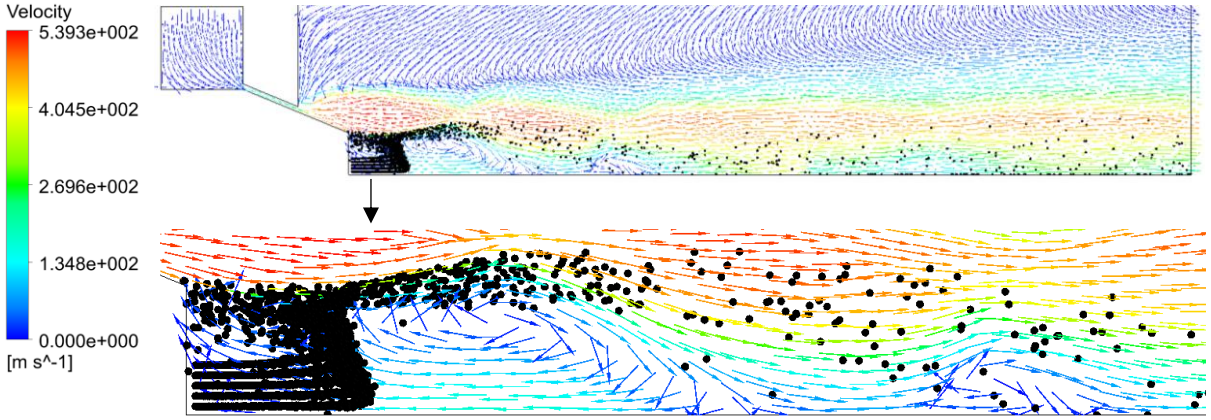

Flow time t = 22 ms

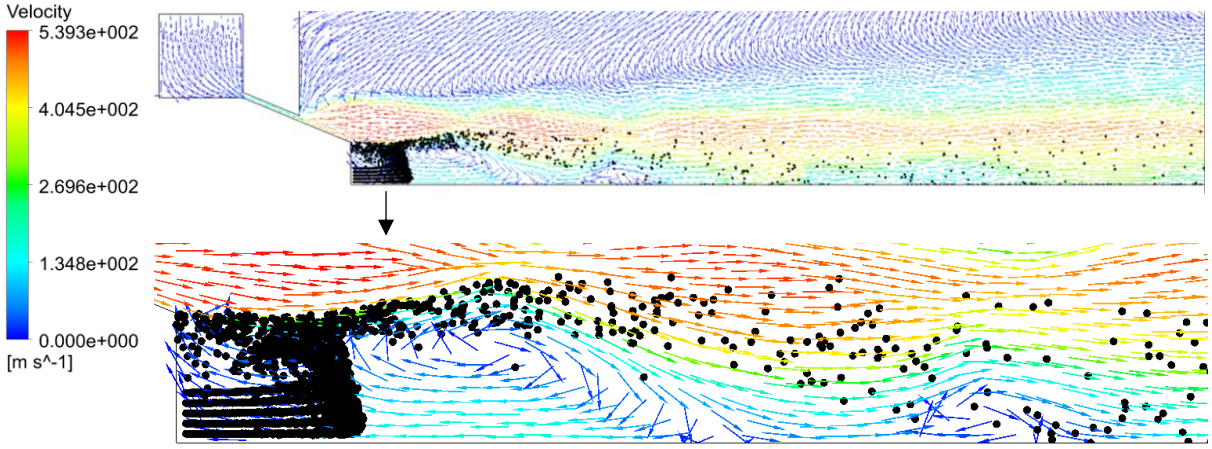

Flow time t = 25 ms

Figure A.26 Particle trajectories and velocity vector plots for flow times t= 22 ms and t= 25 ms

Flowtime: 21-30 milliseconds

The particle mass concentration increases gradually through 30 milliseconds. Figure A.26 and Figure A.27 shows the particle trajectories and velocity vector plots for various timesteps between 21 milliseconds and 30 milliseconds. The particles continue moving further downstream towards the eye of the recirculation zone on entering it. On coming in contact with the eye, the particles from the three injections farthest to the axis reach the zero-velocity state and begin flowing along with the recirculating gases. The particles from the other two injections (nearest to the axis) continue to move further downstream to reach the zero-velocity

state. This imbalance in the distance covered the particles flowing against the recirculating gases leads to a tapered spread of particles in the recirculation zone.

The particles entering the high-speed gas jets begin spreading along the boundary of the recirculation zone. The spread of the particle trajectories continues to increase. On crossing the first oblique shock, the gases begin expanding and the particle trajectories begin spreading as the gases move towards the second oblique shock. On encountering the second oblique shock, few of the particles enter the second recirculation zone, move along with the gases to join the expansion wave. The number of particles entering this recirculation zone increases with increasing flow time as seen previously.

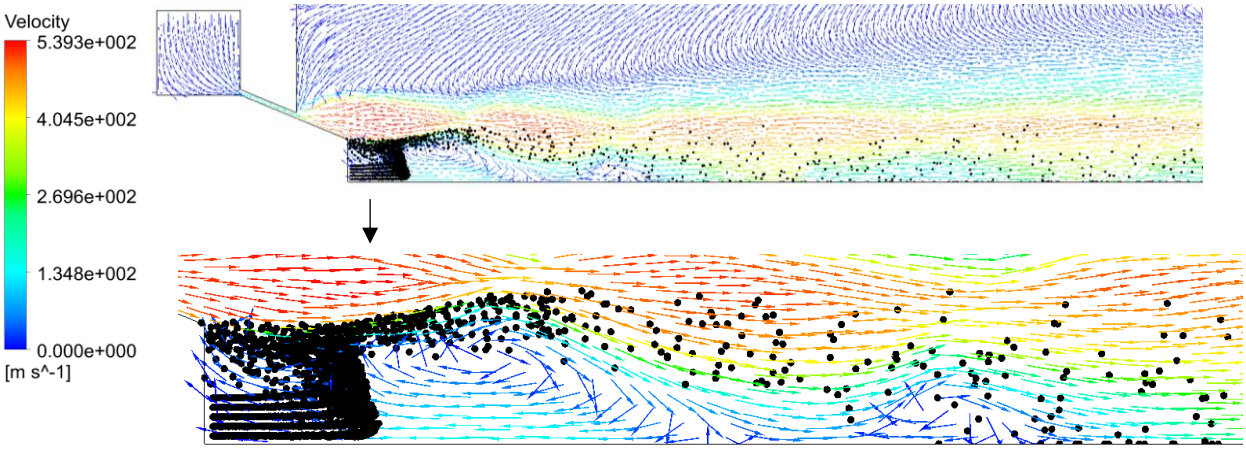

Flow time t = 28 ms

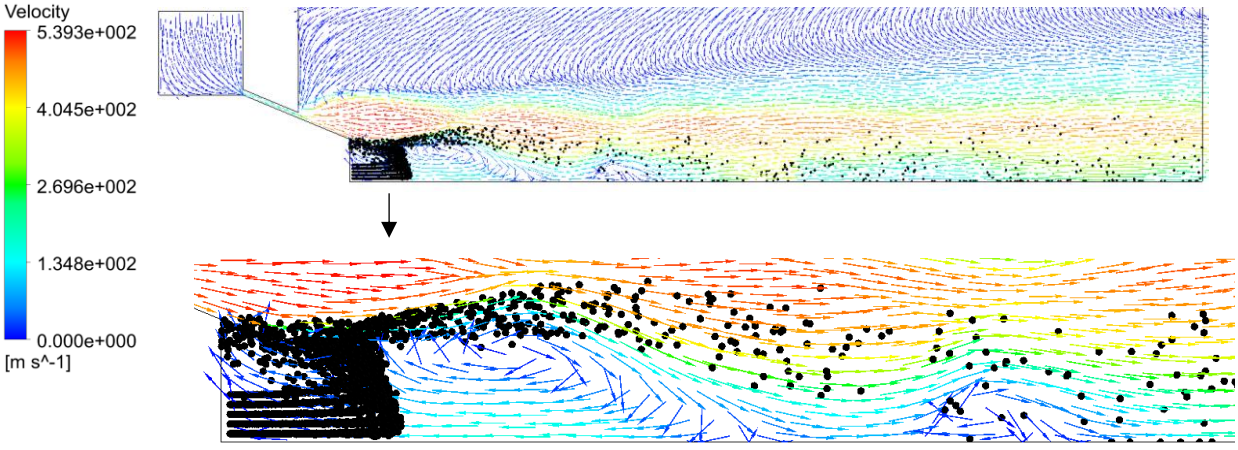

Flow time t = 30 ms

Figure A.27 Particle trajectories and velocity vector plots for the flowtimes t= 28 ms and t= 30 ms

Also, this increased spreading of particle trajectories leads to converging along the axis before and across the second recirculation zone. The particles that converge before and across the recirculation zone join the expanding gas jets after recirculating with the gases. The particles move towards the outlet through series of expansion waves resulting in spreading of particle trajectories.

Flowtime: 31-40 milliseconds

The particle mass concentration increases gradually through 40 milliseconds. Figure A.28 and Figure A.29 shows the particle trajectories and velocity vector plots for various timesteps between 31 milliseconds and 40 milliseconds. The particles exhibit the same behaviour as in the previous 10 milliseconds. The particles from the three injections farthest to the axis enter the expanding gas jets along with the recirculating gases and the rest of the particles flow along with the recirculating gases towards the melt nozzle edge to enter the high-speed gas jets. As the particles from the two injections closest to the axis continue to move further downstream and the particles from the three injections farthest to the axis are obstructed by the eye of the recirculation zone, the tapering of the particle spread becomes more pointed.

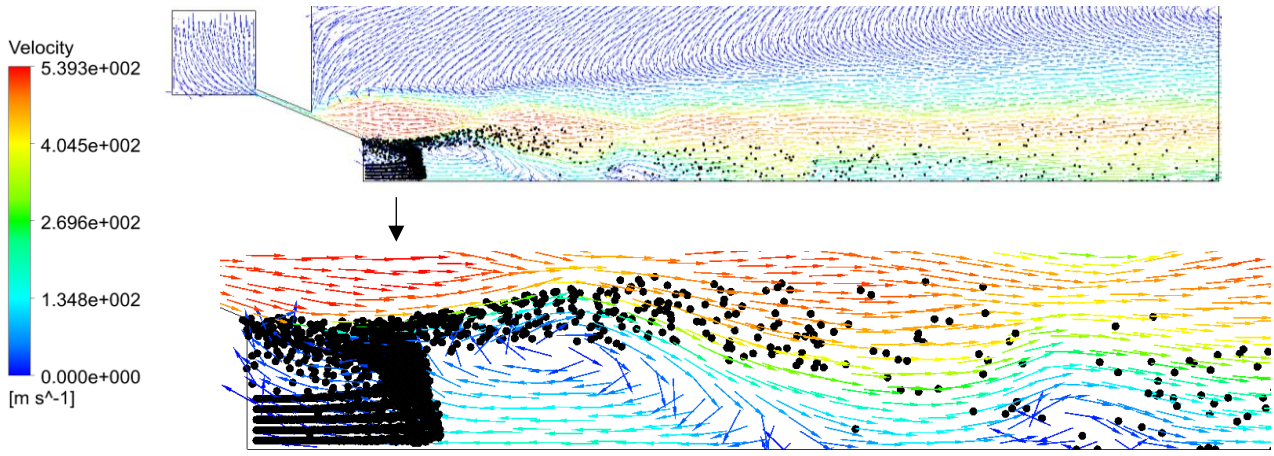

Flow time t = 32 ms

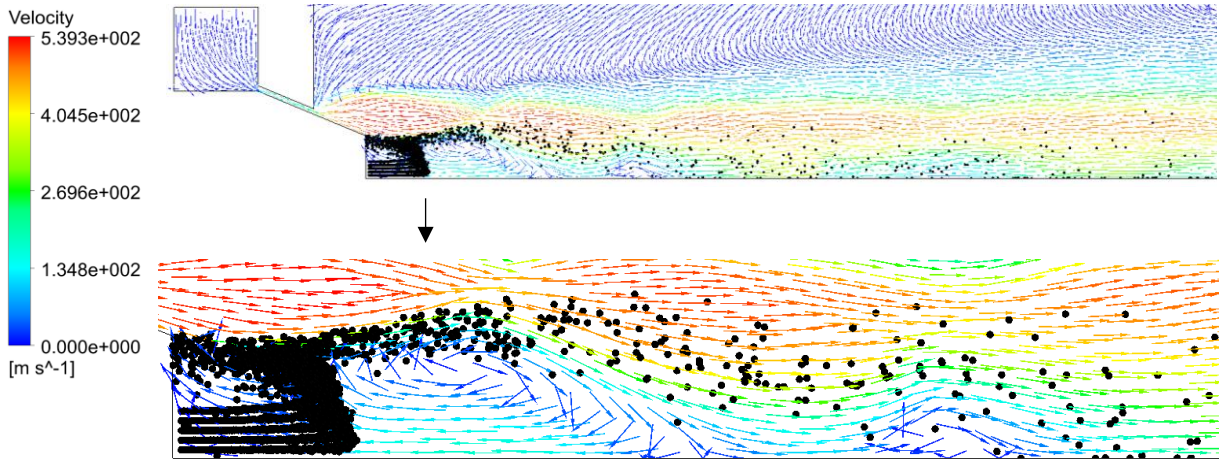

Flow time t = 35 ms

Figure A.28 Particle trajectories and velocity vector plots for flowtimes t= 32 ms and, t= 35 ms

The particles continue to enter the recirculation zone and move towards the first oblique shock. The spreading of the particle trajectories along the boundary of the recirculation zone

increases gradually and few particles enter the recirculation zone, move along with the gases there and join the high-speed jets again. On crossing the first oblique shock, the particles continue to move towards the second oblique shock. The trajectories begin spreading along with the high velocity layers of the expansion wave.

As the particle trajectories converge begin converging before the second recirculation zone, the particles enter into it, recirculate and join the high-speed gas jets. On crossing the second oblique shock, the particles begin moving towards the outlet and the spread of the particle trajectories increase along the various layer of the expansion wave.

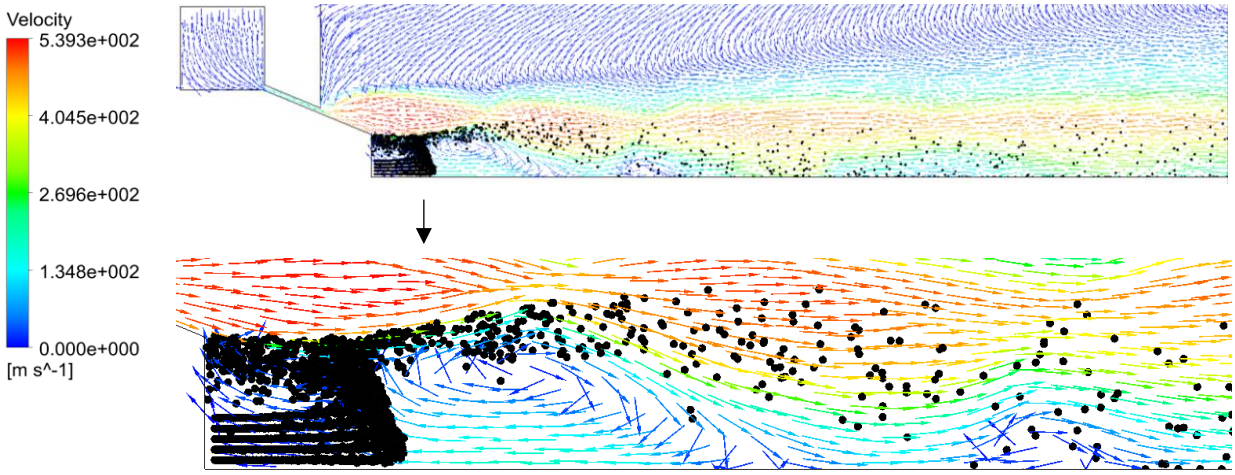

Flow time t = 38 ms

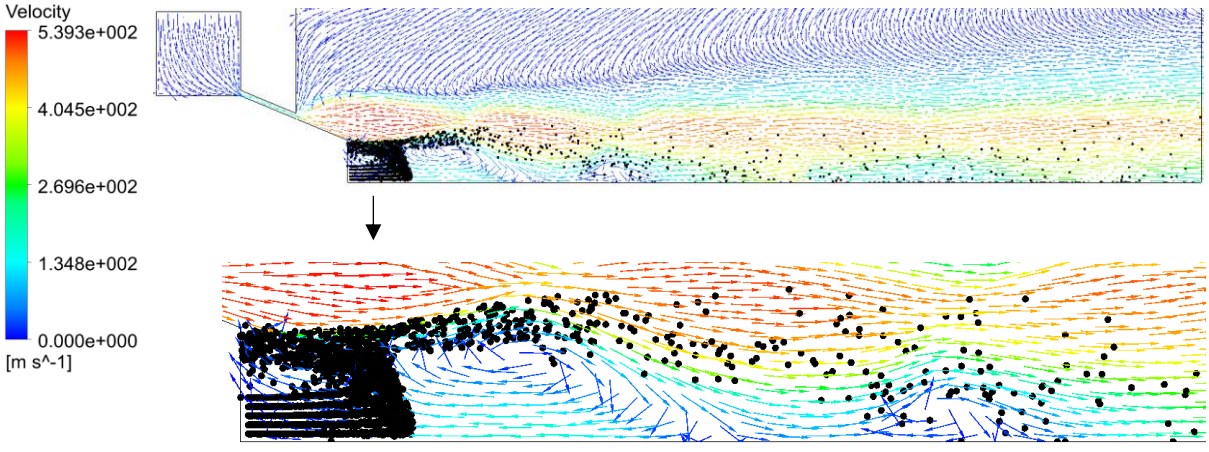

Flow time t = 40 ms

Figure A.29 Particle trajectories and velocity vector plots for flow time t= 38 ms and t= 40 ms

Flowtime: 41-50 milliseconds

The particle mass concentration becomes constant in the last 10 milliseconds. Figure A.30 shows the particle trajectories and velocity vector plots for various timesteps between 41 milliseconds and 50 milliseconds. As the number of particles entering the recirculation zone

is constant, this constant particle mass concentration indicates that number of particles exiting the recirculation zone is constant. The particles do not move further downstream, and particles move similarly as discussed in the previous section. The particles coming in contact with the eye of the recirculation zone enter the expanding gases without flowing back to the melt nozzle edge. The rest of the particles reach the melt nozzle edge and enter the recirculation zone.

The particles do not converge any closer than seen at t=40 ms. The particles move as discussed previously. They travel along the boundary of the recirculation zone towards the first oblique shock. Few of the particles continue to enter into the recirculation zone, recirculate and join the high-speed gas jets. On crossing the first oblique shock, they begin spreading as the gases expand. The trajectories of the particles converge at the second recirculation zone. Particles enter the second recirculation zone and move along the gases in it. Few of the particles travelling along the high velocity layers of the expansion wave continue to travel downstream

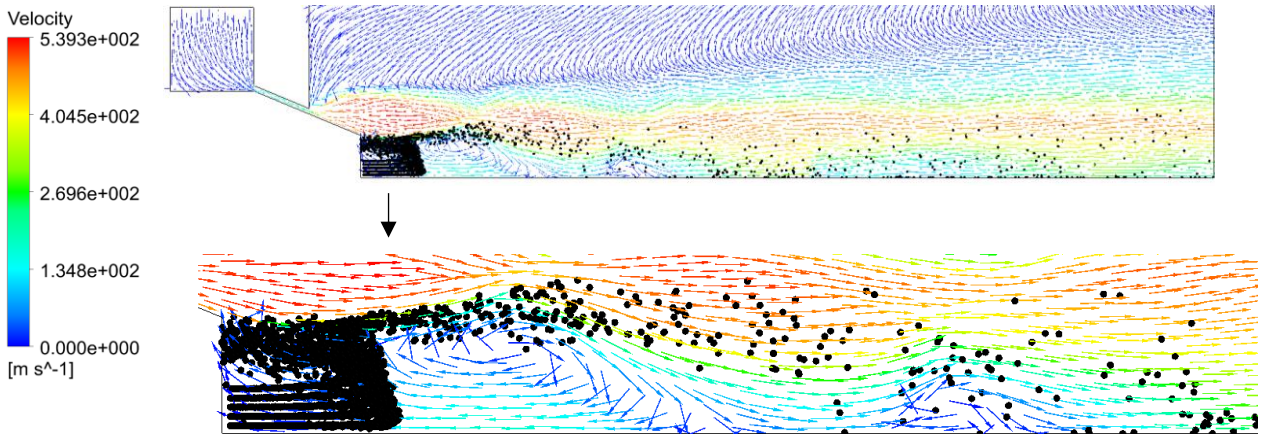

Flow time t = 45 ms

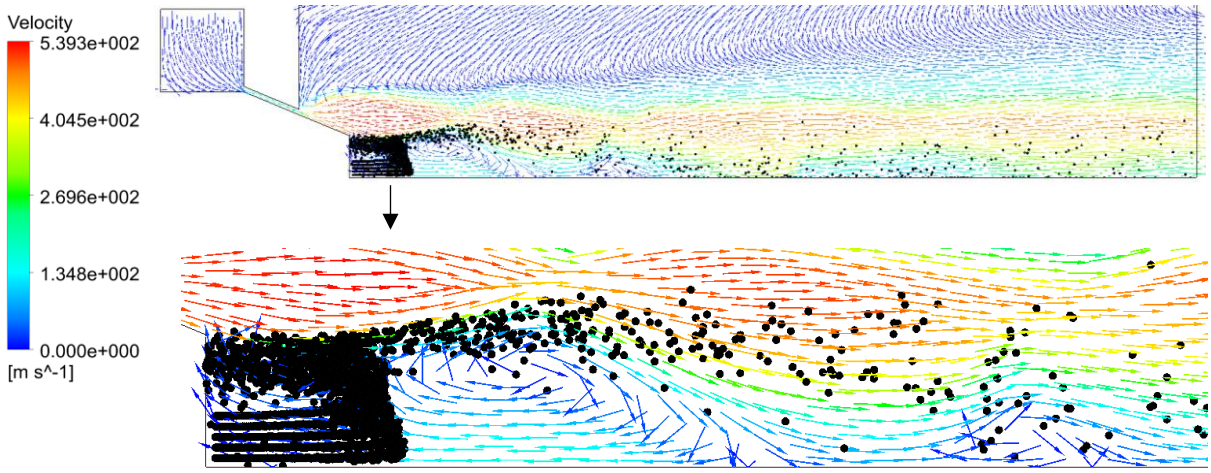

Flow time t = 50 ms

Figure A.30 Particle trajectories and velocity vector plots for flow time t=45 ms and t = 50 ms

without any interaction with this recirculation and converge along the axis. On crossing the second oblique shock, the particles begin moving towards the outlet and the spread of the particle trajectories increase along the various layer of the expansion wave.